PROBING BIOLOGICAL NANO-STRUCTURES WITH

ADVANCED OPTICAL TECHNIQUES

By

Jing Wang

A DISSERTATION

Presented to the Department of Biomedical Engineering

and the Oregon Health & Science University

School of Medicine

In partial fulfillment of

the requirements for the degree of

DOCTOR OF PHILOSOPHY

April 2017

School of Medicine

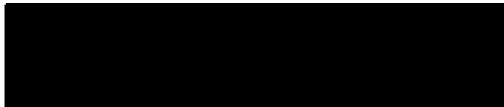Oregon Health & Science University

CERTIFICATE OF APPROVAL

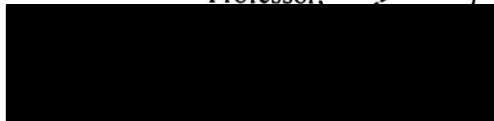This is to certify that the PhD dissertation of

Jing Wang

has been approved

_____
Xiaolin Nan, Ph.D.
Assistant Professor, Dissertation Adviser

_____
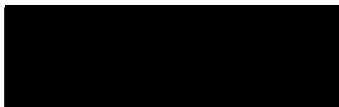Wassana Yantasee, Ph.D., M.B.A.
Associate Professor, Chair

_____
Joe Gray, Ph.D.
Professor,

_____
James Galbraith, Ph.D.
Associate Professor

_____
Jeffrey Iliff, Ph.D.
Assistant Professor

TABLE OF CONTENTS

iv

LIST OF FIGURES

LIST OF TABLES

ACKNOWLEDGEMENTS

It has been a wonderful journey to complete my doctoral dissertation and a subsequent Ph. D. degree. I came into this Ph. D. program as a transferred physics Ph. D. candidate student from the University of Arkansas. It was a tough transition period to get into biology world at the beginning. First time to use pipette; first time to culture cells; even need to update my vocabulary a lot. I had been getting used to designing experiments in advance based on established physical theories rather than making hypothesis. But now, I am about to complete this fun journey with accumulated scientific research experience and great passion to be a bio-physicist in the future.

During this journey, I have received great support from a group of people. With the supporters, I want to give my special and sincere appreciation to my supervisor Professor Xiaolin Nan first for his generous support, thoughtful advising, gentle encouragement and patient directing. All I have learnt from him and his continuous help and support in all stages is the foundation for me to complete the dissertation. I have been very proud and thankful to be chosen to join his group, where my experimental skills and research abilities get well trained and greatly improved. His amazing intuition and abundant creative ideas has and will continue to guide me as a researcher.

I would also like to give my special thanks to all my advisory committee members for their guidance and encouragement through these years. Professor Wassana Yantasee, Professor Joe Gray, Professor James Galbraith, and Professor Jefferey Iliff, their rigorous research attitudes and profound knowledge also benefit me in various aspects.

Thirdly, I would like to show my sincere appreciation to Dr. Min Xiao, who is my previous supervisor when I was in Arkansas. His generous support and knowledge sharing helped me get rid of lots of difficulties on experiment techniques and my life.

I am also very grateful to be able to work with several collaborators. Matthew Creech collaborated with me on imaging FFPE tissue samples with 3D SMLM and was responsible for antigen retrieval and immunostaining protocols. Dr. Steven Randolph (FEI) trained me on the iPALM prototype and helped acquire the initial iPALM images of HER2. My other collaborators, Cymon Kersch and Dr. Devon Anderson, have taught me various aspects of biology through our respective collaborations. Their professional knowledge helped us to approach our goals faster, opened my eyes, and enriched my both biological and technical skills in different areas.

I would also like to thank other members of the Nan lab. Dr. Tao Huang closely collaborated with me on the MSSRM project (Chapter 3), with a focus on instrumentation and algorithm development, where I worked on fluorescent probe screening and testing, all aspects of sample preparation and biological applications (Chapter3, Chapter4, Chapter5). And many thanks to other group members including Dr. Carey Phelps, Ying Zhang, Yerim Lee, and Elliot Gray, and also former member Dr. Li-jung Lin, Dr. Mo Chen, Andrew Nickerson, and Alec Peters. They brought fresh ideas and pleasure environment to our lab during my Ph. D. work and my dissertation preparation.

Last, but certainly not least, I would like to thank my grandparents, my parents, and my husband, Tao Huang, for their love and supports. Most special thanks to my dearest son, Rex, for his endless love, intelligent ideas and good sense of humor.

ABSTRACT

This thesis work focuses on technical developments in the field of superresolution fluorescence microscopy (SRM) and applications of SRM to probing the spatial organization of biological systems at the nanometer and single-molecule scales. Fluorescence microscopy has been a powerful and essential tool for analyzing biological structures and processes due to its noninvasiveness and high molecular specificity. The spatial resolution of conventional fluorescence microscopy, however, is limited to about 250 nm by the diffraction of light. In the last decade or so, a suite of SRM techniques such as stimulated emission depletion (STED) microscopy, photoactivated localization microscopy (PALM) and stochastic optical reconstruction microscopy (STORM), have been invented to circumvent the diffraction limited spatial resolution of fluorescence microscopy. Among these, PALM and STORM are both based on subdiffractive localization of single fluorescent molecules and are the primary technical basis of the present work.

I have constructed and calibrated custom PALM/STORM setups for both 2D and 3D imaging of biological samples, including cultured cells and clinical formalin fixed paraffin embedded (FFPE) samples, demonstrating the superior resolving power of these techniques. Next, we have developed multispectral superresolution microscopy (MSSRM) for cross-talk free, multicolor SRM imaging, by adding a single-molecule spectral detection module to an existing PALM/STORM setup. In MSSRM, we record single-molecule emission spectra concurrently with their positions, such that the identity of a fluorescent molecule could be determined based on the spectra instead of using an emission filter. As such, we were able to distinguish single fluorescent molecules emitting at wavelengths as little as 10-15 nm apart, and to demonstrate 4-color MSSRM imaging of cellular structures with essentially no spectral crosstalk ($<1\%$) using 4 spectrally similar dyes and a single laser excitation.

With the powerful SRM and MSSRM techniques, we studied the spatial regulation of HER receptors in cancer cells. Recent studies suggested that spatial mechanisms may regulate HER2 signaling and that peculiar organization patterns of the receptors may confer resistance to targeted therapy. Using 2D and 3D SRM, we found that both HER2 and EGFR are both enriched in actin-rich, filopodia-like membrane protrusions (FLPs) that are only 100-200 nm wide and several to tens of microns long. Strikingly, HER2 organizes into unusual, helical patterns in the FLPs, likely linked to the actin cytoskeleton through direct or indirect anchorage. These features may serve to organize and stabilize HER signaling complexes but have not been described before due to their small dimensions below the resolution limit of conventional light microscopy. Furthermore, I used SRM to capture the dynamics of HER2 helices in live cells and showed that HER2 helices are dynamic structures that likely form along with the FLPs. Using the MSSRM, I also was able to resolve changes in the nanoscopic spatial distributions of EGFR and HER2 in association with HER2/EGFR interaction during receptor signaling. In particular, EGF stimulation led to retraction of FLPs and formation of nanoscopic membrane ruffles, where HER2 and EGFR are co-enriched and presumably interacting through HER2:EGFR complexes. Lastly, I have used the MSSRM to visualize HER receptor nanoclusters by labeling and imaging the receptor in multiple colors simultaneously, in which case the co-localization between two or more colors indicate clustering. These results demonstrate the utility of SRM and MSSRM in revealing the spatial organization of HER receptors not previously known, which opens a new direction in HER biology.

Besides using the MSSRM for multicolor superresolution imaging, I have also used the MSSRM to map membrane nanodomains, which are hypothetical structures commonly implicated in spatial regulation of biological processes through protein clustering and compartmentalization. By using small molecule, lipophilic probes that exhibit environment-sensitive emission spectra, I was able to obtain a 'spectral' map of the plasma membrane and

endomembranes with nanometer spatial resolution. My results directly prove that cellular membranes are heterogeneous at the nanoscale. Some of the structures revealed in these spectral images may correspond to the hypothetical lipid rafts, and future work to validate these observations are underway.

In summary, our work clearly demonstrated the power of SRM techniques in advancing our understanding of biology by revealing molecular and structural details of biological systems that cannot be resolved previously. By extending the spectral resolution of SRM through the MSSRM, we can now interrogate complex biological structures and processes that involve a multitude of components and potentially establish a molecular atlas of biological systems. Initial studies using these tools have already started to yield new insights into HER receptor signaling at the membrane, which are canonical signaling molecules thought to be well understood. I anticipate that further technical developments and applications of SRM will fundamentally transform our understanding of biology from an 'interactome' or connectivity type of view to a more accurate and realistic, physical view.

Chapter 1   Introduction

Imaging at the nanometer scale is a topic of fundamental scientific importance and technological relevance in medicine. Advanced far-field optical methods that originated in physics and material science have become powerful and indispensable tools for analyzing the organization of life at the nanoscale – the scale of individual biological molecules that make up life. Light in the visible and near infrared (NIR) range is particularly well suited for probing biological samples for its minimal perturbation to living processes and structures. Numerous imaging techniques based on a variety of light-matter interactions and contrast mechanisms allow detailed studies of fixed or live specimens in time and space.

Owing to rapid advances in light source and detection technology, the last decade has seen tremendous progress in biological microscopy, most remarkably the development and application of superresolution fluorescence microscopy (SRM), which bears the promise of transforming biomedical research as highlighted by the 2014 Novel Prize in Chemistry awarded to Drs. Eric Betzig, Stefan Hell and William E. Moerner [1]. Besides celebrating the achievement of breaking the diffraction-limit of light microscopy, the award is also regarded as a demonstration of the success of single-molecule fluorescence spectroscopy since its first advent nearly 40 years ago.

My thesis reflects work in two different areas of optical imaging. While at the University of Arkansas (2010–2014), I worked on experimental investigations of electromagnetically induced transparency (EIT) related phenomena for studying light – atoms interactions [2]. After transferring to OHSU, the focus of my work shifted significantly to using SRM to study biological processes important for understanding and treating cancer. Albeit seemingly disparate, the two research projects share a common theme in that both use light to probe structures, and

hence fundamental rules of physics such as interactions between electromagnetic waves with molecules or atoms apply in both systems. This commonality even traces back to my previous trainings in quantum optics, where validation of theories inevitably involved optics and particularly laser optics and spectroscopy. In this chapter, I describe the basic principles of light, which is needed to understand the mechanics of light microscopy, and interactions between light and matter such as molecules and atoms, followed by a brief introduction to light microscopy and its applications in biomedical research. To set the stage for subsequent chapters, we will touch upon a few important biological structures such as lipid rafts and other cell membrane features that are of primary interest to us. These will serve as a foundation to the following chapters.

1.1 Fundamental physics of light

Our understanding of the nature of light has evolved from 'seeing' light with naked eyes to obtaining the solar spectrum, to realizing that light is a form of electromagnetic radiation, and to developing classical and quantum theories to describe light and light-related phenomena. To date, the nature of light is largely well established – interpreted as as energy quanta named photons in quantum theory and as electromagnetic waves in classical theory.

1.1.1 Light as a wave

The nature of light as a wave has long been recognized through empirical as well as scientific observations, which ultimately prompted Maxwell to establish the classical theory of light as alternating electric and magnetic fields. One of the important characteristics of waves is superposition: several light waves meeting in space to generate a sum wave, a process called interference, which is the basis of a series of wave phenomena to be described below.

Interference. In 1802, Thomas Young (1773-1829), a British physicist, observed that, when multiple light rays meet in space, alternating bright and dark patterns – a result of

constructive and destructive interference - of light could be generated [3,4]. There are many technological applications of interference effects in light. For example, Freshnel bimirror, Michelson interferometer, etc.

It has to be noted that, not every light wave superposition can yield interference; the conditions necessary for the interference, also known as coherent conditions are that: 1). the electromagnetic oscillations of the two light waves overlap (i.e., not orthogonal); 2). the two light waves have the same frequency; 3). the phase relationship between the two light waves remains constant.

The distance or duration over which interference can be observed is respectively dependent on the spatial and temporal coherence properties of the light. That said, ordinary light sources had been used to achieve interference in many applications through methods such as sub-wave and sub-amplitude, which produce interference by dividing the original wavefront (or equivalently, the light ray) or by partial reflection of the original light beam into multiple parts then superimposing the parts. For example, the double-slit interference is a typical sub-wave interference, and the multiple color seen from oil films on water or soap bubbles are examples of sub-amplitude interference.

Diffraction. Light propagates in a uniform medium by a straight line, and at the interface between two different media it is reflected and refracted. Light being an electromagnetic wave, it can also bypass a barrier of which the dimensions are comparable or smaller then the wavelength, a process called optical diffraction, with a resulting intensity pattern resembling that from interference[4]. Italian physicist and astronomer F. M. Grimaldi in the 17th century first accurately described the diffraction phenomenon of light. 150 years later, the French physicist A. J. Fresnel in the 19th century clarified this phenomenon earliest. The diffraction effect makes the intensity distribution from the obstacle different from the intensity distribution of the original, freely

propagating light wave. In practice, diffraction makes details of the sharp edges of the obstacles lost – an important note in understanding spatial resolution.

Wave diffraction has the following general properties: First. the angular spacing of the diffracted wave is inversely correlated with the size of the object causing diffraction. The smaller the size of the object that causes the diffraction, the wider the diffraction fingers it forms, and vice versa. For example, in the single-slit diffraction, $d = \lambda * \sin\theta$. Second, the magnitude of a given diffraction angle depends only on the relative value of the wavelength of the incident wave and the size of the diffractive object. Third, when the object structure causing the diffraction has a periodicity comparable to the wavelength (e.g., a diffraction grating), the pattern after diffraction becomes narrower.

Hence, while in theory any wave can diffract; in practice, the extent to which waves diffraction differ considerably depending on the wave and object geometries. This has implications to many applications. In particular, the imaging quality of the optical imaging system is limited by diffraction. The incident light on the lens will be diffracted to form an airy spot, resulting in light beam cannot converge to an infinitively small point. As such, the larger lens aperture and the shorter the wavelength are, the better the resolution of the imaging system can acquire.

1.1.2 Light as energy quanta (photons)

In early 19th century, Thomas Young, Fresnel and Marius observed the interference, diffraction and polarization phenomena of light. In 1960s to 80s, Hertz studied electromagnetic waves and proved that the light was also an electromagnetic wave [5]. Later, Hertz accidentally discovered that, when light was shine on the gap of a circuit, the gap is more likely to generate a spark, the earliest discovered photoelectric effect. French physicist Lernard and British physicist Tomson confirmed that light illuminating a metal surface will cause the electrons to escape. The wave property of light can only partially explain the photoelectric effect, and a new theory was

needed to explain the photoelectric effect. That's when the community began to pay closer attention to the particle properties of light.

In the 20th century, German physicist Max Planck proposed the concept of energy quantum, which is that light must carry energy in discrete quantities; light can only be absorbed and emitted with an inseparable energy quantum which is called photon. The basic energy increment equals hν, where h is a universal constant now known as Planck's constant and ν is the frequency of the radiation. Since 1907, the American physicist Millikan began to experiment with several important physical quantities related to the photoelectric effect - the frequency of the light, the voltage threshold of the metal – among others, and he calculated the Planck constant h based on the photoelectric effect equation [6]. Next, Bohr applied Plank's ideas to refine the model of an atom [7]. He proposed that electrons populate different orbits with discrete energy levels; when an electron jumps from one orbit to another at a lower energy level, it can give off energy in the form of a photon. These laid the foundation of the quantum theory of light. In 1912-1918, the American physicist Compton proposed that photons not only have energy but also have momentum, and that the momentum of a photon is p=h/λ.

1.2 Light-matter interactions

Light can be used as a tool for probing biological and material structures because of its interactions with various matters. Depending on the exact nature of the interactions, different properties of the matter and/or light itself can be probed. We describe the fundamental processes of light-matter interactions that form the basis for biomedical imaging.
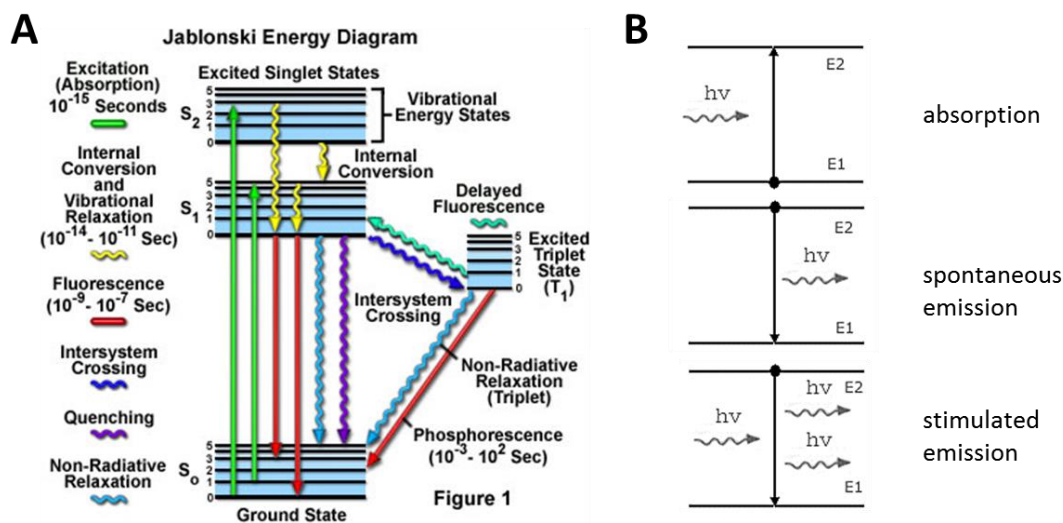
Figure 1.1 Light absorption and emission.

(A) Jablonski diagram of light absorption and emission and associated processes (adapted from Olympus microscopy resource center); (B) Light absorption (top), spontaneous emission (middle), stimulated emission (bottom), (adapted from LASER tutorial).

1.2.1 Light absorption and emission by atoms and molecules

In quantum theory, an electron of an atom, a molecule, or an atomic lattice can absorb a photon only if the energy is matching with a potential energy differences between an energetically high energy excitation state and a low energy ground state. The electron will acquire energy from the photon to transition to an energetically excited state. The typical lifetime of such an excited state is very short, on the order of a few nanoseconds (*ns*). After that, the electron can return to a electronic ground state with the energy difference emitted as a photon. In Bohr's atomic model [7], the orbiting electrons in an atom could only exist in permitted "electronic states" with well-defined energies. Otherwise, photons won't be absorbed. Conservation of energy determines the energy of the photon and thus the 'color' of the absorbed or emitted light. As a result, absorption spectrum of atoms has discrete peaks corresponding to potential transitions between different energy levels, while absorption spectrum of molecules – which have much

6

more complex electronic energy levels - are more continuous with highly overlapping, complex energy transitions.

Beside the energetics, another essential property of these processes is the time scale at which they occur. As described by the Jablonski diagram (Fig. 1.1), light absorption is extremely fast, taking place at a time scale of $\sim 10^{-15}$ second, or 1 femtosecond (*fs*). The absorption of photons by an atom is a probabilistic event, with the probability proportional to the intensity of the light (or the number photons per unit time) falling on the proximate area of the atom; the probability of absorption is commonly referred to as the absorption cross-section of the matter. When an isolated atom is brought into an excited state, it generally stays in the excited state for a very short period of time before emitting a photon and transitioning to a lower energy state. This whole process is called spontaneous emission, which is also a probabilistic event. The average time needed for these processes are on the order of 10^{-9} to 10^{-8} second, i.e., a few *ns*.

In contrast to spontaneous emission, an atom or atomic system in an electronically excited state can also emit a photon when encountering another photon carrying the same energy as the energy gap between the electronically excited state and the corresponding ground state. This process, predicted by Einstein, is named stimulated emission. The main difference of stimulated emission to spontaneous ones is that, in this process the newly emitted photon will be identical in every respect to the stimulating photon – energy (frequency), polarization, propagation direction, and phase. This means that light can be copied and amplified from a single photon traveling inside a closed cavity as long as the round-trip length of the photons is exact multiples of the wavelength of the light. Indeed, $\sim$ 40 years after Einstein's work, light amplification by stimulated emission of radiation (*laser*) was invented, a device that amplifies light through the stimulated emission process. Compared with other light sources, laser is highly monochromatic, directional, and highly coherent, because of the underlying properties of stimulated emission, enabling numerous applications that benefits our modern life and biomedical research.

1.2.2 Light scattering (reflection, refraction)

The scattering of light may be treated as the redirection of light when an incident light ray encounters an obstacle, inhomogeneous media, or a particle (such as an atom) [8]. As light interacts with a particle, the photon gets absorbed and then released by the electron of the particle, resulting in scattered light. The majority of light scattered by the particle is emitted at the identical frequency of the incident light, a process referred to as elastic scattering. The energy of photon is well reserved while the direction information of photons gets lost during this process.

The scattering of light by particles depends on the particle size. The scattering caused by particles smaller than the light wavelength is known as Rayleigh scattering [9]. The best known example is the scattering of sunlight by the molecules of the atmosphere. The blue (short wavelength) components of the sunlight is scattered approximately six times more than the red (longer wavelength) components to give rise to the blue sky. For larger particles, with diameters on the order of light wavelengths or larger, the scattering takes place mainly in the forward direction, and it is less color-dependent, and the process is commonly referred to as Mie scattering [9].

1.2.3 Fluorescence

As light interacts with matters, emission can also result from a chemical reaction (phosphorescence), heat (incandescence) or electronic state transition (fluorescence) [10]. Here, we will only discuss fluorescence, a process also depicted in Fig. 1.1B. When the light shines on atoms/molecules, the electrons around the nucleus to transit from the original orbit to the higher energy orbit, i.e. from the ground state to the first or second excited state. The excited state is not stable, so the electron is restored from the excited state back to the round state, and the energy is released in the form of light (photons). In most cases, the emission wavelength is longer than the absorption wavelength, i.e., the radiation energy is lower. However, if the absorption intensity is

large enough, a two-photon absorption phenomenon may occur, resulting in a radiation wavelength shorter than the absorption wavelength. When the radiation wavelength and absorption wavelength are equal, it is called resonance fluorescence. We will discuss fluorescence in greater details in the context of biological microscopy (section 1.3).

1.2.4 Nonlinear interactions

Nonlinear interaction of light with matter are of fundamental importance for photonic applications. Modern nonlinear optics dates back to the development of the laser in the early 1960s [11]. The availability of an intense coherent light source enabled Franken et al. to observe frequency doubling of a ruby laser by a quartz crystal in 1961. From that point, the field grew rapidly due to the development of new materials, new sources, and new techniques.

The initial work in experimental nonlinear optics started with the demonstration of second-harmonic generation (SHG) [12,13]. In that work, with an intense excitation at a wavelength of 694.3 nm, second harmonic generation at 347.2 nm in crystalline quartz was demonstrated. The conversion efficiency was rather low at the point but was steadily increased over the following years with the aid of higher intensity lasers and appropriate phase-matching techniques. These new experiments including harmonic generation were quite important at that time as they were able to generate a coherent light output with a coherent light input. Numerous nonlinear optical phenomenon were demonstrated afterwards, such as optical bi-stability inside a vapor filled Fabry-Perot interferometer. In the presence of a nonlinear medium within the cavity, the round trip phase shift carried the refractive index term which had the contribution of the nonlinear index. This behavior was explained using the fact that there was the effect of both nonlinear dispersion and nonlinear absorption inside the medium. We will give more detailed explanations in Appendix part.

The initial demonstrations of nonlinear optical effects also set the note for the research work that followed for studying these effects in various integrated optical devices. The achievement of nonlinearities were extended to smaller systems for lowering the threshold powers required to achieve these effects. Since the beginning of the 1990s [14,15], cavities that were of the size of the order of one wavelength of light were starting to be fabricated. These devices with their extremely high confinement of optical energy made possible the lowering of nonlinearity thresholds to the tens of µW power range. Ring resonator devices have also been widely studied in order to enhance the nonlinearities. In addition, a photonic crystal cavity is also expected to have a high density of optical energy stored in very small volumes leading to enhancement of intensity dependent nonlinear effects. This enhancement can be of several orders of magnitude larger than the classical devices. The highly integrable nature of these devices along with the ease of coupling light into them makes them a strong candidate for observing enhanced nonlinear optical phenomena.

1.3 Light microscopy for biological imaging

Light microscopy marks the beginning of modern cell biology, and it has now become an essential set of tools for biomedical research. Improvement has been made in many different aspects, including light sources, illumination schemes, contrast agents, imaging optics and detectors, and so on[16,17]. In biology and medicine, the use of light microscopy is well established and widespread owing in part to the low toxicity of light to biological sample and multiplexing capability; this is particularly the case with fluorescence microscopy[18,19], which has three unique advantages: high contrast, high specificity, and quantitative imaging capability. Additionally, in the last decade or so, superresolution fluorescence microscopy[20-23] has improved the imaging resolution to up to ~10 nanometer (nm) to enable biological imaging at the single biomolecule (1-10 nm) level.

1.3.1 Fundamentals of light microscopy

Historic light microscopes used simple optics (e.g. a lens) to obtain a magnified view of the specimen, where the image magnification and quality were both limited. Modern light microscopes uses much more sophisticated lens systems for sample illumination and signal collection and achieves much better results. Until recently, light microscopes employ a so-called 'finite' optical system to form an image, where the signals collected through the objective lens are projected directly as an image onto a camera or to the observer through a binocular (Fig. 1.2a). This design can be dated back to 1595 and attributed to Robert Hooke. A drawback of this configuration is that any changes in the light path, including changing the focal plane, will alter the image formation geometry and magnification. To overcome this issue, major microscope vendors have largely migrated to an 'infinity' optical system, where the signal from each point in the focal plane generates a set of parallel rays in the space behind the objective - the 'infinity' space, i.e., the image distance is set to infinity - instead of an image, and a tube lens is used to produce an intermediate image (Fig. 1.2b). As such, the location information is converted into the angle of light in the infinity space, which remains invariant when the objective and the tube lens move relative to each other or when other optics (such as emission filters) are inserted within the infinity space. Hence, infinity optical systems allow much greater flexibility in microscope design and in imaging.
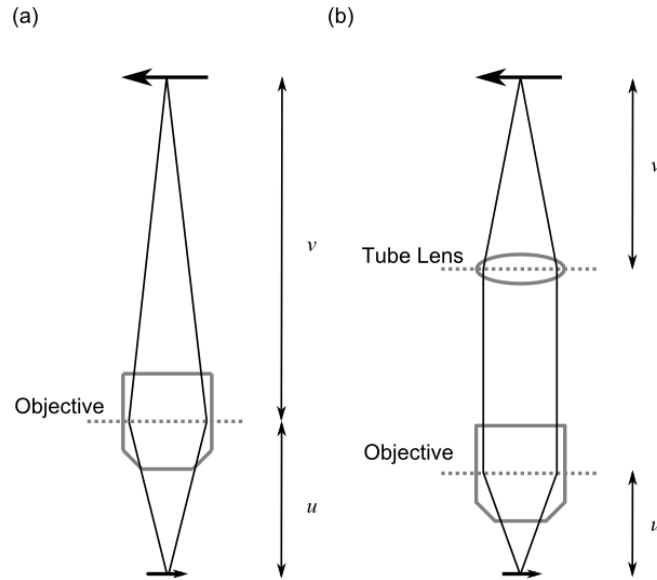
Figure 1.2 Finite (A) and infinite (B) microscopic imaging system.

In both infinite and finite optical systems, the magnification M is determined by the ratio between the object distance u, and the image distance v.

$$M = \frac{u}{v}.$$

In the finite optical system, the object distance is defined as the distance between the object and the front principle plane of the objective, which is the same with the infinite optical system. The definition of imaging distance is different between these two types of systems. The image distance for the finite optical system is defined as the distance between the image and the back principle plane of the objective, while in the infinite system, the image distance is the distance between the image and the back focal plane of the tube lens. As the objective is placed in the front focal plane of the objective, and the image is formed on the back focal plane of the tube lens, the magnification of the infinite system is the ratio of the effective focal length of the tube lens and the effective focal length of the objective. With the improvement of resolution, modern objective lenses start to use a sets of lenses and have sophisticated designs to correct for varieties

12

of aberration (spread of image points, curvature of filed, and geometrical distortion) and chromatic aberration.

A perfect imaging system should collect all the photons from the sample. Practically, however, the amount of light that can be collected by a microscope objective is limited by its physical diameter; the objective can only accept information carried by light within a certain collection cone, which is described by the half cone angle θ. The ability of an objective lens to collect light is also dependent on the refractive index (n) of the immersion medium. A commonly used term for characterizing the light collecting power of an objective is numerical aperture (N.A.), which is defined as

$N.A. = n\ sin\theta,$ where n is the refractive index of the medium next to the front surface of the objective. To improve NA of imaging system, different immersion media have been introduced for high magnification microscopy systems. The most common immersion media are water (n=1.3) and oil (n=1.4-1.5).

1.3.2 Fluorescence microscopy

Basic setup of fluorescence microscopy. Fluorescence is a relatively weak process, with typical absorption cross-sections of fluorophores on the order of 10^{-15} to 10^{-16} cm^2. Thus a fluorescence microscope (FM) typically uses a relatively intense light source to excite the fluorophores specifically attached to the target molecules of interest in the sample. As discussed earlier, in fluorescence the photons emitted are of a different wavelength from the incoming photons, thus offering a route for cleanly separating the illumination light and the signal by, for example, using emission filters. This is in contrast to transmission type light microscopy in which the signals and the illumination light are of the same wavelength.

A typical FM filter set comprises a dichroic mirror, which either transmits light below a certain wavelength and reflects longer wavelengths or does the opposite. Mirrors that reflect and transmit multiple wavelengths bands are referred to as polychroic mirrors and also commonly

used nowadays. Fluorescence signal can be further separated from the excitation light with additional optics such as a long- or band-pass filter (Fig. 1.3), which attenuates light within certain wavelength bands to 10^{-6} to 10^{-8}.

A key element in FM is sample labeling. Through various labeling strategies, fluorophores can be specifically attached to the molecule(s) of interest for FM imaging (Fig. 1.4). Owing to an ever-growing repertoire of fluorophores and specific targeting reagents as well as continuously improving illumination and detection hardware, fluorescence microscopy has become more and more powerful and flexible, with numerous applications developed in the field of medical and biological sciences and beyond.
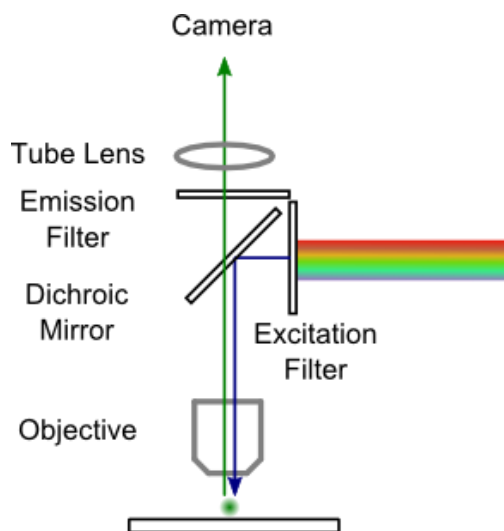
Figure 1.3 Basic setup of a fluorescence microscope.
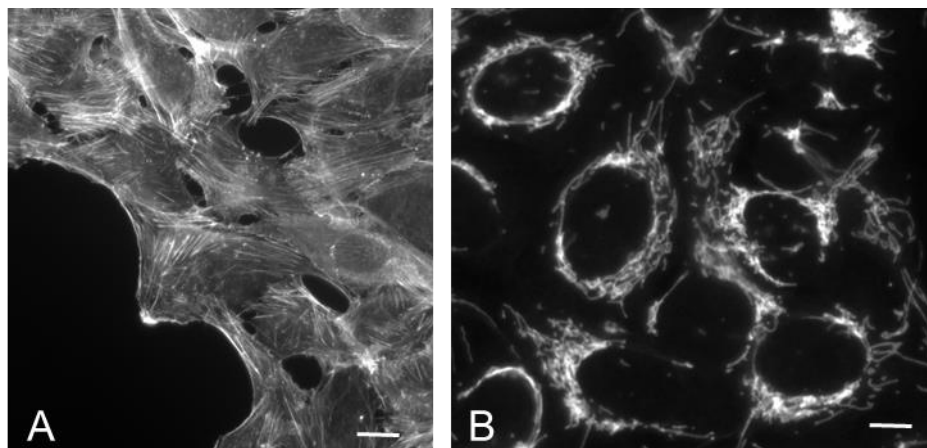
Figure 1.4 Fluorescence labeling and imaging of cellular structures.

(A) Actin and (B) mitochondria labeling in U2OS cells. Scale bar: 5 μm.

Contrast agents for fluorescence microscopy. Biological imaging predominantly involves visible to NIR light as illumination source for best compatibility with the specimens and image sensors. Accordingly, a variety of fluorescent probes that absorb visible to NIR light and emit fluorescence in the same wavelength range have been developed. To date, there are largely three classes of contrast agents for fluorescence imaging, namely small organic fluorophores, fluorescent proteins, and nanocrystals.

Organic fluorophores. Fluorescent compounds based on synthetic small molecules are powerful tools to visualize biological events, such as Cy3 and Alex Fluor 647. A benefit of using synthetic dyes is the flexibility in controlling the properties and direct the position of the fluorophore through chemical approaches. Modern synthetic organic chemistry strategies enable efficient tailoring of the chemical structure to obtain probes for specific biological experiments. Chemistry can also be used to activate fluorophores; new, fluorogenic enzyme substrates and photoactivatable compounds with improved properties have been prepared that facilitate superresolution imaging techniques, such as STORM. Also, chemical reactions in live cells can

be used to direct the spatial distribution of the fluorophore, allowing labeling of defined cellular regions with synthetic dyes.

Fluorescent proteins. The advent of fluorescent proteins (FPs) for genetic labeling of proteins and cellular structures has revolutionized fluorescence microscopy. The original green fluorescent protein (GFP) was discovered back in the early 1960s, when researchers isolated a blue-emitting bioluminescent protein called *aequorin* together with another protein that was eventually named the GFP from *Aequorea victoria* jellyfish. Since then, GFP variants and those derived from other species spanning the entire visible to NIR spectral range have been developed. Most FPs are ~25kD in molecular weight. While this is large compared to organic fluorophores, the advantage of FPs is the ability to genetically encode the fluorophore in the form of fusion expression construct for any gene of interest. Of note, the overall size of an FP, which is just 3-5 nanometers, is significantly smaller than primary-secondary-dye complex.

The photophysical properties of many FPs are often complex and can involve several distinct emissive and no-emissive states, manifested as on-and-off "blinking" when observed at the single molecule level. Photoactivatable FPs (PA-FPs) are a special set of FPs that can be converted from one state to another – either from a nonfluorescent to a fluorescent state or from fluorescing in one color to another color – often times through 'photoactivation' with ultraviolet or violet light. By controlling the dose of photoactivation, it is possible to activate a very small subset of PA-FP molecules to a fluorescent state upon at any moment even when the sample is densely labeled, thus allowing temporal isolation of single PA-FP molecules; this has become the basis of superresolution microscopy through subdiffractive single-molecule localization (see more details in Chapter 2).

Fluorescent nanocrystals. Colloidal semiconductor nanocrystals, also known as quantum dots (QDs), are versatile bioprobes for advanced molecular and cellular imaging. Fluorescent NCs promise to overcome some of the typical limitations of organic fluorophores, particularly the much improved photobleaching characteristics, chemical stability, broad absorption and narrow

16

emission spectra, along with the possibility of tuning spectral properties by varying the core size of QDs. The fluorescence of NCs can be precisely tuned in the whole visible spectrum or even the near-infrared region, thus covering a very wide spectral range (from 400 nm to 2.2 um). The broad absorption spectrum permits efficient excitation at any wavelength shorter than the emission peak, while maintaining the same characteristic narrow, symmetric emission spectrum, regardless of the excitation wavelength. Such spectral feature allows excitation of different color of NCs by means of a single wavelength of light, such that many fluorescent colors that may be detected simultaneously.
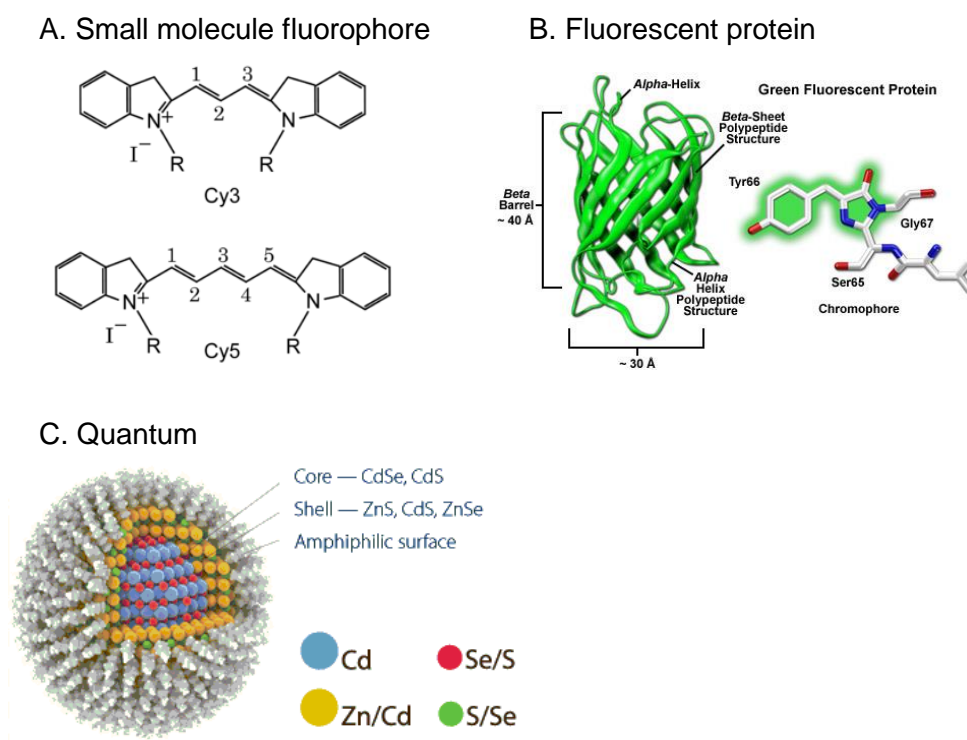
Figure 1.5 Contrast agents for fluorescence microscopy

A. Cy3 and Alexa Fluor 647 Structure; B. Structure of a FP and highlight of chromophore structure (adapted from Zeiss microscopy online campus); Panel C. Quantum Dots (QDs) as an example of fluorescent nanocrystals (adapted from http://www.lumimodule.com).

Illumination and detection schemes. The basic setup described in Figure 1.2 allows fluorescence imaging of biological samples, but the capability of this basic setup is limited. In particular, as the illumination light travels through the sample, signal is generated throughout the interaction volume, of which a large fraction is out-of-focus. The out-of-focus signal does not form a sharp image and instead contributes to background and reduces the sensitivity and the resolution in both the lateral (x, y) and the axial (z) dimensions. Over the last three to four decades, various illumination and detection schemes have been implemented to improve FM.

Confocal microscopy. The most widely used scheme for rejecting out-of-focus signals in FM is confocal microscopy, which blocks out-of-focus fluorescence with a 'confocal' pinhole. The sample is illuminated by a focused beam, one point at a time. To obtain a complete view of the field of view, raster scanning of the illumination point or the sample becomes necessary. Raster scanning can be achieved by a set of scanning (galvo) mirrors that move the beam focus across the field of view. At each illuminated spot, signal is generated, detected, and projected through the objective lens as a point image; this point image is captured a point detector (i.e., one that sees all signals from the sample as from a single, point source, such as a photo-multiplier tube). A pinhole is placed in a plane conjugate to the objective focal plane to allow signal from the focus to pass through and reject out-of-focus signals; the smaller the size of the pinhole, the more stringent the rejection of out-of-focus signal is.

With out-of-focus signals rejected, a confocal microscope has improved resolution on both lateral and axial directions compared with a wide-field microscope. The ability of a confocal microscope to optically slice through the specimen and exclude out-off-focus background while selectively capturing signals from the focal plane makes it a powerful tool for acquiring three-dimensional (3D) images of thick biological specimen. By scanning many sections through the sample, a high resolution 3D view of the sample volume could be reconstructed from the resulting image stack.
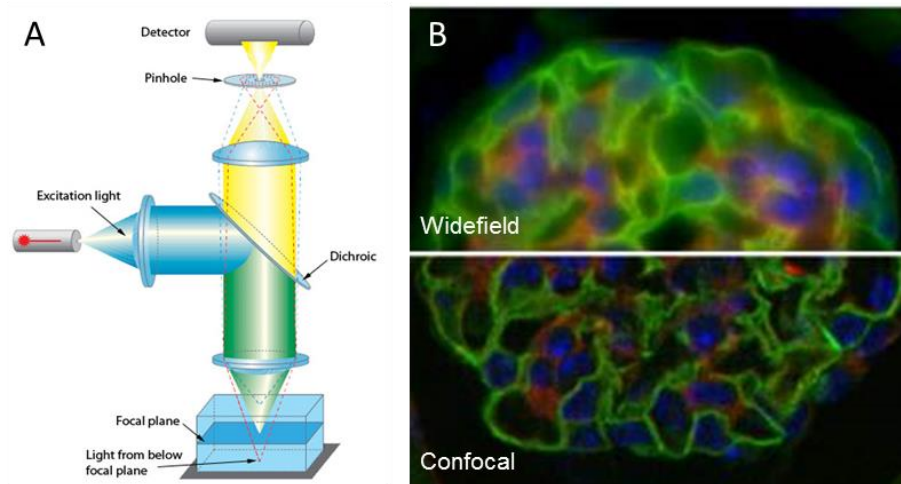
Figure 1.6 Confocal microscopy (adapted from Duke university imaging facility website). (A) Sketch of a typical confocal setup. (B) Comparison of images between confocal microscopy and wide-field microscopy.

Total internal reflection fluorescence microscopy (TIRF). While confocal microscopy obtains information of a single image plane in the sample by rejecting out-of-focus signals, the sample is still illuminated throughout the entire light path. As a result, photobleaching and other light-induced processes (e.g. phototoxicity) are still take place, which can adversely affect the sample. In certain situations, particularly when imaging processes or structures at the coverslip - sample interface, TIRF can be employed to alleviate this problem. In TIRF microscopy, the excitation beam enters the coverslip-sample interface at a large incidence angle; the angle is equal to or greater than the so called c*ritical angle* at which the excitation beam is totally reflected back into the coverslip at the interface. Importantly, the refractive index of cells or other aqueous samples is typically around 1.3-1.4, which is lower than that of the glass (typically ~1.5 or greater); TIRF only occurs when light travels from a medium of high refractive index (glass in this case) to another of a lower refractive index (water in this case). Beyond the critical angle, light no longer penetrates into the low refractive index medium except as an evanescent field that decays rapidly after 100-200 nm, thus confining the illumination volume to a very thin layer, not

19

more than 200 nm above the coverslip. Hence, TIRF has primarily been used to observe processes or molecules near the coverslip, such as biological molecules immobilized on glass or those residing on the bottom membrane of cultured cells.
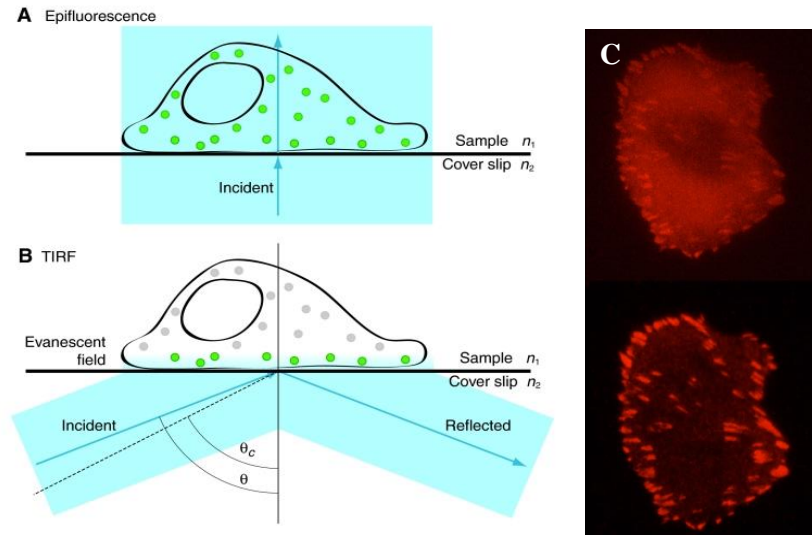
Figure 1.7 Total internal reflection fluorescence (TIRF) microscopy. [24]

A. Epi-fluorescence microscopy illuminates a large volume of the sample at once; B. Total internal reflection fluorescence (TIRF) microscopy illuminates only a thin section of the sample above the coverslip. C. Direct comparison between Epifluorescence and TIRF images.

TIRF microscopy can be used in a wide range of cell biological applications, particularly analysis of the localization and dynamics of molecules and events near the plasma membrane. Membrane-associated processes are in general difficult to image with traditional epifluorescence because details near the cell surface are easily obscured by fluorescence that originates from the bulk of the cell. With TIRF, fluorophores near the adherent cell surface can be selectively illuminated without causing significant excitation or photobleaching of molecules in the cytosol. Furthermore, the imaging depth of TIRF can be tuned to a certain extent by varying the incident angle of the excitation beam. When using an incident angle slightly smaller than the critical angle,

molecular or structures at and close to the cell membrane could both be illuminated, yielding a 'pseudo-TIRF' condition that is often used in our imaging experiments.

1.4 The quest for probing biology at the single-molecule and nanometer scales

The very first view of biological cells was made using a light microscope almost six hundred years ago. Since then, light microscopy has evolved tremendously, and it is still rapidly evolving today; light including fluorescence microscopy techniques have been instrumental to shaping our current understanding biology. Enormous progress has also been made in using X-ray crystallography and electron microscopy to obtain atomic-level structural information of biological molecules such as proteins and nucleotides. Recently, we have also seen an explosion of 'omics' based approaches to generating lists of molecular components in a biological system and to inferring connectivity among the components; this has helped us to bring our understanding of biology to a systems level. A remaining gap in our current understanding of biology, however, is how the building blocks of life – the individual biological molecules – organize into functional complexes, various cellular structures, and then the cell.

Challenge in probing biology at the nanometer and single-molecule scales are manifold. First, the length scales involved are very small; individual biomolecules or molecular complexes are typically 1-10 nm in physical dimensions, which is far beyond the resolution of a conventional light microscope. As discussed earlier in this chapter, the resolution of a light microscope is limited by the diffraction of light. For a microscope equipped with an objective, the effective lateral resolution as defined by the 'Rayleigh Criterion' is $0.61 * \lambda/NA$, where NA is the numerical aperture and λ is the wavelength. This means that even with a very powerful lens (NA = 1.49), the conventional light microscope including TIRF and confocal can only resolve distances greater than 200-250 nm. Hence, conventional light microscopy is about an order of magnitude short in spatial resolution for studying biology at the nanometer and molecular scales.

The second challenge is the multitude of components involved in typical biological processes, for which an imaging method with sufficient multiplicity is needed. For fluorescence based imaging techniques, this would require that the spectral resolution to be sufficiently high, which is a significant challenge given that typical fluorescent molecules exhibit broad emission spectra and spectral crosstalk becomes a major issue as the number of colors increases.

Last but not least, mechanistic studies of biological processes also demands sufficient stoichiometric resolution, or in other words, single-molecule precision. Stoichiometry is an important aspect of biological regulation. For example, many signaling molecules such as cell surface receptors have been shown to organize into nanoscopic clusters (Fig. 1.7), and there have been evidence that monomeric and clustered (or multimeric) forms of the receptors are biologically distinct. Being able to detect, localize, track, and count individual biological molecules would be immensely powerful for dissecting the fundamental mechanisms of biology.
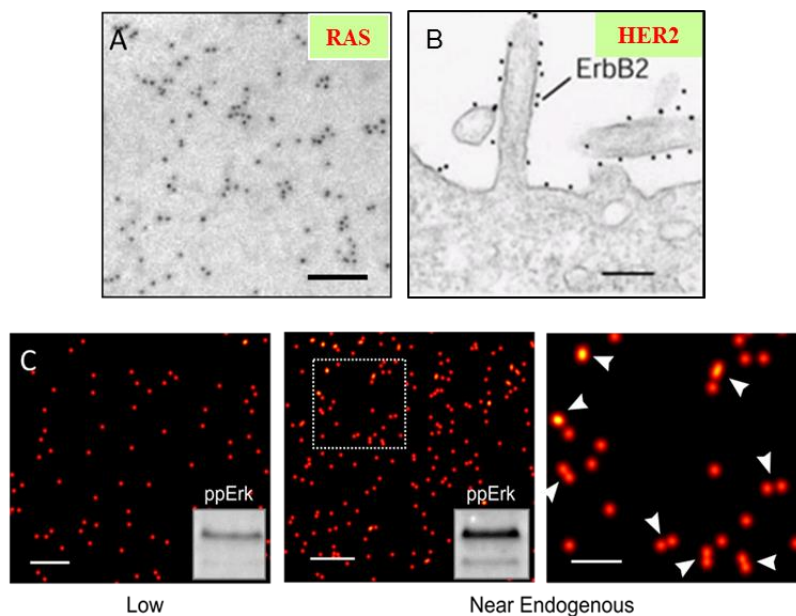
Figure 1.8 Nanoscopic imaging reveals new biology.

(A) Ras nanoclusters [25], scale bar: 100nm; (B) HER2 nanoclusters by immuno-EM [26], scale bar: 100 nm; (C) Mutant KRas (GTP-loaded) exists as monomers at low-expression level and inactive, and becomes dimers at physiological expression levels and biologically active. Right: zoom-in

view of the boxed area in the middle, with white arrows indicating KRas-GTP dimers [27]. Scale bars, 200 nm (left and middle) and 100 nm (right).

Fortunately, in the last two decades or so, advanced optical microscopies including but not limited to single-molecule fluorescence spectroscopy and microscopy as well as a whole suite of 'superresolution fluorescence microscopy' techniques have emerged to tackle one or more of these challenges. With proper detection device, signal from a single fluorescent molecule could be detected and localized[28-30]. Based on these, superresolution microscopy techniques including photoactivated localization microscopy (PALM), stochastic optical reconstruction microscopy (STORM), and their derivatives were invented by combining subdiffractive single-molecule localization with stochastic switching of fluorescent molecules. Although PALM and STORM have only been in existence for about a decade, numerous applications have been developed to demonstrate their power, and we will also report in this thesis, new and better approaches based on these principles are still being continuously developed.

Our lab has used quantitative PALM and STORM to analyze various biological processes. Among others, we were the first to image Ras small GTPases in mammalian cells and show that Ras functions as a dimer when activating downstream signaling pathways such as Raf-MAPK (Fig. 1.7). In this thesis project, we further extend the PALM/STORM techniques to higher spectral resolution to enable broader biological applications.

1.5 Layout of the thesis

The remainder of the thesis is organized as follows. Chapter 2 focuses on visualizing biological structures in cells and tissues by using SRM. Chapter 3 reports a collaborative work on multispectral superresolution microscopy (MSSRM), a new technique developed in our lab that aims at significantly increasing the number of molecular species to be simultaneously imaged with an SRM. Chapters 4 and 5 are dedicated to the biological applications of SRM and MSSRM,

particularly in understanding the nanoscale organization of cell surface receptors in association with specialized membrane domains. In particular, in chapter 4 we study the spatial regulation of HER2 and EGFR, two receptors widely implicated in breast and other types of human cancers, and in chapter 5 we attempt to directly visualize specialized membrane domains through spectrally-resolved single-molecule imaging based on the MSSRM platform. In the *Appendix*, we discuss the work on probing nanostructures of inorganic materials using light conducted at U. Arkansas.

Chapter 2   Superresolution fluorescence

microscopy for visualizing biological structures

The resolution of a microscope is an important characteristic[31-33]. In this chapter, I will first review the principle of superresolution microscopy, with the focus on photoactivated localization microscopy (PALM) and stochastic optical reconstruction microscopy (STORM)[34]. PALM, STORM, and their derived techniques are all based on single-molecule localization, hence are collectively known as single-molecule localization microscopy (SMLM). Secondly, I will present data on setting up and calibrating a three-dimensional SMLM microscope, and on applying the custom SMLM to visualizing biological structures both in cells and in clinical formalin fixed paraffin embedded (FFPE) breast cancer[35].

2.1   Introduction

2.1.1   Overview of superresolution microscopy (SRM) techniques

SRM refers to a class of light microscopy techniques that overcome the diffraction-limit in spatial resolution. Current SRM techniques are predominantly based on fluorescence microscopy (FM). Based on the working principles, they can be categorized into three classes.

The first class utilizes point-spread function (PSF) engineering, and the techniques include stimulated emission depletion (STED) and 4-Pi microscopies[36]. For example, in STED a 'depletion' beam with a donut-shaped PSF is used followed by a regular Gaussian excitation beam to eliminate signals from fluorescent molecules residing at the periphery of the PSF.

The second class is structured illumination microscopy (SIM)[37-40], which makes use of interference between an engineered illumination pattern and sample's intrinsic spatial patterns, to extract high spatial frequency information. The maximum resolution enhancement is 2x for linear

SIM and higher for nonlinear (such as saturated excitation) SSIM, which has demonstrated a 50 nm resolution in two dimensions.

And the third class, which is the focus of this thesis, is based on subdiffractive localization of single fluorescent emitters and is hence named SMLM.

2.1.2   Basic principles of SMLM

Since the SMLM techniques - PALM and STORM – were invented in 2006, many variations of SMLM have been reported (and as a result, numerous acronyms have been introduced). Regardless of the implementation, these techniques are all based on two common concepts: single-molecule localization and stochastic switching of fluorophores.

Single-molecule localization refers to the fact that, although the image of a single fluorophore in any imaging system will be a diffraction-limited spot with a finite size (at least 200 nm for light microscopy), the precision of determining its position from the image can be much higher than the diffraction limit. Each photon emitted by the fluorophore can be regarded as a measurement of the position of the fluorophore, with an uncertainty of Δ due to shot noise (the 'uncertainty principle'). An image formed by N photons can be viewed as N measurements of the same fluorophore's position. Averaging of N measurements of the same PSF yields to a localization precision approximated by $\sigma = \Delta/\sqrt{N}$; here Δ is equivalent to the size of the PSF [41].

Stochastic switching is the process to temporally isolate individual molecules in densely labeled regions, which is common in biological samples. The idea is to use fluorescent probes that can switch between fluorescent and dark states or between two different fluorescent states. When emitting concurrently, the molecules will generate overlapping images. With stochastic switching, however, molecules within a diffraction-limited region can be activated stochastically at different time points so that they can be individually imaged, localized, and subsequently deactivated.

Depending on the labeling density of the sample and the properties of the fluorophores, this iterative imaging process may take a long time to complete. Therefore, a wide-field imaging configuration is typically used. In this configuration, coordinates of all fluorophores that appear in the whole field of view can be obtained at once, thus ensuring a reasonable speed in SMLM imaging.
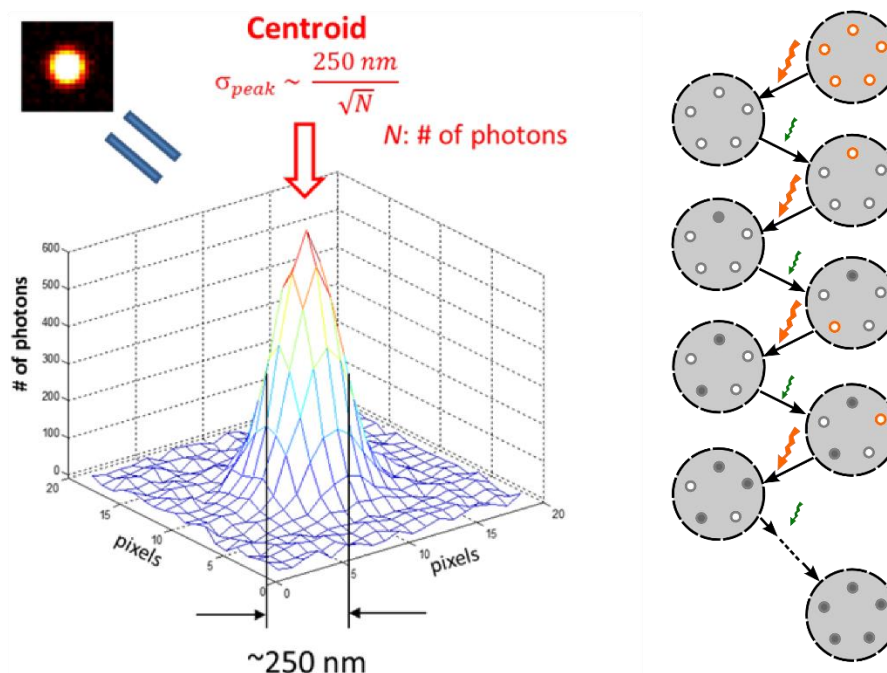
Figure 2.1 Basic principles of SMLM: Single molecule localization and stochastic switching

The scaling of the localization precision with the photon yield indicates that the best achievable spatial resolution with SMLM depends in part on how many photons the fluorophore emits in each switching cycle. In practice, the detected number of photons per switching cycle can vary from several hundred for FPs[42] to several thousands for organic dyes such as Cy5[34]. This results in an improvement in spatial resolution in more than an order of magnitude according to the $N^{1/2}$ scaling rule in theory. A lateral resolution of ~20 nm has been routinely demonstrated experimentally using photoswitchable cyanine dyes (including Alexa Fluor 647).

27

It has to be noted, however, that the resolution of SMLM is also governed by not just photon yield or localization precision but also by sample labeling density[43]. According to the Nyquist sampling theorem, to achieve a resolution of x, the sampling rate needs to be at least 2x; hence, to reach the commonly claimed ~20 nm spatial resolution, the labeling density should be at least 1 label every 10 nm. This is equivalent to ~10,000 labels per μm^2 in a 2D space, which is a fairly high density. Hence, the use of fluorescent probes that can undergo efficient photoswitching, such that single molecules can be temporally isolated and localized even at very high labeling densities, is critical to achieving a high spatial resolution in SMLM.

2.1.3   3D imaging with SMLM

While localization of single-emitters in the lateral direction (x, y) is now well-established, determining the fluorophore position in the axial (z) direction remains challenging. The reasons are twofold: the 3x elongated PSF in the z-direction and the limited focal depth of high numerical aperture objective lenses. In other words, fluorophore localization in the axial direction inherently is less accurate and/or has a much shorter detection range compared with that in the lateral direction. To date, there have been multiple strategies developed for 3D SMLM, with each technique addressing one of the limiting factors, and a single technique that achieves both high (and isotropic x, y, and z) spatial resolution and large penetration depth is not yet available.

The first demonstration of 3D SMLM was introduced in 2008 by Huang *et al.* , where a cylindrical lens was inserted in the imaging path, the point spread function is altered in such a way that the z-position is encoded in the ellipticity of PSF. As a result, the signal for a fluorophore above the focal plane is broadened along one axis, and broadened along the other axis if the object is located below the focal plane (Fig 2.2A). This is relatively easy to implement.

Moerner and colleagues uses a phase mask in the Fourier space to convert the otherwise round PSFs of single fluorescent molecules into spatial patterns that encode the axial position of the fluorophore. The most commonly used spatial pattern is a double-helix[44], with the depth

information being coded into the relative position of the helical nodes (Fig 2.2C). Imaging with these two approaches yields an axial resolution of 50-70 nm, with the imaging depth being restricted to about 1 to 2 μm[45].

A different concept by Juette *et al.* in 2008 allowed 3D imaging by bi-plane imaging[46] (Fig 2.2B). In this approach, the fluorescence signal from each emitter is split in two halves, each focused at slightly different z-planes above and below the focus, and the z-position is encoded in the widths of the two images. Each molecule is generates two images in two slightly different focal planes. Molecules close to one of the imaging planes or between them can be localized with ~75 nm accuracy over an imaging depth of several micrometers. In 2009, Shitengl *et al.* at Jenlia Farm introduced interferometric PALM (iPALM), which by far offers the best axial resolution amongst all 3D SMLM[47] (Fig 2.2D). In this approach, two objective lenses were used on the two opposing sides of the sample, and the sample is sandwiched between two closely placed coverslips. The use of two opposing objectives had already been realized in a number of advanced optical microscopy approaches, such as 4Pi microscopy[48], I5M[49], I5S[50] and STED[51]. A special, three-way beam splitter is used in iPALM to obtain a three-phase intensity diagram. For each detected fluorescent molecule, three images, each with a ~120 degree phase shift with the neighboring image, are generated and captured on three separate detectors. Interference amplitudes measured on the three detectors encodes the z-coordinate of the fluorophores. Owing to the high interference sensitivity, the z-resolution of the iPALM system can approach sub-10 nm.
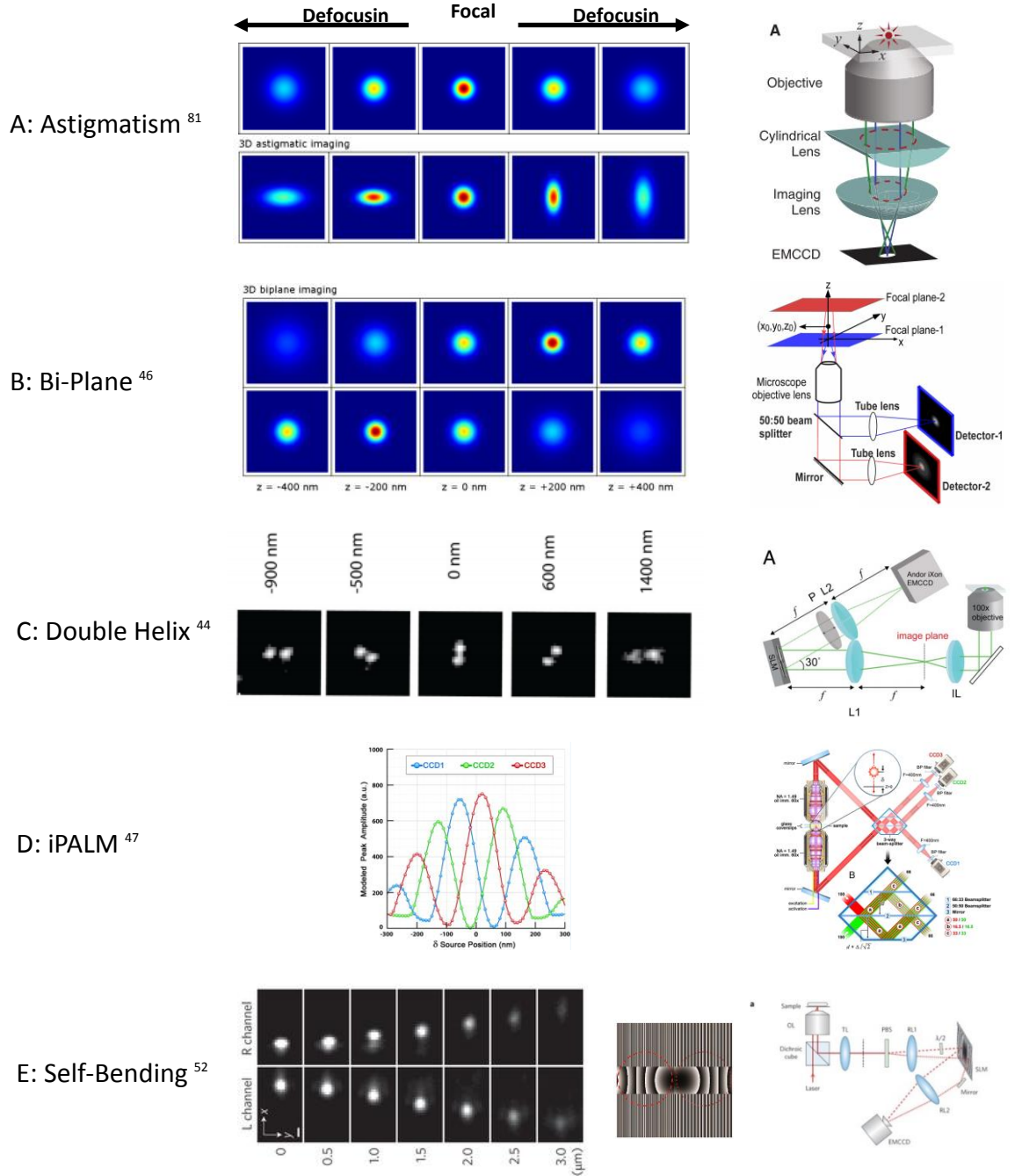
Figure 2.2 Various implementations of 3D SMLM.

In 2014, Jia demonstrated an isotropic 3D super-resolution scheme by engineering the PSF of single molecules into two [52]. Axial information of single molecules is encoded onto the distance between the two PSFs. With this so-called Self-bending point spread function, they were

able to achieve a localization precision of 10-15 nm with an imaging depth of more than 3 micrometers.

2.2 Fluorophores and sample labeling strategies

SMLM requires fluorophores that can undergo stochastic switching. The switching can either be spontaneous (passive) or controlled (active). Several classes of fluorophores and switching mechanisms have been employed to achieve this goal: small molecule fluorophores, fluorescent proteins, and fluorescent nanocrystals. A partial list of fluorophores commonly used in SMLM is shown in Table 2.1[53].

For the importance of fluorophore properties to SMLM image resolution, intensive efforts have been put into developing and characterizing SMLM fluorophores with optimal performance. Historically, there are a number of fundamental requirements for fluorescent probes to be suitable for high-performance imaging. Primarily, the fluorophores must be photostable and bright, i.e. have a high quantum yield. In the case of SMLM, one must have the ability to "control" the spatial emitter density for any given exposure period. This leads to an additional requirement: the duty cycle of the potential fluorophores should be low, meaning they should reside in their fluorescent state only for a small fraction of their lifetime. The final requirement known is that while staying at the fluorescent state, the probe should emit a large number of photons to achieve good localization accuracy.

Another important factor in implementing an SMLM experiment is the imaging buffer. Many organic fluorophores exhibit complete photoswitching when immersed in specialized imaging buffers[54-56]. Depending on the fluorophore, the photoswitching may involve different mechanisms. As will be discussed further in this chapter as well as in Chapter 3, the imaging buffer has an impact on all aspects of fluorophore photophysics such as brightness, switching rate and contrast ratio, among others.

Dye		Excitation Maximum (nm)	Emission Maximum (nm)	Extinction (M^{-1} cm^{-1})	Quantum Yield	Detected Photons Per Cycle		Equilibrium Duty Cycle		Survival Fraction (400 s)		# Switching Cycles (Mean)	
						MEA	βME	MEA	βME	MEA	βME	MEA	βME
Blue-absorbing	Atto 488	501	523	90,000	0.8	1,341	1,110	0.00065	0.0022	0.98	0.99	11	49
	Alexa 488	495	519	71,000	0.92	1,193	427	0.00055	0.0017	0.94	1	16	139
	Atto 520	516	538	110,000	0.9	1,231	868	0.0015	0.00061	0.92	0.86	9	17
	Fluorescein	494	518	70,000	0.79	1,493	776	0.00032	0.00034	0.51	0.83	4	15
	FITC	494	518	70,000	0.8	639	1,086	0.00041	0.00031	0.75	0.9	17	16
	Cy2	489	506	150,000	0.12	6,241	4,583	0.00012	0.00045	0.12	0.19	0.4	0.7
Yellow-absorbing	Cy3B	559	570	130,000	0.67	1,365	2,057	0.0003	0.0004	1	0.89	8	5
	Alexa 568	578	603	91,300	0.69	2,826	1,686	0.00058	0.0027	0.58	0.99	7	52
	TAMRA	546	575	90,430	0.2	4,884	2,025	0.0017	0.0049	0.85	0.99	10	59
	Cy3	550	570	150,000	0.15	11,022	8,158	0.0001	0.0003	0.17	0.55	0.5	1.6
	Cy3.5	581	596	150,000	0.15	4,968	8,028	0.0017	0.0005	0.89	0.61	5.7	3.3
	Atto 565	563	592	120,000	0.9	19,714	13,294	0.00058	0.00037	0.17	0.26	4	5
Red-absorbing	Alexa 647	650	665	239,000	0.33	3,823	5,202	0.0005	0.0012	0.83	0.73	14	26
	Cy5	649	670	250,000	0.28	4,254	5,873	0.0004	0.0007	0.75	0.83	10	17
	Atto 647	645	669	120,000	0.2	1,526	944	0.0021	0.0016	0.46	0.84	10	24
	Atto 647N	644	669	150,000	0.65	3,254	4,433	0.0012	0.0035	0.24	0.65	9	39
	Dyomics 654	654	675	220,000	–	3,653	3,014	0.0011	0.0018	0.79	0.64	20	19
	Atto 655	663	684	125,000	0.3	1,105	657	0.0006	0.0011	0.65	0.78	17	22
	Atto 680	680	700	125,000	0.3	1,656	987	0.0019	0.0024	0.65	0.91	8	27
	Cy5.5	675	694	250,000	0.28	5,831	6,337	0.0069	0.0073	0.87	0.85	16	25
NIR-absorbing	DyLight 750	752	778	220,000	–	712	749	0.0006	0.0002	0.55	0.58	5	6
	Cy7	747	776	200,000	0.28	852	997	0.0003	0.0004	0.48	0.49	5	2.6
	Alexa 750	749	775	240,000	0.12	437	703	0.00006	0.0001	0.36	0.68	1.5	6
	Atto 740	740	764	120,000	0.1	779	463	0.00047	0.0014	0.31	0.96	3	14
	Alexa 790	785	810	260,000	–	591	740	0.00049	0.0014	0.54	0.62	5	2.7
	IRDye 800 CW	778	794	240,000	–	2,753	2,540	0.0018	0.038	0.6	1	3	127

Table 2.1 Organic fluorophores and their photophysical properties for SMLM

(adapted from Dempsey *et al.* Nat. Meth. 2011)

SMLM employs similar labeling strategies to conventional FM such as immunolabeling and fluorescent protein (FP)-tagging. Immunolabeling allows detection of endogenous proteins but the results are highly dependent on the labeling efficiency and the quality of the antibody; FP-tagging offers specific labeling for targets that lack high quality antibodies and a high labeling efficiency at nearly 100%. Between the two strategies, immunolabeling has the two advantages. First, immunolabeling is able to use bright, organic fluorophores, with typical single-molecule photon yields of 1-5,000 photons per switching cycle, in comparison with photoswitchable FPs

that emit only 500-1,000 photons per cycle. Second, immunolabeling has fewer disturbances to existing biological sample, comparing to FP-tagging.

For immunolabeling, a general consideration has been the size of the antibody, and the linker length between the target binding site and the fluorophore. An antibody has a molecular weight of 150 kD and physical size of 10-15 nm, and is often used in a combination of a primary antibody and a secondary antibody, in which case the distance between fluorophore and binding site can be up to 30 nm. This has not been a problem in conventional microscopy, but such a distance can be a problem in the context of superresolution microscopy. Apart from the linker distance, spatial constraints may obstruct large probes from binding to every target molecule. Direct conjugation of fluorophore to the primary antibody could decrease the linker length. Another effective way to overcome the drawback of the antibody size is to use smaller probes such as Fab fragment [57], nanobodies [58,59]. The Fab fragment of an antibody can be obtained by using reducing agents and proteases to cleave the immunoglobulin protein, leaving only the two Fab fragments with ~50 kDa each. Nanobodies, also known as single domain antigen-binding fragments, are only ~15 kDa. While Fabs and nanobodies are potentially better labeling reagents, their commercial availability is currently very limited.

In recent years, new labeling strategies based on chemical tags have become popular. With chemical tags, the protein of interest is genetically fused to a polypeptide sequence, in a similar fashion to creating FP fusion proteins. The chemical tags, however, are nonfluorescent initially and will only become fluorescent after reacting with a small molecule substrate linked to an organic fluorophore. This not only shortens the distance between the target molecule and the fluorophore, but also increases the specificity of labeling. Several different chemical tags have been developed in this category. A frequently used chemical tag is the SNAP tag[60,61], which can be linked to a fluorophore via reaction with fluorescently conjugated O6-benzylguanine. As such, organic fluorophores compatible with SMLM can be used to realize superresolution imaging using genetically encoded tags.

2.3　Materials and methods

Cell Culture: SKBR3 cells were cultured at 37° C and 5% CO_2 in McCoy's 5A media (Thermo Fisher Scientific), supplemented with 10% fetal bovine serum (HyClone Labs, GE Healthcare, Chalfont, UK) and 1% Penicillin/Steptomycin-Glutamine (Thermo Fisher Scientific). U2OS cells were incubated at 37° C and under 5% CO_2 in DMEM supplemented with 10% FBS (Life Technologies, 11995 and 10082 respectively). 8-well chamber plates with #1.5 coverglass bottoms (Lab-Tek II, Thermo Fisher Scientific) were cleaned using NaOH (1 M) for two hours, washed with PBS (3 x 15 min) and left in fresh PBS overnight. Cells were platted at $1x10^5$ cells per well and incubated for 24-48 hours to reach about 70% confluence for imaging.

Immunofluorescence staining: Cultured cells were fixed with 3.7% Paraformaldehyde (PFA) in 1x PHEM buffer (120 mM PIPES, 50 mM HEPES, 19 mM EGTA, 16 mM $MgSO_4$, pH 7.0) for 20 minutes followed by washing with 1x PBS (3 x 5 min). Cells were permeabilized and blocked in a mixture of 3% bovine serum albumin (BSA) and 0.5% Triton X-100 in 1x PBS at pH 7.4 for 30 minutes. Primary antibodies β-Tubulin (1:500, 322600, Life technology), Lamin B1 (1:500, Ab65986, Abcam) was applied to U2OS cells and incubated for 45 minutes at room temperature. Following removal of the primary antibody, cells were washed in 1x PBS (3 x 5 min). AF647 conjugated goat anti-mouse secondary antibody was incubated with the cells at a protein concentration of 0.1 mM for 30 minutes protected from light. The secondary antibody was removed and the cells were washed with 1x PBS (3 x 5 min). The stained cells were post-fixed with 3.7% PFA in 1x PHEM buffer for 10 minutes. Following fixation, the cells were washed with 1x PBS and stored in the dark until imaging. For SKBR3 cells, Alex Fluor 647_Phalloidin (1:100, A22287, Invitrogen) was applied after 30 min permeabilization. Then wash twice to do imaging. For SMLM imaging, 100 nm gold colloid (8.5 x 10^7 particles/mL, Ted Pella, Redding, CA) was suspended in DPBS with Ca^{2+}/Mg^{2+} and applied to the stained cells 20 minutes, and then followed with one PBS wash prior to imaging.

Imaging Buffer: The imaging buffer was prepared similarly to previously described methods, by mixing a Tris Normal (TN) buffer, GLOX, and MEA (β-mercaptoethylamine). In brief, the TN buffer was made by dissolving 10% glucose (w/v, Fisher Chemicals D16-500) in 50 mM Tris buffer with 10 mM NaCl (pH 8.0) where prepared TN buffer was stored at 4° C for up to several months. The GLOX stock solution contained 0.5 mg/mL glucose oxidase (Sigma-Aldrich, G2133-50 kU) and 40 μg/mL catalase (Sigma-Aldrich, C100-50MG). The GLOX mixture was centrifuged briefly at ~3000×g to remove any precipitates prior to use. MEA (Sigma-Aldrich, 30070) was dissolved at 1 M in 0.25 mM hydrogen chloride (HCl) and stored at 4° C for a maximum of two weeks. Prior to each experiment, the imaging buffer was prepared fresh by mixing GLOX, MEA, and TN at a ratio of 1:1:98.

Tissue Selection & Sectioning: Formalin-fixed paraffin-embedded (FFPE) primary, human stage three infiltrating ductal carcinoma (IDC) tissue that had been stored as a formalin fixed paraffin embedded block for 11 years was obtained from the Oregon Health and Science University (OHSU) Knight Tissue Bank (Portland, OR). The tissue samples were acquired and processed under institutional review board (IRB) approval for the OHSU Knight Tissue Bank. Tissue used in all experiments was surgically resected in 2004 and was prescreened for breast cancer grade, stage and hormone receptor status including HER2, estrogen receptor (ER) and progesterone receptor (PR). Tissues selected for this study had high HER2 expression denoted as +3 with robust membrane staining and minimal necrosis (<25%) where the majority of the tissue block contained tumor tissue (>50%). FFPE blocks were cooled to -5° C on ice blocks and serially sectioned using a microtome (RM2125 RTS, Leica Biosystems, Germany) at 2 or 4 μm thickness. Sections were mounted onto charged glass slides (Superfrost Plus Slides, Thermo Fisher Scientific, Carlsbad, CA) and baked in a drying oven at 52° C for 30 minutes.

Labeling Secondary Antibodies: Donkey anti-rabbit secondary antibody (Jackson ImmunoResearch, West Grove, CA) was conjugated to Alexa Fluor 647 (AF647) succinimidyl ester (Thermo Fisher Scientific) using previously published methods. Briefly, the antibody was

35

washed in three changes of 1x PBS using a 10K molecular weight cut off (MWCO) spin column (Vivaspin, Thermo Fisher Scientific) followed by volume adjusted of the washed antibody to 1 mL of PBS (pH 7.4). Fifteen molar equivalents of AF647 succinimidyl ester were added and the reaction was agitated at room temperature for 3 hours. Medium pressure chromatography (NGC Quest 10 Plus w/mutli-wavelength [UV/Vis] detection, Bio-Rad, Hercules, CA) was used to separate the conjugated antibody from unbound fluorophore using a desalting column (Bio-Scale Mini Bio-Gel P-6 Cartridge, Bio-Rad). The purified product was concentrated using 10K MWCO spin filters to a final antibody concentration of 5.0 μM in 200 μL of PBS. Fluorophore and protein concentrations were calculated from absorbance measurements (NanoDrop 2000c, Thermo Fisher Scientific) and used to calculate the final fluorophore to antibody ratio which was ~1.5 for all secondary antibody conjugates.

Automated Hematoxylin and Eosin (H&E) Staining: An Autostainer XL (ST5010, Leica Biosystems, Nussloch, Germany) was used to perform standard H&E staining. The automated staining protocol consisted of the following steps: two changes of xylenes (1 min each), rehydration in an ethanol/water gradient (100%, 95%, and 70% ethanol for 1 min each), followed by washing with deionized (DI) water (1 min). The rehydrated slides were stained with Gill 2 Hematoxylin (5 min, Thermo Fisher Scientific), washed with DI water (90 sec), followed by a brief wash with Nu-Clear II (20 sec, Thermo Fisher Scientific), a subsequent wash with DI water (90 sec), and a final incubation with Bluing Reagent (1 min, Thermo Fisher Scientific). Staining with Eosin Y (0.25% in ethanol, 30 sec, Thermo Fisher Scientific) was completed, followed by three washes with 100% ethanol (1 min each), and three washes with xylenes (1 min each). Lastly, H&E stained slides were cover slipped with Permount (Thermo Fisher Scientific) and allowed to dry flat prior to imaging.

Immunofluorescence Staining: FFPE sections were deparaffinized in xylenes (2 x 10 min) and rehydrated in an ethanol/water gradient series: 100% (2 x 10 min), 95% (5 min), 70% (5 min), and 50% (5 min) ethanol, respectively. The rehydrated slides were briefly immersed in

water and then washed in 1x PBS (10 min). Epitopes were unmasked using a two-step antigen retrieval technique modified from Gerdes *et al*[62] where staining buckets containing Tris buffer (10 mM Tris Base, 0.05% Tween 20, pH 8.0) and Citrate buffer (10 mM Sodium Citrate, 0.05% Tween 20, pH 6.0) were pre-heated simultaneously in a pressure cooker containing 1L of DI water. Slides were pressure-cooked for 20 minutes on the highest setting in Tris buffer. Slides were then transferred to the heated Citrate buffer and cooled to room temperature (45 minutes). Slides were washed once in 0.1% Tween-20 (5 min) and once in PBS (5 min). The tissue sections were permeabilized with 0.4% Triton X-100 in PBS for 45 minutes, washed in PBS (2 x 5 min) and blocked with 3% BSA for 1 hour. Slides were blotted to remove the BSA and the primary antibodies were applied at predetermined concentrations as follows: rabbit monoclonal to ErbB2 (1:100), rabbit polyclonal to TOMM20 (1:50), and rabbit polyclonal to Lamin B1 (1:100). Slides were incubated overnight at 4° C in a humidified chamber and then washed with PBS (3 x 5 min). AF647 conjugated anti-rabbit secondary antibodies (711-005-152, Jackson ImmuoResearch) were applied to the tissue sections at a protein concentration of 0.3 mM and incubated in the dark at room temperature for one hour. Slides were washed in PBS (3 x 5 min), fixed with 3.7% paraformaldehyde (PFA) for 10 minutes, and again washed with PBS (2 x 5 min). The slides were cover slipped (22 x 30 mm, no. 1.5, VWR micro cover glass), sealed with clear nail varnish and stored in the dark at -20° C prior to imaging. Fluoromount-G (Southern Biotech, Birmingham, AL) was used as mounting media for standard fluorescent imaging. For SMLM imaging, fresh imaging buffer was made from stock components (see SMLM imaging buffer preparation section below), applied to the sample and cover slipped 5 minutes before imaging.

   Light & Epi-Fluorescence Microscopy: H&E-stained and standard immunofluorescence samples were imaged using a Zeiss Axio Observer inverted microscope (Zeiss, Oberkochen, Germany). A metal halide light source (PhotoFluor II NIR, 89 North, Burlington, VT) was used for phase contrast and filtered for appropriate fluorescence excitation using a 620 ± 30 nm bandpass excitation filter (Chroma Technologies, Bellows Falls, VT). AF647 fluorescence

emission was imaged using a 700 ± 38 nm bandpass emission filter (Chroma Technologies). Images were collected with an Axiocam 506 monochrome camera (Zeiss) and an Axiocam 105 color camera (Zeiss). Representative images of tissue staining for each target were collected using 5x, 10x, 20x, and 40x objectives. For cell culture, representative images were collected using 40x and 63x objectives. Images were collected with optimal exposure times that ranged from 500–5000 msec. Serially sectioned FFPE tissue were imaged with the aligned monochrome and color cameras enabling the same H&E regions of interest (ROIs) to be imaged as those on the corresponding immunofluorescence stained section.

Epi-fluorescence imaging of FFPE tissue. Conventional, epi-fluorescence microscopy was used to examine immunostained 2 and 4 μm sections of HER2+ breast cancer tissue embedded in FFPE. To evaluate the structural integrity of FFPE sections, three functional and/or structural proteins were selected as imaging targets: HER2, a receptor that is almost exclusively localized to the cell membrane in HER2+ cancers; TOM20, which labels the outer mitochondrial membrane; and Lamin B1, which marks the nuclear membrane. Whereas TOM20 and Lamin B1 label all cell types, HER2 clearly marked the cancer epithelial cells in the breast tissue. The ductal structure of the cancerous epithelial cells was assessed by comparing images of conventional hematoxylin and eosin (H&E) stained sections (Fig. 2.9A) to those of HER2 immunostained sections (Fig. 2.9B). However, even at high magnification, no structural features between the membranes of HER2+ cells were visible by either H&E or fluorescence on a conventional microscope (Fig 2.9C). When stained with TOM20, higher mitochondrial content was seen in the cancerous epithelia cells than in the stroma (Figs. 2.9D and 2.9E). Similar to samples stained with HER2, however, individual mitochondria could not be visualized or assessed for structural differences even at high magnification using conventional microscopy (Fig. 2.9F). When stained with Lamin B1, the malignant tissues demonstrated increased cellularity and large nuclear membranes, which was confirmed using H&E staining (Figs. 2.9G and 2.9H). High magnification images revealed largely rounded nuclear structures, where the nuclear envelopes commonly

appear as a solid line (Fig. 2.9I). Together, these results confirm the specific labeling of all three structural and/or functional markers in the FFPE tissue, which were used in subsequent SMLM imaging studies.

SMLM instrumentation: SMLM measurements were performed on a custom PALM/STORM setup constructed on a Nikon Ti-U inverted microscope frame equipped with an oil immersion objective (APON, 60XOTIRF, NA=1.49, Olympus, effective magnification ~66× on a Nikon microscope body), two lasers emitting at 647 nm (OBIS, Coherent) and 405 nm (CUBE, Coherent), respectively, and an EM-CCD camera (Evolve 512 Delta, Photometrics). Light from the two lasers was expanded, combined, and projected onto the back aperture of the objective through a focusing lens (f=400 mm) to achieve wide field and total internal reflectance (TIRF) illumination. Fluorescence signals were collected through the same objective, separated from the lasers with a quad-edge beamsplitter (Di01-R405/488/561/635, Semrock), and filtered using a band pass filter (FF01-697/75, Semrock) before being imaged on the EM-CCD. The 1.5× tube lens was selected to achieve a total 100× magnification. A weak cylindrical lens (f~1000 mm) was placed in front of the EM-CCD at ~2 inch distance to generate astigmatism for 3D localization (Fig. 2.3).

Data Acquisition: For SMLM imaging of AF647, both the 647 nm laser (1-2 kW/cm^2) and the 405 nm laser (1-10 W/cm^2) were applied to the sample simultaneously. Mechanical shutters individually controlled the two lasers, and the intensity of the 405 nm laser was increased gradually as the imaging progressed to ensure appropriate switching rates of the AF647 fluorophores. At these power densities, the EM-CCD was operated in frame transfer mode at 10-15 ms per frame acquisition time with an EM gain setting around 300, and each data set (SMLM 'movie') contained 20,000 to 50,000 frames. A custom-built focus stabilization system was used in all experiments to maintain the image focus within ±25 nm. All image acquisition was done with micro-manager.[63]

Data processing: Raw SMLM movies were processed using both ThunderSTORM (for 3D data sets)[64] and a custom-written MatLab package (wfiread and palm for 2D data sets)[65]. For 3D data processing, a calibration curve was generated using z-scan images of 40 nm fluorescence beads scattered on a coverslip, and the resulting calibration file was imported into ThunderSTORM to convert the measured widths of individual single molecule images into axial coordinates. Color-coded 3D SMLM images were subsequently generated using ImageJ. Processing of 2D data sets using the wfiread and palm software packages have been previously described.[65]

2.4 Results and discussion

2.4.1 Calibration of the 3D SMLM
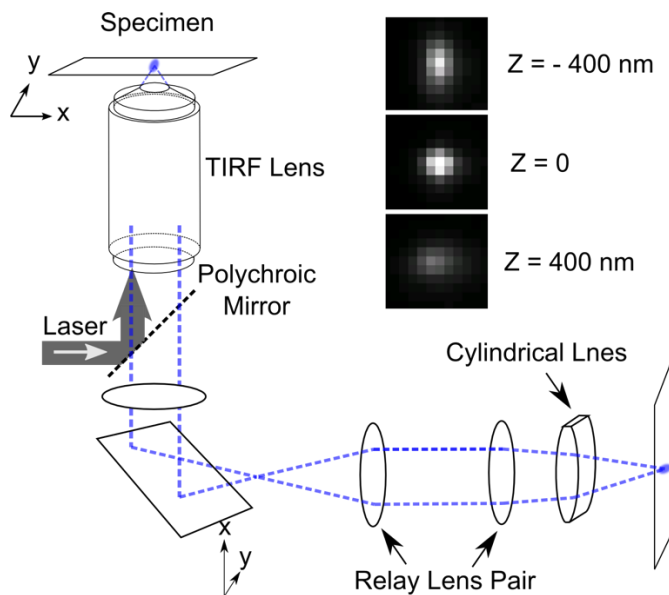
Figure 2.3 3D SMLM set up

A schematic drawing of the 3D SMLM setup is shown in Fig. 2.3, where a cylindrical lens is inserted in front of the camera to induce astigmatism. As a result, the images of a single

emitter appeared elongated in either x or y directions depending on the z-position (Fig. 2.3). To extract axial information of single molecules, I generated calibration curves using 40 nm fluorescent beads with excitation maximum at 660 nm and emission at 680 nm scattered on a coverslip. I adjusted the focal plane so that the PSF of single beads are nearly symmetric. A z-scan was then perform within ± 1 µm z-range with a 10 nm step size. The raw image z-stack was analyzed to extract the localization information (x and y coordinates) as well as the size of the PSFs in both directions (sigma_x and sigma_y). The sigma_x and sigma_y values of all single molecule at each individual focal plane was averaged and plotted against the z-position to generate the calibration curve (Fig. 2.4).
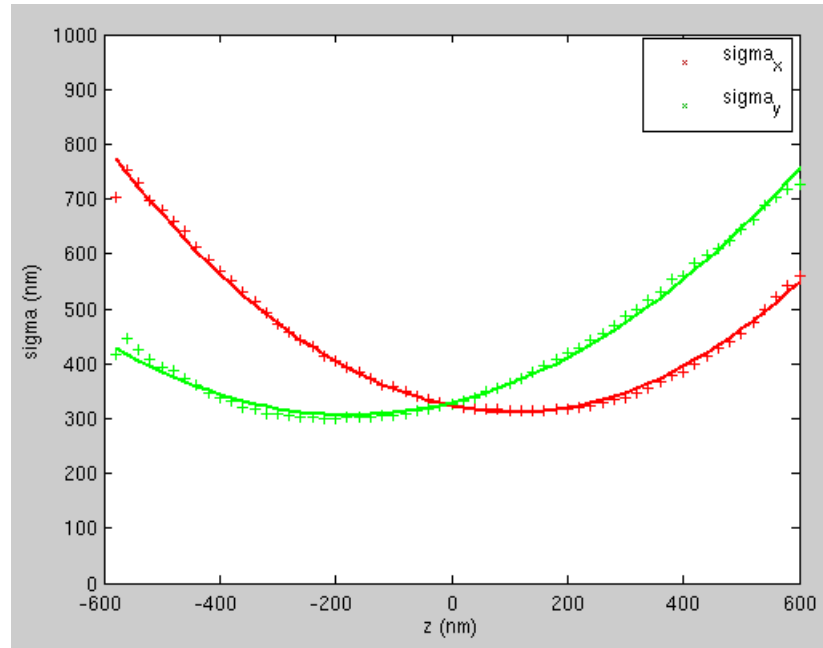
Figure 2.4 Calibration curve of 3D SMLM

The position of cylindrical lens in the imaging system was optimized to achieve better axial accuracy. As shown in Fig 2.4, the calibration curve becomes noisier when the focal plane was further away from the center position, making it less accurate to determine the z-position of

the fluorescent objects at those focal positions. The useful range of the calibration curve is typically not more than 800 nm. When the cylindrical lens is properly positioned and aligned, the focal plane difference between the two lateral directions should be around 400 nm, i.e., half of the useful z-range. In practice, the optimal cylindrical lens was placed through a few rounds of optimization as guided by the calibration curve obtained at each lens position.

Next, the z coordinate of each molecule was determined by matching its PSF parameters (sigma_x and sigma_y) to the calibration curve. The error (E) between the experimental data and calibration curve was calculated using the equation below (2.1), and by minimizing this error the 'correct' z coordinate of the molecule could be computed. Localization events with large residual E are mostly from dimmer molecules or overlapping PSF from multiple emitters in proximity; these events were excluded by applying a threshold of residue E values.

$$E = \sqrt{\left(w_x^{1/2} - w_{xcal}^{1/2}\right)^2 + \left(w_y^{1/2} - w_{ycal}^{1/2}\right)^2} \tag{2.1}$$

2.4.2   Imaging nanostructures in fixed cell with SMLM

The image quality of an SMLM set (including the selection of fluorophore and composition of the imaging buffer media) can be assessed using a sample of a well-known structure, such as cytoskeletal filaments. Therefore, we imaged microtubule and actin structures in cultured cells to show 'the resolution revolution' with SMLM.

2D SMLM Images of Microtubules and Actin. Fig.2.5 (A) is a comparison of an SMLM reconstruction images and a confocal fluorescence image of a sample with fluorescently labeled microtubule in fixed U2OS cells. Microtubules are hollow biopolymers of 25-nm diameter and are key constituents of the cellular cytoskeleton, Fig. 2.5 (D). The exact spatial organization of microtubules and their bundling is of central importance to a number of fundamental cellular processes such as mitosis, cell polarization and the outgrowth of cellular processes. Conventional fluorescence microscopy allows selective labelling of microtubule modification and associated proteins, but cannot resolve individual microtubules within tightly bundled microtubule arrays.

SMLM reconstructed microtubule image has much higher resolution then conventional fluorescence microscope. An intensity profile of a single microtubule along the yellow line is shown in Fig 2.5(B, C), where the hollow structure of microtubules was clearly resolved. The spacing between two sides of the hollow tubules was ~35 nm, which is slightly larger than the diameter of microtubules (~25 nm) due to the size of the antibodies.
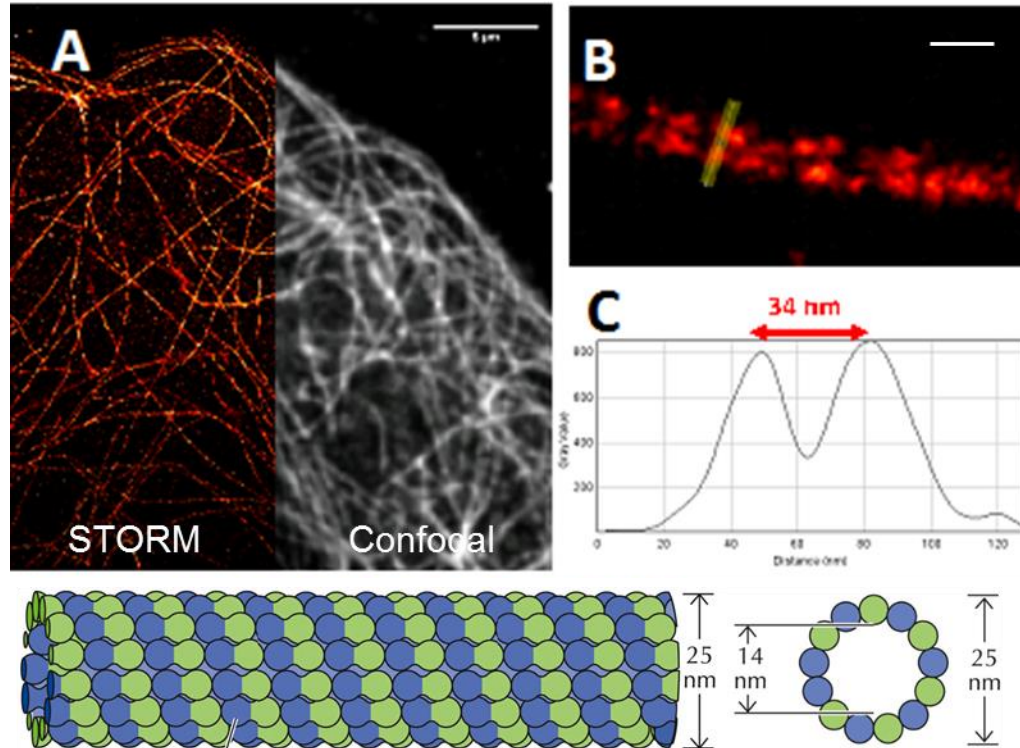
Figure 2.5 2D SMLM image of microtubule in fixed U2OS cell.

(A) Comparison of tubulin images between SMLM and Confocal microscopy. Scale bar: 5 um. (B) Zoom in images of a single tubulin. Scale bar: 100nm. (C) Intensity line profile along the yellow line in (B). (D) Dimensions of microtubules (adapted from THE CELL fourth edition, 12.42).

Next, we tested SMLM imaging capabilities on the actin cytoskeleton in SKBR3 cells. To take full advantage of the high image resolution, we labeled the target structure using small organic molecules by staining actin filaments with AF647-phalloidin, which binds actin filaments

with high specificity. As shown in Fig. 2.6, we can clearly resolve the individual actin bundles in the SMLM image. Interestingly, in these cells, we also observed that actin organized into ~8-membered ring structures, which may be related to invadopodia. Invadopodia are actin-rich protrusions of the plasma membrane that are associated with degradation of the extracellular matrix in cancer invasiveness and metastasis [66]. They have an actin core, which is surrounded by a ring structure enriched in actin-binding proteins, adhesion molecules, integrins, and scaffold proteins. In comparison, the ring structures were completely unresolvable in conventional fluorescent images (Fig. 2.6, bottom image on the right).
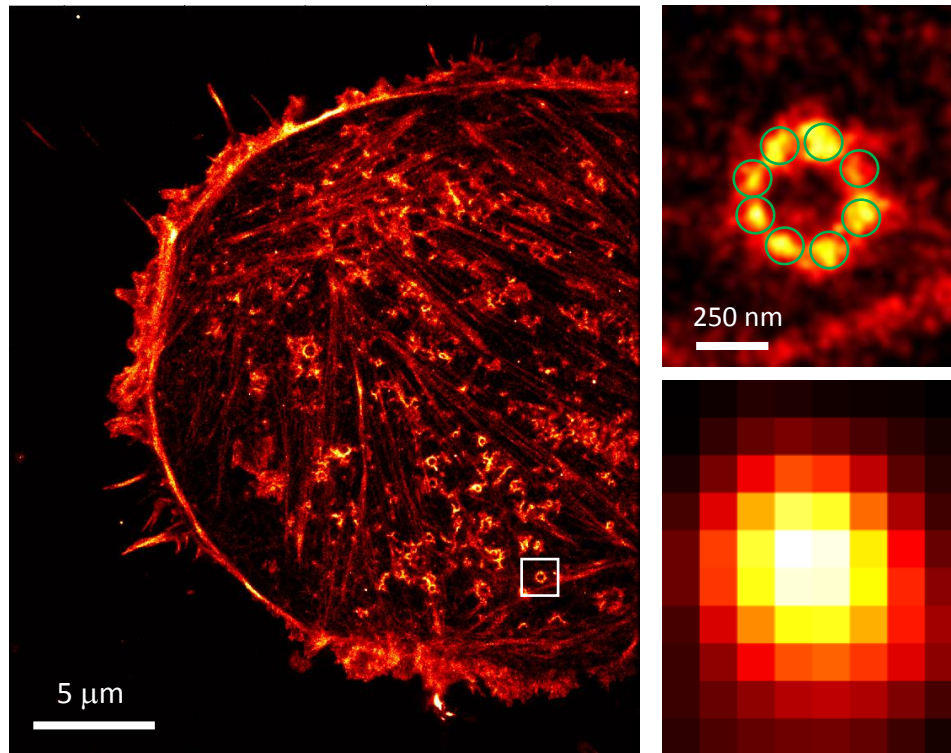
Figure 2.6 2D SMLM image of actin in a fixed SKBR3 cell.

The ability to resolve individual microtubule and actin filaments in cells using fluorescence microscopy opens new possibilities for studying numerous actin, microtubule-related processes in cells. However, most biological structures are three-dimensional with

features extending above and below the focal plane; for these structures, superresolution imaging in 3D is required.

   3D SMLM Images of Microtubules and Lamin. Applying 3D SMLM to cell imaging, we performed indirect immunofluorescence imaging of the microtubule network in U2OS cells, Fig.2.7. Cells were immunostained as in 2D SMLM experiments. The 3D SMLM image not only showed a substantial improvement in resolution over the conventional fluorescence image, but also provided the z-dimension information (color-coded) that was not available in the conventional image. Multiple layers of microtubule filaments were clearly visible in the image. Z range covered from -500 nm to +500 nm with about 60-70 nm axial resolution.
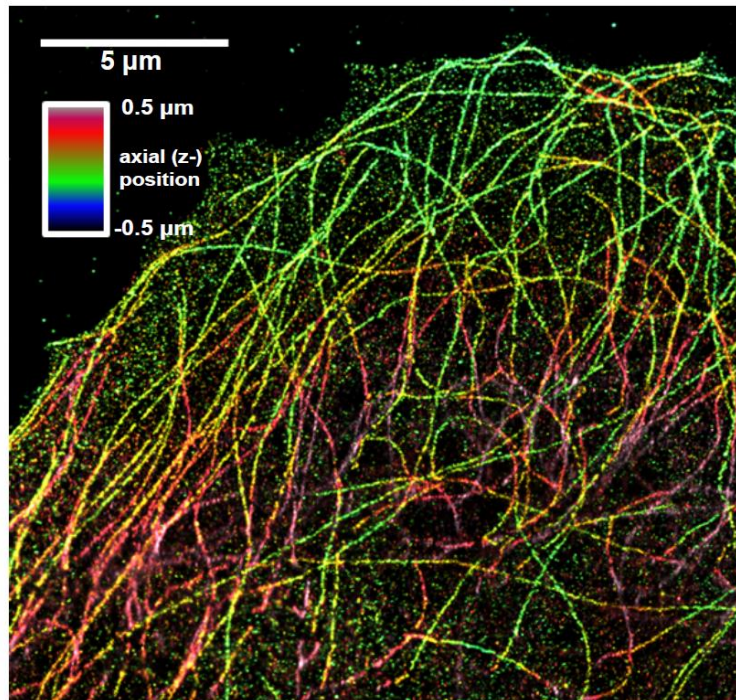
Figure 2.7 3D SMLM image of microtubule in fixed U2OS cell

   3D SMLM can generate superresolution images by localizing both lateral and axial positions of each probe, and acquire a lateral resolution of 20-30 nm and an axial resolution of 50-60 nm using astigmatism imaging. However, it only proved a measure of the average

localization precision within 800-1000 nm depth near the focal plane. The localization precision degrades when the molecule is further away from the focal plane, limiting the z-dimension imaging range if the position of the focal plane is fixed. To extend the z range, typically several micrometers thick, we scanned the axial position of the objective to acquire multiple image slices at focal planes deeper into the cell. Then we stacked these slices to form "whole-cell" 3D images. Fig. 2.8 showed whole nucleus staining with lamin B1. The left side of the Fig. is top view of the nucleus with 500 nm z sectioning. The right one is side view of the nucleus with volume rendering.
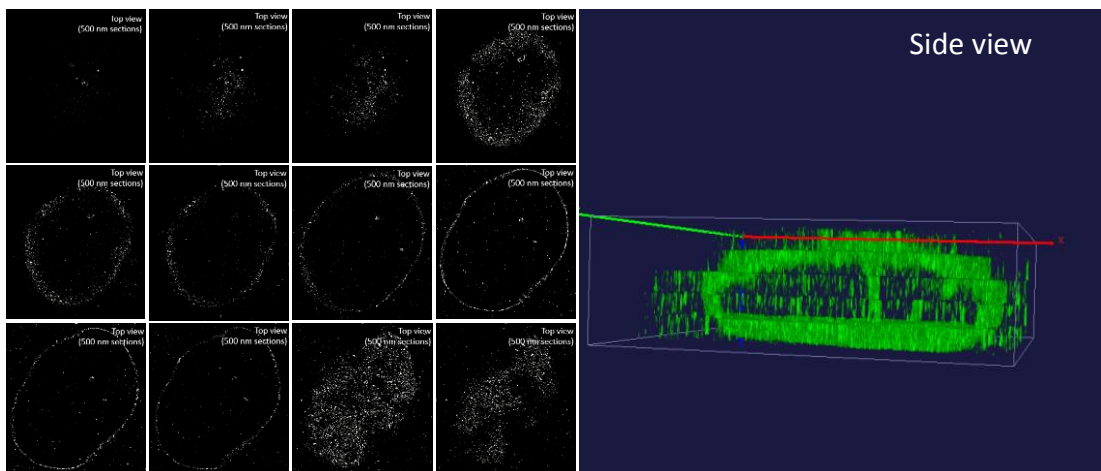
Figure 2.8 3D SMLM image of the whole nucleus of a fixed U2OS cell.

2.4.3 Imaging FFPE tissue sample with 3D SMLM

Formalin-fixed, paraffin-embedded (FFPE) tissue specimens are the mainstay of tissue archiving with well over 400 million FFPE tissue samples assembled in biorepositories. These preserved tissues have the potential to improve our understanding of diseases, especially in oncology where biopsies and resected specimens are routinely maintained in clinical practice. Use of fresh frozen tissue has long been considered the "gold-standard" for molecular assays as proteins and genetic material are preserved in their native state.[67-69] However, ice crystal formation is common, creating artifacts that are not seen in FFPE preserved tissues. Advances in

46

antigen retrieval techniques have made the majority of proteins accessible in FFPE preserved samples, further establishing it as the standard preservation method for simultaneous analysis by immunohistochemistry (IHC) or immunofluorescence (IF) and histomorphology.[70] Additionally, FFPE preserved tissues are also convenient and cost-effective to archive as they can be stored at ambient temperature with perfectly preserved proteomics for decades.

While molecular profiling using *in situ* hybridization, IHC or IF, and other techniques are commonly performed on FFPE sections, visualization of morphological features are still most frequently used for disease diagnosis and pathological analysis. However, both morphological and molecular tissue analyses are limited by the spatial resolution of the instrumentation utilized to assess tissue structure as well as genomic, proteomic and metabolomics profiles. With the advent of SRM including SMLM, visualization of biology at spatial resolutions on the order of 10-20 nm has revealed exciting, new biological phenomena previously invisible to diffraction-limited light microscopy.[71-74] More recently, stimulated emission depletion microscopy (STED) was used to image FFPE human rectal cancer tissues, the first demonstration of any SRM technique successfully applied to FFPE tissues; the images demonstrated preserved antigenicity for up to 17 years for tissues store in FFPE blocks. However, to date 2D high-resolution reconstructions of FFPE tissues with SMLM have not been demonstrated and 3D SRM reconstructions of any variety in FFPE tissues have not been shown due to a number of technical hurdles hampering adequate sample preparation and high quality data collection. Thus, SMLM is an additional SRM technique for FFPE imaging that can offer nanoscale resolution in all three dimensions.

We have utilized SMLM for imaging FFPE tissue sections to reveal ultrastructural details of fluorescently labeled protein targets in both 2D and 3D high-resolution reconstructions. Optimized conditions for reliable retrieving and immunostaining of multiple antigens in breast cancer samples with high specificity and structural integrity were developed. SMLM was used to visualize a) HER2, a membrane receptor overexpressed in ~25% breast cancers;[75] b) TOM20, a

mitochondria outer membrane protein;[76] and c) Lamin B1, a nuclear membrane protein in immuostained thin FFPE sections.
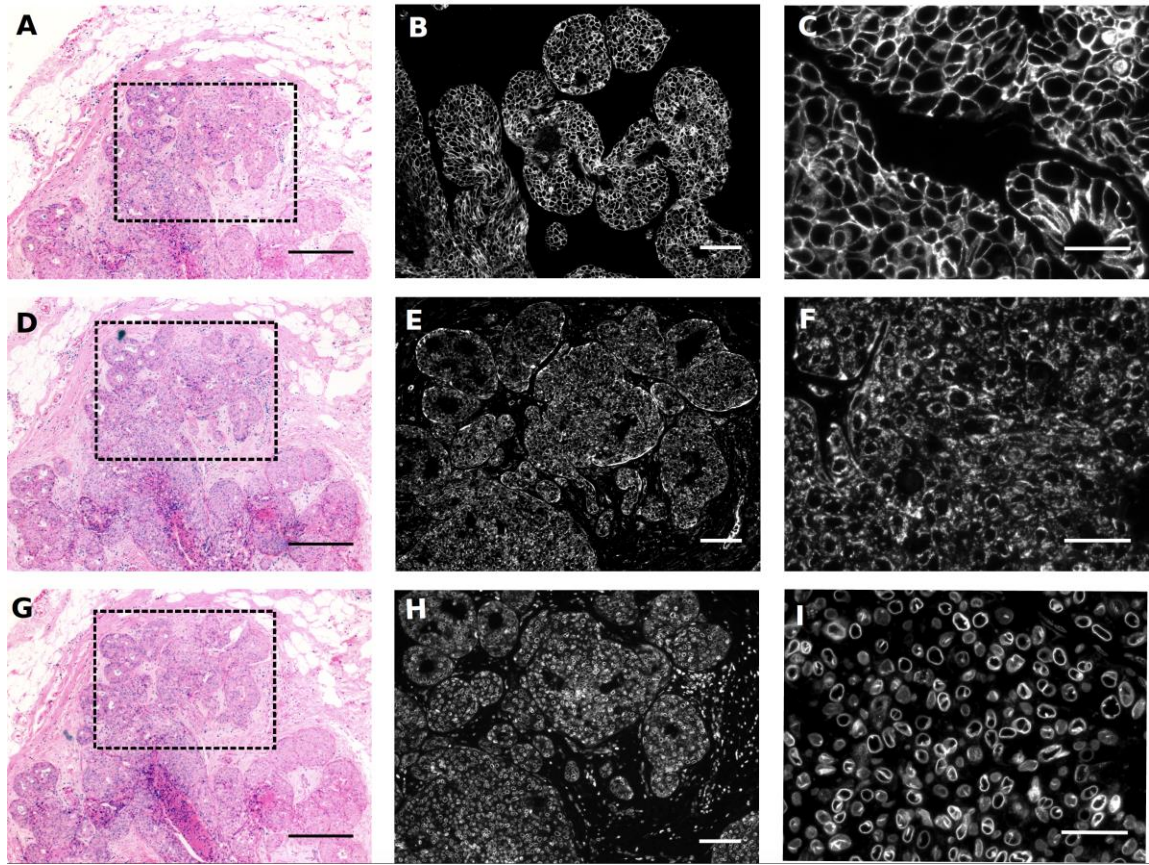
Figure 2.9 Morphology of FFPE HER2 positive, grade 3 IDC breast cancer tissue. Tissue sections were stained with H&E and overview images were collected at 5X magnification to show tumor morphology (A, D, and G). The box in the H&E image represents the field-of-view of the adjacent immunofluorescence images. Scale bars for H&E images = 200 µm. Images of immunofluorescence staining were collected at 10X magnification to demonstrate the tissue patterns of HER2, TOM20, and Lamin B1 proteins (B, E, and H). Scale bars = 50 µm. Additional images were collected at 40X magnification to enhance visualization of ultrastructural features of each immunostain (C, F, and I), scale bars = 20 µm.

SMLM of FFPE reveals functional ultrastructure in tissue. SMLM was used to image tissue sections prepared with the same immunostaining procedures as previously described for HER2, TOM20 and Lamin B1. Enabled by both highly specific labeling of the target molecules and the superior photophysical properties of Alexa Fluor 647, SMLM images of all three molecular targets clearly exhibited distinct structural features absent from conventional epifluorescence images (Fig. 2.10). Fine patterns of membrane-targeted HER2, for example, were clearly visualized even in areas between adjacent epithelial cells, where protrusions between cells were readily demonstrated (Fig. 2.10A). Membrane protrusions enriched in HER2+ cells have been observed in cultured cells using immuno-EM [77] and IF microscopy, and these protrusions have been implicated in persistent localization and signaling of HER2 in breast cancer cells.[78] While morphologically similar protrusions in HER2+ tissues have been reported using various EM techniques,[79] it was not clear whether those were enriched in HER2. Hence, the observation of HER2-enriched protrusions in FFPE sections of breast tumors indicate that similar protrusions appear to exist *in vivo* and may play functional roles in tumor biology.

SMLM images of TOM20 and Lamin B1 also demonstrated the excellent resolving power of SMLM compared with conventional fluorescence microscopy and the well preserved structural details of both the mitochondria and the nuclear envelop in the FFPE samples (Figs. 2.10B and 2.10C). TOM20 images showed unambiguous localization to the mitochondria membrane (Fig. 2.10B). Lamin B1 images revealed additional membrane structures instead of a single, solid line marking the nuclear envelope (Fig. 2.10C). It is currently unclear if these structures arose from tissue cutting artifact, or are in fact novel structures not previously visualized due to resolution limitations of conventional microscopy. Additional assessment is underway to determine the source of these structural features. Assessment of the functional utility of these features will be important in future work to determine if they are related to the region of nuclear envelope sampling or may in fact be important for nuclear organization. Additionally, SMLM imaging of the nuclear envelope also demonstrated the sampling diversity in a single

49

FFPE section where sections through the center of individual nuclei were visible as well as of the outer edges of the nuclear envelope, something not readily distinguished by conventional epifluorescence microscopy (Figs. 2.9I). The tissue blocks used in these studies had been stored at room temperature for 11 years prior to the staining and imaging experiments. The acquired images demonstrated the ability to preserve antigenicity after room temperature storage for more than a decade, similar to previous work using STED microscopy.
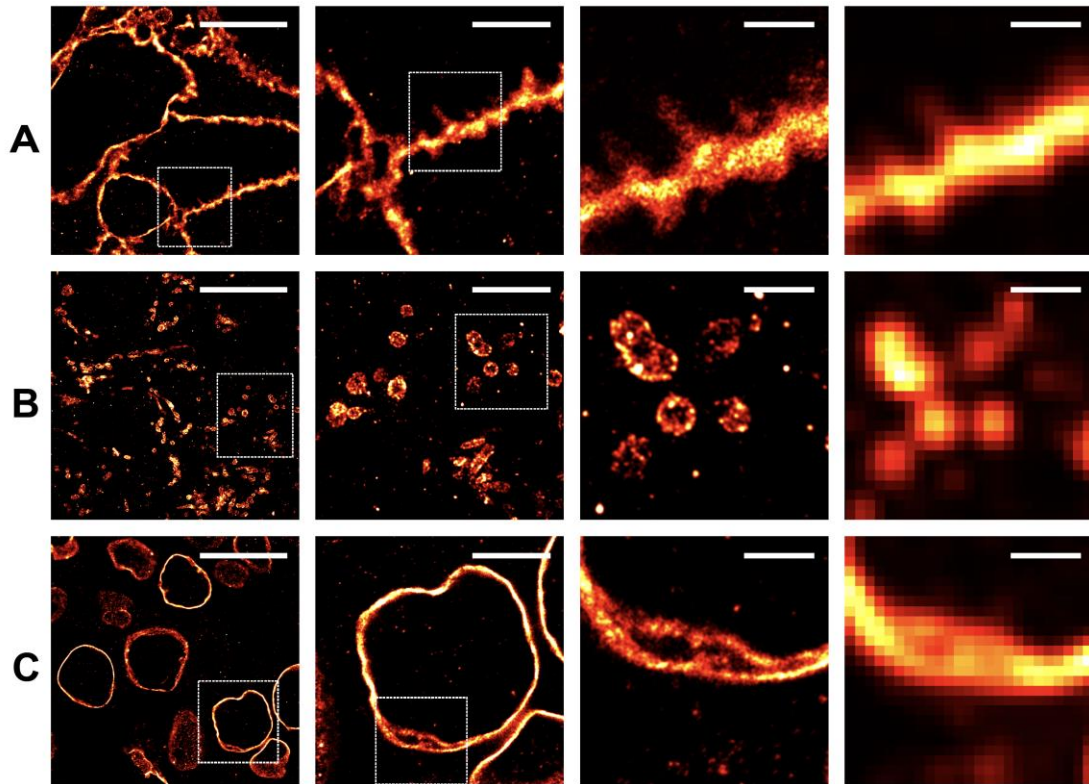
Figure 2.10 2D super resolution imaging of HER2, TOM20, and Lamin B1 in FFPE. SMLM images at varied magnifications demonstrate the ability to resolve tissue ultrastructure not visible using conventional microscopy. Scale bars for each column of images are from left-to-right 10 μm, 4 μm, 1 μm and 1 μm, where the images in the right most column demonstrate a comparative confocal reconstruction further highlighting the necessity of SMLM to visualize nanoscopic features within the tissues. A. Extracellular membrane protrusions were visible between HER2 positive cancer cells. B. The outer membrane of the mitochondria and the tubular

nature of this organelle were prominently resolved by SMLM imaging. C. The lamin network of

the nuclear lumen was highlighted.

SMLM enables 3D visualization of functional ultrastructure. Compared with the 2D

images, which were projections of features within the entire slab, imaging in 3D revealed even

greater ultrastructural features within much finer (~100 nm) optical sections above the coverslip.

For example, membrane vesicles (blebs) with HER2 staining were clearly visible, as previously

demonstrated using stimulated emission depletion (STED) imaging of FFPE tissues. Three

dimensional imaging also facilitated assessment of mitochondrial arrangement within the cytosol

surrounding the nuclei in malignant cells in all directions. Nuclear structure was also more readily

assessed where the top and bottom of the structures were easily visualized as well as folds in the

membrane structure that appeared to be sample artifact in 2D imaging studies (Fig. 2.11).
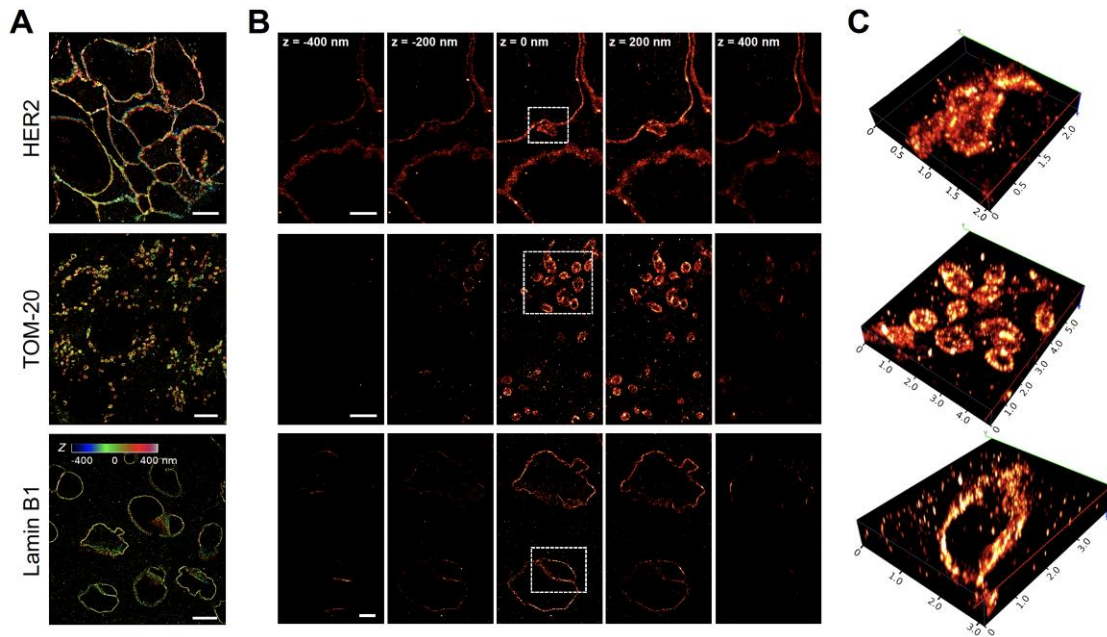
Figure 2.11 Imaging HER2+ tumor FFPE sections with 3D SMLM.

A. Reconstructed 3D SMLM images of FFPE sections immunostained for HER2 (top), TOM-20

(middle), and Lamin-B1 (bottom) with Z-positions of the molecules color coded. B. Slice views

of 3D SMLM images of HER2 (top), TOM-20 (middle), and Lamin-B1 (bottom) in 200 nm increments are demonstrated where each slice represents the projections of all localization events within 20 nm relative to the z-plane. All images were collected on 2 μm sections. C. Volumetric rendering of the boxed areas in B are shown. Scale bars as follows: 10 μm (A), 2 μm (B, top and bottom), 1 μm (B, middle).

In this setting, we estimated that the lateral (x-, y-) resolution was on the order of 20-40 nm and the axial (z-) resolution was around 60-80 nm (Fig. 2.12). The resolution achieved in all three dimensions were slightly lower than previous reports[80,81] or those achieved on culture cells using similar setups, likely due to the slightly elevated background in the single-molecule images and potential mechanical instability of the sections on the coverslip.
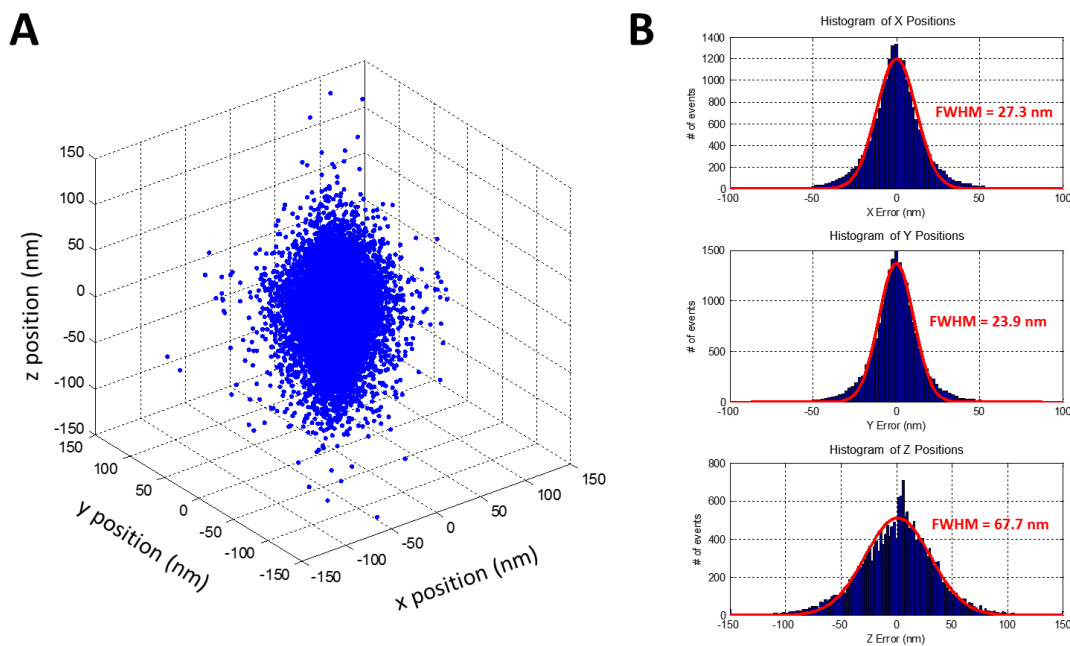
Figure 2.12 Analysis of imaging resolution in all three dimensions.

Imaging resolution was calculated similarly to that reported by Huang *et al.*[81]. Briefly, each fluorescent molecule (AF647 in this case) generated a number of localization events in

successive frames, each at a slightly different (x, y, and z) coordinate. An intensity-weighted average 3D position was calculated and used as the center-of-mass for this group of localization events, where the spread of individual coordinates around the center-of-mass reflected the localization precision of the molecule. (A) Coordinates of localization events from ~5,000 molecules (totaling 10,000-20,000 events) were aligned at the center-of-mass and plotted in 3D, generating a distribution of x, y, and z positions around (0, 0, 0). This particular dataset was from SMLM images of a 2 μm FFPE section immunostained for Lamin (data from HER2 and TOMM20 were similar). (B) Histograms of x (top), y (middle), and z (bottom) positions shown in (A). The red curves are Gaussian fits to the histograms, with standard deviations of 11.9, 10.4, and 29.4 nm in x, y, and z, respectively. These results correspond to FWHM (equivalent to spatial resolution at Nyquist limit) values of 27.3, 2.39, and 67.7 nm in the x, y, and z directions, respectively.

Impact of sample thickness on image quality. Localization precision and hence resolution of SMLM is sensitive to background, which can increase with sample thickness. To assess the effect of slice thickness on imaging resolution, SMLM images on 2 and 4 μm FFPE sections stained for HER2 were compared with respect to background in raw, single-molecule images as well as the quality of reconstructed, high-resolution images. Despite the increased thickness, raw single-molecule images taken on 4 μm sections were of similar quality to those collected on 2 μm sections, both by visual inspection (Fig. 2.13A) and by analyzing the signal-to-noise ratios and goodness of fit of individual single-molecule images (data not shown). Surprisingly, however, in the reconstructed SMLM images of 4 μm sections, there were visibly higher densities of cytosolic HER2 signals in SMLM images of 4 μm sections (Fig. 2.13B) compared with those reconstructed from data collected on 2 μm section (Figs. 2.10-2.11). By contrast, HER2 was predominantly membrane-bound in cultured SKBR3 cells (Chapter 4 unpublished data). Hence, we considered the cytosolic HER2 signals in Fig. 2.13B to be

background or nonspecific staining. A quantitative comparison of background staining for 2 versus 4 μm sections was completed (Fig.2.14), from which it is evident that the thicker section presented higher background. However, the background difference was < 2-fold, with the pixel areas covered by background representing ~4% to ~7% for 2 and 4 μm sections, respectively, both with large spatial variations. The increased background in thicker sections could be due in part to less robust antigen retrieval and immunostaining for thicker tissue section, as some previous reports have suggested. Despite the increased background, signal (~100% pixel coverage on the membrane) to background (4 – 7% pixel coverage in the cytosol) ratio remained high such that it would not prevent practical use of SMLM to image 4 μm thick tissue specimens. That said, the increased background may become a limiting factor if much thicker samples were desired for SMLM imaging. On a practical note, it was much easier to prepare 4 μm sections without tissue damage or cutting artifact. In part for this reason, 4 μm tissue sections are more commonly used in the clinical settings. Thus, the ability to image 4 μm thick FFPE sections with SMLM provides a potential link to clinically relevant sample handling procedures, where the samples can be imaged both by SMLM for nondestructive characterization of tissue ultrastructure and by conventional pathological analyses such as IF and/or H&E.
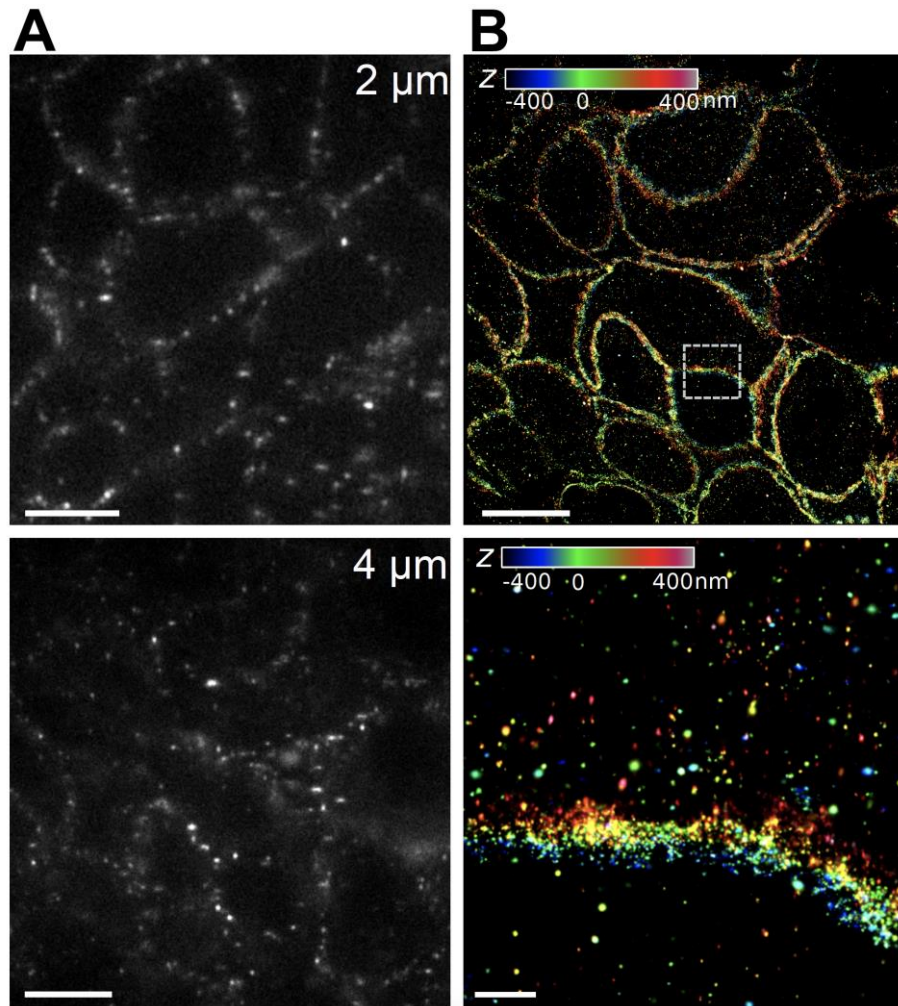
Figure 2.13 Comparing 2 and 4 μm FFPE sections for 3D SMLM imaging.

A. Representative astigmatic single-molecule images collected on 2 and 4 μm sections. B. Reconstructed 3D SMLM image of a 4 μm FFPE tumor section immunolabeled for HER2, with z-positions color coded (see legend). The bottom image shows the zoomed-in view of the boxed area in the top image. Scale bars, 5 μm (left), 10 μm (right, top) and 2 μm (right, bottom).
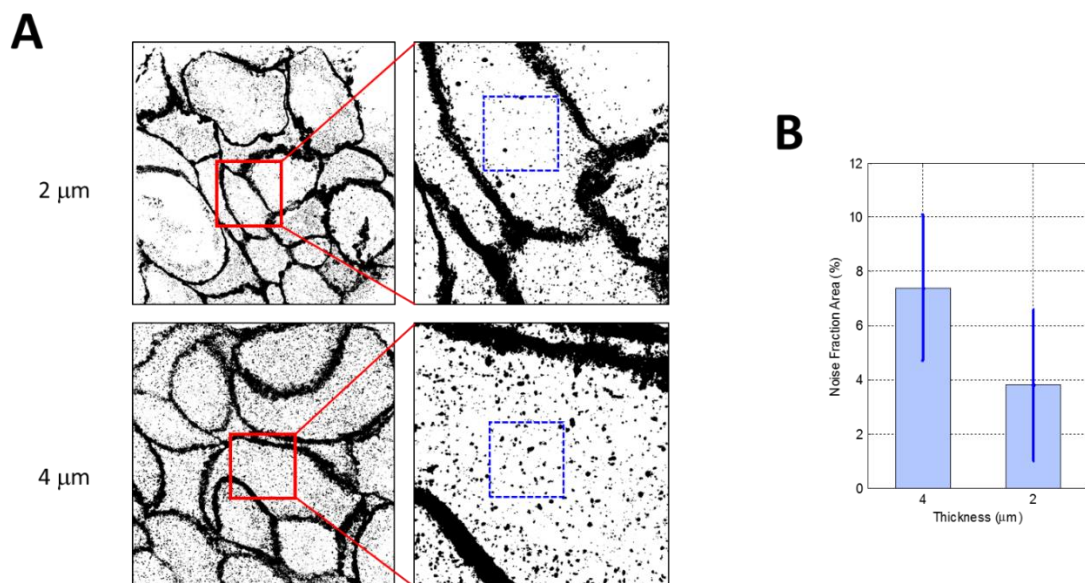
Figure 2.14 Analysis of SMLM image background in 2 and 4 μm sections.

(A) SMLM images of HER2 (as shown in Figures 3.10, 3.12, 3.14) were first converted to binary images using Fiji[82] with automatic threshold values. The black regions indicated high intensity values (i.e., higher densities of localization events). The black outlines depict cell membranes where HER2 molecules were enriched, whereas events in the cytosol likely arose from background staining or imaging artifacts. Note that the effect was much more pronounced for 4 μm sections. Shown on the left are SMLM images of 35×35 μm^2 regions 2 (top) and 4 μm sections, and shown on the right are zoomed-in views of the boxed areas (red boxes, 10×10 μm^2). Blue, dashed boxes in the right panels indicate areas where signal was considered background; (B) Results of the fraction of area covered by background signal, analyzed as particles in the cytosol using the particle statistics function in Fiji. Distributions were obtained by analyzing multiple boxed regions, each approximately 3×3 mm^2 (A, right panel). Sample sizes for 4 and 2 μm sections are 17 and 13, respectively. Error bars indicate standard deviations.

56

2.5 Summary

Herein, we have demonstrated the application of SMLM on cultured cells and FFPE sections for revealing detailed, spatial-molecular data at nanometer resolution. Our results clearly showed the superior resolution that can be obtained in both 2D and 3D SMLM. In particular, FFPE tissues have been used by clinical pathology for almost a century and today, and the developed SMLM imaging methodology adds to the arsenal of measurement technologies utilized by modern precision medicine to characterize proteomic and genomic signatures in health and disease.

Although fluorescence imaging of tissue sections has been completed using both confocal and superresolution microscopies,[83-87] results with SMLM presented here are improved in many respects. The spatial resolution obtained here on FFPE sections with SMLM is ~30 nm laterally and ~70 nm axially, which is on par with previous work with STED[84] and clearly better than conventional confocal microscopy. Both STED and SMLM offer the potential for 3D resolving power, where 3D SMLM imaging has been demonstrated herein and offers a powerful alternative to STED for analyzing biological ultrastructures in cells and archived samples.

Chapter 3   Multispectral superresolution microscopy (MSSRM)

We introduce a new approach for improving the spectral resolution of existing SRM techniques based on simultaneous measurement of single-molecule locations and emission spectra. This technique, termed multispectral superresolution microscopy (MSSRM), allowed us to achieve 10-15 nm spectral resolution in SRM imaging, a 5-10 fold improvement over existing, emission filter-based techniques. This chapter describes the construction, calibration, and fluorophore characterization for the MSSRM, followed by the use of MSSRM for fixed cell 4-color imaging applications.

3.1 Introduction

Superresolution imaging with single-molecule localization microscopy (SMLM) has become an increasingly powerful tool for studying the molecular architecture of cells and tissues at the nanometer scale. As discussed in the previous chapter, SMLM is based on the principle that superresolution images of fluorescently stained samples can be constructed by accumulating subdiffractive localizations of individual fluorophores over time as they stochastically turn on and off. Existing SMLM techniques – (f)PALM[88,89] and (d)STORM[90,91] both take advantage of this approach. Localization of structures with nanometer resolution in a densely labeled sample requires fluorophores that exhibit efficient photoswitching property and moderate to high single-molecule photon output per switching cycle[92]. SMLM imaging of fixed and live cells[93] and single-molecule tracking[94] in live cells allows analysis of static and dynamic molecular structures that previously could not be resolved.

SMLM becomes especially powerful if multiple molecular species or structures can be imaged[95-98] simultaneously, considering the complexity of biological systems. Multicolor SMLM as usually implemented uses dichroic mirrors and bandpass filters to discriminate between fluorophores whose emission spectra are separated by 50-100 nm. This limits the practical spectral resolution of SMLM to 3-4 colors[92,99]. The number of colors can be increased using sophisticated optical setups and image processing algorithms, although spectral crosstalk remains significant for biological applications[99-101]. This limitation may be overcome using multiple rounds of labeling using 3-4 colors per round, for example by combining DNA-PAINT[102] with cyclic immunofluorescence[62,103]. However, these approaches require specialized labeling reagents and time-consuming serial staining and so are not compatible with live cell imaging. They also typically require multiple lasers thereby complicating the imaging scheme and potentially harming the living specimens.

A more powerful approach to multicolor SMLM distinguishes between individual fluorophores based on their spectral signatures instead of using emission filters by recording the position and emission spectrum simultaneously for each fluorophore. This has been achieved using confocal or line scanning schemes, but both are too slow for some uses including live cell imaging. Sonehara *et al.* introduced a prism-based wide field single-molecule spectral imaging scheme to obtain the emission spectra of all fluorescent molecules in the field of view at once[104]. However, the fluorophore positions can only be obtained by separately imaging gold nanoparticles to which the fluorophores were attached. While the authors were able to distinguish 4 fluorophores (emission maxima 540-620 nm), this approach is not practical for SMLM since the gold nanoparticles do not photoswitch or photobleach, and cannot be added to the sample at high densities. Broeken and colleagues used a spatial light modulator to disperse the fluorescence signal from single fluorophores to simultaneously record the positions and spectra, where the zeroth order diffraction recorded the position, and the distance between zeroth and first order

spots corresponds to the emission wavelength. This eliminated the use of separate positional markers while achieving a spectral resolution of ~50 nm[105].

More recently, Zhang *et al.*, introduced a promising form of multicolor SMLM named spectrally-resolved stochastic optical reconstruction microscopy, or SR-STORM, in which two opposing objectives were used in a wide-field imaging scheme[106] to collect two images per fluorophore. Single molecule images collected by one objective were used to determine the positions of fluorophores in the field of view, and images collected by the other objective were dispersed by a prism so that the emission spectra of the same fluorescent molecules can be determined. They used this approach to acquire 4-color images of fixed cells using 4 fluorophores with highly overlapping emission spectra with a nominal spectral resolution of ~10 nm and a spatial resolution of 20-50 nm. This is a significant improvement in spectral resolution over previously reported SMLM techniques. However, the use of two opposing, high numerical aperture objectives requires sandwiching of the sample between two thin cover glasses. This space constraint poses severe challenges to sample loading and environmental control, and it is difficult to apply to live-cell imaging where the cells need to be maintained under physiological conditions with environmental chambers. In addition, it is difficult to implement in commercial high-resolution microscopes since these typically use single-objective configuration.

In this chapter, we describe a new implementation of SR-STORM that overcomes this limitation by acquiring images using a single-objective on a commercial, inverted microscope frame. We refer to this instrument as a <u>M</u>ulti<u>S</u>pectral, <u>S</u>uper <u>R</u>esolution <u>M</u>icroscope (MSSRM). Fluorescence signals in the MSSRM are collected through the objective and split between two optical paths, one of which acquires images showing positional information and the other acquires images showing spectral information. We demonstrate the performance of the MSSRM through acquisition of images of cellular structures in 4 colors with very low spectral crosstalk (2% or lower) using fluorophores previously used in SR-STORM and single laser excitation. We show that we are able to achieve 20-50 nm spatial and ~15 nm spectral resolutions. My labmate also

show use of the MSSRM for simultaneous 3 color single-molecule tracking in live cells at ~20 ms time resolution during which cells are kept under physiological conditions using an on-stage incubator. This technique revealed cell surface proteins that sometimes exhibit random movement patterns and at other times are constrained to move in small domains.

3.2 Materials and Methods

Cell Culture: U2OS cells (human osteosarcoma, ATCC, HTB-96) were maintained at 37°C and under 5% CO_2 in DMEM supplemented with 10% FBS (Life Technologies, 11995 and 10082 respectively). For imaging, LabTek (Thermo, 155409) or μ-Slide (ibidi, 80827) chambers with a #1.5 coverglass bottom were first cleaned by incubating with 1 M NaOH for 2 hours at room temperature, followed by washing 5 times with MilliQ water and incubation with MilliQ water or PBS overnight. Cells were plated in the chambers 36-48 hours prior to imaging in phenol red-free DMEM (Life Technologies, 21063) supplemented with 10% FBS.

Immunofluorescence labelling: For immunostaining of U2OS cells, the cells were briefly washed with PBS before fixation in a PBS buffer containing 3.7% paraformaldehyde and 0.05% glutaraldehyde. The cells were then incubated with WGA-CF680 (Biotium, 29029, 1:100 dilution in PBS) for 20 min, followed by washing 3×5 min with PBS. Cells were permeabilized and blocked in the dilution buffer (PBS with 3% BSA and 0.05% Triton X-100) for 30 min. Next, the cells were incubated with primary antibodies in the dilution buffer for 1 hr. After thorough washing (3×5 min) with PBS, the cells were incubated with secondary antibodies in the dilution buffer for 45 min then washed again in PBS for 3×5 min and stored in PBS until imaging. The primary antibodies used were rabbit anti-Tom20 (Abcam, 78547, 1:500 dilution), chicken anti-vimentin (EMD Millipore, AB5733, 1:5,000 dilution), rat anti-α-tubulin (Thermo, MA1-80017, at 1:2,000 dilution). The secondary antibodies used were donkey anti-rabbit (JacksonLabs, 711-005-152), goat anti-chicken (Thermo, SA5-10073) and donkey anti-rat (JacksonLabs, 712-006-

150) conjugated to DY634 (Dyomics), DL650 (Thermo), CF660C (Biotium), respectively, using manufacturer recommended procedures. Typical dye to antibody conjugation ratios were between 2 and 4. Exact dilutions of dye conjugated secondary antibodies were optimized batch-to-batch.

MSSRM imaging of fluorescently stained cells were performed in PBS buffer supplemented with ~100 mM mercaptoethylamine (MEA, Sigma, 30070) or 1-2% β-mercaptoethanol (BME), 5 ug/mL glucose oxidase (Sigma, G2133-50 kU), 0.4 ug/mL catalase (Sigma, C100-50 MG), and 10% glucose (w/v, Fisher Chemicals D16-500). For all fixed cell imaging experiments, the EM-CCD was operated in frame transfer mode at 10-15 ms per frame acquisition time with an EM gain setting around 300. Additionally, only the center 512×200 pixels (i.e., the positional and spectral channels each occupy a region of 256×200 pixels) were used for recording raw images.

Data acquisition and analysis: Acquisition of raw images was performed using the open source micromanager software suite (https://micro-manager.org/). Image analyses for extracting single-molecule localization and spectra were all performed with custom MatLab (Mathworks, MA) scripts as described previously[65,107].

For spectral analysis, individual molecules were first identified in the positional channel. A corresponding 'center' position for each molecule in the spectral channel was computed based on a transformation matrix, which was determined by registering positional and spectral images of gold fiduciaries on the coverslip taken with the 661 ± 5.5 nm bandpass filter. For each molecule, a 51 (rounded center position ± 25 along the dispersion direction) pixel × 3 (orthogonal direction) pixel region in the spectral image was used as its raw spectrum. The raw spectrum was first smoothed by moving average to locate the pixel with maximum intensity. Next, the precise pixel position of maximum emission was calculated by using a second-order polynomial fitting of pixels surrounding the one with maximum intensity; this was used to calculate *ssd*. For multicolor data, coordinates of each fluorophore were first separated based on *ssd* values as

described in the text; each channel was then rendered separately and recombined in ImageJ (https://imagej.nih.gov/ij/)[82] into a composite image.

3.3 Instrumentation

3.3.1 Experimental setup

The MSSRM was constructed on a commercial, inverted microscope frame (Fig 3.1A). Briefly, lasers emitting at 405 (Coherent OBIS 405, 100 mW), 561 (Coherent Sapphire 561, 150 mW), and 637 nm (Coherent OBIS 637, 140 mW), respectively, were combined and introduced into the back of a Nikon Ti-U microscope equipped with a 60× TIRF objective (Nikon, NA 1.49). The illumination can be continuously tuned between epi-fluorescence and strict TIRF modes by shifting the incident laser horizontally with a translational stage before entering the microscope. For the MSSRM, single edge dichroic mirrors Di02-R561 and LPD02-633RU were used to reflect the laser into the objective and clean up fluorescence signals from the sample; these dichroic mirrors also reflect 405 nm light needed for photoactivation and photoswitching. A short pass filter (Semrock, BLP-633R) was placed in front of the 637 nm laser to clean up the output. The OBIS 637 laser was set to operate at 11° C to bring the center wavelength down to ~635 nm in order to work with the filters.

Fluorescence signals were collected at the side-port of the microscope, with a slit (Thorlabs, VA100) at the intermediate image plane to narrow the field of view. The window width of the slit was fine-tuned after projecting images in both channels onto a single EM-CCD side by side. An infinity space was created by placing a triplet lens (Newport, PAC076, f =125 mm) at the Fourier plane of the intermediate image. A filter wheel was mounted in the infinity space right after the triplet lens to position emission and/or notch filters for further cleanup of the signals and specification of detection wavelength range. A nonpolarizing beam splitter (Thorlabs, BS022) was inserted after the filter mount to divide the signal into positional (30%, transmitted) and spectral (70%, reflected) channels. Signal in each channel was re-focused with another triplet

lens (f=125 mm) before the two channels were combined using a knife-edge mirror (Thorlabs, MRAK25-E02) and projected onto the left and right halves of the same EM-CCD (Andor, iXon Ultra 897), respectively.

To disperse fluorescence signals in the spectral channel, an equilateral prism (Thorlabs, PS863) was placed after the beam splitter and at the Fourier plane of the last focusing (triplet) lens. Two steering mirrors were used to bring the light path back to the original direction (i.e., in the absence of the prism).
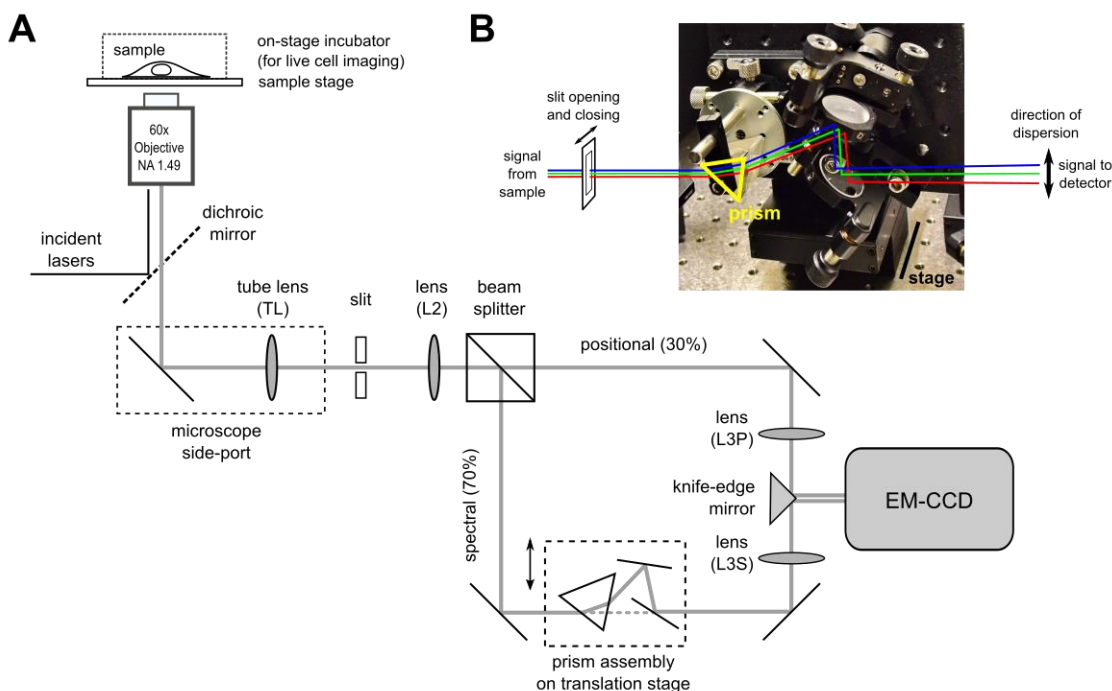
Figure 3.1 The MSSRM setup.

(A) Optical scheme of the MSSRM, constructed based on a standard, single-objective, single-molecule localization microscope. To achieve simultaneous recording of the positions and emission spectra of all fluorescent molecules in the field of view, signals from the sample were split into two channels at 30:70 for the positional and spectral channels, respectively. The signals were then projected to the left and right sides of the detector after passing through the lenses L3S (spectral) and L3P (positional), respectively, and combining on a knife-edge mirror. In the spectral channel, a prism assembly consisting of an equilateral prism and a pair of mirrors was

inserted in the infinity space between lenses L2 and L3S to disperse the signal. The prism assembly was mounted on a translational stage so that it could be moved in and out of the beam path, and the pair of mirrors after the prism was used to align the light path so that the overall direction of light propagation did not change in this channel; (B) Picture of the prism assembly in the microscope setup. The prism was mounted on its side so that the signals came in at the minimum dispersion angle and induced dispersion in the direction perpendicular to the closing direction (horizontal in this case) of the slit.

The same, high numerical aperture objective was used to illuminate the sample and to collect the fluorescence signal. The signal was subsequently split at ~30:70 ratio between a positional channel and a spectral channel, respectively. The resulting signals in the two channels were projected onto the left and right halves of the same EM-CCD to yield two side-by-side images. A prism assembly was then inserted in the Fourier plane in the spectral channel to disperse the signal from each fluorophore into its spectral components. A slit was placed at the intermediate image plane to clip the image to a size matching half of the CCD chip.We constructed the prism assembly on a translational stage to conveniently move it in and out of the light path, similarly to that described by Zhang *et al.*[106]. With the assembly out, the two channels were aligned to yield nearly identical images with sub-pixel precision. The assembly, which comprises an equilateral prism and a pair of mirrors, was then put into the light path of the spectral channel to disperse the signal. The prism also diverts the signal beam, but the diversion is corrected by aligning the pair of mirrors behind the prism to steer the spectral image back to the same location on the EM-CCD as without the prism assembly (Fig. 3.1B). Fine adjustments of the prism assembly are further discussed in the next section. Of note, we chose to orient the prism to disperse light in the direction parallel to the left and right edges of the slit so that the slit edges do not cast shadows in the spectral image (Fig. 3.2).
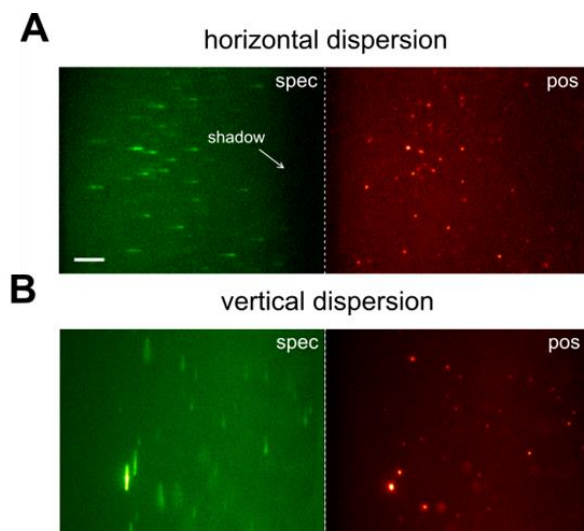
Figure 3.2 Vertical versus Horizontal spectral dispersion

The MSSRM generates a positional image and a spectral image for each fluorescent object in the field of view. With the prism out, the two images are nearly identical, and all the spectral components are focused to the same diffraction-limited spot on the detector (Fig. 3.3A, top). With the prism in, the spectral image of each object becomes elongated along the direction of dispersion and the intensity profile of this image encodes the emission spectrum of the object. Each wavelength component in the signal from an object is deflected at a distinct angle by the prism and projected onto the detector at a specific distance away from the original image without the prism assembly. The distance between the centroids of the positional and spectral images of a fluorophore in the overlaid image is defined as the *spectral shift distance* (*ssd*) for the fluorophore. (Fig. 3.3A, bottom).
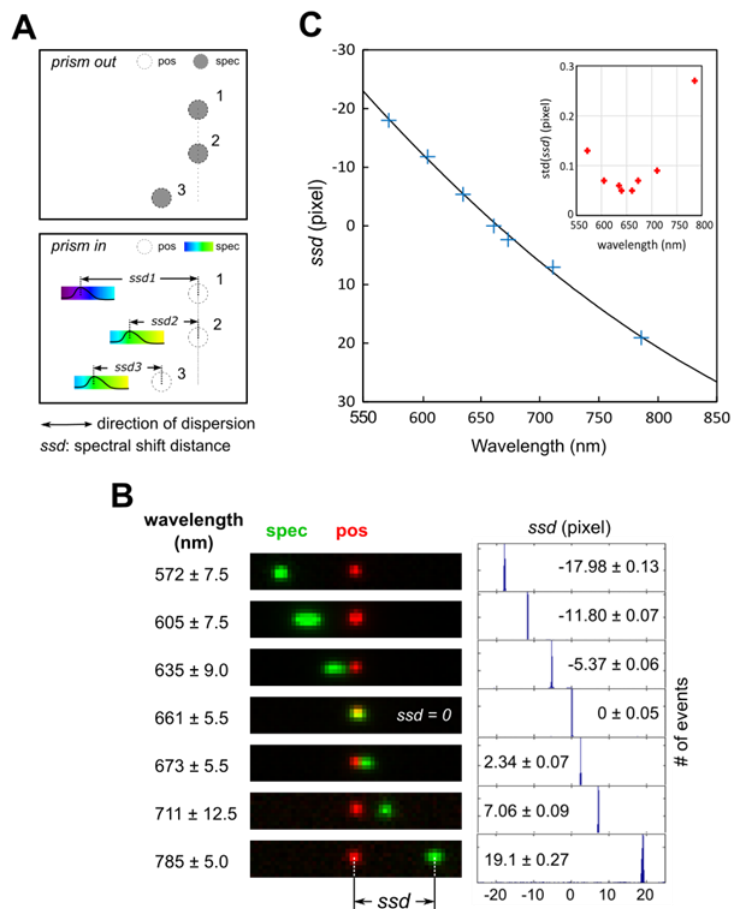
Figure 3.3 Calibration of the MSSRM.

(A) Principles of spectral measurement on the MSSRM. The positional (empty circle) and spectral (filled circle) images were first aligned with high precision before the prism was inserted (top panel). With the prism inserted, the spectral images of all fluorescent objects became elongated, and the intensity profile of each elongated image represented the emission spectrum of the corresponding object (bottom panel). For each object in the overlaid image, its spectral shift distance (ssd) was defined as the distance between the centroid of its positional image and the (sub-) pixel position of maximum emission intensity in the spectral image. In this case, objects 2 and 3 are the same type of fluorophore and they exhibit the same ssd (i.e., ssd2 = ssd3) values, whereas object 1 is in a different color exhibiting a different ssd value (ssd1); (B) Overlaid positional (red) and spectral (green)

67

images of fluorescent beads (broad emission between 500 and 800 nm when excited at 488 or 561 nm) after passing through a series of narrow bandpass filters as indicated. The data point at ~572 nm was taken with 488 nm excitation and the remaining data were taken with 561 nm excitation. The positional and spectral images were intentionally overlapped with subpixel precision at 661±5.5 nm (i.e., ssd = 0.0). Thus, images acquired at shorter wavelengths had negative ssd with the spectral image to the left of the positional image, and the opposite in images taken at longer wavelengths (left). Shown on the right, histograms of ssd at each wavelength with the means and standard deviations indicated; (C) Calibration curve showing the relationship between the center wavelength and the measured ssd values. Inset is the standard deviation of ssd at each wavelength.

3.3.2   Calibration

Spectral calibration of the MSSRM was performed by imaging 40 nm fluorescent beads (Life Technologies, F8793). Narrow bandpass filters were inserted in the infinity space below the objective to specify the wavelength range of signals to reach the detectors. This resulted in a relatively narrow image in the spectral channel to allow for calculation of the distance between the precise centroid positions of each molecule in the two channels. The bandpass filters used for this purpose were all from Semrock with part numbers FF01-572/15, FF01-605/15, FF01-635/18, FF01-661/11, FF01-673/11, FF01-711/25, and LD01-785/10. Of these, the FF01-661/11 filter was used to overlap the positional and spectral images; the same filter was also used prior to and after each MSSRM imaging session to ensure alignment between the two channels and to obtain a transformation matrix specific for the imaging session. The transformation matrix was acquired for each experiment to ensure accurate co-registration between these two channels and optimal spectral accuracy of the MSSRM.

The fluorescent beads emit broadly between 550 nm and 800 nm when excited at 488 or 561 nm. Specific wavelength ranges were selected by inserting filters with 10-20 nm transmission bandwidths, yielding much less elongated and symmetric spectral images to facilitate both alignment and centroid determination (Fig. 3.3B). We adjusted the system using the pair of mirrors in the prism assembly so that the positional and spectral images acquired using a 661 ± 5.5 nm bandpass filter coincided (Fig. 3.3B, middle panel). We noted that the overlap gradually deteriorated towards the periphery because light from peripheral objects enter the prism at different angles than that from a central object. We corrected for this by computing a registration matrix between the two images. This reduced the registration error to ~0.05 pixel across the whole field of view. This is equivalent to a spectral accuracy of ~0.3nm. The same matrix was used to register paired positional and spectral images taken at other wavelengths. In this way, the *ssd* was set to be 0 (±0.05) pixel for objects emitting at 661 nm on the MSSRM (Fig. 3.3B, right panel). We chose 661 nm as the 'central' wavelength because it is roughly at the midpoint of the emission wavelength range for commonly used SMLM fluorophores (~520 to ~800 nm).

We obtained *ssd* values for other wavelengths using six different bandpass filters with center transmission wavelengths ranging from 572 to 785 nm (Fig. 3.3B). Thousands of beads were measured at each wavelength to determine the mean and standard deviation for that *ssd* (Fig. 3.3B, right panel). We designated the *ssd* values at wavelengths shorter than 661 nm to have a negative sign and those at longer wavelengths to be positive. We fitted a second-order polynomial to the calibration curve and used the resulting analytic formula to convert *ssd* values from pixels to wavelength units (Fig. 3.3C). *ssd* values referenced in wavelength or pixel units will be used interchangeably for the rest of this manuscript. Notably, the standard deviations of *ssd* values typically were ≤ 0.1 pixel except for the last data point at 785nm where emission from the beads was weak (Fig. 3.3B and inset in Fig. 3.3C). This indicates that the inherent spectral precision of this MSSRM setup should be better than 0.6 nm.

3.4 Optimize imaging conditions for the MSSRM

3.4.1   Characterization of fluorophore for the MSSRM

The ability to measure single-molecule positions and spectra for individual fluorophores enables multicolor localization microscopy without using emission filters. This is based on the concept that, although the emission spectrum of a fluorescent molecule can be broad (50-100 nm), the centroid of its emission spectrum (i.e., the precise maximum emission wavelength) and hence the *ssd* can be determined with much better precision. The precision is determined by the number of photons collected from the molecule and by environmental variability in the emission spectrum. The narrower the distribution of single-molecule *ssd* values, the less spectral separation is needed between two fluorophores to reliably distinguish them, and thus the more colors could be imaged simultaneously within the same sample. Hence, properties of ideal fluorophores for MSSRM should include:

  (a) good single-molecule brightness;

  (b) complete photoswitching;

  (c) a low fraction of time spent in the *on* state (i.e., the duty cycle)[92];

  (d) a narrow spectral distribution to reduce the *ssd* standard deviation.

Of these, (a)-(c) were the same as conventional SMLM. We tested dozens of fluorophores for their performance for MSSRM including several that had been had been used previously for SMLM or SR-STORM[106], and a subset of these is listed in Fig. 3.4. From these, it is clear that the performance of fluorophores for MSSRM varies greatly. For instance, Alexa Fluor 647 (AF647), one of the best fluorophores for SMLM, has a small *ssd* value standard deviation at ~2.7 nm and makes an excellent MSSRM probe; by contrast, DY703 performs well for SMLM but has ~11 nm fluctuations in *ssd* values and hence is suboptimal for MSSRM. A few other fluorophores showed different fluorescence characteristics in solution and in the MSSRM. In general, the emission spectra are blue shifted. For example, the *ssd* for Atto 725 was expected

at ~750 nm from solution measurements, but was measured to be ~680 nm in the MSSRM. We believe that this is due to light induced fluorophore damage but the exact mechanism remains unclear. We consider such fluorophores to be ill suited to MSSRM imaging.
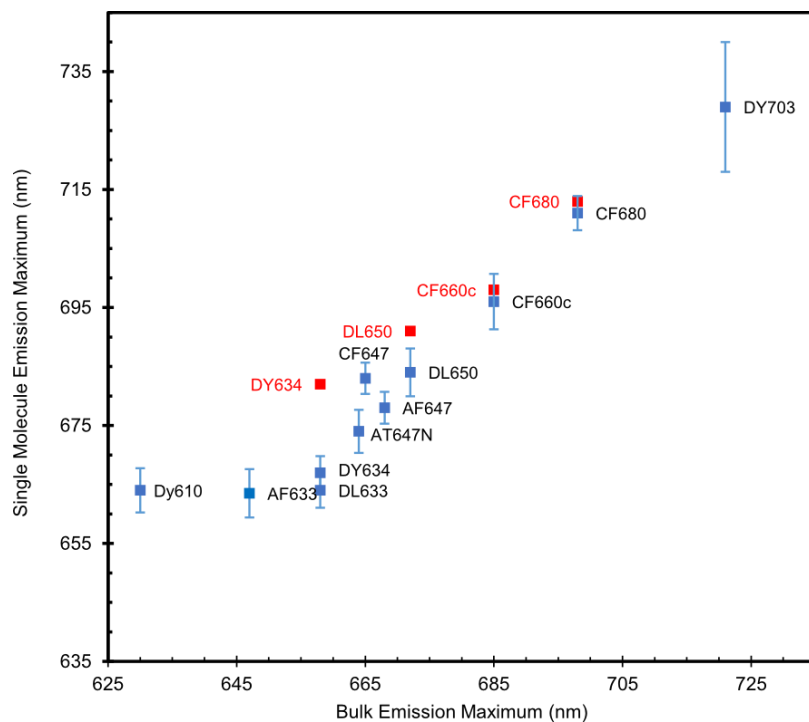
Figure 3.4 ssd of different fluorophores.

Bulk and single-molecule emission properties of selected photoswitchable fluorophores. All fluorophores could be efficiently excited by a 637 nm laser with the exception of DY610, which was excited using a 561 nm laser. The fluorophores in blue were either conjugated to a secondary antibody or phalloidin. Bulk emission maximum wavelengths were measured using a UV-Vis spectrometer, and single-molecule emission maximum wavelengths and standard deviations were measured on the MSSRM (blue and purple) or from SR-STORM (red)[106]. Data for SR-STORM were read from the figures in Zhang et al. for DY634, DL650, CF660C, and CF680, which were used for 4-color imaging therein and in the present work.

The fluorophores Dyomics 634 (DY634), DyLight 650 (DL650), CF660C, and CF680, have been used previously for a 4-color SR-STORM. As expected, they also performed well on the MSSRM, showing efficient photoswitching and good single-molecule photon yields, with median >1,000 photons in the positional channel alone. Their *ssd* values measured on the MSSRM were 662.8nm ± 3.5nm, 680.5nm ± 4.0nm, 696.8nm ± 4.2nm, and 711.9nm ± 2.9 nm (mean ± sd); respectively. Thus, these fluorophores were easily distinguished during MSSRM even though their emission spectra overlap heavily with the emission maxima separated by only 10-15 nm.

One interesting finding during dye screening was that fluorophores show different emission maxima after being conjugated to different targets. As shown in Fig. 3.5, both AF647 and DL650 show variable emission maximum, although in each case the standard deviation remained same. This can be explained by the conformation changed of fluorophores cause by adding antibody to it. The real mechanism hiding behind might be predicted by molecular dynamic simulation. A more practical way will be measure the emission maximum of each secondary antibody with a single color control sample before adding to the final multi-color sample.
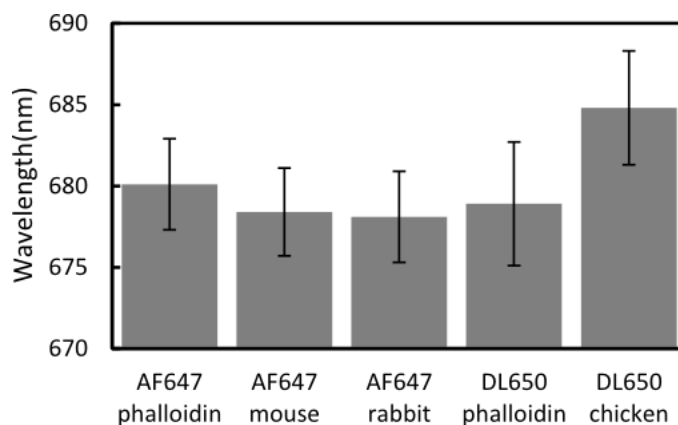
Figure 3.5 Variation in single-molecule emission maximum when a fluorophore is conjugated to different targets.

Two different fluorophores (AF647 and DL650) were conjugated to different targets including phalloidin or different secondary antibodies as indicated, and U2OS cells labeled with these reagents were imaged with the MSSRM. Single-molecule emission spectra were analyzed in each case to yield the mean emission maxima and standard deviations. Note the differences in the mean emission maxima as the same fluorophore is conjugated to different targets.

3.4.2   Imaging buffer for the MSSRM

The photophysical properties as well as the achievable spatial and spectral resolutions of organic dyes are highly dependent on the imaging buffer. For SMLM such as PALM, STORM, and MSSRM, an oxygen-scavenging buffer system with a reducing agent is commonly used. A typical oxygen scavenging buffer comprises a glucose oxidase, its substrate glucose, and a catalase to remove the hydrogen peroxide generated through the oxidation of glucose by the oxidase. This buffer is commonly referred to as GLOX. Another oxygen scavenging system is made of the protocatechuate-3,4-dioxygenase (PCD) and its substrate protocatechuic acid (PCA)[57]. Compared with GLOX, of which the reaction acidifies the solution and renders the buffer much less effective within 1-2 hours, the PCD/PCA system has the advantage of stable PH over an extended duration but is much more expensive.

Either the GLOX or PCD/PCA buffer needs to be supplemented with a reducing agent to create a complex re-dox environment for efficient fluorophore photoswitching. The most commonly used reducing agents for SMLM are mercaptoethylamine (MEA), β-mercaptoethanol (BME), or tris(2-carboxyethyl)phosphine (TCEP) [108]. While the chemical mechanisms of how these reducing agents help fluorophore switching properties are largely unclear, empirical testing has revealed that different reducing agents seem to work best for certain fluorophore backbones. While xanthene- and cyanine-based dyes both perform well in either MEA, BME, or TCEP supplemented GLOX buffers, xanthene-based dyes (such as Alexa Fluor 488 and Alexa Fluor 568) tend to perform better in MEA and cyanine-based dyes (Cy5, Alexa Fluor 647, and Alexa Fluor 750) perform better in BME and TCEP.

Besides the reducing agents, others have also looked into the impact of triplet quenchers on the performance of fluorophores. Among others, COT has been known as an efficient triplet state quencher that improves fluorophore photostability ; it has also recently been added to standard STORM imaging buffers to increase the photon yield and thus the spatial resolution of STORM imaging [57].

Buffer #	Dye	Laser (mw)	Tris	PBS	GLOX	MEA	bME	COT	PCA/PCD	photon(k)	ssd	std(ssd)
1	Dy634	300	0	1	0	0	2	1	0	3.993	0.12	0.49
2	Dy634	300	0	1	1	0	1	1	0	3.499	-0.18	0.51
3	Dy634	300	0	1	0	0	2	1	0	2.677	0.25	0.57
4	Dy634	100	0	1	0	0	1	1	0	2.706	0.16	0.6
5	Dy634	300	1	0	1	0	1	1	1	1.115	-0.04	0.6
6	Dy634	300	0	1	1	0	1	0	0	1.827	-0.05	0.61
7	Dy634	300	0	1	1	0	2	0	0	1.546	-0.02	0.62
8	Dy634	300	0	1	0	1	0	0	1	0.997	-0.16	0.62
9	Dy634	300	1	0	0	0.1	0.5	1	1	1.026	0	0.66
10	Dy634	300	0	1	1	1	0	0	0	1.323	0.01	0.68
11	Dy634	300	1	0	0	1	0	1	1	1.133	0.03	0.68

Table 3.1 Photophysical properties of single Dy634 molecules in various buffers. MEA, BME, GLOX, PCA/PCD, and COT concentrations are relative to 'standard' values (MEA = 10 mM, BME = 1% v/v, GLOX = 1% v/v, PCA/PCD = 1% v/v; COT = 1% v/v). Photon numbers are in thousands (k). Mean and standard deviation of *ssd* are both in pixels (in this case, each pixel ~5.8 nm in wavelength units).

Based on reported buffer recipes, we tested the performance of Dy634 under 11 different buffer conditions. The results are listed in Table 3.1, from which it becomes immediately apparent that the photon yield, mean *ssd* as well as the standard deviation of *ssd* of the same fluorophore can vary widely in different buffers. Of note, the photon number listed here is only for the positional channel, which is just 30% of the total photon flux, as described in previous section.

For a better comparison, we also plotted the photon numbers and std(*ssd*) in bar plots (Fig. 3.6). In general, PBS (PH = 7.4) based buffers show a higher photon yield in comparison with Tris based buffers (PH = 8.0). Additionally, buffers containing BME led to higher photon yield slower initial photo bleaching. Overall, a PBS based GLOX buffer with 1% BME and 1% COT showed the highest photon number (4,930 photons) and best spectral resolution (std(*ssd*) = 0.49 pixel).
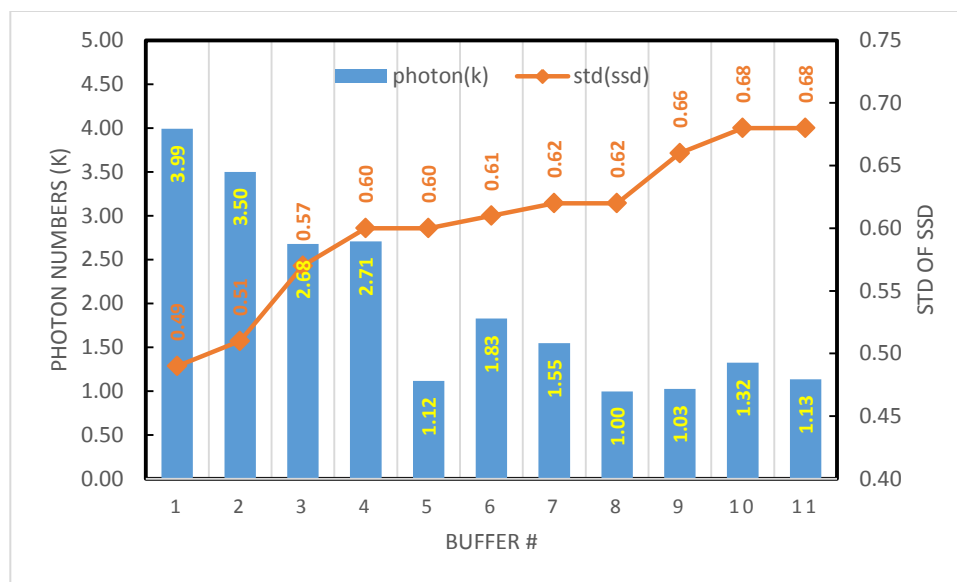
Figure 3.6 Photophysical properties of single Dy634 molecules in various buffers.
The buffer # are corresponding to the order number in Table 3.1

Despite the high photon yield, a drawback of the PBS - GLOX - COT - BME buffer is that it significantly increases the duty cycle of the fluorophore. That is, single fluorescent molecules stay in the 'on' state much longer (to yield more photons) and requires a higher laser power (300 mW vs typically 150 mW) to drive the fluorophores into the dark state. On one hand, a higher photon yield improves the localization accuracy of single molecules and hence the imaging resolution; on the other hand, the high duty cycle increases image background and chances of having overlapping emitters, thus reducing the overall resolution. In practice, the buffer conditions need to be adjusted according to both the photophysical properties of fluorophores as well as the local density of the cellular target.

3.4.3 Multicolor imaging with MSSRM using fluorescent proteins

Labeling biological sample with fluorescent proteins (FP) is widely used in fluorescence microscopy, mainly because their high labeling ratio and specificity. These fluorescent proteins are inherently compatible with MSSRM. So, we tested the performance of variable FPs on

MSSRM system. We picked a few FPs which can be efficiently excited by existing lasers and have higher photon yield according to literature. The spectral absorption and emission maximum are listed in table 3.2.

Fluorescent Protein	Ex (nm)	Em (nm)
Dendra 2	553	573
PAmCherry	564	595
mEOS2	573	584
PATagRFP	562	595
mKikGR-Mito	583	593
PAmKate	586	628

Table 3.2 Spectral properties of variable fluorescent proteins

In general, FPs has relative lower photon yield and broader emission spectral range. We recorded the MSSRM spectrum of single FPs. Then averaged single molecule spectrum are shown in Fig. 3.7.
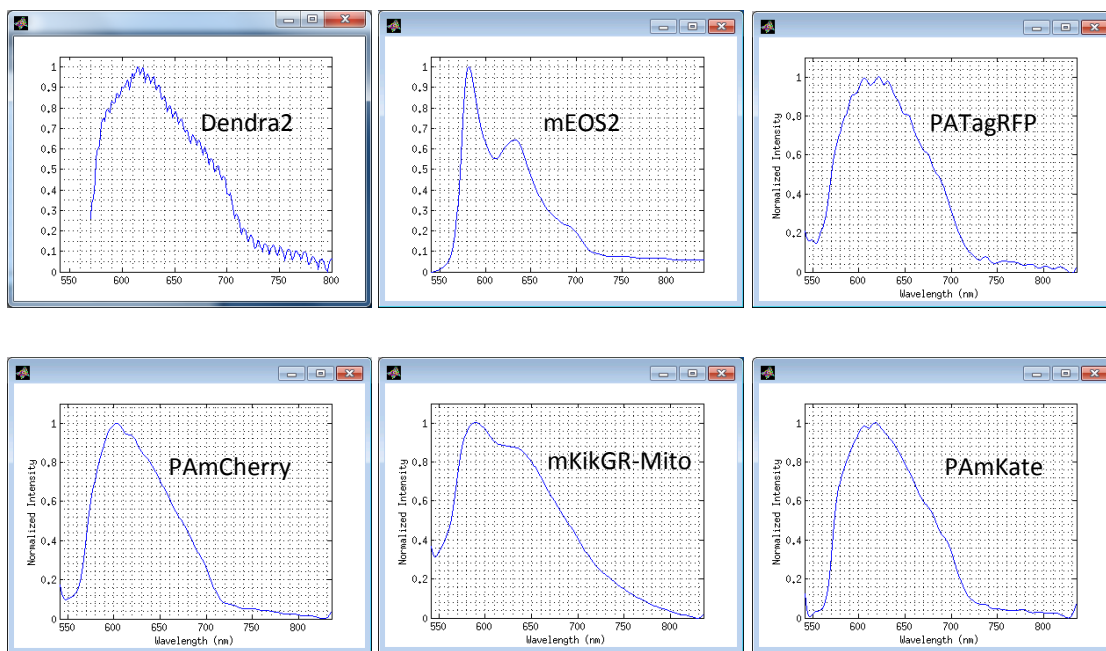
Figure 3.7 Averaged spectral response of fluorescent proteins

The *ssd* values of FPs showed wider distribution compared to organic fluorophores, which is not surprising given the low photon yield of FPs. Most FPs exhibited ~2 pixel standard deviation of *ssd*, which is ~11 nm spectral distribution. Therefore, the best spectral resolution we can achieve with FPs will be around 25 nm. For single laser excitation, it will be hard to have more than 2 color in one channel. This spectral resolution apparently can still be used to double the number of color in SMLM microscopy.

Better spectral resolution can be expected if spectral correlation co-efficiency to standard spectrum was take into account. Efforts along this direction is under going through collaboration with my lab mates.

3.5 Multicolor superresolution imaging with the MSSRM

3.5.1 Multicolor imaging with MSSRM using organic fluorophores

MSSRM images of U2OS cells simultaneously stained with four fluorophores labeling mitochondria (DY634), vimentin (DL650), microtubule (CF660C), and the plasma membrane (CF680) clearly showed four distinct structures with excellent spatial resolution and spectral separation. Well resolved single-molecule images with robust photoswitching were recorded for these samples and the four fluorophores were visually distinguished from each other in overlaid spectral and positional images (Fig. 3.8). Histograms of *ssd* values for all single molecules detected showed four well separated peaks corresponding to the four fluorophores. The histograms were fitted with four Gaussian distributions, each of which had a mean and standard deviation that largely agreed with the single-color results. Based on the fitting results, we defined an empirical *ssd* range for each fluorophore that included ~80% of all events. Events outside of the defined ranges were discarded. We estimate that the false assignment rate between neighboring fluorophores is <0.5% with these cutoff criteria. This leaves sufficient localization events to reconstruct a high-resolution image in each of the four channels with very low spectral crosstalk (Fig. 3.8C). Even lower false assignment rates could be achieved by further narrowing the acceptable *ssd* ranges at the cost of more discarded localization events and potentially less continuous structures.
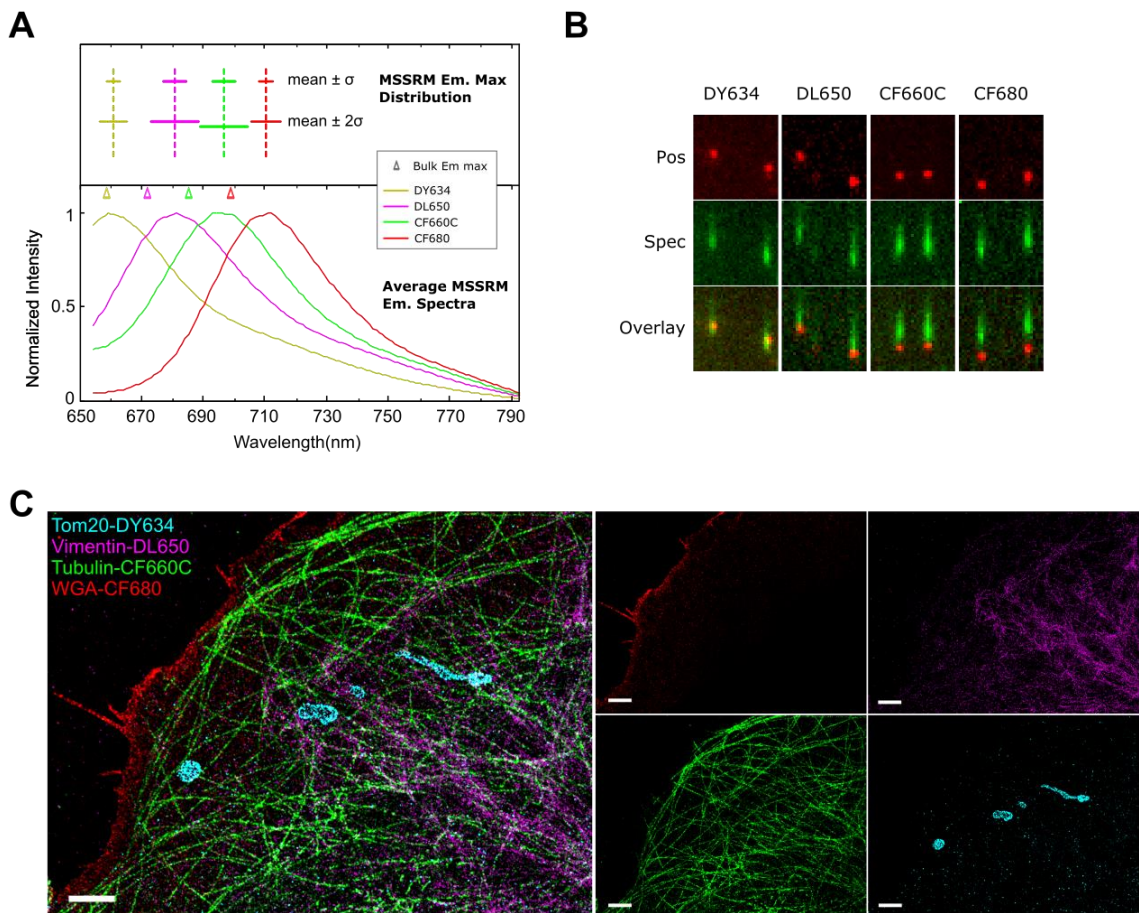
Figure 3.8 Multicolor imaging of cellular structures with the MSSRM in fixed cells.

(A) Average emission spectra of DY634, DL650, CF660C, and CF680 shown in wavelength units in the lower plot, each generated by averaging the MSSRM spectra of ~10,000 single molecules. The upper plot shows the maximum emission wavelengths for the same four dyes measured on the MSSRM, displayed as mean (vertical, dotted line) and the spread (1σ and 2σ as indicated, where σ is the standard deviation). Empty triangles mark the bulk emission wavelengths measured in solution; (B) Positional (top), spectral (middle), and overlaid (bottom) images of single DY634, DL650, CF600C, and CF680 molecules as indicated; (C) Four-color MSSRM image of a U2OS cell labeled for mitochondria (Tom20, cyan), intermediate filaments (vimentin, magenta), microtubules (tubulin, green), and cell membrane (WGA, red). The overlaid image is shown on the left and images in individual channels are on the right. Scale bars, 2 μm.

We also tested whether using only ~30% of the photons in the positional channel would significantly impact the spatial resolution by imaging microtubules in U2OS cells labeled with AF647 via indirect immunofluorescence. We imaged the sample on the MSSRM using standard STORM imaging buffer and acquisition settings and used similar settings in data processing (in particular, the same threshold for picking up single particles) as in conventional STORM. The reconstructed image (Fig. 3.9) clearly shows the hollow structure of microtubules, a commonly used standard for assessing imaging resolution of STORM[92]. We measured the widths of the microtubules to be ~39 nm. This is comparable to other reported measurements and is consistent with an average spatial resolution of ~26 nm as previously reported[59,92].
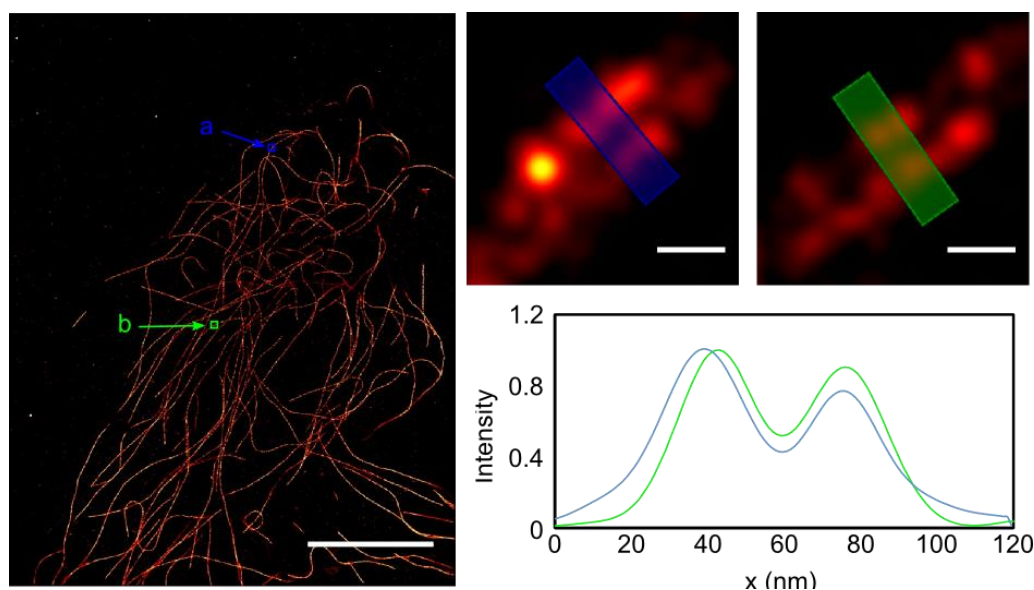
Figure 3.9 Resolving microtubule hollow structure with 30% of photons on the MSSRM. U2OS cells were labeled with rat anti-α-tubulin antibody and AF647-conjugated donkey anti-rat secondary antibody (see *Materials and Methods*) and imaged on the MSSRM using standard STORM imaging buffer (GLOX + 100 mM MEA in PBS). Shown on the left is an overview of microtubules in a cell, with regions a (blue) and b (green) shown in zoom-in views on the top

right panels. Line profiles of the boxed regions are shown in blue and green, respectively. Scale bars, 10 μm (left) and 50 nm (right). Note that the positional channel only received ~30% of the photons emitted from each AF647 molecule.

An advantage of MSSRM is that images in different 'color' channels are inherently aligned, and no further co-registration is required. This is because single molecules in different colors are imaged all together with exactly same CCD at same time. To demonstrate this point, microtubule of U2OS cells were immune stained with 3 of the same sets of organic dyes. Images in 3 channels are overlapped as shown in Fig. 3.10. This proves that achromatic abbreviation can be ignored with current resolution of MSSRM. The only concern left for MSSRM is potential achromatic aberration of the prism and the objective.
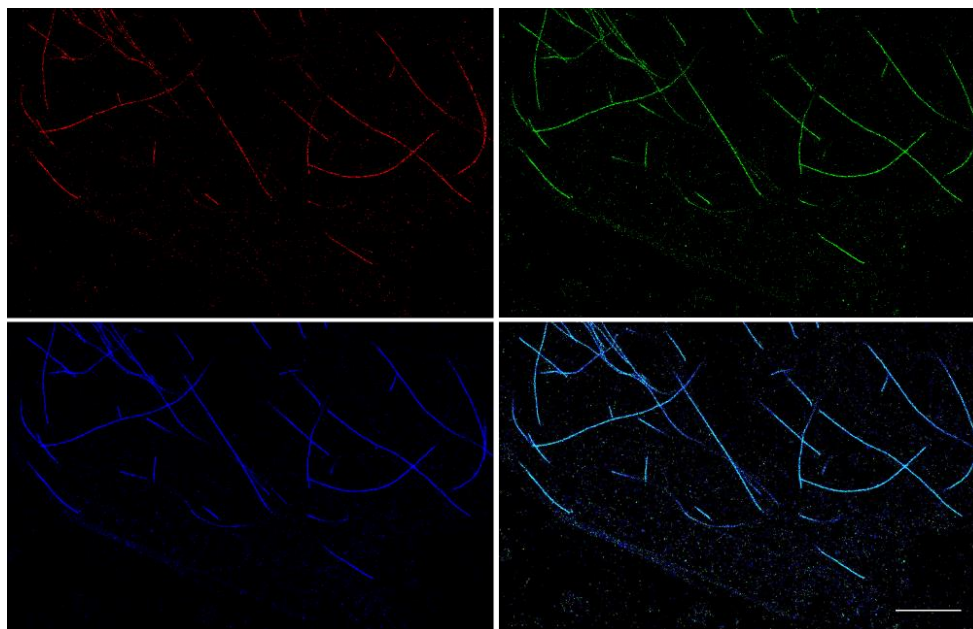
Figure 3.10 Images in the different color channels acquired on the MSSRM are inherently aligned. U2OS cells were simultaneously labeled with DY634 (red, top left), DL650 (green, top right), CF680 (blue, bottom left), and imaged with the MSSRM. The color channels were separated during data processing based on single-molecule emission spectra. Images in each color channel

were overlaid to generate a composite image (bottom right), in which cyan indicates complete overlap of the three colors. Scale bar, 5 μm.

3.6 Discussion

In this chapter, we show that multicolor spatial and spectral imaging using single-molecule localization principles can be achieved using the MSSRM – a simple to use, single objective epi-illumination system that is well suited to both fixed and live cell imaging. The MSSRM records paired positional and spectral images for each fluorescent molecule in the *on* state, where the positional image is used to determine the location and the spectral image is used to determine fluorophore identity (i.e. 'color'). Using fluorophores tested herein, the MSSRM achieves far better spectral resolution at 10-15 nm compared with 'conventional' SMLM (50-100 nm) without compromising spatial resolution. By including additional excitation lasers (e.g. 561 or 488 nm) and provided an optimal set of fluorophores with emission wavelengths spanning the ~500 to ~850 nm range, the MSSRM has the potential to image samples labeled with up to 20 different colors. If implemented, this would offer a transformative tool for analyzing complex, multicomponent interactions in intact biological specimen.

The MSSRM can use fluorophores with broad emission and significant spectral overlap as long as the *ssd* values for each fluorophore do not vary substantially. The fluorophores used in this study for both fixed and live cell experiments satisfy these criteria; their *ssd* values typically fluctuate within just 3-5 nm, and the shapes of the single-molecule spectra are mostly invariant across the sample (this work and Zhang *et al.*[106]). We show that this is true even when the molecules are moving. This allowed us to use a panel of fluorophores whose emission spectra maxima differed by only ~15 nm. We established fluorophore classification criteria that allowed ~80% of the fluorophore events to be localized while misclassifying only 1-2%. The

misclassification rate could be further reduced by adopting a more stringent assignment strategy but at the expense of discarding more localization events. Although here we only used *ssd* values to distinguish fluorophores, other spectral properties such as the shape of the emission spectra could also be used to further improve fluorophore identification. Additionally, synthesis and screening of fluorophores that exhibit even narrower *ssd* distributions than those used in this study would be beneficial.

The ability to use spectrally proximal fluorophores in MSSRM (and SR-STORM[106]) offers a number of advantages. First, all the fluorophores can be efficiently excited at once with a single laser, which greatly simplifies experimentation and reduces the total laser power and the associated phototoxic effects during live cell imaging[109]. Second, registration errors between the different 'color' channels are essentially eliminated by using fluorophores with closely spaced emission maxima (e.g. ~15 nm apart). In MSSRM, positions of all fluorescent molecules are recorded through the same optical path regardless of color, and "color" is assigned computationally during post processing. Hence, images in the different 'color' channels are automatically aligned. Residual registration errors mostly originate from lateral chromatic aberrations of the optics (including the objective lens). However, this error is negligible since the emission wavelengths of the different fluorophores are so close. That said, image registration will be necessary if multiple dichroic mirrors are used in experiments involving multiple excitation lasers.

The MSSRM differs from the SR-STORM in that the MSSRM uses a single-objective, epi-fluorescence configuration. This difference has significant implications in practical use of the techniques. Among others, the MSSRM can be constructed on most commercial, inverted microscope frames, and existing SMLM setups can be easily modified to perform MSSRM. More importantly, this configuration makes the MSSRM fully compatible with live cell imaging. The free space above the objective can now be used for environmental incubators to maintain cells under physiological conditions, and chambered slides instead of sandwiched coverslips can be

used for both live and fixed cell imaging. Importantly, this benefit did not come with a noticeable cost in either spectral (as discussed above) or spatial resolutions, in part owing to the good photon yields of the fluorophores such that the resolutions were mostly not photon-limited. We note that, while this manuscript was in preparation, Mlodzianoski *et al* also reported a single objective spectral PALM; however, proof of its superior spectral and spatial resolution and utility in imaging and tracking in three or more colors has not been demonstrated[110].

Imaging spectroscopy has become an increasingly attractive approach to studying biology given the rich information contained in molecular spectra. Besides the aforementioned reports[106,110] and the present work, a number of recent studies have used spectral information in superresolution microscopy for multicolor imaging[111] or improved spatial resolution[112]; spectral imaging has also been used to greatly increase the multiplexity of fluorescence life-time microscopy[113]. In addition to multicolor imaging, we also recognize the possibility of using MSSRM with environment-sensitive fluorophores[114] to assess heterogeneities in micro- and nano-environment, an inherent and important property of biological systems (Chapter 5).

In summary, we have shown that the MSSRM provides a flexible and powerful platform for multiplexed single-molecule localization with rich spatial and spectroscopic information. We realized nanoscopic imaging of multiple cellular structures of multiple molecular species simultaneously in fixed cells using a single laser excitation and a panel of spectrally similar dyes with minimal spectral crosstalk.

Chapter 4   Spatial regulation of HER receptors in cancer cells studied with superresolution microscopy

The high spatial resolution of SRM, now with much enhanced spectral resolution offered through the MSSRM, enabled us to study the spatial orientation of complex biological systems such as receptor assembly on the cell surface. Using the human epidermal receptor HER family receptors in breast cancer cells as an example, I show how three dimensional and multicolor superresolution imaging helps to reveal the otherwise hidden details of cell signaling.

4.1 Introduction

4.1.1 HER family receptors in breast cancer

As of 2016, breast cancer remains the second most prevalent cancer in the U.S., and is the most common cancer amongst US women[115]. In cancer medicine, most of the causes of death are tumor metastasis, i.e., dissemination of tumor cells and invasion into distant organs. According to different prognoses and response to chemotherapy on the basis of tumor morphology, degree of differentiation and expression level of certain receptors including estrogen receptor (ER), the progesterone receptor (PR), and the receptor tyrosine kinase HER2, histopathologic analysis categorizes breast cancers into different subtypes. In addition to histopathologic classification, microarray-based gene expression profiling can help to categorize the subtypes of breast cancer at

molecular level. Numerous studies have focused on how molecular subtypes of breast cancer could be useful in planning treatment for clinics and developing new therapies[116].

Among these histopathologic breast cancer subtypes, HER2-positive (HER2+, with HER2 amplified and/or overexpressed) and triple-negative (ER, PR and HER2 negative) tumors have been shown to have increased risk of metastases and poorer prognoses compared with other subtypes such as luminal (ER+) and rare, special subtypes [117,118]. Interestingly, in both HER2+ and triplet negative breast cancers, other HER family receptors including EGFR (HER1) and HER3 as well as their ligands, EGF and heregulins (HRGs), play important roles in regulating tumor properties [119-122].

Despite initial success in targeting both HER2 and EGFR in breast cancer, a significant fraction of patients relapse [123]. To date, mechanisms of neither sensitivity nor resistance to these targeted therapies have been clearly understood, and much is still yet to be learned about the biology underlying HER receptor signaling under pathologic and pharmacologic conditions. Below I briefly summarize the current status of HER biology, particularly in the context of breast cancers.

4.1.2 Structure and biology of the HER family receptors

The human epidermal growth factor receptor 2 (*HER2*) gene, also known as *Neu* or ErbB2 in rat, is a member of the human epidermal receptor (*HER*) gene family, comprising four closely related genes: *HER1 (EGFR)*, *HER2*, *HER3*, and *HER4*. Widely expressed in epithelial cells, interstitial cells and nerve tissue, HER genes encode the corresponding receptor tyrosine kinase (RTK) and play an important role in the development process. Among them, HER1 and HER2 are proto-oncogenes that have been included in a variety of human tumors.

All HER receptors consist of an extracellular binding domain (ECD) at the N-terminus, a transmembrane domain (TM), and an intracellular tyrosine kinase (TK) domain at the C-terminus [124,125]. The ECD is further divided into four subdomains I, II, III, and IV, starting from the N-

terminus, with domains I and III involved in ligand binding[125,126] and subdomains II and IV in homo- or heterodimer formation. With the exception of HER2, all HER receptors take a 'closed' conformation in the ECD prior to ligand binding, in which subdomains II and IV are somewhat buried and cannot mediate receptor dimerization. Ligand binding to HER1, HER3 or HER4 opens up the ECD to expose subdomains II and IV, thereby allowing the receptor to dimerize with another receptors nearby. The EGFR has been a classic example of ligand-induced receptor homo-dimerization. HER2 is different in that its ECD remains in an open conformation, and the receptor is ready to dimerize with another, ligand-bound HER receptor. As such, HER2 is the preferred dimer partner of the other HER receptors.

Dimerization at the N-terminus brings two receptors into the same complex and initiates auto-phosphorylation of their kinase domains at the C-terminus. Depending on the signaling context, multiple tyrosine residues can become phosphorylated, and the resulting phosphotyrosine (pTyr) residues can act as binding sites for a number of downstream effector molecules containing Src Homology 2 (SH2, e.g. Src) or pTyr binding (PTB) domains. Many of these effectors are scaffold proteins for the assembly of multi-protein complexes. For example, Grb2 has one SH2 and two SH3 domains to allow binding to the activated receptor (via SH2) and other proteins that contain SH3-binding domains (e.g. SOS, which is an enzyme that catalyzes GTP-loading of Ras GTPases). Notably, Her3 does not have a kinase site, and requires another kinase (e.g. HER2) to activate the phosphorylation process in order to achieve its cellular activities. Subsequently, an array of processes including the canonical Ras-Raf-MAPK and the PI3K-Akt-mTOR signaling cascades can be activated (Fig. 4.1B).
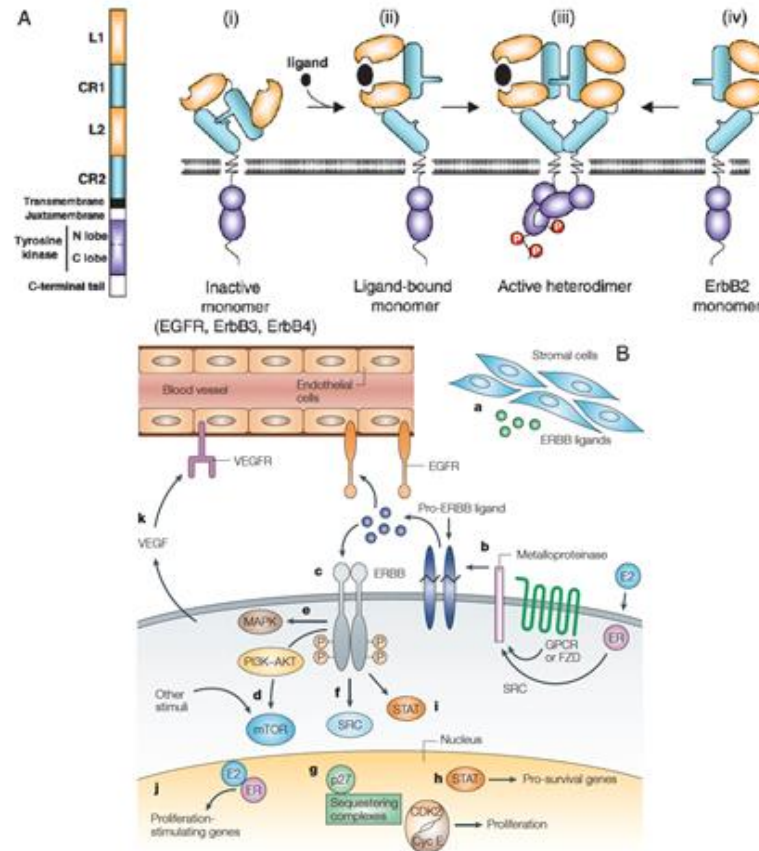
Figure 4.1 HER receptors signaling pathway

(A) HER family receptor structures (adapted from M. J. Wieduwilt *et al.*, 2008[127]); (B) HER Signaling pathways (adapted from reference[125]). CR = cysteine rich domain.

Under physiological conditions, HER receptor activation is ligand dependent. Biochemical research has revealed a wide-range of ligands such as growth factors for the HER receptors. EGFR, HER3, and HER4 each bind to an overlapping set of ligands, but HER2 does not have any known ligands. The specificities between known HER receptors and common ligands are as follows: a) EGF and heparin-binding (HB-EGF) bind only to EGFR , b) betacellulin (BTC) binds to EGFR and HER4 [128], and c) Neu differentiation factors (NDFs) like heregulin-1 bind to HER3 and HER4. Although HER2 itself does not have a known ligand, it can partner with all of the other, ligand-bound receptors of the HER family (i.e., HER1-4) to form

dimers and in so doing HER2 can achieve a wide array of signaling activities to regulate cell proliferation, invasion, migration, to name a few. In fact, heterodimers of HER2 and another HER receptor are more stable and its signaling is more potent compared to any other homodimers or heterodimers formed within the HER family of receptors.

Moreover, HER2 is normally incompetent in forming homo-dimers, but when highly over-expressed, HER2 can form active homodimers, a process independent of ligands. In cells over-expressing HER2, HER3 and EGFR can heterodimerize with HER2 in the absence of ligands. Thus, depending on the ligand and the availability of other receptors, different downstream adaptor and activator proteins can be involved in HER signaling to activate the respective downstream signaling pathways.

4.1.3 Breast cancer therapies targeting HER family receptors

The central role of HER family receptors in human tumors, its availability to extracellular manipulation, and relatively detailed understanding of the underlying biochemistry have made these receptors attractive targets for pharmacological intervention[123,129]. The main therapeutic approaches developed in efforts to inhibit HER receptors in human cancers are monoclonal antibodies (mAbs) and tyrosine kinase inhibitors (TKIs). Other approaches such as inhibition of downstream effector pathways (e.g. PI3K-Akt) and genetic knockdowns via small interference RNA (siRNA) are also important in breast cancer treatment but will not be discussed here.

Trastuzumab (or Herceptin) is a clinical, humanized monoclonal antibody directed against the extracellular domain of HER2. It is also the first Food and Drug Administration (FDA)-approved targeted therapy for advanced HER2+ breast cancer [123]. Introduced by Genetech (now Roche), Trastuzumab significantly improved clinical efficacy better than chemotherapy alone as first or second line treatment, which has been regarded as an example of a successful targeted therapy [130]. There are at least three suggested mechanisms through which Trastuzumab inhibits HER2+ tumor [129]: a) inducing internalization and degradation of HER2 [131]; b) antibody-

dependent cellular cytotoxicity (ADCC) inflicted by the presentation of Trastuzumab on HER2+ cells, which attracts immune cells to attack the tumor. Clynes et al. showed that natural killer cells target HER2+ cells coated with Trastuzumab via a CD16-mediated ADCC mechanism [132]; and c) inhibition of the MAPK and PI3K/Akt pathways through disruption of HER2 homodimers, which leads to cell cycle and growth arrest [133,134].

Besides Trastuzumab, new therapeutic agents are continuously being developed and clinically tested. Another FDA-approved anti-HER2 monoclonal antibody, Pertuzumab (also known as Perjeta), targets an extracellular epitope distinct from that targeted by Trastuzumab. Pertuzumab binds HER2 near the center of domain II, blocking a binding pocket necessary for receptor dimerization and signaling. While Trastuzumab inhibits HER2 homodimers, which mostly exists in tumor cells with very high HER2 expression levels, Pertuzumab is able to block HER2 signaling by eliminating both HER2 homodimers and HER2-HER1/3/4 heterodimers. Interestingly, Nahta et al. showed that combining the two antibodies resulted in synergistic inhibition of HER2+ breast cancer cell growth[135], although the underlying mechanism is currently unclear.

Despite demonstrated clinical benefits, Trastuzumab is effective in only ~70% patients with HER2+ tumor; even for these patients the response is transient, and the disease progresses typically within a year [136]. These results suggest primary (or inherent) and secondary (or acquired) resistance. To date, several resistance mechanisms have been proposed: first, altered availability of HER2 to Trastuzumab through truncation of the antibody-binding domain [137] or physical masking of the receptor by cell surface proteins (e.g. mucin) [138]; second, activation of alternative receptor pathways, most notably c-Met [139] and IGF-1R [140]; and third, mutations in downstream signaling pathways such as loss of PTEN or acquisition of activating PI3K mutations [134]. All these mechanisms lead to re-activation of the PI3K-Akt and/or Raf-MAPK pathways and in consequence, continued or even promoted growth of the tumor cells.
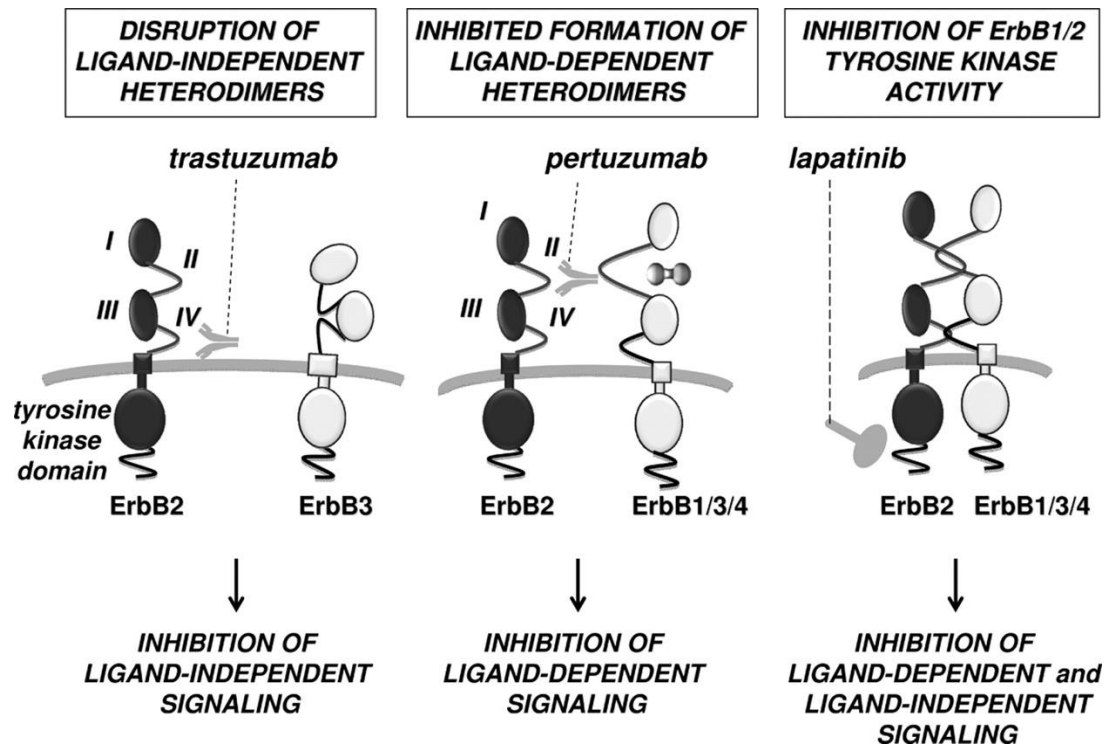
Figure 4.2 Mechanisms of action of Trastuzumab, Pertuzumab, and Lapatinib

(adapted from G. W. De Keulenaer [141])

Besides the mAbs, several TKIs such as Lapatinib and Erlotinib have also been used in clinic to target HER2 as well as other RTKs within or outside of the HER family. Lapatinib is an orally active, low molecular weight TKI that specifically and reversibly inhibits EGFR and HER2. It binds to the ATP binding site of both receptors to prevent receptor phosphorylation and subsequent activation of the Raf-MAPK or PI3K/Akt pathways. The response of Lapatinib in patients is associated with the EGFR and HER2 expression levels, and also the expression of phosphorylated-HER2 with pre-treatment.

As in the case of mAbs, tumor resistance to Lapatinib (and other TKIs) quickly develops, with the median duration of response less than one year. Of the tumors the acquired Lapatinib resistance, a significant fraction had mutations in the EGFR kinase domain such that the receptor no longer responds to this TKI. In addition, some mechanisms that led to tumor resistance to

Trastuzumab were also implicated in acquired resistance to Lapatinib or other TKIs – such as upregulation of alternative receptors including Met and IGF-1R, and mutations in downstream signaling pathways (e.g. PI3K activation or PTEN loss), suggesting that similar adaptation mechanisms could be evoked in the tumor cells when signaling from the HER receptors is blocked by either the mAbs or the TKIs.

4.1.4 Regulation of HER and other RTK signaling via spatial mechanisms

For the importance of HER receptors in cancer, continuous efforts have been put on developing new targeting agents and better understanding of tumor resistance to existing therapy. These efforts have led to discoveries of new mechanisms that regulate HER signaling. In particular, spatial mechanisms that involve nanoscopic organization of HER2 receptors at the membrane has been shown to play critical roles in regulating HER receptor signaling and causing drug resistance, additionally to the well-established biochemical mechanisms.

Previous high-resolution imaging studies using electron microscopy (EM) have revealed that HER receptors follow a nonrandom distribution on the membrane. HER2 and some of its signaling partners appear to segregate into distinct nanodomains on the cell membrane. On prepared membrane sheets, immuno-EM showed that HER2, EGFR, HER3, and PI3K each form a distinct type of nanoscale membrane patch [26] (Fig. 4.3 A). Depending on the cellular or signaling context, these nanodomains exhibit different spatial overlap patterns. For example, HER2 and HER3 nanodomains partially overlap when Heregulin (HRG) is added, whereas those of EGFR and HER2 overlap when EGF is the ligand. On embedded thin sections of cells, immuno-EM revealed that some of these HER2 'nanodomain' are actually filopodia-like protrusions (FLPs). The HER2-enriched FLPs are only ~100 nm in diameter and vary in length from submicron to tens of μms, and they are abundant on the cell surface (Fig. 4.3 B). Localization to the FLPs renders HER2 resistant to endocytosis, which was thought to lead to

resistance to HER2-targeted therapy through persistent membrane localization and signaling of HER2 [79].
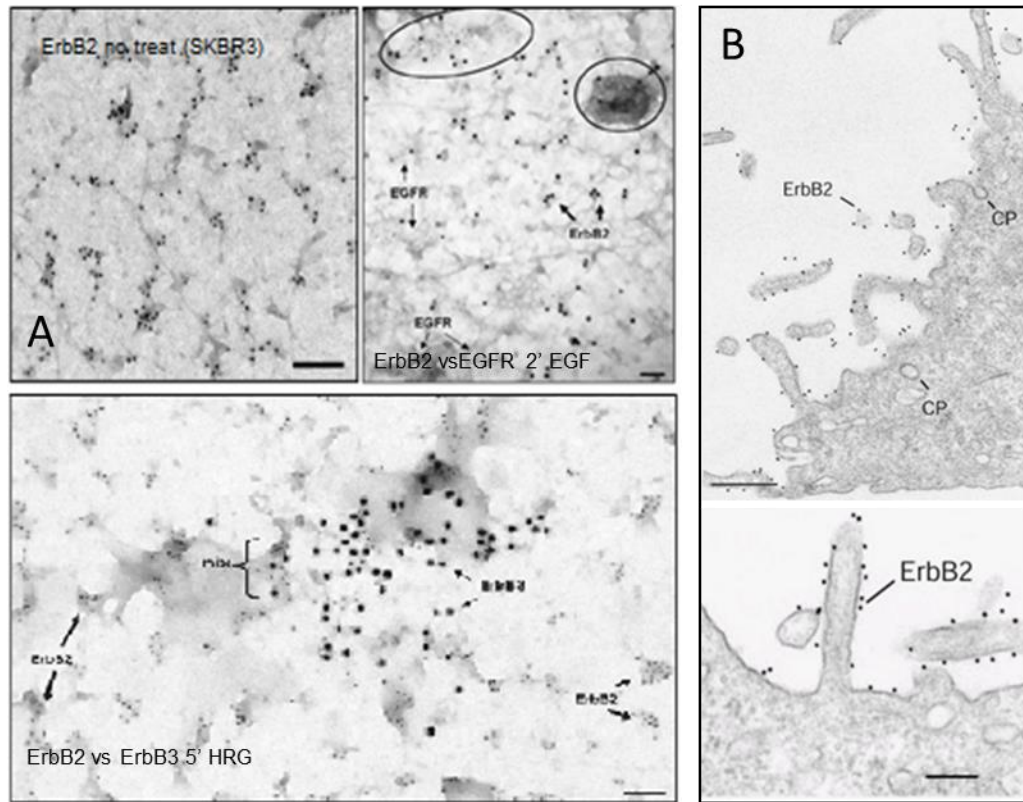
Figure 4.3 EM images of clustered EGFR, HER2 and HER3

(A) Previous EM studies showing EGFR, HER2 and HER3 each form a distinct nanoscale patch and co-clustering under stimulation (adapted from Yang *et al.*[26]); (B) previous EM studies showing HER2 clusters and localization to FLPs (adapted from Hommelgaard *et al.*[79]);

Another mechanism of resistance to HER2-targeted therapy also involves spatial localization of HER receptors and other RTKs [142,143]. When HER2+ cells are treated with TKIs, within hours there is significant upregulation in the expression and/or the membrane localization of other HER receptors such as HER3, as well as other kinases including RTKs [144,145], to compensate for the loss of HER2-pathway activity, leading to resistance to HER2-targeted therapy. Depending on the subtype of the HER2+ tumor, different RTKs may be involved. For

example, in luminal-like HER2+ breast cancer cells, HER3 and IGF-1R are primarily responsible for the compensatory signaling when the cells are treated with RTK inhibitors; by contrast, basal-like HER2+ cells mostly use EGFR and cMet to counteract HER2 inhibition [145].
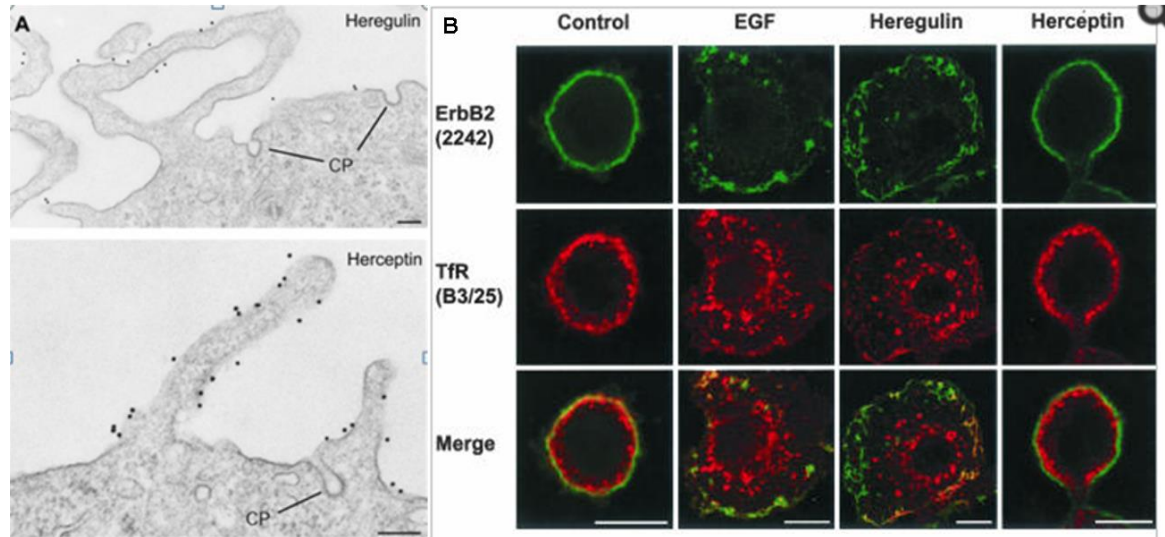
Figure 4.4 Spatial distribution of HER receptors

(A) Spatial organization of HER receptors[79](B) Localization to the FLPs may prevent HER2 from being endocytosed, resulting in persistent signaling, which is a mechanism of resistance to HER2 targeted therapy[79].

Apparently, understanding how the multitude of RTKs are spatially and biochemically coupled with each other to promote cell proliferation and survival is key to improving current cancer therapeutic strategies. The challenge in achieving such understanding is at least two fold: the small length scales involved in the spatial organization of each HER receptor (e.g. the localization to the FLPs) and of other related RTKs, and the multitude of molecular components involved in these processes. While immuno-EM has been instrumental in revealing many of these details, it is inherently limited in terms of applicability to intact cells and the number of molecular species that can be imaged at once. As will be detailed in this chapter, new imaging tools such as

the MSSRM offers a unique opportunity to investigate spatiotemporal mechanisms of HER signaling.

4.1.5 Outline of this chapter

In this chapter, I aim to uncover details of how HER receptors are organized in cells and mechanisms of how the spatial mechanisms regulate HER signaling and mediate response to targeted therapies. I will utilize superresolution microscopy (SRM), in 3D or in multiple colors, to analyze the spatial organization of HER receptors and other biomolecules in HER2+ breast cancer cells. Specifically, both 2D- and 3D-SRM will be used to map the signaling molecules and scaffold proteins at the nanometer scale in intact breast cancer cells, with a special focus on filopodia-like protrusions that are enriched in HER2 (or EGFR). The organization of HER2 structures will be visualized in both live and fixed cells. The MSSRM, which allows multiplexed imaging of 4+ different species simultaneously in the same biological sample with 10-20 nm spatial resolution, will be used to map HER2-RTK interactions at the single-molecule scale, where the RTK can be HER2 itself (homo-dimerization or –multimerization) or another RTK such as HER3 (heterodimerization).

4.2 Materials and Methods

Tissue culture. SKBR3 (human breast cancer, HER2+, ATCC, HTB-30) were cultured at 37° C and 5% CO_2 in McCoy's 5A medium (Thermo Fisher Scientific) supplemented with 10% FBS (Life Technologies, 10082), HCC1569 (human breast cancer, HER2+, ATCC, CRL_2330) were cultured at 37° C and 5% CO_2 in RPMI 1640 medium (Thermo Fisher Scientific) supplemented with 10% FBS (Life Technologies, 10082), and A431 (human epidermoid carcinoma, EGFR+, ATCC, CRL-1555) cells were maintained at 37° C and under 5% CO_2 in DMEM supplemented with 10% FBS (Life Technologies, 11995 and 10082 respectively). For imaging, LabTek (Thermo, 155409) or µ-Slide (ibidi, 80827) chambers with a #1.5 coverglass

bottom were first cleaned by incubating with 1 M NaOH for 2 hours at room temperature, followed by washing 5 times with PBS and incubation with PBS overnight. A431 cells were plated in the chambers 36-48 hours prior to imaging in phenol red-free DMEM (Life Technologies, 21063) supplemented with 10% FBS.

Antibody conjugation. 100 ul antibody (Herceptin 1.6 mg/ml or Cetuximab 2.0 mg/ml) mixed with 10 ul 1M NaHCO$_3$ which was freshly prepared. The dye AF647, DY634, DL650 and CF680 were stocked in DMSO respectively with the same concentration 10 ug/ul. We added different amount of dye to make a final dye concentration roughly 20 mM. Wrapped the mixture with tin foil and vortex for 2-3 hours at room temperature. Followed by purification with size exclusion chromatography (NAP-5 column purification). Fluorophore and protein concentrations were calculated from absorbance measurements and used to calculate the final fluorophore to antibody ratio: d/p=2.0 (Herceptin_AF647), d/p=3.7 (Herceptin_CF680), d/p=1.7 (Cetuximab_AF647), d/p=1.1 (Cetuximab_DY634), d/p=1.1 (Cetuximab_DY650), d/p=2.2(Cetuximab_CF680).

Herceptin Fab generation. Briefly, we used the Pierece^{TM} Fab Preparation Kit (Thermo Scientific, 44985) to generate efficient FAB from IgG Herceptin. Herceptin were cleaved with papain, and the Fab fragment was purified by Thermo Scientific NAb Protein A Plus Spin Column. We conjugated AF647 directly to Herceptin_Fab afterwards. The final antibody concentration is 0.75mg/ml, and d/p ration is 2.3.

Immunostaining. Cultured cells were fixed with 3.7% Paraformaldehyde (PFA) in 1x PHEM buffer (120 mM PIPES, 50 mM HEPES, 19 mM EGTA, 16 mM MgSO$_4$, pH 7.0) for 20 minutes followed by washing with 1x PBS (3 x 5 min). For labelling C-termins anti-HER2 and anit_EGFR, cells were permeabilized and blocked in a mixture of 3% bovine serum albumin (BSA) and 0.5% Triton X-100 in 1x PBS at pH 7.4 for 30 minutes. For Herceptin and Cetuximab labelling, cells were only blocked in 5% BSA for 30 mins. Primary antibodies anti-HER2 (1:500, 322600, Life technology), anti_EGFR (1:200, Ab65986, Abcam) was applied to SKBR3 cells and

incubated for 45 minutes at room temperature. Herceptin (1.6mg/ml, 1:100) and Cetuximab (2.0 mg/ml 1:100) was applied to SKBR3 cells and A431 Cells for most of the experiment for labelling HER2 and EGFR respectively. Following removal of the primary antibody, cells were washed in 1x PBS (3 x 5 min). AF647 conjugated goat anti-mouse/anti-rabbit/anti-human secondary antibody was incubated with the cells at a protein concentration of 0.1 mM for 30 minutes protected from light. The secondary antibody was removed and the cells were washed with 1x PBS (3 x 5 min). The stained cells were post-fixed with 3.7% PFA in 1x PHEM buffer for 10 minutes. Following fixation, the cells were washed with 1x PBS and stored in the dark until imaging.

   SRM and MSSRM imaging. SRM and MSSRM imaging were both performed on a custom MSSRM setup described in Chapter 3. For imaging anti-HER2/Herceptin/anti-EGFR/Cetuximab labeled samples with STORM, the standard STORM imaging buffer with 10 mM MEA was used (see Chapter 3). In single color SRM experiment, 100 nm gold nanoparticles were used as fiduciary markers, and in MSSRM experiment, 50 nm gold nanoparticles were used. A custom built focus stabilization is used to maintain the image focus to within approximately ±25 nm. Image acquisition was also performed in a manner similar to that described in chapters 3 and 4, using primarily the μManager package and saved as the OMERO Tiff format (.tiff).

   Data processing. SRM and MSSRM image analysis was done with home-written MatLab scripts as described in chapters 3 and 4. Briefly, the raw MSSRM image stack was first split into the positional and the spectral channels. Positional images from SRM or MSSRM experiments were then analyzed to extract the precise locations of each molecule. Next, the localizations were transformed into the MSSRM channel using a transformation matrix, as determined by registering the positional and spectral images of gold nanoparticles taken at 561 nm with a narrow bandpass filter, such that the emission spectrum of each molecule comprising ±25 pixels of the spectral image around the positional centroid could be obtained. After quality check, the spectral images were then analyzed to determine the maximum emission wavelength in each case. A histogram of

all the single molecule emission maxima is used to guide the assignment of spectral (*ssd*) ranges for determining the color of each localization event. After color separation, images in each channel were rendered separately in Matlab, saved as TIF files and re-combined in ImageJ for multicolor display and other manipulations.

4.3 Results and discussion

4.3.1 Nanoscopic spatial organization of HER/EGFR in cancer cells

HER2 preferentially localizes to FLPs. I first utilized STORM for imaging the spatial distribution of HER2 proteins on the membrane surfaces of SKBR3 cell line, which is HER2+ , especially focusing on the protrusions.

I initially labeled HER2 with Herceptin, an HER2 antibody that can bind to the ectodomain of HER2 receptor. As expected, SRM images of HER2 in SKBR3 cells labeled with Herceptin (indirectly with AF647) shows an almost exclusive localization on the cell membrane (labeling with or without permeabilization). Moreover, there is an apparent enrichment of HER2 in the filopodia-like protrusions (FLPs, Fig. 4.5). This observation recapitulates previous results from immuno-EM, except a much higher labeling density is typically observed in SRM than in previous immuno-EM. In many cases, HER2 labeling extends from the body of FLPs to the base and beyond, where HER2 apparently follows a filamentous structure, indicating a potential link to F-actin, the core of FLPs.
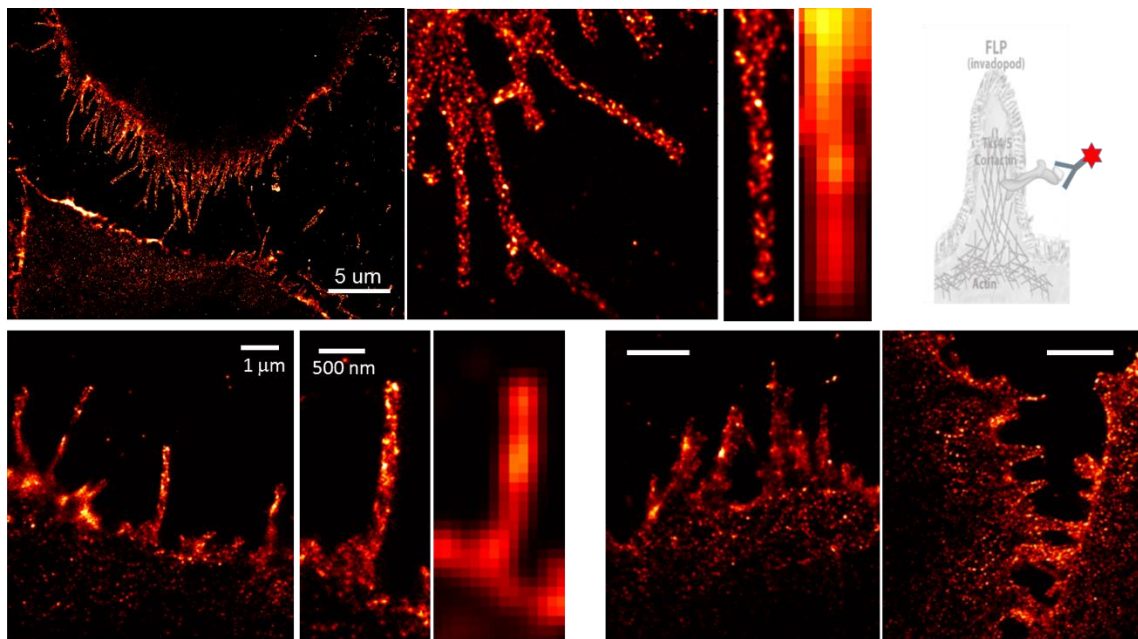
Figure 4.5 Spatial distribution of HER2 in SKBR3 cells.
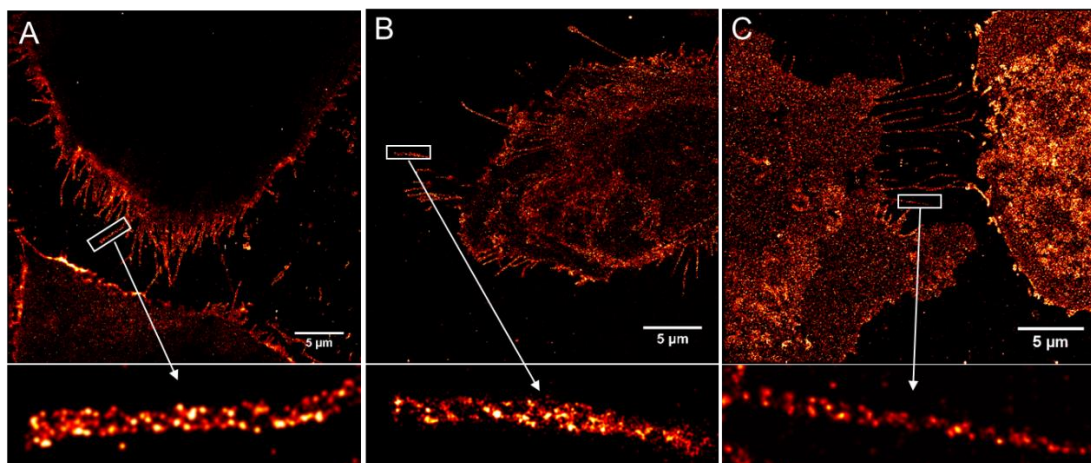
Figure 4.6 SRM images of HER2 showed helical like pattern.

(A) SRM images of HER2 showing helical structures taken with Herceptin AF647; (B) SRM images of HER2 showing helical structures taken with anti-HER2 AF647; (C) SRM images of HER2 helices taken with Herceptin Fab AF647.

Aside from their enrichment in FLPs, HER2 molecules are seen across the whole cell membrane. Under TIRF illumination conditions, the basal membrane has scattered localization events of HER2. I occasionally observed linear formations of HER2 in the 'flat' regions of the basal membrane. Another distinct feature that often appeared in the images were patches of HER2 in the basal membrane, which I suspect were membrane ruffles or similar structures that take the observed shapes when formed against the hard, glass surface (data not shown).

HER2 organizes into helices along FLPs. Besides the relative enrichment of HER2 in thin, filopodia-like protrusions, high resolutions images also revealed that in a significant fraction of FLPs, HER2 molecules were organized into helical structures along the long axis of FLPs (Fig. 4.5). In the image shown in Fig. 4.5, HER2 in most of FLPs had some degree of helical formation. Importantly, similar helical structures of HER2 were observed using full length Herceptin (Fig. 4.5 and Fig. 4.6A), an anti-HER2 targeting the C-terminus of HER2 (Fig. 4.6B), or the Fab

fragment derived from Herceptin (Fig. 4.6C), suggesting that the observed helical structures are not due to labeling with certain antibodies.
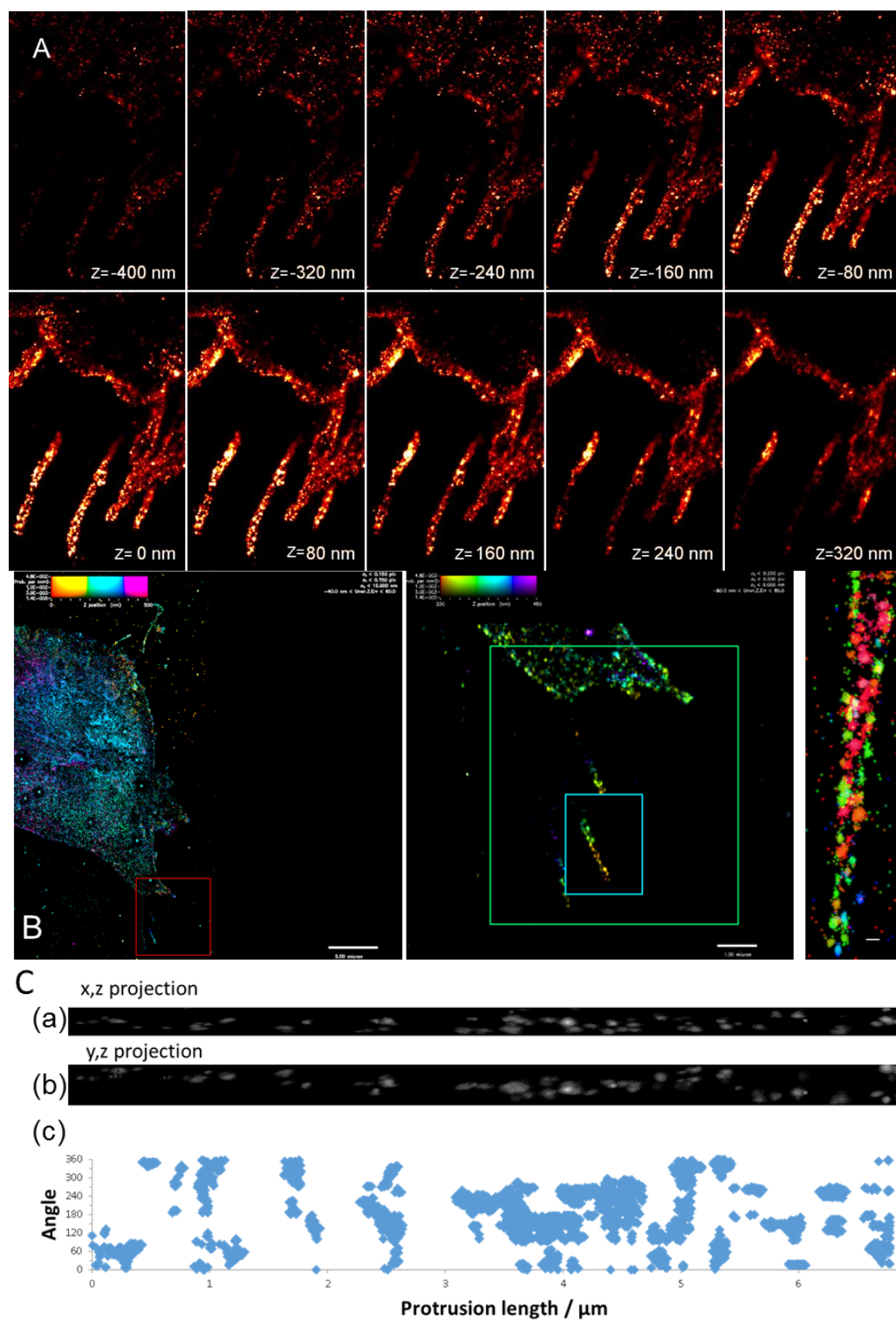
Figure 4.7 3D SRM images of HER2 showed helical pattern.

(A) A virtual 3D stack of HER2 images by 3D-STORM; (B) & (C) iPALM image of HER2 helical structure and intensity profile along the long axis.

The helical organization of HER2 can be visualized with even better clarity by using 3D SRM. Two 3D SRM techniques, 3D-STORM (based on astigmatism) and iPALM (based on interferometry) were used for this purpose. Fig. 4.7 (A) shows a virtual 3D stack of HER2 images in 20 nm axial steps acquired with 3D-STORM, in which crossing of opposite helical strands of HER2 could be clearly resolved in multiple FLPs. Here the spatial resolutions in xy, and z are estimated to be ~20 nm and ~50 nm, respectively. Compared with 3D-STORM iPALM system is the combination of photoacitvated localization microscopy with the single-photon, simultaneous multiphase interferometry that provides isotropic 3D, sub-10 nm protein localization. Through an ongoing collaboration with the FEI Company, I had access to a prototype iPALM system on which I collected iPALM images of SKBR3 cells labeled with Herceptin as in 3D-STORM. As expected, the helical structures of HER2 are even more evident in the iPALM images, owing to the high spatial resolution (Fig. 4.7C).
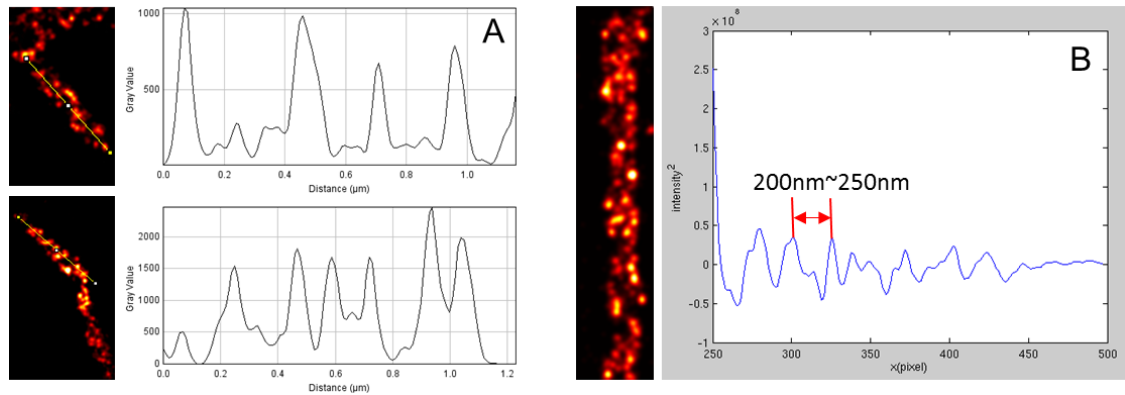
Figure 4.8 Analyzing the periodicity of HER2 helices associated with FLPs.

(A) Intensity line profile along the protrusions; (B) autocorrelation analysis of the protrusion

In Fig. 4.7 C, the apparent pitch of the HER2 helix was a few hundred nm. To better characterize this helical organization of HER2, I imaged hundreds of FLPs in SKBR3 cells, which vary in

length, width, helical pitch, etc. Interestingly, even for FLPs where HER2 did not exhibit a clear helical pitch, analysis of the HER2 labeling intensity along the protrusions reveal some degree of periodicity (Fig. 4.8A). I have also used autocorrelation analysis to identify repeating patterns in the HER2 intensity profile along the FLPs; this approach can reveal periodicity in structures even if the signal is obscured by noise. Using this approach, we found that on average, the periodicity of HER2 helices along the FLPs is 200-250 nm (Fig. 4.8B). These analyses indicate that the helical organization of HER2 along the FLPs is likely a fundamental property of HER2, the FLPs, or both.

HER2 helices are dynamic structures. FLPs are dynamic structures with various functions in cell physiology [146]. Since HER2 helices are associated with FLPs, it is likely that the helices are also dynamic. If so, HER2 helices could either form concurrently with the FLPs, in which case the helical arrangement of HER2 would be due to mechanisms related to that driving FLPs formation; or it could form after FLPs have already formed through a separate mechanism.

To address these possible mechanisms, I have used live-cell SRM to resolve the dynamics of HER2 in SKBR3 cells. For this purpose, I have conjugated AF647 directly to Herceptin (at ~1:1 antibody to fluorophore ratio), incubated live SKB3 cells with ~100 nM Herceptin-AF647 for 5-10 min, and swapped out the medium for dye-free medium containing the imaging buffer prior to imaging. A similar experimental scheme was used previously by Jones *et al.* to image the dynamics of transferrin receptors, except that we used a dilute STORM imaging buffer (at 1/4 to 1/10 of normal concentration) to have minimal impact on the cells but still sufficient to induce complete photoswitching of AF647. Indeed, Herceptin-AF647 bound to the surface of SKBR3 cells undergoes efficient photoswitching under mild illumination conditions (~100 W/cm^2), enabling live-cell STORM imaging of HER2-associated structures with excellent spatial resolution. I typically use a frame rate of 50-120 frames/second (i.e., 8 – 20 ms per frame) to match the switching rate of single AF647 molecules; as such, by using 250 - 1000 raw frames

to reconstruct a superresolution snapshot, I achieved 2-8 s time resolution in imaging HER2-AF647.

An example time sequence of STORM images of HER2 is shown in Fig. 4.9 A. The time interval between each image is 2 s. The sequence captured the genesis of a HER2-enriched FLP (t=+2 s), its maturation (t = +4s and +6s), and disassembly (t = +8 and +10 s); a clearer view of the HER2 helix can be seen in Fig. 4.9 B, where localization events from 1000 frames were used to reconstruct the snapshot. The helix structure of HER2 could already be clearly visualized at t = +2s, and its shape seemed to change as the FLP undergoes dynamic transformations, although HER2 organization remained as a helix throughout the lifetime of the FLP.
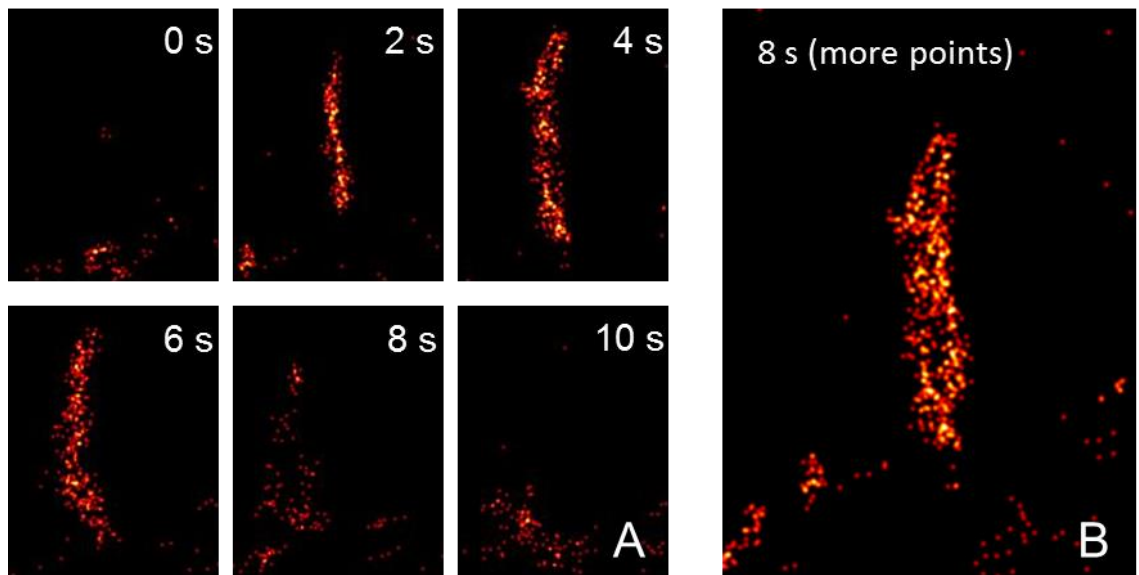
Figure 4.9 FLP-associated HER2 helices are dynamic structures.

In other cases, I routinely observed the elongation and shrinkage of individual FLPs in SKBR3 cells with live-cell SRM (data not shown). More interestingly, the HER2-enriched FLPs seem to be able to sense growth factors such as EGF, as addition of this growth factor to the medium induced massive retraction of the FLPs followed by formation of lamellapodia where the FLPs used to be (Fig. 4.10). Of note, the expression level of EGFR in SKBR3 cells is relatively low, although EGFR does appear to be present along the FLPs at a relatively low density (data

not shown). In this case, EGF mostly likely induced formation of EGFR: HER2 heterodimers since HER2 is in excess relative to EGFR. This demonstrates that HER signaling in turn regulates the FLPs. Thus, there exists a mutual regulation between the spatial organization and the signaling of HER2 and potentially other receptors.
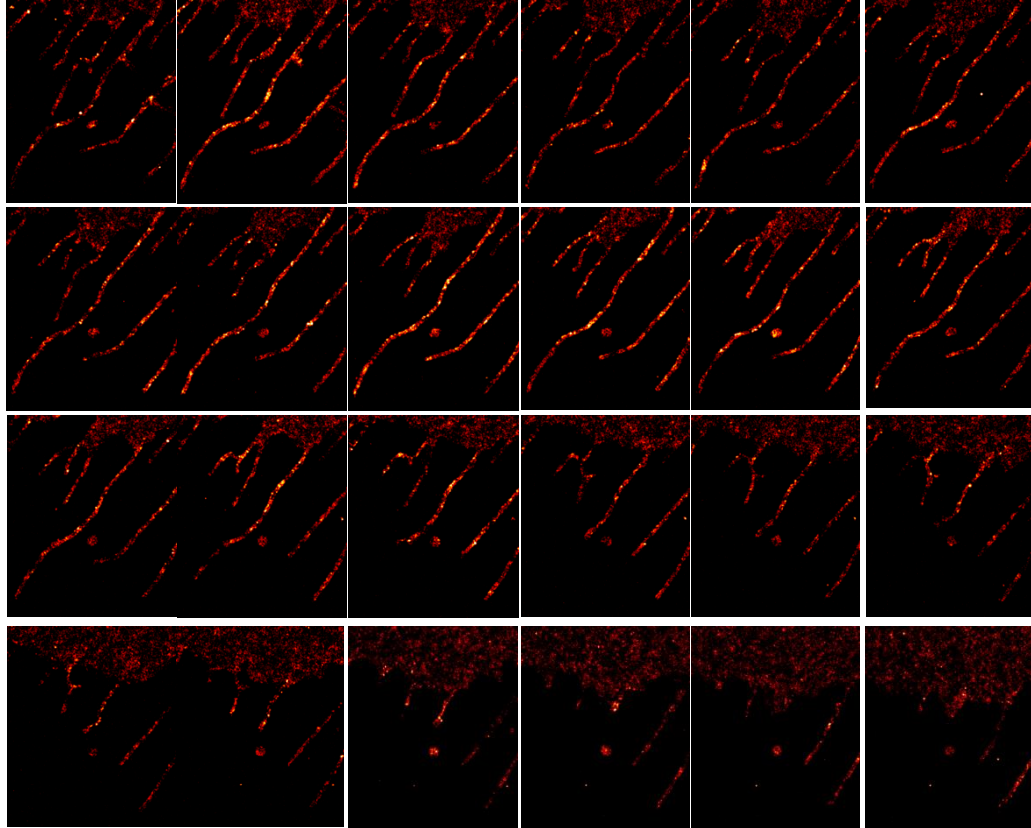
Figure 4.10 EGF causes massive remodeling of FLPs in SKBR3 cells.

Spatial organization of EGFR (HER1) in cancer cells. Compared with HER2, of which the over-expression is somewhat restricted to a few cancer types (e.g. breast), EGFR is over-expressed in a broad range of cancers such as colorectal, lung, pancreas, and breast, among others, and it has been a common drug target in these cancers [125,143]. In breast cancer, a subset (basal-like) of HER2+ cells also express considerable levels of EGFR, in comparison to another subset (luminal-like) HER2+ cells, and these two subsets exhibit different signaling patterns and responses to targeted therapy [147,148]. Since EGFR and HER2 belong to the same family and are

known to form heterodimers during signaling, we asked whether EGFR is spatially organized in cancer cells in a similar fashion as HER2.

To this end, I used STORM to image EGFR in several cancer cell lines using a therapeutic monoclonal antibody, Cetuximab (also known as Erbitux), which binds to the extracellular domain of EGFR to competitively block EGF or other ligands from binding to EGFR [149]. We used two breast cancer cell lines, SKBR3 and HCC1954, which express moderate levels of EGFR [150] (and unpublished data from Hu *et al.)*. To represent the case of high level EGFR expression, we also included an epidermoid carcinoma cell line, A431, which has been used as a model cell line to study EGFR[151]. In all cases, I used indirect immunofluorescence with an anti-human secondary antibody conjugated to AF647 for signal detection.

Interestingly, in the resulting STORM images of EGFR in SKBR3 cells, I observed significant heterogeneity in the expression level of the receptor as judged by the densities of localization events. For those cells with low EGFR expression levels, it is difficult to discern a clear pattern of spatial organization, so I focused on those with moderate expression levels of EGFR, features that resemble HER2 in SKBR3 cells could be clearly visualized – some EGFR molecules seem to organize into filamentous structures in the central, 'flat' regions of the membrane (Fig. 4.11 A), and by contrast, at the periphery of the cell, EGFR molecules are distributed along the FLPs in a discontinuous pattern (Fig. 4.11 B). Very similar patterns of EGFR spatial organization could be observed in HCC1569 cells (Fig. 4.11 C). In fact, in HCC1569 cells, EGFR often times appeared to be following a helical trace similar to that of HER2 in SKBR3 cells, although the density of localizations was typically too low to confirm such a trace.

To overcome the above difficulties associated with low-expression levels of EGFR, we also imaged A431 cells using the same strategy. Consistent with the extremely high expression levels of EGFR in these cells, both the 'filamentous' organization and FLP-localization of EGFR could be resolved much more clearly (Fig. 5.11 D). In particular, there is a high degree of

enrichment of EGFR in the FLPs, similarly to that observed by Lidke *et al.* [152]. Using 3D superresolution imaging techniques including both 3D-STORM and iPALM, I show that EGFR seems to indeed also follow helical paths along the FLPs, although the pitch is somewhat larger (1-2 μm judging from the images).
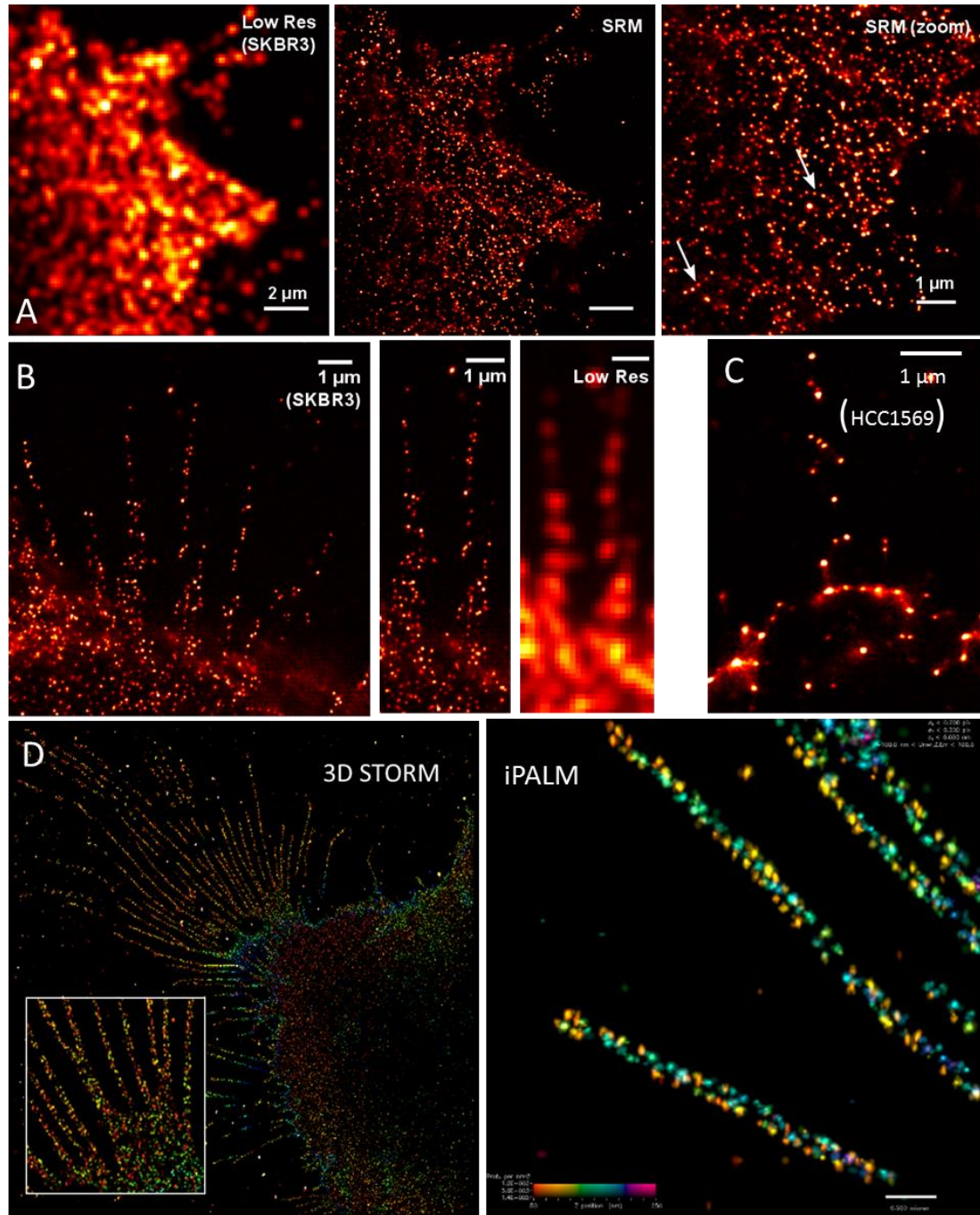
Figure 4.11 3D superresolution imaging of EGFR in cancer cells.

While the results from A431 cells are interesting, I am also aware that the spatial organization of EGFR can be influenced by the expression level, and hence the clear spatial patterns of EGFR observed A431 may or may not hold for EGFR in SKBR3, HCC1569, or other cell lines. That said, results from these cancer cell lines indicate that there were some similarities between EGFR and HER2 in their overall distribution (including the organization in FLPs) that deserves further investigation.

Potential connection between HER helices and actin-binding proteins. As the helical organization of HER2 (and likely EGFR) along FLPs has not been observed before, little is known about what drives the formation of these structures. Results from the live-cell STORM imaging experiments, as discussed earlier in this chapter, seems to suggest formation of HER2 helices along with the associated FLP to be a possible mechanism. If so, the formation of HER2 helices may be mediated through similar or related mechanisms that drive FLP formation. For the lack of literature in these specialized, HER2-enriched membrane protrusions, we resort to literature related to the more generic filopodia, which exists in a wide variety of cell types and are much better studied.

The biology of filopodia has been studied for decades[146,153]. Filopodia are actin-rich plasma-membrane protrusions involved in many fundamental processes including cell migration, adhesion, and endocytosis, to name a few[146]. Typical filopodia are thin (100-300 nm in diameter), finger-like structures in which actin filaments organize into parallel bundles, held together by crosslinking proteins such as fascin (Fig. 4.12). This is in contrast to another commonly observed actin structure, lamellipodia, which are thin (100-200 nm) and sheet-like (i.e., wide) protrusions filled with a branched network of actin. Of note, it has now been widely appreciated that the structure, molecular component, formation mechanism, and biological function of filopodia can vary widely depending on the cell type and the biological context. For example, in addition to the HER2-enriched FLPs, another cancer-associated FLP reported by Shibue *et al.* seems to be enriched in integrin β1 and associated with tumor cell metastasis. Interestingly, the integrin-

enriched FLPs are also present in metastatic breast cancer cells such as BT549, MDA-MB-231, but not in non-metastatic cell lines such as SKBR3 [154], indicating a major difference between the two FLPs.
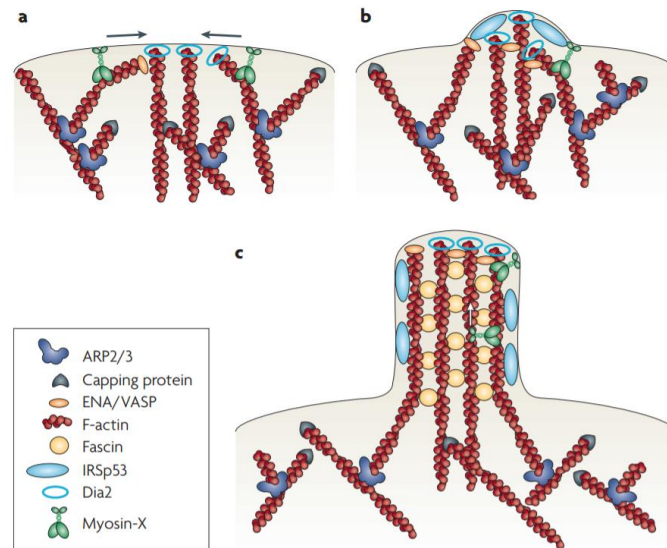
Figure 4.12 Current working model of filopodia growth [146]

The formation of filopodia is not fully understood. In a working model proposed recently, the growth of filopodia begins with clustering of barbed ends of proximal actin filaments by formin proteins like Dia2; next, motor proteins, most notably Myosin X, transport additional membrane components to the site of initiation. This is joined by the so-called I-BAR proteins, such as insulin-receptor substrate p53 (IRSp53), to further deform and tabulate the membrane [155]. Continuous addition of actin monomers at the barbed end (pointing away from the cell body) lead to elongation of the actin filaments, and crosslinking by fascin and α-actinin makes a solid actin bundle in the core of the filopodia. Once the FLP is formed, substances can be transported to and from the tip of FLPs either passively through diffusion or actively through Myosin X or other motor proteins.

As stabilization of HER2 helices on the membrane would likely require a structural scaffold, we hypothesized that some of the structural components of filopodia may participate in

HER2 helix formation through direct or indirect interactions with HER2. This hypothesis is corroborated by the fact that HER2 (and apparently, EGFR as well) molecules are in a filamentous arrangement resembling that of cortical F-actin; this filamentous arrangement is ever more obvious at the 'base' of the FLPs, which is the interface between FLPs and the branched F-actin network underneath the membrane. While HER2 helix could result from a direct connection between HER2 and F-actin, it would also require that a slow, helical pitch to exist along the F-actin bundle in the FLP core. However, cryo-EM characterization of HER2-enriched FLPs in SKBR3 cells clearly suggest that, as in conventional filopodia, the actin bundle in these FLPs are also arranged as parallel protofilaments and there does not appear to be a 'helical' pitch matching that of the HER2 helices (Mulder and Zhang *et al.*, unpublished). Hence, it is more likely that some actin-binding proteins involved in filopodia formation act as the scaffold of HER2 helices in the FLPs. Among the known actin-binding proteins in filopodia, one protein attracted most of our attention – Myosin X.

Myosin X is a motor protein that walks along filamentous found to localize primarily to regions with dynamic actin reorganization, such as the tips of filopodia, the edges of lamellipodia and membrane ruffles. In these actin-rich protrusions, myosin X plays a role in filopodia formation, extension and sensing, possibly by transporting actin-binding proteins to the tips through its motor activities, and by linking membranes and actin through the PH2-binding domain at its N-terminal, cargo-binding domain [156]. More interestingly, single-molecule tracking *in vitro* revealed that myosin X walks possessively in a hand-over-hand manner following a left-handed and irregular helical path along both single actin filaments and bundles; the pitch of the helical path varies between a few hundred nm to ~1 μm , very similar to what we observed on HER2 in the FLPs. Moreover, a number of recent studies have implicated upregulation of Myosin X, in part attributed to p53 mutation, in breast cancer metastasis [157,158]. We therefore decided to use STORM imaging to study the spatial organization of Myosin X in SKBR3 cells.
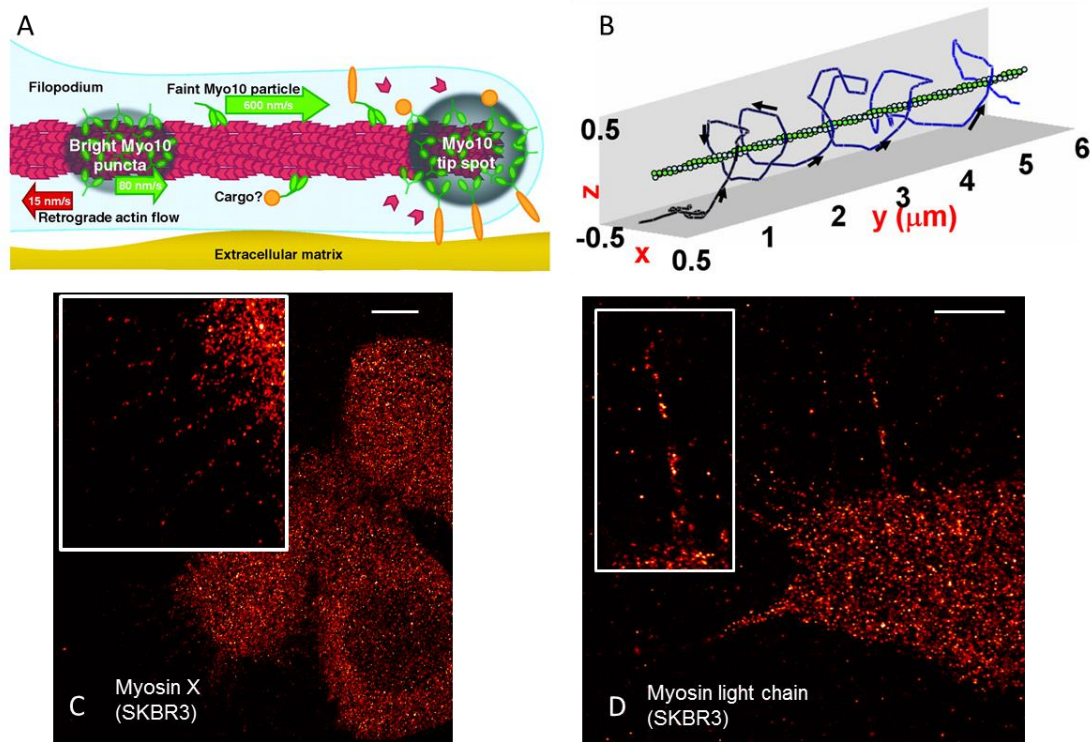
Figure 4.13 Myosin X in filopodia.

(A) Role of Myosin X in filopodia formation and structure [159]; (B) Helical path of Myosin X while walking along actin filaments and bundles. Image adapted from [159] (C) Spatial distribution of Myosin X in SKBR3 cells revealed by STORM imaging after labeling with an antibody against middle region of the target protein. (D) STOMR imaging of myosin light chain in SKBR3 cell. Scale bar is 5 um.

I used two different antibodies, one for myosin X heavy chain (Fig. 4.13 C) and the other for myosin light chain (MLC, Fig. 4.13 D), respectively, to label Myosin X in SKBR3, with mild permeabilization. Both Myosin X heavy chain and MLC expression were abundant in both the cell body (membrane) and in the FLPs in SKBR3 cells; the spatial distributions of both antigens were similar to previous reports using conventional fluorescence microscopy [160]. At the resolution afforded by STORM, however, we clearly visualized that MLC frequently exhibit a filamentous

organization reminiscent of F-actin, suggesting binding to myosin motors to cortical actin. Staining patterns of Myosin X is less regular in the flat regions of cell membrane. In the FLPs, both Myosin X and MLC appeared to be spotty, making it challenging to detect a regular pattern such as a helix, but MLC did seem to form a non-random pattern in the FLPs that potentially belongs to a helix (Fig. 4.13 D). Based on these results, it is not yet conclusive whether Myosin X directly interact with HER2 to give rise to the helices. It is possible that while Myosin X can drive HER2 molecules to form helices when the FLPs form, the motor proteins were disengaged from HER2 or HER2-connected structures. Future experiments on following the dynamics of both HER2 and Myosin X in the same cells and FLPs would be much more informative to revealing the potential roles of Myosin X in formation of HER2 helices.

4.3.2 Direct visualization of HER receptor interactions in SKBR3 cells.

EGFR : HER2 interaction upon EGF stimulation. It has been well established that HER receptors function through homo- or heterodimers to mediate cell signaling [161]. As both HER2 and EGFR seem to follow non-uniform and nanoscopic spatial distributions on the cell membrane, an interesting question arises: how do HER receptors dimerize while each exhibit special, nanoscopic organizations?

To address this question, I have used the MSSRM to image both EGFR and HER2 in 2-3 colors. I aimed to directly visualize the localizations of these receptors with high (~20 nm) precision, such that the interactions between the receptors could be directly assessed based on co-localization events at the same length scale. However, HER receptors are ~18 nm in length when in dimers (when the receptor is in extended conformation), and the sizes of primary and secondary antibodies are each 10-15 nm, adding to a distance up to ~30 nm between the position of the fluorophore (which is measured in SRM / MSSRM) and that of the receptor. As a result, two receptors that are next to each other (i.e., in a dimer) could appear as $30 * \sqrt{2} \sim 42$ nm. This adds to the challenge of co-localization analysis at the 'superresolution' scale (Fig. 4.14 A).
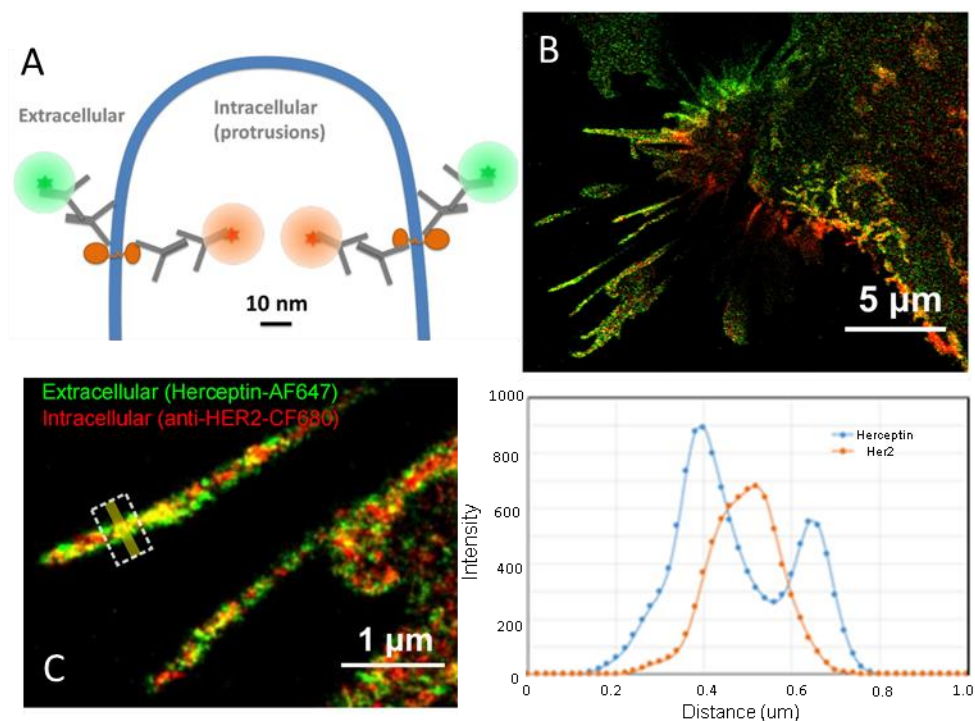
Figure 4.14 Simultaneous imaging of N- and C-termini of HER2 in SKBR3 cells with the MSSRM.

To demonstrate this point, I simultaneously labeled the extracellular and intracellular domains of HER2 in SKBR3 cells, using Herceptin and an anti-HER2 (C-terminus) antibody, respectively. The secondary antibodies used for the two antibodies are conjugated to AF647 (Herceptin) and CF680 (anti-HER2), respectively. AF647 and CF680 are clearly distinguishable on the MSSRM (see Chapter 3), allowing me to map the N- and C-termini of HER2 in the same protrusion (Fig. 4.14 B). As expected, the C-terminal signal (red) is predominantly in the middle of the FLPs, and the N-terminal signal is predominantly in the outside (Fig. 4.14 C). Due to the small diameter and circular cross-section of the FLPs, signals from the C-terminus of HER2 receptors distributed along the FLP almost collapsed into a single band (Fig. 4.14 D, red curve) with the intensity at the center being the strongest. By contrast, Herceptin signal was well resolved as two bands with lower intensity at the center; the distance between the two bands was ~130 nm, indicating that on average AF647 (green in Fig. 4.14 A) was ~65 nm away from CF680

(red in Fig. 4.14 A). Considering that HER2 is ~18 nm long, this distance is equivalent to ~50 nm separation between the two fluorophores even when the target be ~0 nm in length. Hence, the relative positions of two 'co-localized' proteins could manifest as separated by as much as ~50 nm in the resulting 'superresolution' image when indirect immunostaining is used for both; of note, this number may vary depending on the actual localization precision of both fluorophores or when direct immunostaining is used.

With this in mind, I next studied how HER2 and EGFR are localized relative to each other in SKBR3 cells under resting (serum starved and no EGF treatment) or stimulated (EGF treatment) conditions. Shown in Fig. 4.15 A is an example MSSRM image of HER2 (red, Herceptin) and EGFR (green, Cetuximab) in resting SKBR3 cells. With both HER2 and EGFR probed using antibodies binding to their N-termini, we expected that the two receptors within a dimer to be mostly within 30 nm (20 nm localization uncertainty for both). Clearly, HER2 was much more localized to the FLPs in comparison with EGFR, which was more 'homogeneous' across the membrane and is not particularly enriched in the FLPs. This is similar to the observation with single-color STORM (Fig. 4.5 & 4.6). In zoom-in views of the FLPs, helical patterns of HER2 were again evident, and EGFR molecules seemed to be scattered along the length of FLPs. In both the 'flat' regions of the membrane and the FLPs, there were no clear 'co-localization' between the two receptors. In the FLPs, EGFR even seemed to be mostly residing where HER2 signal was low.

EGF stimulation was known to trigger an open conformation of EGFR to facilitate dimerization another HER-family receptor, which would be HER2 in SKBR3 cells. As shown in Fig. 4.15 B, EGF stimulation caused retraction of most FLPs (in comparison with Fig. 4.15 A), indicative of active cell signaling presumably from EGFR:HER2 heterodimers that in part resulted in remodeling of the F-actin cytoskeleton. This observation is similar to that that shown in Fig. 4.10 Concomitantly, a high density of ruffle-like structures emerged in the previously 'flat' regions of the plasma membrane. These ruffles were only ~100 nm in width and a few hundred

nm to 1 μm in length. Similar to the HER2-enriched FLPs, these ruffle-like structures were abundant in HER2 and likely also filled with F-actin, although verification with F-actin staining would be necessary. Interestingly, EGFR (Fig. 4.15 B), appeared to be more frequently associated with these new, HER2-enriched ruffles in comparison to when both were in the FLPs. In particular, EGFR signals were more concentrated in the ruffles in comparison with the regions surrounding the ruffles, and within the ruffles EGFR and HER2 signals were often directly overlapping. Hence, these nanoscopic ruffles are acting as scaffolds or platforms for efficient EGFR and HER2 interaction; presumably, by confining both into narrow, nanoscopic structures.
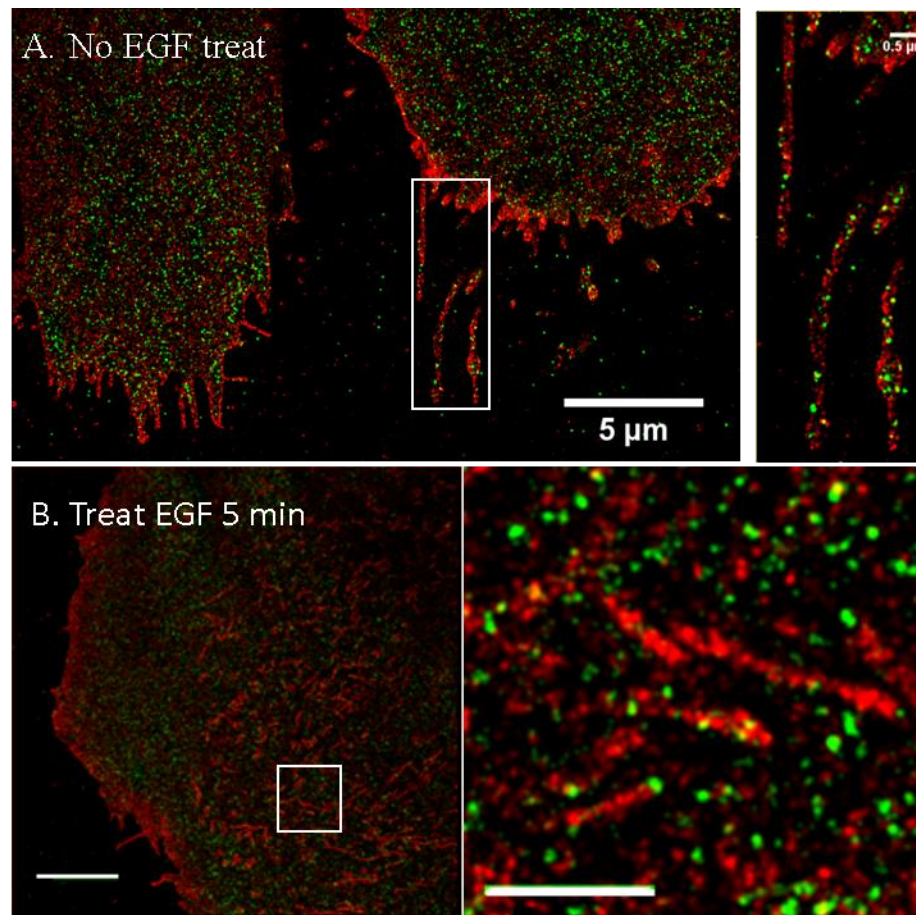
Figure 4.15 MSSRM imaging of HER2 and EGFR in SKBR3 cells.

(A) Resting cells; (B) stimulated with EGFR for 5 min.

4.3.3 Probing HER receptor clustering with MSSRM

While it has been well established that homo- and heterodimers of HER receptors are the functional units of signaling, accumulating evidence suggests that formation of higher order structures including protein clusters on the cell membrane plays a critical in regulating the biological activities of these receptors. Among others, spatiotemporal regulation of HER receptor signaling through dynamic localization to and cluster formation in membrane domains such as lipid rafts, caveolae, and clathrin-coated pits have been observed [162-165]. A few studies on using superresolution microscopy to visualize HER clusters in cells have also been reported recently [166-168]. However, a quantitative characterization of the biophysical parameters of HER receptors (or any biological molecules in general), and their associated membrane domains, have not been established. The high spectral resolution offered by the MSSRM provides unique opportunities for quantitative analysis of HER receptors and membrane nanodomains in cells. I focus on the clustering of HER receptors in this chapter, and a more detailed discussion and experimental study of membrane domains will be covered in the next chapter.

As shown earlier in this chapter, STORM imaging of both HER2 and EGFR yielded punctate structures in SKBR3, HCC1549, and A431 cells (Figs. 4.11). Zoom-in views of each of the puncta in each case reveals a high density of localization events (Fig. 4.16). The diameter of the clusters can vary between 50 – 150 nm; in comparison, the localization precision of AF647 in STORM experiments is typically better than 30 nm. Hence, it is already apparent from the physical dimensions of the localization 'clusters' that EGFR (and HER2) forms clusters on the cell membrane. However, the clustering of localization events could reflect the contribution of many cycles of blinking from a single fluorescent molecule (AF647 in this case) or from multiple AF647 molecules that are in spatial proximity, or both. At the current spatial resolution of STORM, it is not possible to distinguish localizations within the same 'cluster' arising from

different AF647 molecules; it is therefore also nontrivial to determine how many AF647 molecules (or antibodies) are within each cluster of localization events. This is a typical situation in current efforts to derive quantitative, copy-number information about protein clustering from PALM and STORM images; in fact, determining whether a protein of interest forms clusters or not remains a challenge by itself even with PALM and STORM, despite some success in selected cases [169-171].
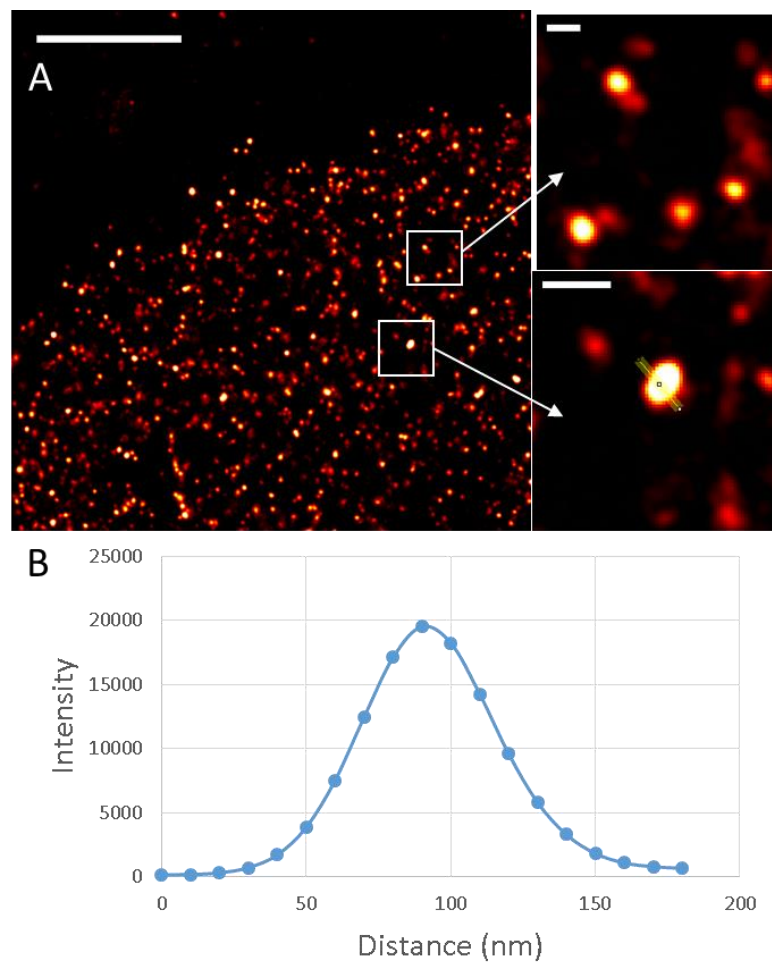
Figure 4.16 STORM image of EGFR clusters

(A) Imaging EGFR cluster in cells using existing STORM. Scale bar: 2um (left image); 200 nm (right top image); 100 nm (right bottom image). (B) Intensity line scan profile of cluster (right bottom image in (A).)

Here, I propose a new approach to deriving the clustering properties of proteins based on immunostaining and MSSRM imaging with organic fluorophores. As stated above, a major challenge in the quantitative analysis of protein clustering using localization microscopy is being unable to distinguish repeated blinking of the same fluorescent molecule from photoswitching of multiple molecules in spatial proximity. Our strategy to address this challenge is to label different molecules with different colors and image them with the MSSRM simultaneously, such that the photoswitching of multiple molecules can be easily distinguished from repeated blinking of the same molecule based on 'color' information. In this case, appearance of multiple colors within the same cluster of localization events would indicate clustering. This is the same concept as co-localization between different molecular species, except that here the co-localization analysis is performed between different molecules of the same species. While this strategy could be implemented with standard, multicolor SRM, potential issues with spectral crosstalk and registration error could jeopardize the quantitation of the imaging results.

Since EGFR was shown to localize to membrane domains and form clusters, I have used EGFR as an example target to demonstrate this strategy (Fig. 4.17 A). Specifically, I directly conjugated three aliquots of Cetuximab, each to one of the three fluorophores – DY634, DL650, and CF680 – and labeled A431 cells with all three aliquots simultaneously. The resulting sample was then imaged on the MSSRM to obtain the relative spatial distribution of EGFR molecules labeled in any of the three colors. The MSSRM image of all three colors is shown in Fig. 4.17 B, which resembles the image obtained from a regular STORM experiment. The corresponding histogram of *ssd* values shown in Fig. 4.17 C, indicating excellent spectral separation among the

120

three fluorophores. The image in Fig. 4.17 B was then split into three channels, red (DY634), green (DL650), and blue (CF680), and overlaid again to yield the image in Fig. 4.17 D.

By visual inspection, I could already observe frequent co-localization events between any of the two or among all the three color channels, indicating the presence of multiple EGFR molecules, with each color labeling one or more EGFR molecules, within the spatial proximity of 50-200 nm. As shown in the right panels of Fig. 4.17 D, within an apparent EGFR cluster, localization events of the same color appears as a cluster of 50-100 nm by themselves, similar to that observed in Fig. 4.11 localization clusters of different colors typically exhibited a partial overlap, consistent with the fact that each localization cluster arose separately from one or more EGFR molecules.
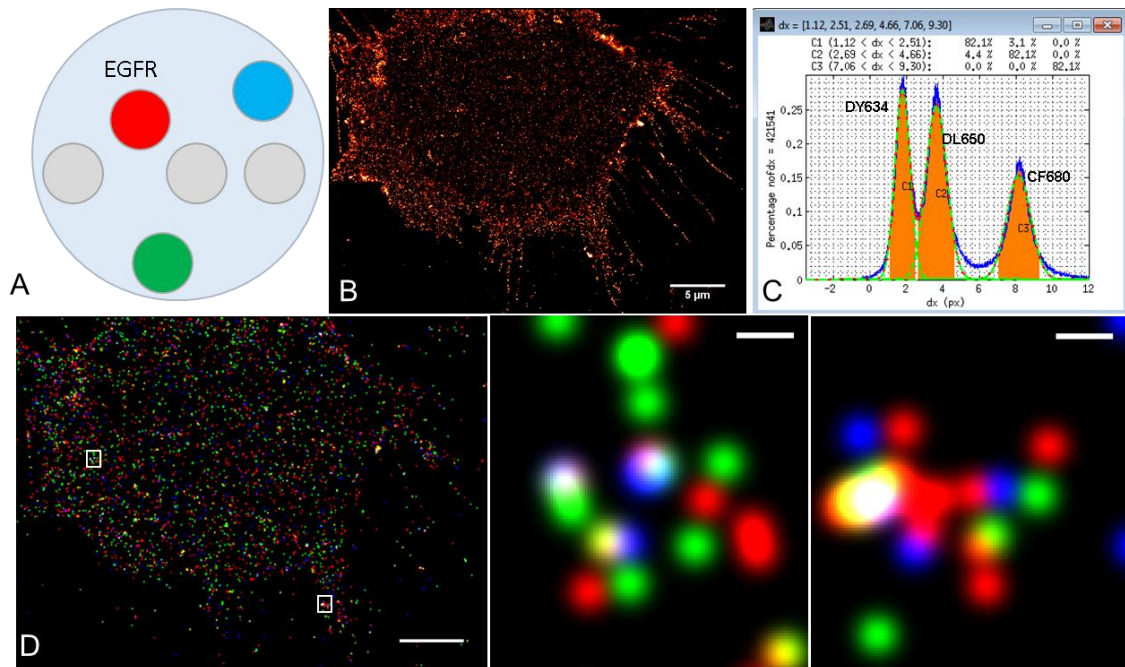
Figure 4.17 Analyzing EGFR cluster with the MSSRM.

(A) The imaging strategy; (B) MSSRM images of EGFR in A431 cell with all three color fluorophores, DY634, DL650, and CF680; (C) Spectral histogram of all three fluorophores for the image in (B); (D) Left: 3-color MSSRM image of (B) after color separation. Right: zoom-in

views of the boxed areas in the left image. Scale bars: 5 μm (left image), 200 nm (right two images)

This result demonstrated that it is possible to detect protein clusters based on multicolor SRM, for which MSSRM works particularly well. Based on the resulting multicolor images, quantitative analysis of the cluster populations with 4, 3, 2, and 1 color combinations could yield a definitive cluster size distribution. I note that multiple other factors impact the final MSSRM image of protein clusters, such as the dye to antibody ratio, labelling efficiency, detection efficiency, incomplete photo-conversion, and localization precision and so on. In most cases, these parameters can be measured and be incorporated into the data analysis algorithms to accurately extract the true clustering properties of the target. This is currently underway in the Nan lab.

Chapter 5   Mapping membrane nanodomains in cells with multispectral superresolution microscopy (MSSRM)

Spatial regulation of biological functions often involves compartmentalization of molecular components in nanoscopic structures, with membrane nanodomains such as lipid rafts being one of the classic examples. Many experimental approaches have been developed to study membrane domains, but none have provided definitive evidence for the existence, molecular composition, physical size, and dynamics of the putative membrane domains. This is in a large part due to the small length scales and the difficulty in labeling the nanodomains without interfering with their composition and function. In this chapter, we combine the MSSRM with small molecule, lipophilic probes that exhibit environment-sensitive emission spectra to map the nanoscopic heterogeneities of membranes inside a cell.

5.1 Introduction

Biological membranes define the boundary of cells, cell nuclei, and many other intracellular organelles. The membranes are also home to a wide variety of biomolecules, provide sites for intra- and intercellular signaling, and in so doing create both diversity and precision control for the biological cell.

5.1.1   Molecular compositions and structure of biological membranes.

The basic structure of biological membranes is a lipid bilayer with embedded or tethered proteins. Most common lipids are amphiphilic molecules with hydrophilic headgroups and

hydrophobic tails, which self-assemble into a bilayer 3-4 nm thick in water with the hydrophobic tails in both layers packed in the middle to form a hydrophobic 'core' and the hydrophilic headgroups facing the aqueous phase. The plasma membrane of eukaryotic cells comprises highly diverse lipid species that can be roughly divided into three groups: phospholipids, neutral lipids and glycolipids, with phospholipids being the principle constituents[172] (Fig. 5.1). Each of these lipids has unique molecular structures and physicochemical properties and contributes to the organization and functions of the plasma membrane in different ways. Similarly, other cellular membranes also contain far more lipid species than needed to form simple bilayers, presumably tailored for the specific functions of each membrane system.
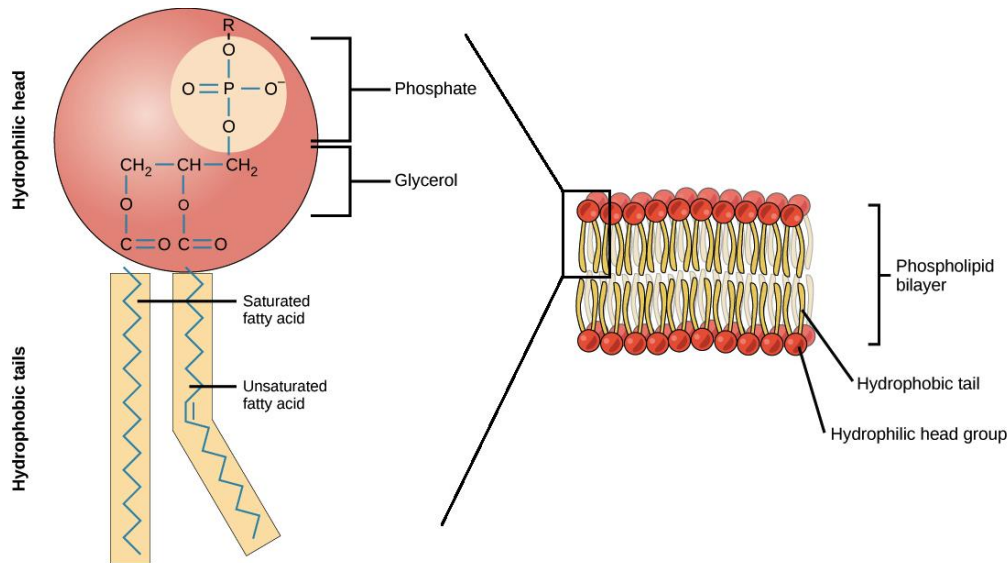
Figure 5.1 The lipid bilayer (Image modified from OpenStax Biology)

Among the numerous types of phospholipids (Fig. 5.2 A) found in biological membranes, phosphtidylcholine (PC), phosphatidylethanolamine (PE), sphingolipids, phosphatidylserine (PS), and phosphatidylinositol (PI) exist in significant quantities [173,174]. As the most abundant form of phospholipids, PCs are built upon a glycerol backbone with two fatty acids and a phosphorylcholine group attached to positions (*sn-*) 1, 2, and 3, respectively. The most common

type of PC has a saturated fatty acid residue at *sn*-1 and an unsaturated fatty acid at *sn*-2 of the glycerol backbone (e.g. palmitoyl-oleyl-*sn*-phosphatidylcholine, or POPC)[174]. PCs with saturated and long acyl chains (such as dipalmitoyl phosphocholine, or DPPC) or with unsaturated, short acyl chains are also present in cell membranes.

Another major class of phospholipids is sphingolipid, which has a sphingoid base instead of a glycerol molecule as the backbone. The most common sphingoid base found in animal tissues is a sphingosine consisting of a monounsaturated aliphatic chain, a primary amine, and two hydroxyl groups. Sphingosines can be modified to give rise to ceramide (Fig. 5.2 C), which can further be linked to a phosphoryl-choline group at *sn*-1 to yield sphingomyelin (Fig. 5.2 B). Located between the polar head group and the non-polar hydrocarbon chains, the hydroxyl and amide groups of sphingolipids can both participate in hydrogen bonding and mediate the interactions between the sphingolipids as well as interactions with other lipids in the membrane [175]. In particular, self-association between sphingolipids has been thought to increase the impermeability and rigidity of the membrane.
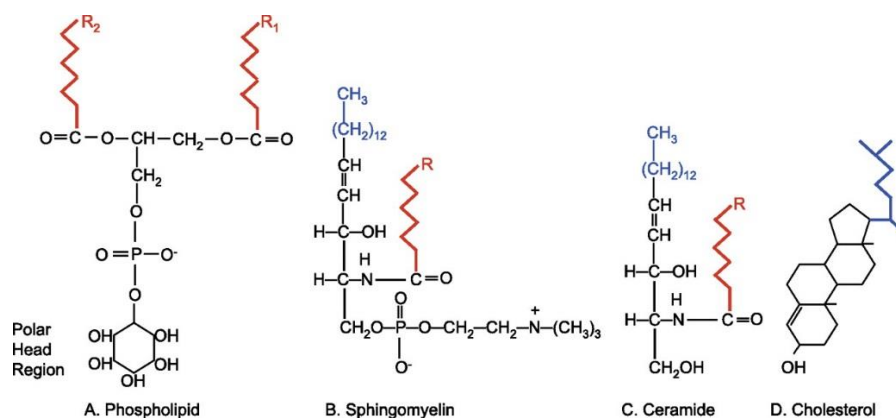
Figure 5.2 Membrane lipid structures.

A: structure of a phosopholipid (specifically, phosphatidylinositol).

B: structure of sphingomyelin. C: structure of ceramide. D: structure of cholesterol. (modified from Kathleen M. Eyster, 2007)

In contrast to phospholipids, neutral lipids do not carry any charged group. One class of neutral lipids enriched in significant amounts in the plasma membrane is sterols, with cholesterol (Fig. 5.2 D) being the principle form in vertebrates, at approximately one-half of the total amount of phospholipids in the plasma membrane (ref). Cholesterol also exists in varying amounts in endomembranes, and its concentrations there are actively maintained at a much lower level through mechanisms that are not yet completely understood. Another important form of neutral lipid is fatty acid esters, for examples cholesterol esters (CE) and triacylglycerol (TAG, also known as triglyceride or simply, fat) typically existing as cytoplasmic lipid droplets [176,177].

Another important aspect of the spatial organization of biological membranes is the asymmetric distribution of many lipid species between the two leaflets of the lipid bilayer. For example, PS and PE are preferentially localized on the cytoplasmic leaflet of red blood cells, while PC and sphingomyelin (SM) are predominantly on the exoplasmic leaflet [178]. In particular, PS contributes to ~10% of the total phospholipid content of the plasma membrane but is almost exclusively shielded from the external leaflet except during certain cellular processes such as apoptosis. Both passively governed by the intrinsic biophysical properties of lipids and actively maintained by lipid transporters , this asymmetry plays important roles in various membrane mediated biological processes. Among others, lipid rafts were thought to be a phenomenon on the exoplasmic side of the plasma membrane, although certain membrane proteins such as H-Ras seem to be linked to lipid rafts despite that they reside on the inner leaflet of the plasma membrane [33,179,180].

5.1.2   Phase segregation in the lipid bilayer and domain formation

The diversity of lipids found in biological membranes is critical to the structural and functional diversity of the membranes. Depending on the length and saturation of the aliphatic chains as well as the charge, hydrophobicity, and orientation of the headgroups, each lipid species contribute to the local and global structure of the lipid bilayer in a distinct manner. Moreover,

numerous membrane proteins, either embedded or tethered to either side of the bilayer, participate in membrane organization through interactions with specific lipid species, at times leading to the formation of membrane structures with well-defined morphology.

The aliphatic tails of lipids make up the hydrophobic core of a lipid bilayer through hydrophobic interactions, and the length and saturation of each lipid species has a direct impact on the packing of the bilayer. Long, saturated chains can make extensive contacts and pack tightly to form ordered, sometimes almost crystalline structures. Short acyl chains have limited contacts with other lipids, and their packing is typically less ordered. Unsaturated side chains have one or more kinks in their structures and cannot be packed tightly, hence these lipids contribute to disordered, i.e., more fluidic, membrane structures. As mentioned earlier, sphingolipids can associate with each other and in so doing enhance the packing [181,182].

In the formation of lipid bilayers, cholesterol plays a very specific role. The molecule has four rings in its structure, three of which are six-carbon rings and the other a five-carbon ring. The four rings are juxtaposed to produce a rigid and planar molecule that can be inserted into parts of a lipid bilayer close to the polar head of the phospholipids, where there are typically void spaces among certain head groups. As such, cholesterol acts as a 'glue' to render the lipid bilayer more rigid, decreases membrane fluidity and permeability, and may also reduce the natural lateral or flip-flop of phospholipids between the inner and outer leaflets of the lipid bilayer.

The distinct structure and packing energetics of the different lipid species give rise to interesting phenomena when they co-exist in the same membrane system, most importantly phase segregation, or the partitioning of certain lipid species into distinctive domains. For example, lipids with long, saturated side chains tend to partition into the same domain, often times also with sphingolipids and cholesterol. This thermodynamic phase separation results in plasma membranes named lipid rafts, as first hypothesized in 1997 by Kai Simons and Elina Ikonen [183].
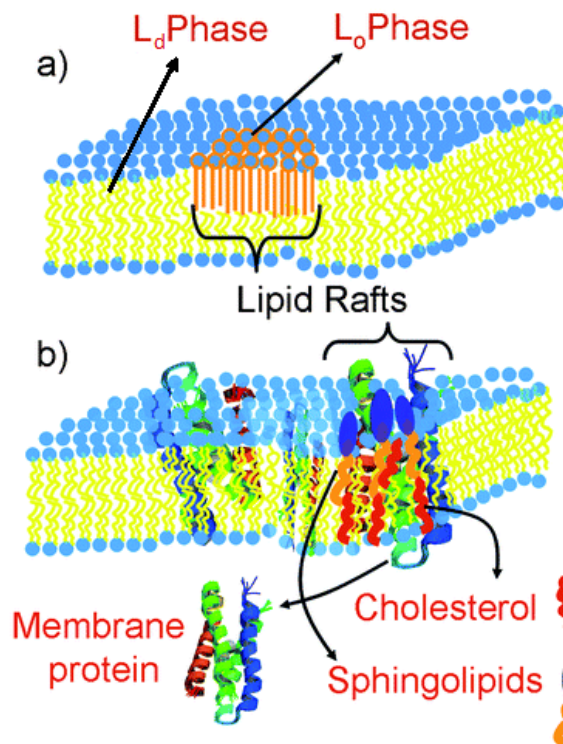
Figure 5.3 Structure and formation of lipid rafts.

based on a) lipid ordering/disordering; b) combination of membrane proteins, sphingolipids and cholesterol. (modified from Chandrashekhar V. Kulkarni. 2012)

Rafts are usually associated with liquid ordered (Lo) membrane phases or detergent-resistant membrane (DRM) fractions. In artificial model membrane, Lo phases were observed with enriched rafts components, such as sphingolipids, cholesterol and saturated lipids. On the other hand, the liquid disordered (Ld) phase which is in actual biological membranes surrounded by unsaturated lipids are called lipid rafts. Lipid rafts are more abundant at the plasma membrane but can also be found in endocytic and secretory pathways. As cholesterol is an important component in the DRMs, its depletion using reagents such as methyl-β-cyclodextran (mβCD) has been used as a means to disrupt the various raft domains, allowing interrogation of their biological functions[184].

5.1.3 Membrane (lipid and protein) nanodomains in biology

The lipid (membrane) raft concept was initially proposed based on studies of membrane trafficking, and to date they are implicated in a wide range of biological processes including lipid and protein sorting[185], cell signaling[185,186], immune response[187], to name a few. A key piece of evidence for lipid rafts was the observation that in polarized epithelial cell models, cholesterol, sphingolipids and glycosylphosphatidylinositol (GPI)-anchored proteins were selectively delivered to the apical plasma membrane from the Golgi, whereas PC is preferentially delivered to the basolateral membranes [183,186,188]. This was the first indication that cell membranes were also able to segregate different lipid species for controlled trafficking and led to the original lipid rafts hypothesis [183].

Although artificial membranes made of lipids can mimic the phase separation between lipids, proteins are an integral part of biological membranes, including the raft domains [189]. Depending on the structure and the biochemical properties of the membrane protein, its interactions with lipids may differ. For example, cell surface receptors are transmembrane (TM) proteins, and receptors possessing different transmembrane domains can target to different lipid domains depending on the structure and hydrophobicity of the TM domain [181,190]. Some proteins such as the Ras GTPases tether to the inner leaflet of the membrane via lipid groups, typically added during post-translational modifications, and the lipid adducts can participate in membrane packing and determine what lipid domains the protein will be associated with [191]. For example, KRas is farnesylated, which is unsaturated and tend to locate to Ld domains, whereas HRas is farnesylated and doubly palmitoylated, which results in a dynamic distribution between ordered and disordered domains [192]. Caveolin has a palmitoylation group and is a typical raft-associated protein [193]. Proteins can also tether to the outer leaflet of the membrane by a glycophosphatidylinositol (GPI-) group, which is also a product of post-translational modification. These proteins, known as GPI-anchored proteins, are thought to localize to lipid rafts, and GPI-GFP is often used as a genetically encoded lipid raft marker [194].

The ability to isolate membrane domains, to manipulate them in cells (e.g. disrupting lipid rafts with mβCD), as well as to visualize them in fluorescence and electron microscopies has led to significant progress on understanding the biological functions of these lipid-protein structures. The physical segregation of proteins into distinct membrane domains may regulate the conformation, oligomerization, and other properties of the proteins as well as their accessibility to regulatory or effector molecules. Proteins sorted to the same membrane domains will have a much greater chance to interact with other, hence the domains can acts as nano- or microscopic containers for specific biological processes. Additionally, depending on the functional status of a protein, it may redistribute between different membrane domains where different downstream molecules reside or when the biological reaction needs to be attenuated or abolished. For example, EGFR was thought to reside in caveolae but migrate out of these membrane domains upon EGF binding and receptor activation, followed by clathrin-coated pit formation, receptor endocytosis and degradation, and signal attenuation [162,165].

5.1.4   Current approaches to studying membrane domains

A clear understanding of membrane domains requires high resolution mapping of both the proteins and the lipids in cells. Unlike protein imaging, however, lipids are small molecules that prone to perturbations by tagging with fluorophores, and they typically are difficult to probe with fluorescent proteins or antibodies. Additionally, the membrane domains can be only a few tens to a few hundred nanometers in size and are transient structures. These pose significant challenges to studies aiming at mapping the spatial, chemical, and physical properties of membrane domains. Nonetheless, there have been a number of different experimental techniques applied to study membrane domains, which have offered valuable insight into the organization and functions of biological membranes. A partial list of commonly used approaches along with their capabilities and limitations is shown in Table 5.1; we also highlight a few techniques in the following section.

Technique	Description	Advantages	Disadvantages	References
Biochemical Fractionation	Density gradient based fractionation after nonionic detergent extraction	Enriches detergent resistant membrane for analyzing the components	No spatial information; bulk averaging of different types of membrane domains	[195-197]
Extraction with cold, non-ionic detergent	Applies cold detergent to cultured cells, and membrane fractions resistant to the extraction are left behind	Allows imaging studies of the domains with both fluorescence and electron microscopies	May cause smaller membrane domains to coalesce; destroys other context of the membrane domains	
Electron microscopy	High resolution imaging of lipid structures in cells in combination with immuno-gold labeling	Very detailed view of local membrane structures to help identify domains with distinct morphologies	Sample preparation is lengthy and destructive; no live cell dynamics; and limited number of colors	[193,198]
Fluorescence microscopy	Fluorescence labeling and imaging of tagged lipids, cholesterol, or proteins, sometimes after crosslinking	A variety of fluorescence techniques such as FRET, FCS, and superresolution imaging can be applied	Resolution can still be limited; tagging of lipids is difficult and often times perturbative	[199-201]

Table 5.1 Common approaches for studying membrane nanodomains

Biochemical fractionation. Fractionation is one of the traditional approaches for isolating 'raft' membranes for subsequent characterizations. This method relies on the resistance of lipid ordered domains to cold detergent, and it involves extraction of cells with nonionic detergents followed by separation of a low-density fraction on sucrose or other gradients. Detergents such as 1% Triton X-100, Lubrol WX, Lubrol PX, Brij 58, Brij 98 and others have been successfully used to isolate lipid rafts [202]. Although this approach has been instrumental to lipid raft research, there has been concerns about potential artefacts including lipid and protein clusters caused by detergent extraction. For example, there is evidence that individual, tiny lipid rafts (<50 nm) may coalesce into large, continuous membrane sheets, suggesting that the

131

biophysical properties of the residual membrane after detergent extraction may differ significantly from actual lipid rafts. For these concerns, the method offers little or limited information of the spatial distribution, organization, and dynamics of lipid drafts in intact cells. That said, this approach remains effective for concentrating and analyzing the chemical constituents that comprise raft domains.

Electron microscopy (EM). For the high spatial resolution (~1 nm) and clear contrast of lipids after heavy metal staining, EM has been among the most widely used techniques for characterizing membrane nanodomains. Both scanning EM (SEM) and transmission EM (TEM) are suited for imaging the topology of cell membranes, along with many other cellular organelles, and in well prepared samples the lipid bilayer could be clearly resolved in TEM [193]. Moreover, using antibody-conjugated metal (e.g. gold) nanoparticles, specific biological molecules can be localized with nanometer spatial resolution, allowing direct association of molecular constituents with membrane domains [198,203]. Caveolae appeared as distinct shaped invaginations on the membrane in the EM, and immuno-EM has helped to reveal that formation of nanoscopic clusters is a common feature for membrane-bound proteins. For obvious reasons, EM is limited to static imaging of a thin slice of fixed samples, and the number of molecular species that can be studied at once with EM is not more than two. Besides caveolae and clathrin-coated pits, no other membrane domains are known to possess distinct contrasts to be readily identified in EM images. To overcome these limitations, volumetric EM techniques, multicolor EM, and correlative light (including superresolution) and electron microscopy have emerged as a powerful extensions to traditional EM and are becoming the mainstay for biological imaging.

Fluorescence microscopy. Fluorescence microscopy (FM) enables specific labeling of a variety of molecular species, including protein, lipids, and glycans, and thus is a powerful modality for dissecting the molecular compositions and probing the spatial and temporal dynamics of membrane nanodomains. To date, fluorescent analogs of most types of lipids have been made and used to visualize the trafficking and partitioning of lipids in model as well as

physiological membranes. For example, in 2007 Baumgart and Webb *et al.* demonstrated that giant plasma membrane vesicles (GPMVs) isolated from mammalian cells can display similar phase segregations as model membrane systems do, by using fluorescently labeled lipid analogs, providing direct visual evidence for the existence previously speculated membrane rafts in actual biological membranes . Prior *et al.* used FM to visualize the membrane domains to which HRas proteins are localized, after antibody-mediated crosslinking of a putative membrane marker [25].

In addition to providing direct visualization, FM is also the platform for a number of other fluorescence techniques suited for studying membrane nanodomains. Examples of these are fluorescence correlation spectroscopy (FCS) and fluorescence resonance energy transfer (FRET) [200]. FCS measures the diffusion of fluorescently tagged molecules within the membrane, which is a sensitive approach to the spatial and structural heterogeneities of the membrane [199]. FRET is the energy transfer between two spectrally overlapping fluorophores, designated the donor and the acceptor, respectively, when they are within a few nanometers. As the energy transfer efficiency is very sensitive to distance, FRET is a powerful approach to detecting spatial aggregation of membrane molecules. Zacharias *et al.* genetically fused membrane-targeting sequences to monomeric CFP (mCFP) and YFP (mYFP), a widely used FRET pair, and used FRET to detect whether lipid moieties attached to the targeting peptides could induce lateral segregation. Among the targeting sequences tested, palmitoyl and geranylgeranyl sequences were shown to induce raft-like aggregation of the attached protein (in this case, mCFP or mYFP) whereas a prenyl group (such as a farnesyl group typically found at the C-terminus of Ras GTPases) cannot [201].

Although the various FM techniques have lent us versatile tools for studying membrane nanodomains, spatial resolution of conventional FM is limited by the diffraction of light to ~250 nm at best. This inadequate spatial resolution prevents accurate characterization of the biophysical properties, such as the size and relationship with other cellular structures, of the membrane nanodomains.

5.1.5 Proposed new approach for mapping lipid nanodomains

An ideal tool for studying membrane nanodomains needs to be able to map both the proteins and lipids with sufficient spatial and molecular resolutions. The approaches described above are limited in one or more aspects. In the last chapter, we described approaches to quantitative characterization of protein nanodomains (nanoclusters) based on the MSSRM. In this chapter, we propose a new approach to studying lipids in the membrane nanodomains based on the MSSRM. Combining the two capabilities on the MSSRM in the same experiment will provide unparalleled capability for studying the lateral organization of membranes.

Our approach involves the use of environment-sensitive lipid probes that exhibit different emission properties depending on the chemical compositions of the immediate neighborhood. This environment-sensitive emission property of fluorophores is called solvotochromic in literature. Many classes of solvotochromic fluorophores have been developed, with fluorescent properties dependent on lipid polarity (nile red) [204], charge (F2N12S) [205], membrane potential [206], PH, and many others. To date, the use of solvotochromic fluorophores in superresolution microscopy is not widespread in part because many of the fluorophores have not demonstrated good photophysical properties suited for the purpose.

In this chapter, I set out to test the use of small molecule, solvotochromic fluorophores that can probe the lipid environment for superresolution imaging, such that the nanoscopic heterogeneities of the membrane organization could be reported by the localization and the emission spectra of individual fluorescent molecules. Among others, I have tested the well known fluorophore nile red, of which the emission spectra varies depending on the polarity of the lipids and notably the cholesterol content [207]. I have also tested another fluorophore, FM4-64, which exhibits a broad emission spectra when excited by 561 nm.

Besides conventional STORM imaging based on photoswitching of individual dye molecules, we also utilized point accumulation for imaging in nanoscale topography (PAINT) , which does not require the fluorophore to be photoswitchable but rather relies on the much

slowed diffusion or increased brightness of the fluorophore upon binding to the membrane. Of note, both nile red and FM4-64 dyes are virtually nonfluorescent in aqueous buffer but becomes brightly fluorescent when inserted into the lipid bilayer, thus allowing PAINT imaging of the fluorogenic binding events. With either regular STORM or PAINT (Fig. 5.4), my results clearly demonstrate the feasibility of using environment-sensitive dyes and the MSSRM to report the nanoscopic heterogeneities in membrane organization.
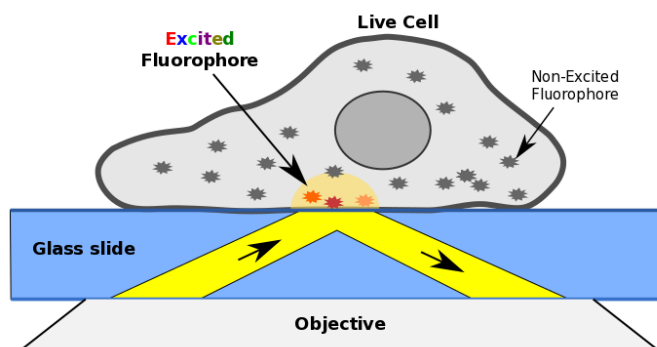
Figure 5.4 Principle of the 6 (PAINT) technique for superresolution imaging.

5.2 Materials and Methods

Tissue culture. U2OS (human osteosarcoma, ATCC, HTB-96) and A431 (human epidermoid carcinoma, EGFR+, ATCC, CRL-1555) cells were both maintained at 37° C and under 5% CO_2 in DMEM supplemented with 10% FBS (Life Technologies, 11995 and 10082 respectively). For imaging, LabTek (Thermo, 155409) or μ-Slide (ibidi, 80827) chambers with a #1.5 coverglass bottom were first cleaned by incubating with 1 M NaOH for 2 hours at room temperature, followed by washing 5 times with MilliQ water and incubation with MilliQ water or PBS overnight. Cells were plated in the chambers 36-48 hours prior to imaging in phenol red-free DMEM (Life Technologies, 21063) supplemented with 10% FBS.

Sample labeling. Nile red (Sigma-Aldrich, 72485) was stored in aceton at a stock concentration of 5mg/ml at 4 °C, and FM4-64 (Invitrogen, T3166) was stored in the original vial

from the manufacturer 1mg dissolved in 100 ul DMSO. For SRM and MSSRM imaging with nile red, U2OS and A431 cells were first briefly washed in PBS (PH = 7.4) and fixed in 3.7% PFA (in PBS) at room temperature for 20 min. For STORM imaging, nile red was added to the sample right before imaging, at a final concentration of 500 ng/ml. For PAINT, nile red was added at a final concentration of 500pM~1nM.

FM4-64 labeling was performed as suggested by the manufacturer's protocol. Briefly, an ice cold working solution in Hank's balanced salt solution (HBSS) was first prepared from the stock. The cells were quickly incubated with the work solution on ice for ~1 min and fixed with 3.7% PFA at room temperature right after staining.

SRM and MSSRM imaging. SRM and MSSRM imaging were both performed on a custom MSSRM setup described in Chapter 3. For imaging nile red and FM4-64 labeled samples with STORM, the standard STORM imaging buffer with 10 mM MEA was used; for imaging these samples with PAINT, the samples were immersed in PBS (PH = 7.4) with either no oxygen scavenger (GLOX) or with GLOX diluted in PBS at 1:1,000 (i.e., 1/10 of the normal GLOX concentration). In all cases, 50 nm gold nanoparticles were used as fiduciary markers, and a custom built focus stabilization is used to maintain the image focus to within approximately ±25 nm.

Image acquisition was also performed in a manner similar to that described in chapters 3 and 4, using primarily the μManager package and saved as the OMERO Tiff format (.tiff).

Data analysis. SRM and MSSRM image analysis was done with home-written MatLab scripts as described in chapters 3 and 4. Briefly, the raw MSSRM image stack was first split into the positional and the spectral channels. Positional images from SRM or MSSRM experiments were then analyzed to extract the precise locations of each molecule. Next, the localizations were transformed into the MSSRM channel using a transformation matrix, as determined by registering the positional and spectral images of gold nanoparticles taken at 561 nm with a narrow bandpass filter, such that the emission spectrum of each molecule comprising ±25 pixels of the spectral

image around the positional centroid could be obtained. After quality check, the spectral images were then analyzed to determine the maximum emission wavelength in each case. A histogram of all the single molecule emission maxima is used to guide the assignment of spectral (*ssd*) ranges for determining the color of each localization event. After color separation, images in each channel were rendered separately in Matlab, saved as TIF files and re-combined in ImageJ for multicolor display and other manipulations.

5.3 Results and Discussion

5.3.1 SRM imaging of the cell membrane using lipophilic dyes.

I first tested the possibility of using common lipophilic dyes, nile red and FM4-46, for imaging the cell membrane with SRM based on STORM or PAINT principles. The results demonstrated that the two fluorophores are suited for both STORM and PAINT-based superresolution imaging, with each fluorophore and imaging condition seemingly to reveal a somewhat different subset of membrane structures.

Nile red is an oxazine derivative that has been historically used to stain lipid droplets (enriched in TAGs and cholesterol esters), in which case nile red is efficiently excited at 510-540 nm and emits fluorescence at 570-600 nm at a quantum efficiency of 70-90%. Nile red also stains phospholipids, which have higher polarity, and the excitation and emission wavelengths are 530-550 nm and 600-650 nm, respectively, with a quantum efficiency typically around 40-60%. Consistent with this notion, under a regular, epi-fluorescence microscope, nile red clearly stains the cell membrane of U2OS and A431 with punctate structures indicative of lipid droplets in the cytosol (data not shown). In a standard STORM imaging buffer containing both GLOX and 10 mM MEA, the photoswitching of nile red is also efficient as in the case of other oxazine fluorophores (such as Atto 655) [208] (Fig. 5.5 A). Of note, the image was acquired using only ~30% of the total photons, with the remaining 70% going to the spectral channel (see Chapter 3). The

resulting STORM image taken under relaxed total internal reflection (TIR) conditions clearly reveal various lipid structures including both the membrane and intracellular lipid droplets (Fig. 5.5 B-C).
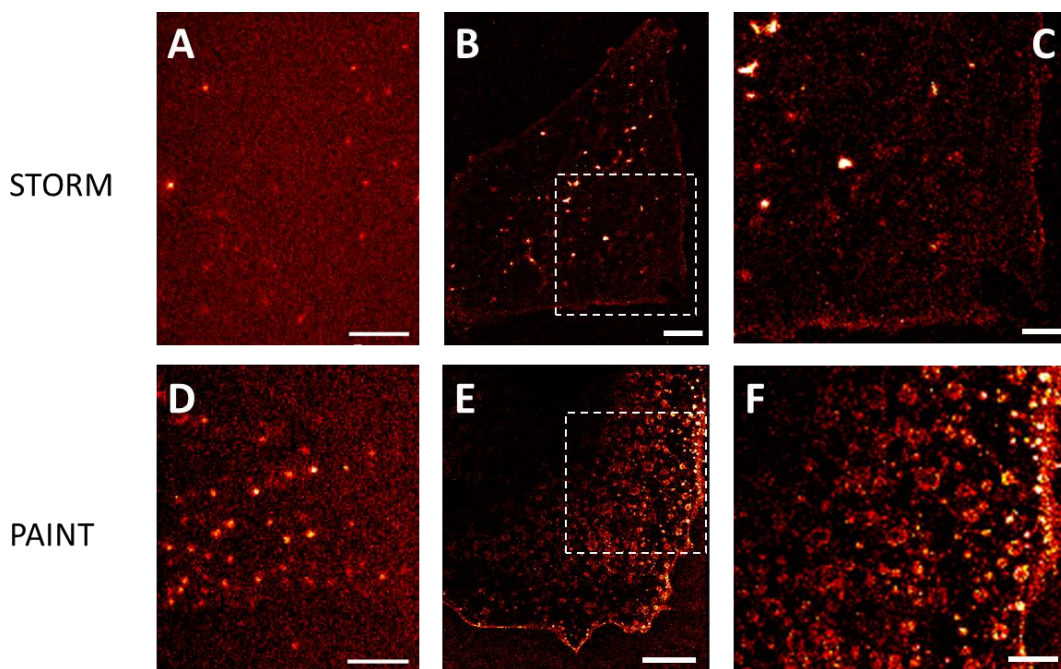
Figure 5.5 Superresolution imaging of membrane structures in cells using nile red. (A) Single-molecule images of nile red in STORM imaging buffer containing GLOX and 10 mM MEA; (B) Example STORM image of U2OS cells stained with nile red, with a zoom-in view of the boxed area shown in (C); (D) Single-molecule image of nile red imaged with PAINT in PBS; (E) Example PAINT image of U2OS cells stained with nile red, with a zoom-in view of the boxed area show in (F). Scale bars, 5 μm in (A-B) and (D-E) and 2 μm in (C) and (F). (A-C) were acquired using a 561 nm laser excitation. (D-F) were acquired using a 531 nm laser excitation, and images taken with a 561 nm laser excitation were similar.

Nile red is barely fluorescent in PBS buffer (quantum yield <5%) and only becomes fluorescent upon binding to the lipid bilayer, hence binding of individual nile red molecules with various lipid structures in cells generates discrete fluorescent bursts when a low concentration

(<10 nM) of nile red is retained in the imaging buffer (Fig. 5.5 D), an alternative approach to performing single-molecule localization microscopy known as PAINT [209]. Although only ~30% of the photons were used for the positional image, most of the individual bursts yielded a good number of photons to allow precise localizations of the events with very good resolution. Indeed, in the reconstructed PAINT image, both the plasma membrane and intracellular vesicles were clearly resolved.

Comparing the reconstructed STORM and PAINT images of U2OS cells stained with nile red, we noticed that the two approaches reported overlapping but not identical membrane structures. In STORM images, the strongest contrast came from punctate lipid droplets, and the membrane stain is present but weak. In PAINT images, the most evident features are the plasma membrane and intracellular vesicles; the latter appeared to be mostly hollow, indicative of vesicles instead of lipid droplets, except for those that were right next to the plasma membrane, which might be too small to be resolved as hollow structures. Given that STORM and PAINT are based on different photophysical and chemical principles, it is not too surprising to see that STORM and PAINT images using the same dye (nile red) would give rise to different structures. At present, however, it is unclear why PAINT preferentially highlights structures with lipid bilayers whereas STORM favors the lipid droplets.

Another lipophilic dye, FM4-64, also performed well for STORM imaging. FM4-64 is a small molecule, styryl compound that is well soluble in water but remains essentially nonfluorescent until it inserts into the outer leaflet of the plasma membrane. After binding, the dye may be quickly endocytosed (depending on the cell line), thus the labeling is typically performed at low (ice cold) temperatures. After labeling and fixation, U2OS cells were imaged using a 561 or 647 nm laser in a standard STORM imaging buffer containing GLOX and 10 mM MEA. Individual FM4-64 molecules were clearly recorded with high signal to background ratio (Fig. 5.6 A), enabling high resolution imaging of the stained membrane structures (Fig. 5.6 B-C). Of note, in this experiment we used the non-fixable FM4-64, and we frequently observed that the

139

FM4-64 molecules exhibited some mobility even though the sample had been chemically fixed. Nevertheless, the mobility is limited and was largely overcome by recording the raw images at high frame rates.
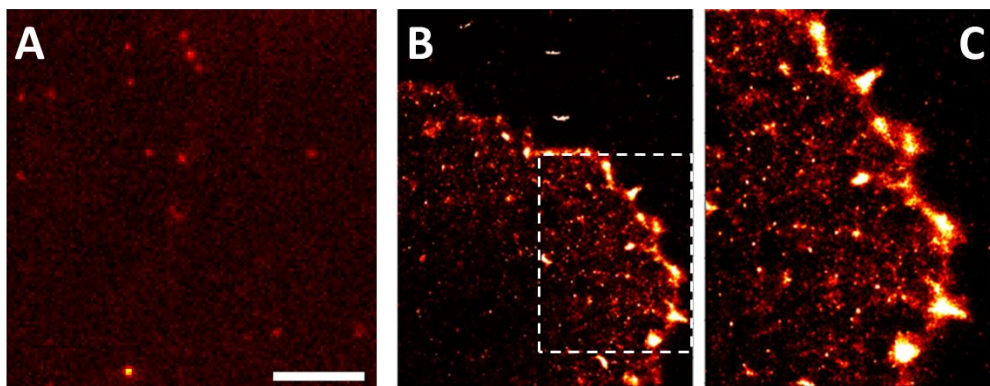
Figure 5.6 STORM imaging of cell membrane organization by FM4-64.

U2OS cells were labeled live at 4 C with FM4-64 for 1-2 min and immediately fixed in 3.7% PFA / PBS for 20 min. Cells were imaged in GLOX / PBS buffer with 10 mM MEA and with a 647 nm laser. Scale bar, 5 μm.

5.3.2   Spectral analysis of nile red and FM4-64

The images of nile red- or FM4-64 stained U2OS cells shown above were all acquired on the MSSRM, with the spectral images of all fluorescent molecules recorded alongside their positional images. This allowed us to analyze the emission profile of each nile red or FM4-64 molecule as they emerged at distinct locations in the cell. As such, we were able to obtain a nanoscopic map of the spectral properties of the fluorescent molecules, which should contain information about membrane heterogeneity.

Spectral analysis revealed that the maximum emission wavelengths of all nile red molecules fell in a broad range from 580 nm (system cutoff wavelength) to 700 nm. The histogram of maximum emission wavelength could roughly be divided into two peaks, with the first one at 590 ±10 nm and the second at 600-700 nm. Presumably, the first, small peak

corresponds the populations of nile red molecules that inserted into a more neutral (nonpolar) lipid environment, and the second corresponds to another population that inserted into a more polar lipid environment.

Based on the single-molecule maximum emission wavelength information, we converted the STORM and PAINT images of nile-red stained U2OS cells into spectrally-encoded images, where the color of each pixel represent the emission wavelength (Fig. 5.7). In Fig. 5.7 B, many cytosolic structures could be seen; interestingly, these intracellular structures exhibit a wide range of spectral properties, with some highly enriched in neutral lipids (cyan – blue colored) whereas others mostly polar lipids (yellow to red colored).
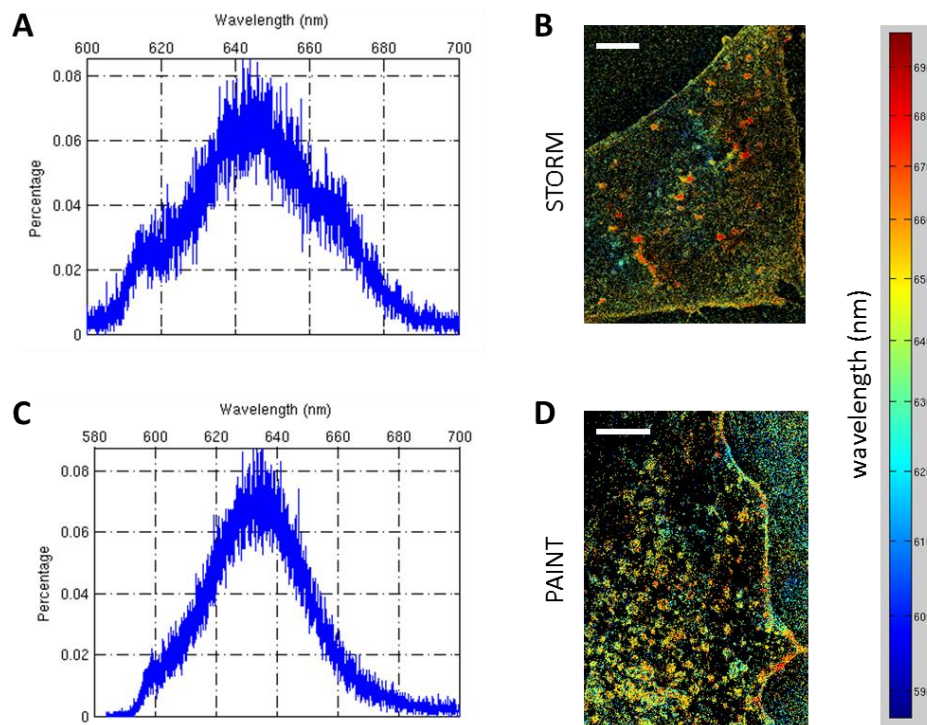
Figure 5.7 Spectrally resolved superresolution imaging of membrane structures in U2OS cells. (A) Emission spectrum of STOMR image; (B) STOMR image of Nile Red; (C) Emission spectrum of PAINT image; (D) PAINT image of Nile Red. Scale bars, 5 μm.

The PAINT image (Fig. 5.7 D) showed strong staining of both plasma membrane and various endomembranes. From the color-coded spectral image, it becomes apparent that the chemical properties of the membranes vary widely. The plasma membrane is in general yellow but some segments are more enriched in neutral lipids (cyan-blue color) whereas other segments appeared to be mostly polar lipids. The same is true for the numerous intracellular vesicles.

Spectral analysis of individual FM4-64 molecules also revealed a broad distribution of maximum emission wavelength (Fig. 5.8 A), as expected from the broad emission spectra. Two populations, one emitting at 685 ± 15 nm and the other around 730 ± 20 nm, could be clearly discerned from the histogram (Fig. 5.8 B). In this case, we split the single-molecule coordinates into two channels based on the spectral information, and yielded two superresolution images of membrane structures, both of which labeled by FM4-64 but exhibiting different emission properties (Fig. 5.8 B). The two populations are clearly different, with one (670-700 nm) featuring both the peripheral membrane and many other structures (green channel in Fig. 5.8 A) and the other (700-730 nm) present predominantly at the peripheral membrane (red channel in Fig. 5.8 B). At present, we do not know what causes the spectral heterogeneity, but it is likely linked to biochemical heterogeneity in the membrane structures stained by FM4-64.
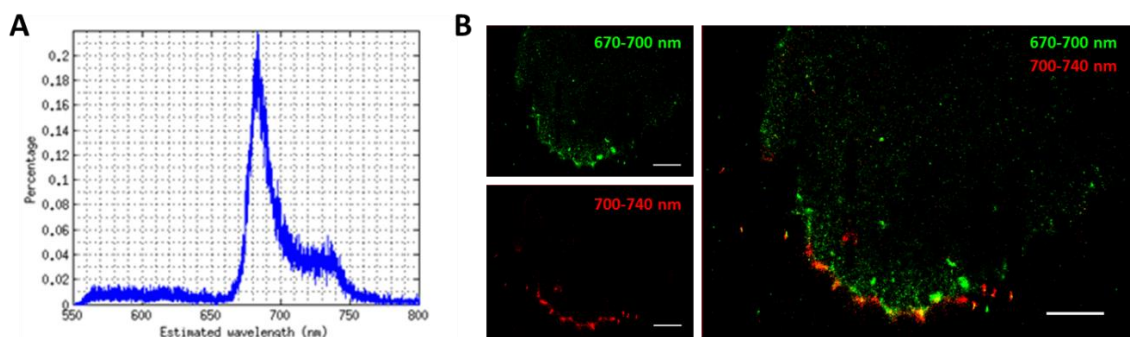
Figure 5.8 MSSRM imaging of membrane structures in U2OS cells using FM4-64.

(A) Histogram of the maximum emission wavelength of single FM4-64 molecules, acquired under relaxed TIRF mode on the MSSRM using 561 nm excitation; (B) Reconstructed MSSRM images of U2OS cells stained with FM4-64 using the spectral range of 670-700 nm (green) and

700-740 nm (red), shown as separate images on the left and combined on the right. Scale bars, 5 μm.

5.3.3 Spectral imaging of membrane structures in other cell types

With the initial success in imaging membrane structures in U2OS cells by using solvotochromic fluorophores on the MSSRM, I also explored the use of this approach to probing lipid structures in cell lines with more active metabolism. In particular, many cell lines exhibit increased biogenesis of lipid droplets that are enriched in neutral lipids such as TAG and CE; these types of lipids should give rise to different emission spectra of nile red than phospholipids. Among other cell lines, we have attempted to image lipids in A431 (human epidermoid carcinoma) cells.
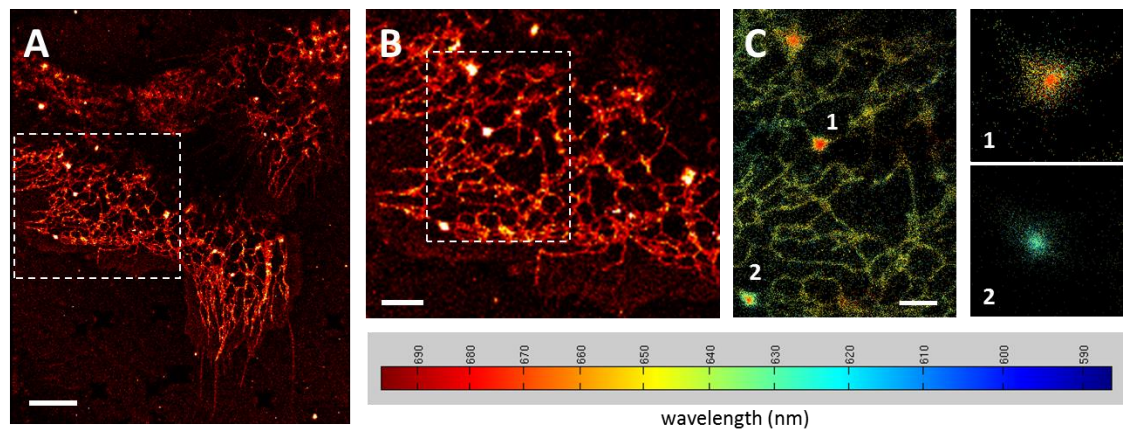
Figure 5.9 MSSRM imaging of membrane structures in A431 (human epidermoid) cells using nile red.

(A) Positional SRM image of an A431 cell stained with nile red, revealing extensive network of membrane structures resembling the ER, with punctate lipid structures attached to certain sites on the network; a zoom-in view of the boxed area is shown in (B); (C) Spectral SRM image of the boxed area in (B), with two lipid puncta (1 and 2) shown on the right in zoom-in views. Scale bars, 5 μm (A), 2 μm (B), and 1 μm (C).

A431 cells have many lipid droplets when examined under a transmission microscope, which are highly refractive structures with varying sizes (data not shown). Interestingly, when imaged with PAINT using nile red on the MSSRM, an extensive network of membranes that resemble the endoplasmic reticulum (ER) was clearly resolved in the resulting image (Fig. 5.9 A). Many bright, solid structures were attached to certain sites on the putative ER network, and these are likely lipid droplets that were thought to originate from the ER and grew into larger droplets via poorly understood mechanisms. Interestingly, these droplet-like structures did not all show the same nile red spectra; instead, some appeared to be more enriched in neutral lipids (cyan-blue color, for example 2 in Fig. 5.9 C) whereas others appeared to be a mixture of neutral and polar lipids (yellow color, for example 1 in Fig. 5.9 C), indicating that the structures may vary in chemical composition and that some of these may even be structures other than lipid droplets.

5.4 Conclusions and future work

Albeit preliminary, the data shown above clearly demonstrate the feasibility of mapping nanoscopic membrane heterogeneities by using environment-sensitive dyes with the MSSRM. In these experiments, the emission wavelength of the same fluorophore species can vary depending on the local environment, such that for each fluorescent molecule recorded and localized by the SRM, important properties such as the lipid polarity of its immediate surroundings can be simultaneously probed through the emission property of the fluorophore. As such, spatial heterogeneities of certain cellular properties could be reported with nanometer spatial resolution. While spectral imaging has been used to study membrane heterogeneities before, those studies were limited in spatial resolution and therefore inadequate in addressing membrane organizations at the nanometer scale.

My results also demonstrate that, different types of heterogeneities are reported by different fluorescent probes. For example, although nile red and FM4-64 are both lipophilic dyes, they cleared revealed different membrane structures in both STORM and PAINT. The differences

were already evident in the positional images and became more dramatic when comparing the spectral images. On one hand, this may confound the interpretation of MSSRM imaging results, because the affinity and spectral response of different dyes to the same membrane structure can differ significantly. On the other hand, this may also offer unique opportunities for more thorough characterization of biological membranes, by using a combination of multiple solvotochromic fluorophores, each reporting a somewhat different membrane property.

Although my work proved that it is possible to map the nanoscopic heterogeneity of cellular structures by using our approach, a remaining challenge is to how to attribute the measured spectral heterogeneity to specific membrane structures. I propose two potential approaches to achieving that goal. The first is to take advantage of the multicolor imaging capability of the MSSRM, such that fluorescent markers for specific membrane domains, such as caveolins for caveolae and GPI-anchored proteins for raft domains, can be used alongside the environment-sensitive probes in the same experiment such that spectra heterogeneities may be directly associated with known membrane domains. The second is use correlative MSSRM and electron microscopy, where the MSSRM enables chemically selective mapping and EM enables high resolution visualization of the cellular context – including the topology of many membrane-bound structure, the cytoskeleton, to name a few – such that a direct link between spectrally identified membrane domains and morphologically distinct membrane structures could be established. The two approaches are not exclusive and can be combined in certain scenarios. Together, these new nanoscopic investigations will likely yield exciting new insight into the chemical, structural, and functional heterogeneities of biological membranes.

Appendix: Observation of discrete diffraction pattern in an optically induced lattice

A.1 Electromagnetically induced transparency (EIT)

The interaction strength between a light field and atoms depends critically on the frequency of the light field. When the light frequency is on resonance to a particular atomic transition, the optical response of the medium is dramatically enhanced. However, this is usually accompanied by a strong absorption during the light propagation through such resonant medium. EIT, termed by Harris and co-workers [210], can be used to eliminate the linear absorption by quantum interference at the resonant frequency of an atomic transition. In addition, the steep normal linear dispersion and greatly enhanced nonlinearity are usually accompanied near the atomic resonance under EIT conditions [211].

A typical three-level lambda-type atomic system for EIT is shown in Fig. A.1. A weak probe field and a strong coupling field with frequencies ω_p and ω_c interact with the transitions |1>-|3> and |2>-|3>, respectively. The transition of |1>-|2> is dipole-forbidden. The combined effect of the probe and coupling fields is to induce the atoms into a superposition state between the states |1> and |2>, i.e. the dark state, which has no contribution from the excited state |3>. Therefore, due to destructive quantum interference between two possible routes, i.e., directly via the |1>-|3> pathway, or indirectly via the |1>-|3>-|2>-|3> pathway, there is no possibility of excitation to |3>, leading to a vanishing absorption for the probe field [211]. There are several ways to describe EIT process, such as density-matrix [212], dressed-state [213], probability amplitude [210], perturbation theory [214], Bloch vector [215], etc, and all these methods will lead to the same results except that the corresponding physical pictures give different insights in some aspects. In the following, we will choose the density-matrix method to model the EIT effect.
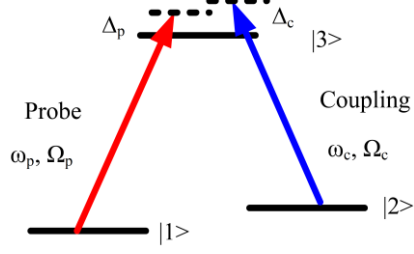
Figure A.1 A typical three-level lambda-type atomic system for EIT

In the interaction picture, the Hamiltonian of the three-level atom interacting with a coupling field and a probe field in a rotating frame can be written as [211]

$$H_{int} = -\frac{\hbar}{2}\begin{bmatrix} 0 & 0 & \Omega_p^* \\ 0 & 2(\Delta_p - \Delta_c) & \Omega_c^* \\ \Omega_p & \Omega_c & 2\Delta_p \end{bmatrix} \tag{A.1}$$

Here $\Omega_p = \mu_{13}E_p/\hbar$ and $\Omega_c = \mu_{23}E_c/\hbar$ are the Rabi frequencies of the probe and coupling fields, and $\Delta_p = \omega_p - \omega_{13}$ and $\Delta_c = \omega_c - \omega_{23}$ are the frequency detunings of the probe and coupling fields, respectively. Then, the equations for the density-matrix elements under dipole and rotating-wave approximations are given by [216,217]

$$\dot{\rho}_{22} = -\Gamma_{21}\rho_{22} + \Gamma_{32}\rho_{33} + \frac{i}{2}(\rho_{32}\Omega_c^* - \rho_{23}\Omega_c),$$

$$\dot{\rho}_{32} = -(\Gamma_{31}\rho_{33} + \Gamma_{32}\rho_{33}) + \frac{i}{2}(\rho_{23}\Omega_c - \rho_{32}\Omega_c^* + \rho_{13}\Omega_p - \rho_{31}\Omega_p^*),$$

$$\dot{\rho}_{21} = -\tilde{\gamma}_{21}\rho_{21} + \frac{i}{2}\rho_{31}\Omega_c^* - \frac{i}{2}\rho_{23}\Omega_p, \tag{A.2}$$

$$\dot{\rho}_{31} = -\tilde{\gamma}_{31}\rho_{31} + \frac{i}{2}\rho_{21}\Omega_c + \frac{i}{2}(\rho_{11} - \rho_{33})\Omega_p,$$

$$\dot{\rho}_{32} = -\tilde{\gamma}_{32}\rho_{32} + \frac{i}{2}(\rho_{22} - \rho_{33})\Omega_c + \frac{i}{2}\rho_{12}\Omega_p,$$

148

Here, we define $\tilde{\gamma}_{21} = \gamma_{21} - i(\Delta_p - \Delta_c)$, $\tilde{\gamma}_{31} = \gamma_{31} - i\Delta_p$, and $\tilde{\gamma}_{32} = \gamma_{32} - i\Delta_c$. Γ_{mn} is the

natural decay rate between level |n> and level |m>; and $\gamma_{mn} = \frac{1}{2}(\Gamma_n + \Gamma_m)$.

If we assume that the coupling field is much stronger than the probe field, i.e $\Omega_p \ll \Omega_c$,

and the population is all in the ground state, i.e. $\rho_{11} \approx 1$, $\rho_{22} \approx \rho_{33} \approx 0$, then by solving Eq.

(A.2) at the steady-state condition, we can get [216]

$$\rho_{31} = \frac{i\Omega_p/2}{\tilde{\gamma}_{31} + \frac{|\Omega_c|^2/4}{\tilde{\gamma}_{21}}}. \tag{A.3}$$

The susceptibility of the atomic medium is proportional to ρ_{31}. Figs A.2(a) and (b) show the

linear susceptibility of the atomic medium for the two-level system, i.e. $\Omega_c = 0$, and the three-

level EIT system, i.e. $\Omega_c \neq 0$, respectively. The black solid curves represent the real parts of the

susceptibilities, while the red dotted curves are the imaginary parts. From Fig. A.2(b), it is clear

that the absorption is significantly suppressed near the atomic resonance, leading to a

transparency window, and the slope of the dispersion near the resonance changes from negative

to positive for a three-level EIT system. Usually, the negative dispersion slope leads to fast light,

while the positive dispersion slope gives rise to slow light. However, in the two-level system, the

absorption is too strong to make the study of fast light difficult. In an EIT system, since the

absorption can be negligible, the effect of the slow light owing to the steep positive dispersion is

quite clear [216]. A lot of evidence of slow light has been experimentally observed , for example,

Hau et al. has demonstrated that the speed of light can be reduced down to 17 meters per second

in an ultracold EIT system [218]. Moreover, it was quickly realized that the light can be not only

slowed down, but also stored in an EIT medium, which is known as optical memory or quantum

memory [219,220].
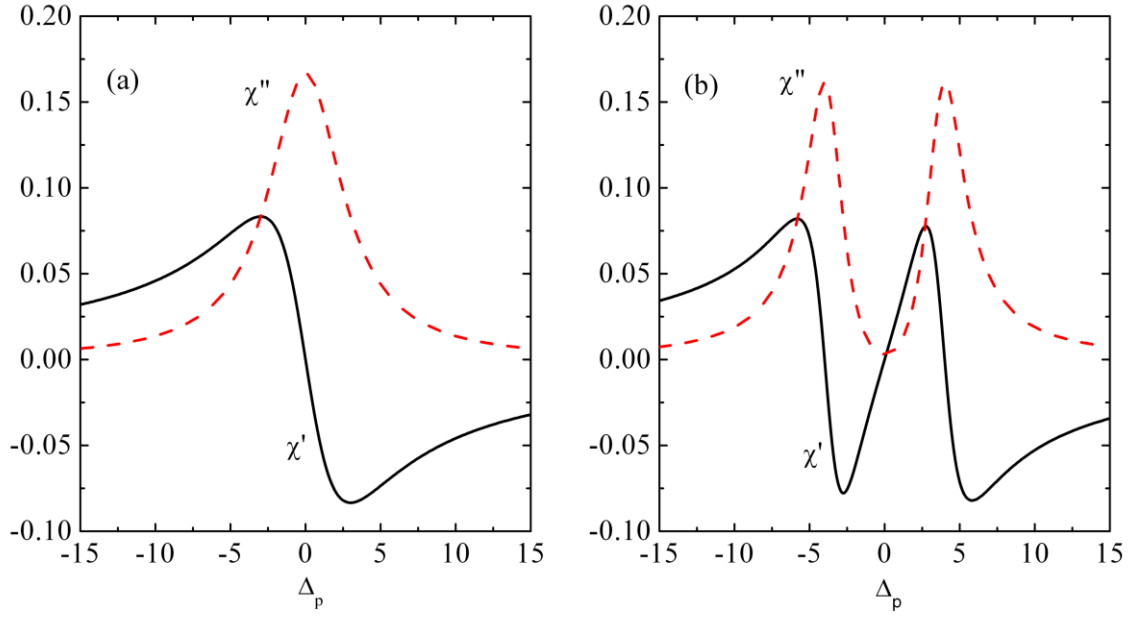
Figure A.2 Linear susceptibility of the atomic medium, where χ' and χ" represent the real and imaginary parts, respectively.

(a) Two-level system, i.e. $\Omega_c = 0$. (b) Three-level EIT system, i.e. $\Omega_c \neq 0$ [211].
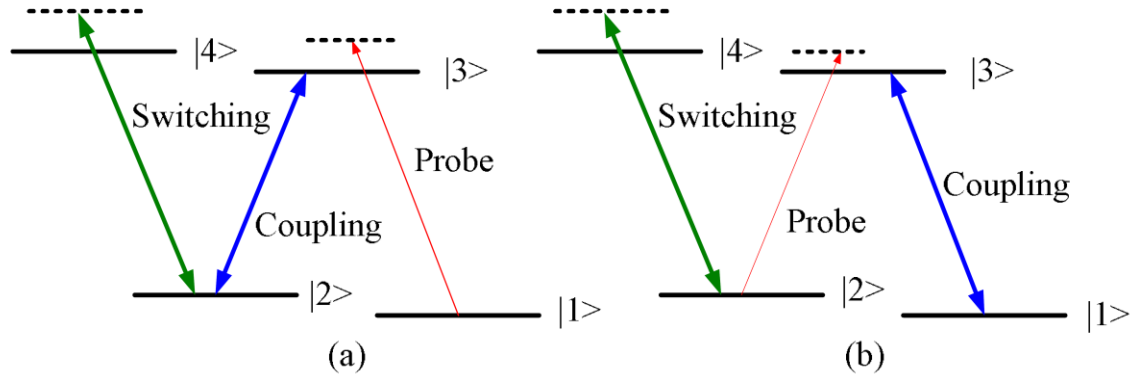
Fig. A.3: Two different types of four-level N-type systems.

Beside the three-level lambda-type atomic system, the ladder and V-type configurations can also be used to study EIT. Moreover, by adding more light fields to drive additional atomic transitions based on the principal lambda scheme, a variety of other interesting schemes will

emerge, such as N-type , M-type , inverted-Y-type , tripod-type , double-lambda-type [221,222], etc. Among those different configurations, the four-level N-type atomic system can generally be divided into two main schemes depending on the placement of the additional driving field. One is related to two-photon absorption, as shown in Fig. A.3(a). The other is with an active Raman gain , as shown in Fig. A.3(b), in which the weak probe field can be amplified.

A.2 Generation of parity-time symmetric potentials in an N-type atomic system

There are two basic axioms in quantum theory, one is that the energy levels must be real and the other is that the time evolution must be unitary. A simple condition is that when every element in the matrix of the Hamiltonian is real and symmetric, these two laws are guaranteed, however, this is not the most general condition. A more general condition is known as Hermiticity, which can be found in all the quantum mechanics text books. However, about 25 years ago, a new group of Hamiltonians have been discovered, which are not Hermitian, but they can also satisfy these two laws. This new kind of Hamiltonian is called PT symmetric. Non-Hermitian

PT-symmetric Hamiltonians have attracted considerable attention since they were first proposed by Bender and Boettcher in 1998. Under certain conditions, such PT-symmetric Hamiltonians display entirely real spectra-a property often thought to belong exclusively to Hermitian systems. Quite recently, this counter-intuitive behavior has been theoretically and experimentally demonstrated in a number of optical settings that judiciously engage both gain and loss processes. This was accomplished by exploiting the mathematical isomorphism existed between the quantum Schrödinger and the paraxial wave equations.

Along different lines, in multilevel atomic media, both the linear and nonlinear optical properties of EIT phenomena have been intensively investigated in the past two decades. A host of intriguing spatial phenomena have been observed in EIT-related systems, including

electromagnetically induced focusing and waveguiding, as well as self-imaging, grating behavior and soliton propagations.

In this section, I will present a theoretical proposal to show that PT-symmetric conditions can be achieved in an atomic assemble involving EIT-related four-level atoms by spatially engineering the complex refractive indices of the coherently-prepared atomic medium. In optical regime, PT symmetric condition demands that n(x) = n*(-x), i.e. the real and imaginary parts of the refractive index profiles must be symmetric and anti-symmetric functions of the transverse coordinate x, respectively. To illustrate the basic properties regarding PT symmetry, let's see a simple coupled waveguides model in the following.
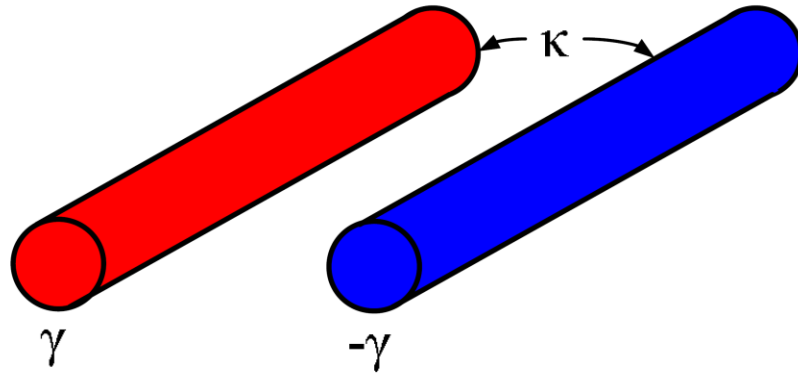
Figure A.4 Coupled waveguides model.

The coupled waveguides model is shown in Fig. A.4. The two waveguides are coupled with a coefficient of κ, and one waveguide has absorption γ and the other has gain $-\gamma$. These two waveguides form a basic PT symmetric system. The coupled mode equations for the two waveguides can be obtained as

$$
\begin{cases}
i\frac{d\Psi_1}{dz} + \kappa\Psi_2 - i\gamma\Psi_1 = 0 \\
i\frac{d\Psi_2}{dz} + \kappa\Psi_1 + i\gamma\Psi_2 = 0
\end{cases}
\tag{A.4}
$$

With z as the propagating direction and Ψ_i (i=1,2) as the waveguide modes. Then the Hamiltonian for the above system can be written as

$$H = \begin{pmatrix} i\gamma & -\kappa \\ -\kappa & -i\gamma \end{pmatrix}.$$ (A.5)

And the eigenvalues are given as

$$E_n = \pm\sqrt{\kappa^2 - \gamma^2}$$ (A.6)
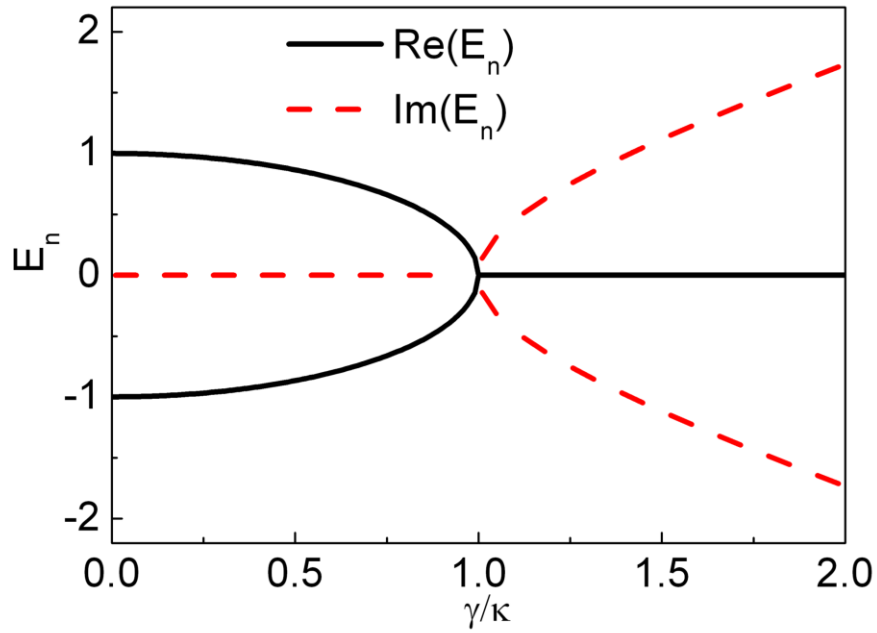
Figure A.5 Eigenvalues for the coupled waveguides system [45].

Equation (A.6) is plotted in Fig. A.5. From Eq. (A.6) or Fig. A.5, one can find that the eigenvalues are real if $\kappa \gg \gamma$, and the eigenvalues become complex if $\kappa \ll \gamma$. Therefore, $\gamma/\kappa = 1$, is called the PT-symmetric threshold and above the threshold case is called PT symmetry breaking. In more sophisticated systems, PT-symmetric threshold is determined by many parameters, and gain/loss ratio is one of them.

The realization of PT symmetry in atomic media offers several advantages over solid-state systems. For example, optical structures like coupled waveguide systems can be easily reconfigured, tuned, and effectively controlled in an atomic medium through various external parameters, i.e., frequency detunings and Rabi frequencies of the coupling and pump fields. In addition, by introducing or interfering coupling beams or by using spatial light modulators, PT-symmetric optical lattices can be readily established in the spatial domain. Recently, several PT-symmetric optical configurations in solid-state systems have been suggested as means to realize nonreciprocal energy transport, perfect laser absorber, laser amplifiers, etc. To date, all experimental studies carried out in PT-symmetric optics have relied on gain/loss arrangements using solid-state materials . Therefore, the implementation of PT-symmetric potentials in atomic media will pave the way for new avenues in exploring such interesting phenomena.

A four-level N-type atomic system is considered, as shown in Fig. A.6(a). The signal, coupling, and pump fields drive the atomic transitions |1>-|3>, |2>-|3>, and |1>-|4>, respectively. The four-level N-type systems with active Raman gain are distinct from the other type of N-type systems that are based on two-photon absorption. Throughout this work, and without any loss of generality, we focus our attention on the Rubidium N-type atomic system with active Raman gain. By choosing appropriate parameters, the two coupling (blue, ii) and two pump (green, iii) beams, which propagate in the z direction, form a coupled waveguide structure, with one providing gain while the other having absorption. The signal (red, i) beam propagates in the same direction along with the coupling and pump beams, as shown in Fig. A.6(b).
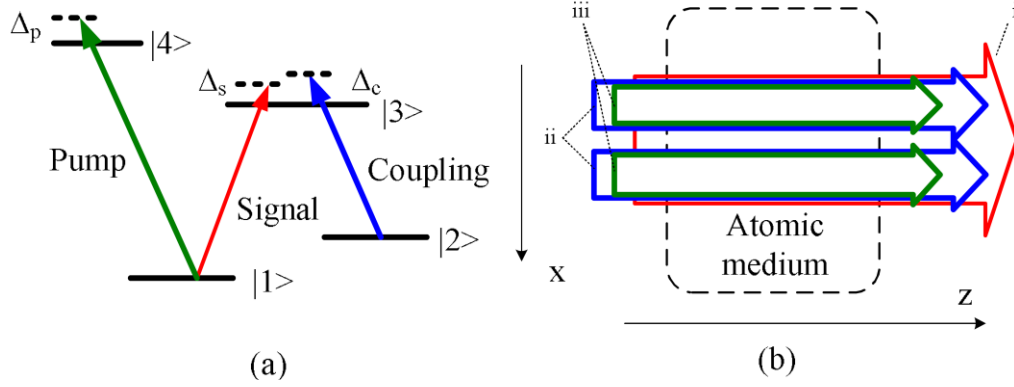
Figure A.6 Principle of Experimental design.

(a) The relevant four-level N-type atomic system. (b) The schematic diagram with signal (red, i), coupling (blue, ii), and pump (green, iii) fields. X and Z represent the transverse and longitudinal directions of propagation, respectively.

Under the rotating-wave approximation, the density-matrix equations for the four-level N-type atomic system are given by

$$\dot{\rho}_{22} = \Gamma_{42}\rho_{44} + \Gamma_{32}\rho_{33} - \Gamma_{21}\rho_{22} + \frac{i}{2}(\rho_{32}\Omega_c^* - \rho_{23}\Omega_c),$$

$$\dot{\rho}_{33} = \Gamma_{43}\rho_{44} - \Gamma_{32}\rho_{33} - \Gamma_{31}\rho_{33} + \frac{i}{2}(\rho_{23}\Omega_c - \rho_{32}\Omega_c^* + \rho_{13}\Omega_s - \rho_{31}\Omega_s^*),$$

$$\dot{\rho}_{44} = -(\Gamma_{43} + \Gamma_{42} + \Gamma_{41})\rho_{44} + \frac{i}{2}(\rho_{14}\Omega_p - \rho_{41}\Omega_p^*),$$

$$\dot{\rho}_{21} = -\tilde{\gamma}_{21}\rho_{21} + \frac{i}{2}\rho_{31}\Omega_c^* - \frac{i}{2}\rho_{24}\Omega_p - \frac{i}{2}\rho_{23}\Omega_s,$$

$$\dot{\rho}_{31} = -\tilde{\gamma}_{31}\rho_{31} + \frac{i}{2}\rho_{21}\Omega_c - \frac{i}{2}\rho_{34}\Omega_p + \frac{i}{2}(\rho_{11} - \rho_{33})\Omega_s, \qquad\qquad\text{(A.7)}$$

$$\dot{\rho}_{41} = -\tilde{\gamma}_{41}\rho_{41} - \frac{i}{2}\rho_{43}\Omega_s + \frac{i}{2}(\rho_{11} - \rho_{44})\Omega_p,$$

$$\dot{\rho}_{32} = -\tilde{\gamma}_{32}\rho_{32} + \frac{i}{2}(\rho_{22} - \rho_{33})\Omega_c + \frac{i}{2}\rho_{12}\Omega_s,$$

$$\dot{\rho}_{42} = -\tilde{\gamma}_{42}\rho_{42} - \frac{i}{2}\rho_{43}\Omega_c + \frac{i}{2}\rho_{12}\Omega_p,$$

$$\dot{\rho}_{43} = -\tilde{\gamma}_{43}\rho_{43} + \frac{i}{2}\rho_{13}\Omega_p - \frac{i}{2}\rho_{42}\Omega_c^* - \frac{i}{2}\rho_{41}\Omega_s^*,$$

Where $\Omega_s = \mu_{13}E_s/\hbar$, $\Omega_c = \mu_{23}E_c/\hbar$, and $\Omega_p = \mu_{14}E_p/\hbar$ are the Rabi frequencies of the signal, coupling, and pump fields respectively. For simplicity we define $\tilde{\gamma}_{21} = \gamma_{21} - i(\Delta_s - \Delta_c)$, $\tilde{\gamma}_{31} = \gamma_{31} - i\Delta_s$, $\tilde{\gamma}_{41} = \gamma_{41} - i\Delta_p$, $\tilde{\gamma}_{32} = \gamma_{32} - i\Delta_c$, $\tilde{\gamma}_{42} = \gamma_{42} - i(\Delta_c + \Delta_p - \Delta_s)$, and $\tilde{\gamma}_{43} = \gamma_{43} - i(\Delta_p - \Delta_s)$. Γ_{mn} is the natural decay rate between level |n> and level |m>; and $\gamma_{mn} = (\Gamma_n + \Gamma_m)/2$. Here, $\Delta_s = \omega_s - \omega_{31}$, $\Delta_c = \omega_c - \omega_{32}$, and $\Delta_p = \omega_p - \omega_{41}$ are the frequency detunings for the signal, coupling and pump fields, respectively. The susceptibility of atomic medium can be obtained through the expression $\chi = \frac{2N\mu_{13}}{\varepsilon_0 E_s}\rho_{31}$. Given that $n = \sqrt{1+\chi} \approx 1 + \chi/2$, $\chi = \chi' + i\chi''$, and $n = n_0 + n_R + in_I$, the real and imaginary pars of the refractive index can be written as $n_R \approx \frac{1}{2}\chi' = \frac{N\mu_{13}}{\varepsilon_0 E_s}Re(\rho_{31})$ and $n_I \approx \frac{1}{2}\chi'' = \frac{N\mu_{13}}{\varepsilon_0 E_s}Im(\rho_{31})$. Here, $n_0 = 1$ is the background index of the atomic medium.

Usually, the general result for the linear susceptibility of such four-level N-type atomic system with active Raman gain cannot be obtain in a compact form. In order to obtain an analytical solution, we can assume that all the atoms are at level |2>, i.e., $\rho_{22} \approx 1$, $\rho_{11} \approx 0$, $\rho_{33} \approx 0$, and $\rho_{44} \approx 0$. Since the signal field is relatively weak compared with the coupling and pump fields ($\Omega_s \ll \Omega_c, \Omega_p$), by solving Eq. (A.7) under the steady-state limit, the density-matrix element ρ_{13} can be obtained as

$$\rho_{31} = \frac{i\Omega_s\Omega_c^2(\Omega_c^2 - \Omega_p^2 + 4\tilde{\gamma}_{42}^*\tilde{\gamma}_{43}^*)}{2\tilde{\gamma}_{32}^*[(\Omega_c^2 - \Omega_p^2)^2 + 4(\tilde{\gamma}_{21}\tilde{\gamma}_{31} + \tilde{\gamma}_{42}^*\tilde{\gamma}_{43}^*)\Omega_c^2 + 4(\tilde{\gamma}_{31}\tilde{\gamma}_{43}^* + \tilde{\gamma}_{21}\tilde{\gamma}_{42}^*)\Omega_p^2 + 16\tilde{\gamma}_{21}\tilde{\gamma}_{31}\tilde{\gamma}_{42}^*\tilde{\gamma}_{43}^*]}. \tag{A.8}$$

Such assumption is valid when coupling frequency detuning Δ_c is large. However, due to the near resonant cases are considered in this section, we will use numerical method in the following calculations.

We begin by considering the realization of a dual channel PT-symmetric potential (two waveguides as shown in Fig. A.6(b)) that could allow exchange of optical energy between the

two channels. This is possible by employing two different coupling fields side by side-each having an identical Gaussian intensity profile while the susceptibility of the signal field varies in the x direction as a function of the coupling field intensity. Since the coupling fields are from two independent lasers and the overlapped region between them is relatively small, the phase effect between them is not considered here. In this case the total spatial intensity distribution of the coupling beams has the form of

$$I_c(x) = A(e^{\frac{-(x-a)^2}{2\sigma^2}} + e^{\frac{-(x+a)^2}{2\sigma^2}}), \tag{A.9}$$

where A is a constant, 2a is the separation between the centers of the two potential channels, and $2\sqrt{2ln2}\sigma$ is the full-width-at-half-maximum (FWHM) of the beam width. Even though the coupling intensity spatial profiles for these two channels are identical, by choosing different coupling frequency detunings (Δ_c), one can actually introduce gain in one waveguide and absorption in the other one. The advantage offered by this scheme is that the refractive index now spatially varies only with the coupling intensity, since all the other parameters are fixed in each waveguide.

In this arrangement, perhaps the most challenging task is to find the proper coupling frequency detunings with proper choice of other parameters for a simultaneous gain and absorption in these two channels, respectively. To do so, we first have to identify the relation between the susceptibility and the coupling frequency detuning. By solving Eq. (A.7) numerically, one can obtain the real (dispersion) and imaginary (gain/absorption) parts of the susceptibility versus the coupling detuning for various coupling intensities as shown in Figs. A.7(a) and (b), respectively. The parameters used in this example are: $\Delta_s = \Delta_p = 0$, $\Omega_s/2\pi = 0.1$ MHz, $\Omega_p/2\pi = 6$ MHz, $\Gamma_{31}/2\pi = \Gamma_{32}/2\pi = \Gamma_{41}/2\pi = \Gamma_{42}/2\pi = 3$ MHz, $\Gamma_{21} = \Gamma_{43} = 0$, and $\Omega_c/2\pi = 2$, 1, and 0.5 MHz for black (solid), red (dashed), and blue (dotted) curves, respectively
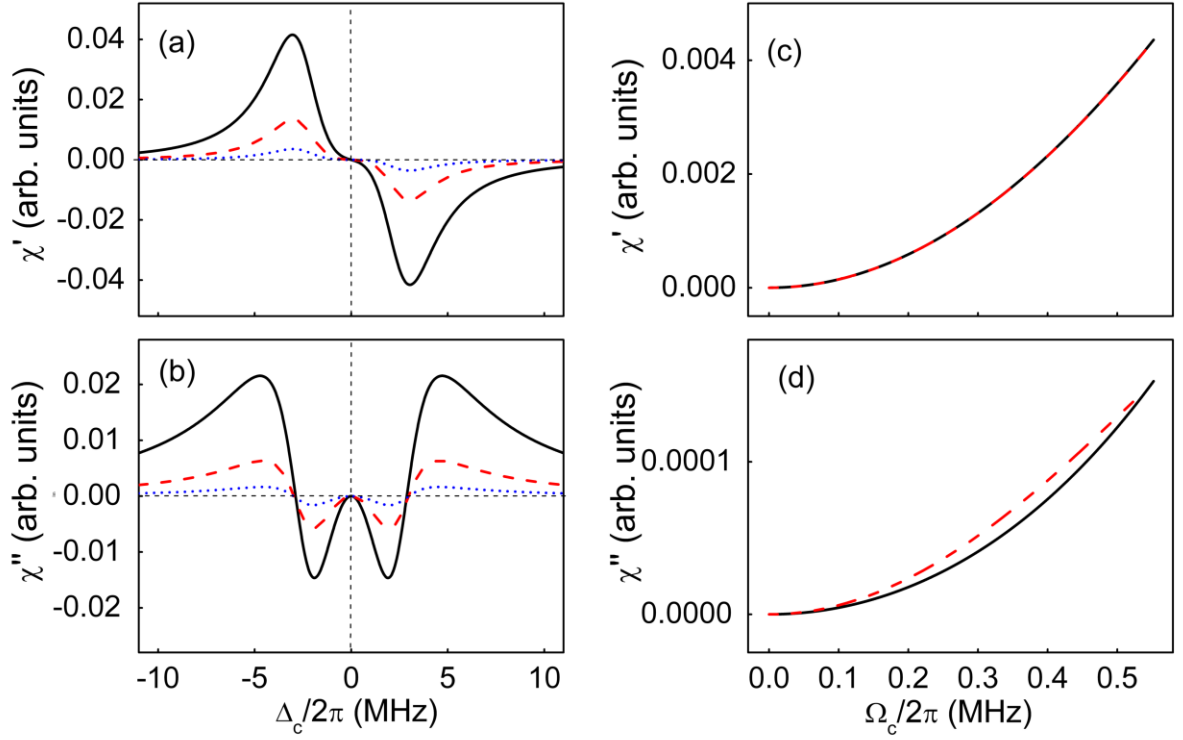
Figure A.7 Effects of frequency modulation.

(a) The real (dispersion) and (b) imaginary (gain/absorption) parts of the susceptibility versus the coupling frequency detuning. $\Omega_c/2\pi$= 2, 1, and 0.5 MHz for black (solid), red (dashed), and blue (dotted) curves, respectively. The (c) real and (d) imaginary parts of the susceptibility versus the coupling Rabi frequency. The black (solid) / red (dashed) curves represent χ' and χ'' for the gain/absorption waveguides. The chosen parameters are $\Delta_c/2\pi$=-2.939 and -3.045 MHz for the gain and absorption waveguides, respectively.

To achieve waveguiding, the signal field is focused at the center of each waveguiding channel that is formed by the joint actions of the coupling and pump beams, i.e., the maximum coupling intensity regions. Therefore, the real part of the susceptibility needs to get larger with increasing coupling intensity. For this reason, the coupling detunings should be negative. Also, we notice that the imaginary part of the susceptibility is close to zero when the coupling detuning

is ~ -2.992 MHz, and in the vicinity of this zero point, absorption is induced on the left side, while gain on the right. Such property, commonly referred to as refractive index enhancement with vanishing absorption, has been widely studied in both near-resonant and far-off resonant atomic systems.

A.3 Observation of discrete diffraction pattern in an optically induced lattice

Optical waveguide lattices have been a subject of intensive studies recently. Such periodic arrays of evanescently coupled optical waveguides exhibit a range of interesting properties which are otherwise unattainable in the bulk. One of the best known examples is the discrete diffraction of light in optical waveguide arrays. Such photonic lattices have been used to directly observe and study optical analogs of many fundamental quantum mechanical effects like Bloch oscillation, Zener tunneling, quantum random walks, and Anderson localization to mention a few. In addition, optically induced photonic waveguide lattices have been also utilized to observe one and two dimensional discrete spatial solitons in photorefractive crystals.

On the other hand, it has been known that optical wave-guiding effects can be achieved in coherently prepared atomic media with electromagnetically-induced transparency (EIT). In general, EIT makes an absorptive medium transparent to a weak probe field. Such transparency results from the destructive quantum interference induced by a strong coupling field. This in turn leads to an enhanced nonlinear susceptibility in the spectral region of the induced transparency and is associated with a steep dispersion. In multi-level atomic systems, many intriguing spatial phenomena have been observed in EIT-related systems. These include electromagnetically induced focusing, self-imaging, electromagnetically induced gratings, and soliton formation. All these interesting observations result from the spatial variation of the refractive index in an EIT or EIT-related atomic medium. In such coherent atomic systems, one can simply control different experimental parameters to get an optimal configuration for desired applications.

159

We utilize the EIT effect to spatially modify the refractive index of the Doppler-broadened rubidium atoms. In this manner, we establish an optically induced lattice in the transverse direction, so that discrete diffraction patterns can be formed when a weak probe beam propagates through the induced lattice. We have also observed that the diffraction pattern can be controlled through the atomic parameters such as two-photon detuning and temperature, as well as orientations of the coupling and probe beams. A periodic arrangement of such optical waveguides has not been explored in atomic media to the best of our knowledge.

A.3.1 Experimental setup and theory

Figure A.8 Experimental setup.

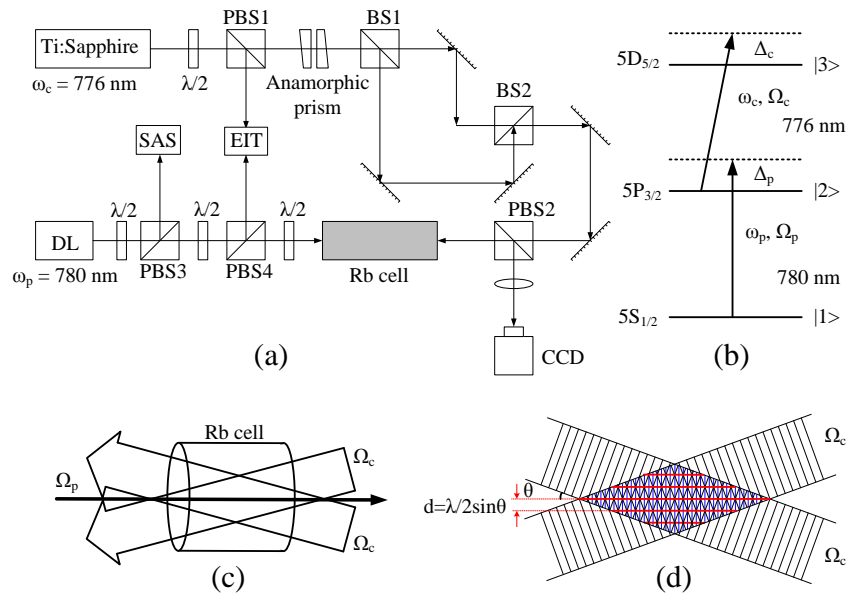(a) Experimental setup: PBS, polarization beam splitter; SAS, saturation absorption spectroscopy; EIT, monitoring the two-photon electromagnetically induced transparency condition; $\lambda/2$, half-wave plate; (b) The relevant three-level rubidium atomic system; (c) The schematic for generating an optically induced lattice in a hot rubidium vapor cell. (d) Snapshot of the optical lattice in (c)

The experimental setup and the associated atomic energy levels of 87Rb are shown in Figs. A.8 (a) and (b). The coupling beams are obtained from a Ti:Sapphire ring laser working at 776 nm driving the transition between levels |2> and |3> (5P3/2→5D5/2). The probe beam on the other hand, comes from a single-mode tunable diode laser (Toptica DL 100) with stabilized current and temperature, operating at the wavelengths of 780 nm and probes the lower transition between levels |1> and |2> (5S1/2→5P3/2). The coupling and probe lasers are both continuous waves. A polarization beam splitter (PBS1) is used to split the initial coupling beam into two beams. The reflected (vertically-polarized) beam is used as the coupling beam for setting an EIT reference signal. The transmitted beam (horizontally-polarized and nearly circular in shape), is transformed into an elliptical shape by using an anamorphic prism pair. After passing through a beam splitter (BS1), the coupling beam splits into two beams with the same intensities and the same spatial shapes. These two elliptically-shaped coupling beams then recombine at BS2 and propagate toward a 7.5 cm long Rb cell while maintaining an angle of $2\theta \approx 0.4^\circ$ with respect to each other, as shown in Figs. A.8(c) and (d). As a result of interference between these two coupling beams a standing wave appears in the transverse direction whose period is determined to be $d = \lambda/(2\sin\theta) \approx 112$ μm. It is worth mentioning that a standing wave in the propagating direction with a period of $\lambda/(2\cos\theta)$ is created simultaneously, however, in this work, we only consider the lattice in the transverse direction. The Gaussian-shaped probe beam counter-propagates with respect to the two strong coupling beams and overlaps well with the optical lattice induced by these two coupling beams inside the atomic vapor cell. The input probe beam size before cell is ~ 100 μm. The output of the probe beam is imaged onto a CCD camera with a lens to ensure that the CCD takes the images of the output plane of the cell. The frequency detunings of the probe and coupling fields are $\Delta_p = \omega_p - \omega_{12}$ and $\Delta_c = \omega_c - \omega_{23}$, respectively.

The key ingredient of this experiment is to make a good optically induced lattice so that the probe light can be confined at the discrete sites in the weakly guiding waveguides of the lattice, which means that the contrast of the real part of the refractive index, i.e. the difference of

161

the refractive index at nodes and antinodes of the optically induced lattice, should be large

enough to guide the light, while in the meantime the absorption contrast (the imaginary part of the

refractive index) should be as small as possible to reduce the effect of the absorption on the

output images, and this is the reason why we choose the single photon detuning, i.e. the probe and

coupling detunings, to be ~ 400 MHz. By utilizing the density-matrix method, we can obtain the

spatially modified refractive index as a function of the transverse coordinate x, which is due to

the periodical modulation of the coupling beam intensity from the interference, as shown in Fig.

A.9. Such modulated index profile clearly indicates a one-dimensional optical lattice.
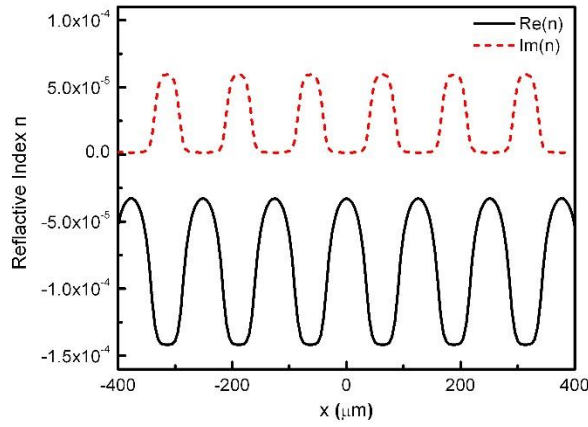
Figure A.9 Simulation result.

Numerically calculated plots of the spatially modified real (solid line) and imaginary (dashed line)

parts of the refractive index modulation, respectively. Here, Δ_c = -400 MHz, Δ_p = 390 MHz, and

$\Omega_c = 200\cos2(x/40)$.
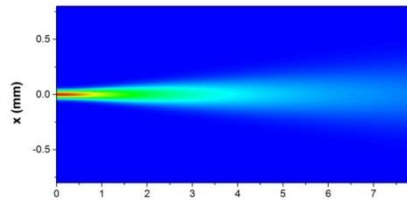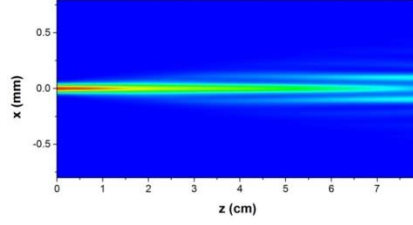
Figure A.10 Theoretical simulations of the probe beam propagation.

(a) Normal diffraction of a Gaussian beam without the coupling beam; (b) Evolved discrete

diffraction of the weak Gaussian beam in an optical lattice.

The diffraction pattern of a weak probe Gaussian beam propagating in such an optical

lattice can be numerically simulated by using beam propagation method, as presented in Fig.

A.10. The parameters used in this simulation are as follows: the lattice space is ~ 126 μm, the

complex refractive index is $n = n_0 + (10^{-5} + 0.5 \times 10^{-5} i) \cos(x/x_0)$. $n = n_0 + \left(10^{-5} + 0.5 \times 10^{-5} i\right) \cos(x/x_0)$ Here $n_0 = 1$ is the background index of the atomic medium and x0 = 20 μm is a

scale factor. In the absence of the coupling beams, the output of the probe field through the Rb

cell still maintains a Gaussian shape with normal diffraction, as shown in Fig. A.10(a). However,

when the optically induced lattice is introduced (in the presence of the interfering coupling

beams), the discrete diffraction occurs as depicted in Fig. A.10(b), which has a dramatically

changed output profile as compared to that of Fig. A.10(a).

A.3.2 Experimental results and discussion
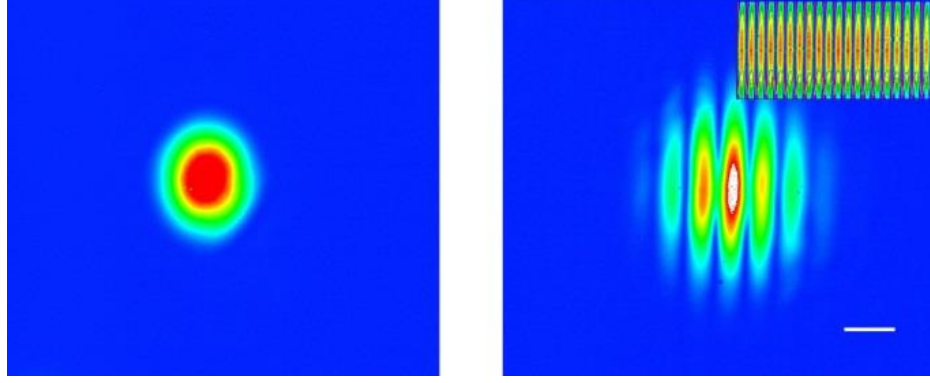
Figure A.11 Experimental results of the probe beam's output intensity images.
(a) Output of a Gaussian probe beam propagating through the cell with the coupling beams blocked. (b) Output of a Gaussian probe beam after propagating through an optical lattice.

The experimentally measured output intensities of the probe beam are displayed in Fig. 4 for the two cases, i.e. without and with the optically induced lattice. As shown in Fig. A.11(a), in the absence of the coupling beams, the output of the probe beam still remains Gaussian, since only normal diffraction occurs when the probe light passes through the cell, whereas, as shown in Fig. A.11 (b), when the coupling beams are present, the output of the probe beam appears stripe pattern, this is because discrete diffraction happens when the probe beam passes through the optical lattice, which has been predicted in Fig. A.10(b). The distance between the adjacent bright channels in Fig. A.11(b) is the same as the separation of the waveguides in the optical lattice. The power of each coupling beam and the probe beam are 17.0 mW and 1.5 mW, respectively.
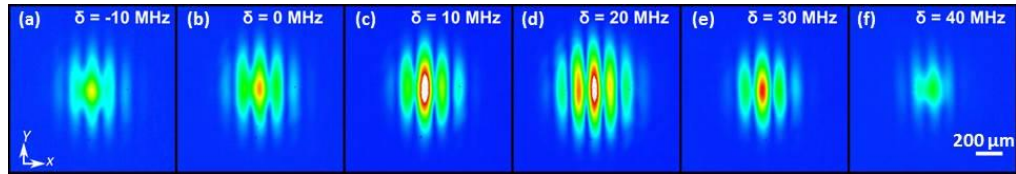
Figure A.12 Experimentally observed diffraction patterns.

Experimentally observed diffraction patterns of the probe beam propagating through the optical lattice, as the two-photon detuning δ is changed. (a) δ = -10, (b) δ = 0, (c) δ = 10, (d) δ = 20, (e) δ = 30, and (f) δ = 40 MHz, respectively.

The diffraction pattern is sensitive to several experimental parameters. The first one is lattice constant, which is determined by the angle between the two coupling beams. After the frequency detunings of both the coupling and probe fields are set, we need to carefully adjust the lattice spacing to match the optimal refractive index in order to enhance the contrast of the diffraction pattern. Another parameter is the temperature of the vapor cell. The refractive index obeys $n \sim \frac{N\mu_{12}}{\varepsilon_0 E_p}\mathrm{Re}(\rho_{21})$ $n \sim \frac{N\mu_{12}}{\varepsilon_0 E_p}\mathrm{Re}(\rho_{21})$, where μ_{12} μ_{12} represents the dipole moment between state |2> and |1>, and N is the atomic density. Increasing the temperature of the Rb cell increases the density of Rb atoms, which gives a larger refractive index contrast. In our experiment, the temperature is kept at about 100 °C, and the refractive index contrast is estimated to be 10^{-5}. The third parameter is the relative position between the incident probe beam and the induced optical lattice. The input probe beam can be either centered between two maxima or on top of one maximum. Changing the relative input position in the transverse direction will significantly alter the diffraction pattern. In our experiment, the probe beam is centered on one maximum of the induced lattice, i.e. the center of one waveguide. The output image has the brightest strip in the center, and the intensities of strips on both sides will gradually decrease but still be symmetric. The fourth parameter is the two-photon frequency detuning $\delta = \Delta_c + \Delta_p$. The diffraction pattern is very sensitively dependent on δ. We can only find discrete diffraction patterns within a frequency detuning window of ~ 60 MHz near the two-photon (EIT) resonance, as shown in Fig. A.12. When δ is about 20 MHz, the most clear and brightest diffraction pattern is obtained as shown in Fig. A.12(d). As δ shifts away from the optimal point of 20 MHz, the contrast of diffraction

pattern for the observable discrete spots drops significantly. In Figs. A.11 and A.12, the white areas present the highest intensity and the blue areas have the lowest intensity. It is worth mentioning that the diffraction patterns in Figs. A.11 and A.12 are the images on the output plane of the cell, therefore, they are quite different from the Fraunhofer diffraction from electromagnetically induced grating. Also, in principle, it is possible to observe the discrete diffraction pattern as predicted in Fig. A.10 (b) from the side view of the cell.

In conclusion, we have experimentally observed discrete diffraction patterns in an optically induced lattice created by interferring two strong coupling beams in a three-level rubidium atomic system inside a vapor cell. The change of the diffraction pattern under different two-photon frequency detunings has been experimentally invesitigated. In addition, theoretical simulation has been performed to better understand such discrete diffraction phenomenon in optical lattices. Since optically induced lattices in coherently prepared atomic media offer a wide range of controlling parameters, the demonstrated results can provide a versatile platform and a novel way in experimentally studying optical lattices. Given that gain/loss and nonlinearity can also be incorporated in such systems, EIT-induced optical lattices can also be utilized to investigate optical solitons as well as PT-symmetry related phenomena.

References

1   Moerner, W. E. Single-Molecule Spectroscopy, Imaging, and Photocontrol: Foundations for Super-Resolution Microscopy (Nobel Lecture). *Angew Chem Int Ed Engl* **54**, 8067-8093, doi:10.1002/anie.201501949 (2015).

2   Sheng, J., Wang, J., Miri, M.-A., Christodoulides, D. N. & Xiao, M. Observation of discrete diffraction patterns in an optically induced lattice. *Optics express* **23**, 19777-19782 (2015).

3   Young, T. The Bakerian lecture: Experiments and calculations relative to physical optics. *Philosophical transactions of the Royal Society of London* **94**, 1-16 (1804).

4   Born, M. & Wolf, E. *Principles of optics: electromagnetic theory of propagation, interference and diffraction of light*. (Elsevier, 1980).

5   Vainshtein, L. A. Electromagnetic waves. *Moscow Izdatel Radio Sviaz* (1988).

6   Pais, A. Einstein and the quantum theory. *Reviews of Modern Physics* **51**, 863 (1979).

7   Bohr, N. in *Niels Bohr, 1913-2013*   13-33 (Springer, 2016).

8   Van de Hulst, H. C. & Twersky, V. Light scattering by small particles. *Physics Today* **10**, 28-30 (1957).

9   McCartney, E. J. Optics of the atmosphere: scattering by molecules and particles. *New York, John Wiley and Sons, Inc., 1976. 421 p.* (1976).

10   Guilbault, G. G. *Practical fluorescence*. Vol. 3 (CRC Press, 1990).

11   Paschotta, R. Encyclopedia of laser physics and technology. (2008).

12   Shen, Y.-R. The principles of nonlinear optics. *New York, Wiley-Interscience, 1984, 575 p.* **1** (1984).

13   Prasad, P. N. & Williams, D. J. *Introduction to nonlinear optical effects in molecules and polymers*. (Wiley New York etc., 1991).

14   Nöckel, J. U. & Stone, A. D. Ray and wave chaos in asymmetric resonant optical cavities. *arXiv preprint chao-dyn/9806017* (1998).

15   Ritter, S. *et al.* An elementary quantum network of single atoms in optical cavities. *Nature* **484**, 195-200 (2012).

16   Cremer, C. & Cremer, T. Considerations on a laser-scanning-microscope with high resolution and depth of field. *Microscopica acta*, 31-44 (1974).

17   Sheppard, C. & Wilson, T. The theory of the direct-view confocal microscope. *Journal of microscopy* **124**, 107-117 (1981).

18   Agard, D. A., Hiraoka, Y., Shaw, P. & Sedat, J. W. Fluorescence microscopy in three dimensions. *Methods in cell biology* **30**, 353-377 (1989).

19   Brakenhoff, G., Van der Voort, H., Van Spronsen, E., Linnemans, W. & Nanninga, N. Three-dimensional chromatin distribution in neuroblastoma nuclei shown by confocal scanning laser microscopy. (1985).

20   Hell, S. W. & Wichmann, J. Breaking the diffraction resolution limit by stimulated emission: stimulated-emission-depletion fluorescence microscopy. *Optics letters* **19**, 780-782 (1994).

21   Hell, S. W. & Kroug, M. Ground-state-depletion fluorscence microscopy: A concept for breaking the diffraction resolution limit. *Applied Physics B: Lasers and Optics* **60**, 495-497 (1995).

22   Hell, S. W. Toward fluorescence nanoscopy. *Nature biotechnology* **21**, 1347-1355 (2003).

23   Hell, S. W. Far-field optical nanoscopy. *science* **316**, 1153-1158 (2007).

24   Mattheyses, A. L., Simon, S. M. & Rappoport, J. Z. Imaging with total internal reflection fluorescence microscopy for the cell biologist. *J Cell Sci* **123**, 3621-3628 (2010).

25   Prior, I. A., Muncke, C., Parton, R. G. & Hancock, J. F. Direct visualization of Ras proteins in spatially distinct cell surface microdomains. *J Cell Biol* **160**, 165-170, doi:10.1083/jcb.200209091 (2003).

26   Yang, S. *et al.* Mapping ErbB receptors on breast cancer cell membranes during signal transduction. *J Cell Sci* **120**, 2763-2773, doi:10.1242/jcs.007658 (2007).

27   Nan, X. *et al.* Ras-GTP dimers activate the Mitogen-Activated Protein Kinase (MAPK) pathway. *Proc Natl Acad Sci U S A* **112**, 7996-8001, doi:10.1073/pnas.1509123112 (2015).

28   Cai, L., Friedman, N. & Xie, X. S. Stochastic protein expression in individual cells at the single molecule level. *Nature* **440**, 358-362 (2006).

29   Kneipp, K. *et al.* Single molecule detection using surface-enhanced Raman scattering (SERS). *Physical review letters* **78**, 1667 (1997).

30   Yildiz, A. & Selvin, P. R. Fluorescence imaging with one nanometer accuracy: application to molecular motors. *Accounts of chemical research* **38**, 574-582 (2005).

31   Abbe, E. Beiträge zur Theorie des Mikroskops und der mikroskopischen Wahrnehmung. *Archiv für mikroskopische Anatomie* **9**, 413-418 (1873).

32   Gray, N. Knowing the limit. *Nat. Milestones Light Microscopy* (2009).

33   Rayleigh, L. XV. On the theory of optical images, with special reference to the microscope. *The London, Edinburgh, and Dublin Philosophical Magazine and Journal of Science* **42**, 167-195 (1896).

34   Rust, M. J., Bates, M. & Zhuang, X. Sub-diffraction-limit imaging by stochastic optical reconstruction microscopy (STORM). *Nature methods* **3**, 793-796 (2006).

35   Creech, M. K., Wang, J., Nan, X. & Gibbs, S. L. Superresolution Imaging of Clinical Formalin Fixed Paraffin Embedded Breast Cancer with Single Molecule Localization Microscopy. *Scientific Reports* **7** (2017).

36   Hell, S. & Stelzer, E. H. Fundamental improvement of resolution with a 4Pi-confocal fluorescence microscope using two-photon excitation. *Optics Communications* **93**, 277-282 (1992).

37   Bailey, B., Farkas, D. L., Taylor, D. L. & Lanni, F. Enhancement of axial resolution in fluorescence microscopy by standing-wave excitation. *Nature* **365**, 44 (1993).

38   Gustafsson, M. G. Surpassing the lateral resolution limit by a factor of two using structured illumination microscopy. *Journal of microscopy* **198**, 82-87 (2000).

39   Gustafsson, M. G. *et al.* Three-dimensional resolution doubling in wide-field fluorescence microscopy by structured illumination. *Biophysical journal* **94**, 4957-4970 (2008).

40   Schermelleh, L. *et al.* Subdiffraction multicolor imaging of the nuclear periphery with 3D structured illumination microscopy. *Science* **320**, 1332-1336 (2008).

41   Thompson, R. E., Larson, D. R. & Webb, W. W. Precise nanometer localization analysis for individual fluorescent probes. *Biophysical journal* **82**, 2775-2783 (2002).

42   Betzig, E. *et al.* Imaging intracellular fluorescent proteins at nanometer resolution. *Science* **313**, 1642-1645 (2006).

43   van de Linde, S., Wolter, S., Heilemann, M. & Sauer, M. The effect of photoswitching kinetics and labeling densities on super-resolution fluorescence imaging. *Journal of biotechnology* **149**, 260-266 (2010).

44   Pavani, S. R. P. *et al.* Three-dimensional, single-molecule fluorescence imaging beyond the diffraction limit by using a double-helix point spread function. *Proceedings of the National Academy of Sciences* **106**, 2995-2999 (2009).

45   Allen, J., Ross, S. & Davidson, M. Practical considerations for single molecule localization microscopy. (2014).

46   Juette, M. F. *et al.* Three-dimensional sub–100 nm resolution fluorescence microscopy of thick samples. *Nature methods* **5**, 527-529 (2008).

47   Shtengel, G. *et al.* Interferometric fluorescent super-resolution microscopy resolves 3D cellular ultrastructure. *Proceedings of the National Academy of Sciences* **106**, 3125-3130 (2009).

48   Hell, S. W., Lindek, S., Cremer, C. & Stelzer, E. H. Measurement of the 4pi-confocal point spread function proves 75 nm axial resolution. *Applied Physics Letters* **64**, 1335-1337 (1994).

49   Gustafsson, M., Agard, D. & Sedat, J. I5M: 3D widefield light microscopy with better than 100nm axial resolution. *Journal of microscopy* **195**, 10-16 (1999).

50   Shao, L. *et al.* I 5 S: wide-field light microscopy with 100-nm-scale resolution in three dimensions. *Biophysical journal* **94**, 4971-4983 (2008).

51   Klar, T. A. & Hell, S. W. Subdiffraction resolution in far-field fluorescence microscopy. *Optics letters* **24**, 954-956 (1999).

52   Jia, S., Vaughan, J. C. & Zhuang, X. Isotropic three-dimensional super-resolution imaging with a self-bending point spread function. *Nature photonics* **8**, 302-306 (2014).

53   Dempsey, G. T., Vaughan, J. C., Chen, K. H., Bates, M. & Zhuang, X. Evaluation of fluorophores for optimal performance in localization-based super-resolution imaging. *Nature methods* **8**, 1027-1036 (2011).

54   Vogelsang, J. *et al.* A reducing and oxidizing system minimizes photobleaching and blinking of fluorescent dyes. *Angewandte Chemie International Edition* **47**, 5465-5469 (2008).

55   Vogelsang, J., Cordes, T., Forthmann, C., Steinhauer, C. & Tinnefeld, P. Controlling the fluorescence of ordinary oxazine dyes for single-molecule switching and superresolution microscopy. *Proceedings of the National Academy of Sciences* **106**, 8107-8112 (2009).

56   Ha, T. & Tinnefeld, P. Photophysics of fluorescent probes for single-molecule biophysics and super-resolution imaging. *Annual review of physical chemistry* **63**, 595-617 (2012).

57   Olivier, N., Keller, D., Gonczy, P. & Manley, S. Resolution doubling in 3D-STORM imaging through improved buffers. *PLoS One* **8**, e69004, doi:10.1371/journal.pone.0069004 (2013).

58   Szymborska, A. *et al.* Nuclear pore scaffold structure analyzed by super-resolution microscopy and particle averaging. *Science* **341**, 655-658, doi:10.1126/science.1240672 (2013).

59   Ries, J., Kaplan, C., Platonova, E., Eghlidi, H. & Ewers, H. A simple, versatile method for GFP-based super-resolution microscopy via nanobodies. *Nat Methods* **9**, 582-584, doi:10.1038/nmeth.1991 (2012).

60   Klein, T. *et al.* Live-cell dSTORM with SNAP-tag fusion proteins. *Nature methods* **8**, 7-9 (2011).

61   Jones, S. A., Shim, S.-H., He, J. & Zhuang, X. Fast, three-dimensional super-resolution imaging of live cells. *Nature methods* **8**, 499-505 (2011).

62   Gerdes, M. J. *et al.* Highly multiplexed single-cell analysis of formalin-fixed, paraffin-embedded cancer tissue. *Proc Natl Acad Sci U S A* **110**, 11982-11987, doi:10.1073/pnas.1300136110 (2013).

63   Edelstein, A. D. *et al.* Advanced methods of microscope control using muManager software. *J Biol Methods* **1**, doi:10.14440/jbm.2014.36 (2014).

64   Ovesny, M., Krizek, P., Borkovec, J., Svindrych, Z. & Hagen, G. M. ThunderSTORM: a comprehensive ImageJ plug-in for PALM and STORM data analysis and super-resolution imaging. *Bioinformatics* **30**, 2389-2390, doi:10.1093/bioinformatics/btu202 (2014).

65   Nickerson, A., Huang, T., Lin, L. J. & Nan, X. Photoactivated Localization Microscopy with Bimolecular Fluorescence Complementation (BiFC-PALM). *J Vis Exp*, e53154, doi:10.3791/53154 (2015).

66   Murphy, D. A. & Courtneidge, S. A. The 'ins' and 'outs' of podosomes and invadopodia: characteristics, formation and function. *Nat Rev Mol Cell Biol* **12**, 413-426, doi:10.1038/nrm3141 (2011).

67   Cejas, P. *et al.* Chromatin immunoprecipitation from fixed clinical tissues reveals tumor-specific enhancer profiles. *Nat Med*, doi:10.1038/nm.4085 (2016).

68   Lucena-Aguilar, G. *et al.* DNA Source Selection for Downstream Applications Based on DNA Quality Indicators Analysis. *Biopreserv Biobank*, 1-7, doi:10.1089/bio.2015.0064 (2016).

69   Oh, E. *et al.* Comparison of Accuracy of Whole-Exome Sequencing with Formalin-Fixed Paraffin-Embedded and Fresh Frozen Tissue Samples. *PLoS One* **10**, e0144162, doi:10.1371/journal.pone.0144162 (2015).

70   Lou, J. J. *et al.* A review of room temperature storage of biospecimen tissue and nucleic acids for anatomic pathology laboratories and biorepositories. *Clin Biochem* **47**, 267-273, doi:10.1016/j.clinbiochem.2013.12.011 (2014).

71   Baday, M. *et al.* Multicolor super-resolution DNA imaging for genetic analysis. *Nano Lett* **12**, 3861-3866, doi:10.1021/nl302069q (2012).

72   Pereira, C. F., Rossy, J., Owen, D. M., Mak, J. & Gaus, K. HIV taken by STORM: super-resolution fluorescence microscopy of a viral infection. *Virol J* **9**, 84, doi:10.1186/1743-422X-9-84 (2012).

73   Ptacin, J. L. *et al.* A spindle-like apparatus guides bacterial chromosome segregation. *Nat Cell Biol* **12**, 791-798, doi:10.1038/ncb2083 (2010).

74   Sochacki, K. A. *et al.* Imaging the post-fusion release and capture of a vesicle membrane protein. *Nat Commun* **3**, 1154, doi:10.1038/ncomms2158 (2012).

75   Iqbal, N. & Iqbal, N. Human Epidermal Growth Factor Receptor 2 (HER2) in Cancers: Overexpression and Therapeutic Implications. *Mol Biol Int* **2014**, 852748, doi:10.1155/2014/852748 (2014).

76   Eliyahu, E. *et al.* Tom20 mediates localization of mRNAs to mitochondria in a translation-dependent manner. *Mol Cell Biol* **30**, 284-294, doi:10.1128/MCB.00651-09 (2010).

77   Hommelgaard, A. M., Lerdrup, M. & van Deurs, B. Association with Membrane Protrusions Makes ErbB2 an Internalization-resistant Receptor. *Molecular Biology of the Cell* **15**, 1557-1567, doi:10.1091/mbc.E03-08-0596 (2004).

78   Jeong, J. *et al.* PMCA2 regulates HER2 protein kinase localization and signaling and promotes HER2-mediated breast cancer. *Proc Natl Acad Sci U S A* **113**, E282-290, doi:10.1073/pnas.1516138113 (2016).

79   Hommelgaard, A. M., Lerdrup, M. & van Deurs, B. Association with membrane protrusions makes ErbB2 an internalization-resistant receptor. *Mol Biol Cell* **15**, 1557-1567, doi:10.1091/mbc.E03-08-0596 (2004).

80   Huang, B., Jones, S. A., Brandenburg, B. & Zhuang, X. Whole-cell 3D STORM reveals interactions between cellular structures with nanometer-scale resolution. *Nat Methods* **5**, 1047-1052 (2008).

81   Huang, B., Wang, W., Bates, M. & Zhuang, X. Three-dimensional super-resolution imaging by stochastic optical reconstruction microscopy. *Science* **319**, 810-813 (2008).

82   Schindelin, J. *et al.* Fiji: an open-source platform for biological-image analysis. *Nat Methods* **9**, 676-682, doi:10.1038/nmeth.2019 (2012).

83   Dani, A., Huang, B., Bergan, J., Dulac, C. & Zhuang, X. Superresolution imaging of chemical synapses in the brain. *Neuron* **68**, 843-856, doi:10.1016/j.neuron.2010.11.021 (2010).

84   Ilgen, P. *et al.* STED super-resolution microscopy of clinical paraffin-embedded human rectal cancer tissue. *PLoS One* **9**, e101563, doi:10.1371/journal.pone.0101563 (2014).

85   Sams, M. *et al.* Spatial cluster analysis of nanoscopically mapped serotonin receptors for classification of fixed brain tissue. *J Biomed Opt* **19**, 011021, doi:10.1117/1.JBO.19.1.011021 (2014).

86   Schedin-Weiss, S., Caesar, I., Winblad, B., Blom, H. & Tjernberg, L. O. Super-resolution microscopy reveals gamma-secretase at both sides of the neuronal synapse. *Acta Neuropathol Commun* **4**, 29, doi:10.1186/s40478-016-0296-5 (2016).

87   Schoen, M. *et al.* Super-Resolution Microscopy Reveals Presynaptic Localization of the ALS/FTD Related Protein FUS in Hippocampal Neurons. *Front Cell Neurosci* **9**, 496, doi:10.3389/fncel.2015.00496 (2015).

88   Betzig, E. *et al.* Imaging intracellular fluorescent proteins at nanometer resolution. *Science* **313**, 1642-1645, doi:10.1126/science.1127344 (2006).

89   Hess, S. T., Girirajan, T. P. & Mason, M. D. Ultra-high resolution imaging by fluorescence photoactivation localization microscopy. *Biophys J* **91**, 4258-4272, doi:10.1529/biophysj.106.091116 (2006).

90   Rust, M. J., Bates, M. & Zhuang, X. Sub-diffraction-limit imaging by stochastic optical reconstruction microscopy (STORM). *Nat Methods* **3**, 793-795, doi:10.1038/nmeth929 (2006).

91   Heilemann, M. *et al.* Subdiffraction-resolution fluorescence imaging with conventional fluorescent probes. *Angew Chem Int Ed Engl* **47**, 6172-6176, doi:10.1002/anie.200802376 (2008).

92   Dempsey, G. T., Vaughan, J. C., Chen, K. H., Bates, M. & Zhuang, X. Evaluation of fluorophores for optimal performance in localization-based super-resolution imaging. *Nat Methods* **8**, 1027-1036, doi:10.1038/nmeth.1768 (2011).

93   Jones, S. A., Shim, S. H., He, J. & Zhuang, X. Fast, three-dimensional super-resolution imaging of live cells. *Nat Methods* **8**, 499-508, doi:10.1038/nmeth.1605 (2011).

94   Manley, S. *et al.* High-density mapping of single-molecule trajectories with photoactivated localization microscopy. *Nat Methods* **5**, 155-157, doi:10.1038/nmeth.1176 (2008).

95   Xu, K., Zhong, G. & Zhuang, X. Actin, spectrin, and associated proteins form a periodic cytoskeletal structure in axons. *Science* **339**, 452-456, doi:10.1126/science.1232251 (2013).

96   Shroff, H. *et al.* Dual-color superresolution imaging of genetically expressed probes within individual adhesion complexes. *Proc Natl Acad Sci U S A* **104**, 20308-20313, doi:10.1073/pnas.0710517105 (2007).

97   Bates, M., Huang, B., Dempsey, G. T. & Zhuang, X. Multicolor super-resolution imaging with photo-switchable fluorescent probes. *Science* **317**, 1749-1753, doi:10.1126/science.1146598 (2007).

98   Pereira, P. M., Almada, P. & Henriques, R. High-content 3D multicolor super-resolution localization microscopy. *Methods Cell Biol* **125**, 95-117, doi:10.1016/bs.mcb.2014.10.004 (2015).

99   Bates, M., Dempsey, G. T., Chen, K. H. & Zhuang, X. Multicolor super-resolution fluorescence imaging via multi-parameter fluorophore detection. *Chemphyschem* **13**, 99-107, doi:10.1002/cphc.201100735 (2012).

100   Gunewardene, M. S. *et al.* Superresolution imaging of multiple fluorescent proteins with highly overlapping emission spectra in living cells. *Biophys J* **101**, 1522-1528, doi:10.1016/j.bpj.2011.07.049 (2011).

101   Lampe, A., Haucke, V., Sigrist, S. J., Heilemann, M. & Schmoranzer, J. Multi-colour direct STORM with red emitting carbocyanines. *Biol Cell* **104**, 229-237, doi:10.1111/boc.201100011 (2012).

102   Jungmann, R. *et al.* Multiplexed 3D cellular super-resolution imaging with DNA-PAINT and Exchange-PAINT. *Nat Methods* **11**, 313-318, doi:10.1038/nmeth.2835 (2014).

103   Lin, J. R., Fallahi-Sichani, M. & Sorger, P. K. Highly multiplexed imaging of single cells using a high-throughput cyclic immunofluorescence method. *Nat Commun* **6**, 8390, doi:10.1038/ncomms9390 (2015).

104   Sonehara, T., Sakai, T., Haga, T., Fujita, T. & Takahashi, S. Prism-based spectral imaging of single-molecule fluorescence from gold-nanoparticle/fluorophore complex. *Journal of fluorescence* **21**, 1805-1811, doi:10.1007/s10895-011-0875-6 (2011).

105   Broeken, J., Rieger, B. & Stallinga, S. Simultaneous measurement of position and color of single fluorescent emitters using diffractive optics. *Opt Lett* **39**, 3352-3355, doi:10.1364/OL.39.003352 (2014).

106   Zhang, Z., Kenny, S. J., Hauser, M., Li, W. & Xu, K. Ultrahigh-throughput single-molecule spectroscopy and spectrally resolved super-resolution microscopy. *Nat Methods* **12**, 935-938, doi:10.1038/nmeth.3528 (2015).

107   Nickerson, A., Huang, T., Lin, L. J. & Nan, X. Photoactivated localization microscopy with bimolecular fluorescence complementation (BiFC-PALM) for nanoscale imaging of protein-protein interactions in cells. *PLoS One* **9**, e100589, doi:10.1371/journal.pone.0100589 (2014).

108   Vaughan, J. C., Dempsey, G. T., Sun, E. & Zhuang, X. Phosphine-Quenching of Cyanine Dyes as a Versatile Tool for Fluorescence Microscopy. *Journal of the American Chemical Society* **135**, 1197 (2013).

109   Frigault, M. M., Lacoste, J., Swift, J. L. & Brown, C. M. Live-cell microscopy - tips and tools. *J Cell Sci* **122**, 753-767, doi:10.1242/jcs.033837 (2009).

110   Mlodzianoski, M. J., Curthoys, N. M., Gunewardene, M. S., Carter, S. & Hess, S. T. Super-Resolution Imaging of Molecular Emission Spectra and Single Molecule Spectral Fluctuations. *PLoS One* **11**, e0147506, doi:10.1371/journal.pone.0147506 (2016).

111   Shechtman, Y., Weiss, L. E., Backer, A. S., Lee, M. Y. & Moerner, W. E. Multicolour localization microscopy by point-spread-function engineering. *Nat Photon* **10**, 590-594, doi:10.1038/nphoton.2016.137 (2016).

112   Dong, B. *et al.* Super-resolution spectroscopic microscopy via photon localization. *Nat Commun* **7**, 12290, doi:10.1038/ncomms12290 (2016).

113   Niehorster, T. *et al.* Multi-target spectrally resolved fluorescence lifetime imaging microscopy. *Nat Methods* **13**, 257-262, doi:10.1038/nmeth.3740 (2016).

114   Klymchenko, A. S. & Mely, Y. Fluorescent environment-sensitive dyes as reporters of biomolecular interactions. *Prog Mol Biol Transl Sci* **113**, 35-58, doi:10.1016/B978-0-12-386932-6.00002-8 (2013).

115   Fauci, J. M. *et al.* Prognostic significance of the relative dose intensity of chemotherapy in primary treatment of epithelial ovarian cancer. *Gynecol Oncol* **122**, 532-535, doi:10.1016/j.ygyno.2011.05.023 (2011).

116   Harrell, J. C. *et al.* Genomic analysis identifies unique signatures predictive of brain, lung, and liver relapse. *Breast cancer research and treatment* **132**, 523-535 (2012).

117   Carey, L. A. *et al.* The triple negative paradox: primary tumor chemosensitivity of breast cancer subtypes. *Clin Cancer Res* **13**, 2329-2334, doi:10.1158/1078-0432.CCR-06-1109 (2007).

118   Neve, R. M. *et al.* A collection of breast cancer cell lines for the study of functionally distinct cancer subtypes. *Cancer Cell* **10**, 515-527, doi:10.1016/j.ccr.2006.10.008 (2006).

119   Lee-Hoeflich, S. T. *et al.* A central role for HER3 in HER2-amplified breast cancer: implications for targeted therapy. *Cancer Res* **68**, 5878-5887, doi:10.1158/0008-5472.CAN-08-0380 (2008).

120   Xia, W. *et al.* An heregulin-EGFR-HER3 autocrine signaling axis can mediate acquired lapatinib resistance in HER2+ breast cancer models. *Breast Cancer Res* **15**, R85, doi:10.1186/bcr3480 (2013).

121   Nahta, R., Hortobagyi, G. N. & Esteva, F. J. Growth factor receptors in breast cancer: potential for therapeutic intervention. *Oncologist* **8**, 5-17 (2003).

122   Masuda, H. *et al.* Role of epidermal growth factor receptor in breast cancer. *Breast Cancer Res Treat* **136**, 331-345, doi:10.1007/s10549-012-2289-9 (2012).

123   Gu, G., Dustin, D. & Fuqua, S. A. Targeted therapy for breast cancer and molecular mechanisms of resistance to treatment. *Curr Opin Pharmacol* **31**, 97-103, doi:10.1016/j.coph.2016.11.005 (2016).

124   Lemmon, M. A. & Schlessinger, J. Cell signaling by receptor tyrosine kinases. *Cell* **141**, 1117-1134, doi:10.1016/j.cell.2010.06.011 (2010).

125   Hynes, N. E. & Lane, H. A. ERBB receptors and cancer: the complexity of targeted inhibitors. *Nat Rev Cancer* **5**, 341-354, doi:10.1038/nrc1609 (2005).

126   Zhang, H. *et al.* ErbB receptors: from oncogenes to targeted cancer therapies. *J Clin Invest* **117**, 2051-2058, doi:10.1172/JCI32278 (2007).

127   Wieduwilt, M. J. & Moasser, M. M. The epidermal growth factor receptor family: biology driving targeted therapeutics. *Cell Mol Life Sci* **65**, 1566-1584, doi:10.1007/s00018-008-7440-8 (2008).

128   Moon, W. S. *et al.* Expression of betacellulin and epidermal growth factor receptor in hepatocellular carcinoma: implications for angiogenesis. *Human pathology* **37**, 1324-1332 (2006).

129   Vu, T. & Claret, F. X. Trastuzumab: updated mechanisms of action and resistance in breast cancer. *Front Oncol* **2**, 62, doi:10.3389/fonc.2012.00062 (2012).

130   Slamon, D. J. *et al.* Use of chemotherapy plus a monoclonal antibody against HER2 for metastatic breast cancer that overexpresses HER2. *N Engl J Med* **344**, 783-792, doi:10.1056/NEJM200103153441101 (2001).

131   Klapper, L. N., Waterman, H., Sela, M. & Yarden, Y. Tumor-inhibitory antibodies to HER-2/ErbB-2 may act by recruiting c-Cbl and enhancing ubiquitination of HER-2. *Cancer Res* **60**, 3384-3388 (2000).

132   Clynes, R. A., Towers, T. L., Presta, L. G. & Ravetch, J. V. Inhibitory Fc receptors modulate in vivo cytotoxicity against tumor targets. *Nat Med* **6**, 443-446, doi:10.1038/74704 (2000).

133   Junttila, T. T. *et al.* Ligand-independent HER2/HER3/PI3K complex is disrupted by trastuzumab and is effectively inhibited by the PI3K inhibitor GDC-0941. *Cancer Cell* **15**, 429-440, doi:10.1016/j.ccr.2009.03.020 (2009).

134   Nagata, Y. *et al.* PTEN activation contributes to tumor inhibition by trastuzumab, and loss of PTEN predicts trastuzumab resistance in patients. *Cancer Cell* **6**, 117-127, doi:10.1016/j.ccr.2004.06.022 (2004).

135   Nahta, R., Hung, M. C. & Esteva, F. J. The HER-2-targeting antibodies trastuzumab and pertuzumab synergistically inhibit the survival of breast cancer cells. *Cancer Res* **64**, 2343-2346 (2004).

136   Gajria, D. & Chandarlapaty, S. HER2-amplified breast cancer: mechanisms of trastuzumab resistance and novel targeted therapies. *Expert Rev Anticancer Ther* **11**, 263-275, doi:10.1586/era.10.226 (2011).

137   Scott, G. K. *et al.* A truncated intracellular HER2/neu receptor produced by alternative RNA processing affects growth of human carcinoma cells. *Mol Cell Biol* **13**, 2247-2257 (1993).

138   Nagy, P. *et al.* Decreased accessibility and lack of activation of ErbB2 in JIMT-1, a herceptin-resistant, MUC4-expressing breast cancer cell line. *Cancer Res* **65**, 473-482 (2005).

139   Shattuck, D. L., Miller, J. K., Carraway, K. L., 3rd & Sweeney, C. Met receptor contributes to trastuzumab resistance of Her2-overexpressing breast cancer cells. *Cancer Res* **68**, 1471-1477, doi:10.1158/0008-5472.CAN-07-5962 (2008).

140   Lu, Y., Zi, X., Zhao, Y., Mascarenhas, D. & Pollak, M. Insulin-like growth factor-I receptor signaling and resistance to trastuzumab (Herceptin). *J Natl Cancer Inst* **93**, 1852-1857 (2001).

141   De Keulenaer, G. W., Doggen, K. & Lemmens, K. The vulnerability of the heart as a pluricellular paracrine organ. *Circulation research* **106**, 35-46 (2010).

142   Wilson, T. R. *et al.* Widespread potential for growth-factor-driven resistance to anticancer kinase inhibitors. *Nature* **487**, 505-509, doi:10.1038/nature11249 (2012).

143   Chong, C. R. & Janne, P. A. The quest to overcome resistance to EGFR-targeted therapies in cancer. *Nat Med* **19**, 1389-1400, doi:10.1038/nm.3388 (2013).

144   Sergina, N. V. *et al.* Escape from HER-family tyrosine kinase inhibitor therapy by the kinase-inactive HER3. *Nature* **445**, 437-441, doi:10.1038/nature05474 (2007).

145   Stuhlmiller, T. J. *et al.* Inhibition of Lapatinib-Induced Kinome Reprogramming in ERBB2-Positive Breast Cancer by Targeting BET Family Bromodomains. *Cell Rep* **11**, 390-404, doi:10.1016/j.celrep.2015.03.037 (2015).

146   Mattila, P. K. & Lappalainen, P. Filopodia: molecular architecture and cellular functions. *Nat Rev Mol Cell Biol* **9**, 446-454, doi:10.1038/nrm2406 (2008).

147   Prat, A. *et al.* Research-based PAM50 subtype predictor identifies higher responses and improved survival outcomes in HER2-positive breast cancer in the NOAH study. *Clin Cancer Res* **20**, 511-521, doi:10.1158/1078-0432.CCR-13-0239 (2014).

148   Yersal, O. & Barutca, S. Biological subtypes of breast cancer: Prognostic and therapeutic implications. *World J Clin Oncol* **5**, 412-424, doi:10.5306/wjco.v5.i3.412 (2014).

149   Graham, J., Muhsin, M. & Kirkpatrick, P. Cetuximab. *Nat Rev Drug Discov* **3**, 549-550, doi:10.1038/nrd1445 (2004).

150   Kao, J. *et al.* Molecular profiling of breast cancer cell lines defines relevant tumor models and provides a resource for cancer gene discovery. *PLoS One* **4**, e6146, doi:10.1371/journal.pone.0006146 (2009).

151   Merlino, G. T. *et al.* Amplification and enhanced expression of the epidermal growth factor receptor gene in A431 human carcinoma cells. *Science* **224**, 417-419 (1984).

152   Lidke, D. S. *et al.* Quantum dot ligands provide new insights into erbB/HER receptor-mediated signal transduction. *Nat Biotechnol* **22**, 198-203, doi:10.1038/nbt929 (2004).

153   Small, J. V. & Celis, J. E. Filament arrangements in negatively stained cultured cells: the organization of actin. *Cytobiologie* **16**, 308-325 (1978).

154   Shibue, T., Brooks, M. W., Inan, M. F., Reinhardt, F. & Weinberg, R. A. The outgrowth of micrometastases is enabled by the formation of filopodium-like protrusions. *Cancer Discov* **2**, 706-721, doi:10.1158/2159-8290.CD-11-0239 (2012).

155   Suetsugu, S., Toyooka, K. & Senju, Y. Subcellular membrane curvature mediated by the BAR domain superfamily proteins. *Semin Cell Dev Biol* **21**, 340-349, doi:10.1016/j.semcdb.2009.12.002 (2010).

156   Kerber, M. L. & Cheney, R. E. Myosin-X: a MyTH-FERM myosin at the tips of filopodia. *J Cell Sci* **124**, 3733-3741, doi:10.1242/jcs.023549 (2011).

157   Cao, R. *et al.* Elevated expression of myosin X in tumours contributes to breast cancer aggressiveness and metastasis. *Br J Cancer* **111**, 539-550, doi:10.1038/bjc.2014.298 (2014).

158   Arjonen, A. *et al.* Mutant p53-associated myosin-X upregulation promotes breast cancer invasion and metastasis. *J Clin Invest* **124**, 1069-1082, doi:10.1172/JCI67280 (2014).

159   Sun, Y. *et al.* Single-molecule stepping and structural dynamics of myosin X. *Nat Struct Mol Biol* **17**, 485-491, doi:10.1038/nsmb.1785 (2010).

160   Kamioka, H., Sugawara, Y., Honjo, T., Yamashiro, T. & Takano-Yamamoto, T. Terminal differentiation of osteoblasts to osteocytes is accompanied by dramatic changes in the distribution of actin-binding proteins. *Journal of bone and mineral research* **19**, 471-478 (2004).

161   Yarden, Y. & Sliwkowski, M. X. Untangling the ErbB signalling network. *Nat Rev Mol Cell Biol* **2**, 127-137, doi:10.1038/35052073 (2001).

162   Mineo, C., Gill, G. N. & Anderson, R. G. Regulated migration of epidermal growth factor receptor from caveolae. *J Biol Chem* **274**, 30636-30643 (1999).

163   Ichinose, J., Murata, M., Yanagida, T. & Sako, Y. EGF signalling amplification induced by dynamic clustering of EGFR. *Biochem Biophys Res Commun* **324**, 1143-1149, doi:10.1016/j.bbrc.2004.09.173 (2004).

164   Nagy, P. *et al.* Activation-dependent clustering of the erbB2 receptor tyrosine kinase detected by scanning near-field optical microscopy. *J Cell Sci* **112 (Pt 11)**, 1733-1741 (1999).

165   Casaletto, J. B. & McClatchey, A. I. Spatial regulation of receptor tyrosine kinases in development and cancer. *Nat Rev Cancer* **12**, 387-400, doi:10.1038/nrc3277 (2012).

166   van Lengerich, B., Agnew, C., Puchner, E. M., Huang, B. & Jura, N. EGF and NRG induce phosphorylation of HER3/ERBB3 by EGFR using distinct oligomeric mechanisms. *Proc Natl Acad Sci U S A*, doi:10.1073/pnas.1617994114 (2017).

167   Wang, Y. *et al.* Regulation of EGFR nanocluster formation by ionic protein-lipid interaction. *Cell Res* **24**, 959-976, doi:10.1038/cr.2014.89 (2014).

168   Kaufmann, R., Muller, P., Hildenbrand, G., Hausmann, M. & Cremer, C. Analysis of Her2/neu membrane protein clusters in different types of breast cancer cells using localization microscopy. *J Microsc* **242**, 46-54, doi:10.1111/j.1365-2818.2010.03436.x (2011).

169   Nan, X. *et al.* Single-molecule superresolution imaging allows quantitative analysis of RAF multimer formation and signaling. *Proc Natl Acad Sci U S A* **110**, 18519-18524, doi:10.1073/pnas.1318188110 (2013).

170   Lee, S. H., Shin, J. Y., Lee, A. & Bustamante, C. Counting single photoactivatable fluorescent molecules by photoactivated localization microscopy (PALM). *Proc Natl Acad Sci U S A* **109**, 17436-17441, doi:10.1073/pnas.1215175109 (2012).

171   Puchner, E. M., Walter, J. M., Kasper, R., Huang, B. & Lim, W. A. Counting molecules in single organelles with superresolution microscopy allows tracking of the endosome maturation trajectory. *Proc Natl Acad Sci U S A* **110**, 16015-16020, doi:10.1073/pnas.1309676110 (2013).

172   Bretscher, M. S. Membrane structure: some general principles. *Science* **181**, 622-629 (1973).

173   Zambrano, F., Fleischer, S. & Fleischer, B. Lipid composition of the Golgi apparatus of rat kidney and liver in comparison with other subcellular organelles. *Biochimica et Biophysica Acta (BBA)-Lipids and Lipid Metabolism* **380**, 357-369 (1975).

174   Lubin, B., Chiu, D., Bastacky, J., Roelofsen, B. & Van Deenen, L. Abnormalities in membrane phospholipid organization in sickled erythrocytes. *Journal of Clinical Investigation* **67**, 1643 (1981).

175   Boggs, J. M. Lipid intermolecular hydrogen bonding: influence on structural organization and membrane function. *Biochimica et Biophysica Acta (BBA)-Reviews on Biomembranes* **906**, 353-404 (1987).

176   Van Meer, G., Voelker, D. R. & Feigenson, G. W. Membrane lipids: where they are and how they behave. *Nature reviews Molecular cell biology* **9**, 112-124 (2008).

177   Spector, A. A. & Yorek, M. A. Membrane lipid composition and cellular function. *Journal of lipid research* **26**, 1015-1035 (1985).

178   Op den Kamp, J. A. Lipid asymmetry in membranes. *Annual review of biochemistry* **48**, 47-71 (1979).

179   Prior, I. A. *et al.* GTP-dependent segregation of H-ras from lipid rafts is required for biological activity. *Nature Cell Biology* **3**, 368-375 (2001).

180   Parton, R. G. & Hancock, J. F. Lipid rafts and plasma membrane microorganization: insights from Ras. *Trends in cell biology* **14**, 141-147 (2004).

181   Pike, L. J. Growth factor receptors, lipid rafts and caveolae: an evolving story. *Biochimica et Biophysica Acta (BBA)-Molecular Cell Research* **1746**, 260-273 (2005).

182   Cremesti, A. E., Goni, F. M. & Kolesnick, R. Role of sphingomyelinase and ceramide in modulating rafts: do biophysical properties determine biologic outcome? *FEBS letters* **531**, 47-53 (2002).

183   Simons, K. & Ikonen, E. Functional rafts in cell membranes. *Nature* **387**, 569 (1997).

184   Mahammad, S. & Parmryd, I. Cholesterol depletion using methyl-β-cyclodextrin. *Methods in Membrane Lipids*, 91-102 (2015).

185   Staubach, S. & Hanisch, F. G. Lipid rafts: signaling and sorting platforms of cells and their roles in cancer. *Expert Rev Proteomics* **8**, 263-277, doi:10.1586/epr.11.2 (2011).

186   Simons, K. & Toomre, D. Lipid rafts and signal transduction. *Nat Rev Mol Cell Biol* **1**, 31-39, doi:10.1038/35036052 (2000).

187   Manes, S., del Real, G. & Martinez, A. C. Pathogens: raft hijackers. *Nat Rev Immunol* **3**, 557-568, doi:10.1038/nri1129 (2003).

188   Caldieri, G. & Buccione, R. Aiming for invadopodia: organizing polarized delivery at sites of invasion. *Trends in cell biology* **20**, 64-70 (2010).

189   Lucero, H. A. & Robbins, P. W. Lipid rafts–protein association and the regulation of protein activity. *Archives of biochemistry and biophysics* **426**, 208-224 (2004).

190   Holowka, D. *et al.* Lipid segregation and IgE receptor signaling: a decade of progress. *Biochim Biophys Acta* **1746**, 252-259, doi:10.1016/j.bbamcr.2005.06.007 (2005).

191   Plowman, S. J. & Hancock, J. F. Ras signaling from plasma membrane and endomembrane microdomains. *Biochim Biophys Acta* **1746**, 274-283, doi:10.1016/j.bbamcr.2005.06.004 (2005).

192   Prakash, P. & Gorfe, A. A. Lessons from computer simulations of Ras proteins in solution and in membrane. *Biochim Biophys Acta* **1830**, 5211-5218, doi:10.1016/j.bbagen.2013.07.024 (2013).

193   Parton, R. G. & Simons, K. The multiple faces of caveolae. *Nat Rev Mol Cell Biol* **8**, 185-194, doi:10.1038/nrm2122 (2007).

194   Nichols, B. J. *et al.* Rapid cycling of lipid raft markers between the cell surface and Golgi complex. *J Cell Biol* **153**, 529-541 (2001).

195   Brown, D. A. & Rose, J. K. Sorting of GPI-anchored proteins to glycolipid-enriched membrane subdomains during transport to the apical cell surface. *Cell* **68**, 533-544 (1992).

196   Melkonian, K. A., Chu, T., Tortorella, L. B. & Brown, D. A. Characterization of proteins in detergent-resistant membrane complexes from Madin-Darby canine kidney epithelial cells. *Biochemistry* **34**, 16161-16170 (1995).

197   Lisanti, M. P. *et al.* Characterization of caveolin-rich membrane domains isolated from an endothelial-rich source: implications for human disease. *The Journal of cell biology* **126**, 111-126 (1994).

198   Lillemeier, B. F., Pfeiffer, J. R., Surviladze, Z., Wilson, B. S. & Davis, M. M. Plasma membrane-associated proteins are clustered into islands attached to the cytoskeleton. *Proc Natl Acad Sci U S A* **103**, 18992-18997, doi:10.1073/pnas.0609009103 (2006).

199   He, H. T. & Marguet, D. Detecting nanodomains in living cell membrane by fluorescence correlation spectroscopy. *Annu Rev Phys Chem* **62**, 417-436, doi:10.1146/annurev-physchem-032210-103402 (2011).

200   Glebov, O. O. & Nichols, B. J. Lipid raft proteins have a random distribution during localized activation of the T-cell receptor. *Nat Cell Biol* **6**, 238-243, doi:10.1038/ncb1103 (2004).

201   Zacharias, D. A., Violin, J. D., Newton, A. C. & Tsien, R. Y. Partitioning of lipid-modified monomeric GFPs into membrane microdomains of live cells. *Science* **296**, 913-916, doi:10.1126/science.1068539 (2002).

202   Macdonald, J. L. & Pike, L. J. A simplified method for the preparation of detergent-free lipid rafts. *J Lipid Res* **46**, 1061-1067, doi:10.1194/jlr.D400041-JLR200 (2005).

203   Plowman, S. J., Muncke, C., Parton, R. G. & Hancock, J. F. H-ras, K-ras, and inner plasma membrane raft proteins operate in nanoclusters with differential dependence on the actin cytoskeleton. *Proc Natl Acad Sci U S A* **102**, 15500-15505, doi:10.1073/pnas.0504114102 (2005).

204   Greenspan, P., Mayer, E. P. & Fowler, S. D. Nile red: a selective fluorescent stain for intracellular lipid droplets. *J Cell Biol* **100**, 965-973 (1985).

205   Klymchenko, A. S. *et al.* Visualization of lipid domains in giant unilamellar vesicles using an environment-sensitive membrane probe based on 3-hydroxyflavone. *Biochim Biophys Acta* **1788**, 495-499, doi:10.1016/j.bbamem.2008.10.019 (2009).

206   Kao, W. Y., Davis, C. E., Kim, Y. I. & Beach, J. M. Fluorescence emission spectral shift measurements of membrane potential in single cells. *Biophys J* **81**, 1163-1170, doi:10.1016/S0006-3495(01)75773-6 (2001).

207   Mukherjee, S., Raghuraman, H. & Chattopadhyay, A. Membrane localization and dynamics of Nile Red: effect of cholesterol. *Biochim Biophys Acta* **1768**, 59-66, doi:10.1016/j.bbamem.2006.07.010 (2007).

208   Lee, S. F., Verolet, Q. & Furstenberg, A. Improved super-resolution microscopy with oxazine fluorophores in heavy water. *Angew Chem Int Ed Engl* **52**, 8948-8951, doi:10.1002/anie.201302341 (2013).

209   Sharonov, A. & Hochstrasser, R. M. Wide-field subdiffraction imaging by accumulated binding of diffusing probes. *Proc Natl Acad Sci U S A* **103**, 18911-18916, doi:10.1073/pnas.0609643104 (2006).

210   Harris, S. E., Field, J. & Imamoğlu, A. Nonlinear optical processes using electromagnetically induced transparency. *Physical Review Letters* **64**, 1107 (1990).

211   Fleischhauer, M., Imamoglu, A. & Marangos, J. P. Electromagnetically induced transparency: Optics in coherent media. *Reviews of modern physics* **77**, 633 (2005).

212   Scully, M. O. Enhancement of the index of refraction via quantum coherence. *Physical review letters* **67**, 1855 (1991).

213   Imamoğlu, A. & Harris, S. E. Lasers without inversion: interference of dressed lifetime-broadened states. *Optics letters* **14**, 1344-1346 (1989).

214   Wilson, E. A., Manson, N. & Wei, C. Perturbing an electromagnetic induced transparency within an inhomogeneously broadened transition. *Physical Review A* **67**, 023812 (2003).

215   Kasapi, A. Three-dimensional vector model for a three-state system. *JOSA B* **13**, 1347-1351 (1996).

216   Gea-Banacloche, J., Li, Y.-q., Jin, S.-z. & Xiao, M. Electromagnetically induced transparency in ladder-type inhomogeneously broadened media: Theory and experiment. *Physical Review A* **51**, 576 (1995).

217   Scully, M. O. & Zubairy, M. S.   (AAPT, 1999).

218   Hau, L. V., Harris, S. E., Dutton, Z. & Behroozi, C. H. Light speed reduction to 17 metres per second in an ultracold atomic gas. *Nature* **397**, 594-598 (1999).

219   Appel, J., Figueroa, E., Korystov, D., Lobino, M. & Lvovsky, A. Quantum memory for squeezed light. *Physical review letters* **100**, 093602 (2008).

220   Choi, K. S., Deng, H., Laurat, J. & Kimble, H. Mapping photonic entanglement into and out of a quantum memory. *Nature* **452**, 67-71 (2008).

221   Hemmer, P. *et al.* Efficient low-intensity optical phase conjugation based on coherent population trapping in sodium. *Optics letters* **20**, 982-984 (1995).

222   Jain, M., Xia, H., Yin, G., Merriam, A. & Harris, S. Efficient nonlinear frequency conversion with maximal atomic coherence. *Physical review letters* **77**, 4326 (1996).